4.3-μm TE CO_2 LASER DYNAMICS

by

ROBERT KENNETH BRIMACOMBE, B.Eng.

A Thesis

Submitted to the School of Graduate Studies

in Partial Fulfilment of the Requirements

for the Degree

Doctor of Philosophy

McMaster University

4.3-μm TE CO_2 LASER DYNAMICS

DOCTOR OF PHILOSOPHY (1984)
(Physics)

McMASTER UNIVERSITY
Hamilton, Ontario

TITLE: 4.3-μm TE CO_2 Laser Dynamics

AUTHOR: Robert Kenneth Brimacombe, B.Eng. (Royal Military College of Canada)

SUPERVISOR: Professor J. Reid

NUMBER OF PAGES: xvii, 232

ABSTRACT

This thesis describes a detailed study of the dynamics of the 4.3-μm CO_2 laser. Pulsed laser action at 4.3-μm is achieved by using a 10.4-μm sequence CO_2 laser to optically pump CO_2 molecules which have been excited in a discharge. Quantitative data regarding the processes involved in 4.3-μm lasing are presented, and techniques for optimization of performance are described. Single-line output energies of 15 mJ/pulse and peak powers of 100 kW/pulse are obtained using a conventional transversely-excited (TE) CO_2 discharge 88 cm in length. Furthermore, it is shown that pulse energies are scalable to several hundred millijoules.

The construction of a high power sequence CO_2 pump laser is discussed in detail. The laser utilizes an atmospheric pressure TE discharge 88-cm long and an intracavity hot CO_2 cell. Output energies of up to 6 J/pulse are obtained. Other work involves the characterization of discharge-excited CO_2 and the optimization of discharge operation. Several discharge parameters are measured including mode temperatures, collision-broadened linewidths, and overlapping gain and absorption coefficients. These measurements provide accurate input data for a rate-equation model of the 4.3-μm laser.

The study of 4.3-μm dynamics involves extensive measurements of small-signal gain and energy extraction. By making quantitative

comparisons between these measurements and the rate-equation model, the influence of various parameters on the operation of 4.3-μm lasers is examined. The factors which dominate the dynamics of 4.3-μm lasers are found to be the short collisional lifetime of the 4.3-μm upper laser level, the degree of discharge excitation, and the presence of interfering absorptions. As a result, efficient operation is restricted to discharge pressures below 100 Torr and CO_2 contents of less than 5 percent. The conditions which optimize performance are identified, and guidelines for scaling the 4.3-μm laser to higher pulse energies are presented.

ACKNOWLEDGMENTS

I would sincerely like to thank my supervisor, Dr. John Reid, for his guidance and support throughout the course of this work.

I also have the pleasure of thanking the following people: Dr. Tom Znotins, with whom I shared a most enjoyable collaboration on the sequence work and other projects; Dr. Hugh Morrison, who developed the computer model used in Sect. 6.2; Miss Karen Fox, who provided the tunable diode laser measurements; and Mr. Ray Auyeung, who helped in proofreading this manuscript. In addition, I am grateful to the personnel of Lumonics, Inc. for their assistance, and to NSERC for providing financial support.

Lastly and most certainly, I wish to express my deepest thanks to my wife, Lyn. Her assistance in typing and proofreading this manuscript, as well as the constant encouragement and support she has given me, have been a great help in completing this work.

TABLE OF CONTENTS

TABLE OF CONTENTS (Cont'd)

TABLE OF CONTENTS (Cont'd)

LIST OF FIGURES

LIST OF FIGURES (Cont'd)

LIST OF FIGURES (Cont'd)

LIST OF FIGURES (Cont'd)

LIST OF FIGURES (Cont'd)

LIST OF FIGURES (Cont'd)

LIST OF TABLES

CHAPTER 1

INTRODUCTION

Laser oscillation in CO_2 was first observed by Patel *et al.* in 1964 [1,2]. This discovery came at a time when the search for new laser transitions in ionic and molecular species was near its peak, and no particular attention was paid to CO_2. However, it was soon realized that CO_2 lasers were unique in that they possessed very high efficiencies and output powers. Today, multikilowatt CW CO_2 lasers are commercially available and CO_2 laser pulse energies in excess of 10 kJ are employed in inertial confinement fusion research. CO_2 lasers are widely used in medical, scientific, military, and industrial applications.

Conventional CO_2 lasers operate on two low lying rotational-vibrational bands. These are the $(00^01\text{-}02^00)$ and $(00^01\text{-}10^00)$ bands centered at 9.4 and 10.4 μm respectively, and referred to as the regular bands (a detailed description of CO_2 energy levels and laser transitions is given in Chapt. 2). The regular bands consist of more than 80 discrete laser lines which range in wavelength from approximately 9 to 11 μm. The strongest lines provide CW powers of a few tens of watts and pulse energies of several joules from typical commercially available lasers having a gain length of one meter.

In addition to their excellent output characteristics, CO_2 lasers are simple to construct and operate and are relatively low in

cost. Thus they are commonly used in applications, such as laser isotope separation, laser photochemistry, and optical pumping of molecular gases to produce mid- and far-infrared lasers. However, the CO_2 laser is limited in these frequency-dependent applications to situations where the laser frequency coincides with an absorption line of the molecule under consideration. This limitation provides a strong incentive to increase the number of output wavelengths available from CO_2 lasers.

Many new lines have been obtained in the 9 to 12 μm region by using isotopic forms of CO_2 in the laser [3]. In addition, laser oscillation has been reported on CO_2 transitions other than the regular bands. The most powerful of these other transitions are the 9.4-μm (00^02-02^01) and 10.4-μm (00^02-10^01) bands, referred to as the sequence bands. The sequence bands are analogous to the regular bands except that sequence transitions occur between higher lying energy levels, and have different frequencies due to the slight anharmonicity of the CO_2 molecule. Sequence band lasing was first observed by Reid and Siemsen in 1976 [4]. Oscillation was obtained on more than 80 sequence lines and CW output powers were ~50 % of that available on the regular lines [5]. The use of isotopic CO_2 lasers and sequence band lasers greatly increases the number of available lines with significant output powers, but still provides output in only the 9 to 12 μm wavelength region.

In 1979, Znotins et al. [6] reported a CO_2 laser which utilizes a sequence band optical pump pulse to produce a 4.3-μm output pulse. This system provides a source of coherent radiation in a wavelength region where few other lasers operate. The 4.3-μm region is of interest for applications such as laser isotope separation, laser photochemistry,

optical pumping, and atmospheric monitoring. The prospect of scaling up the 4.3-μm laser to generate high power pulses motivated the research described in this thesis.

The principle of operation of the 4.3-μm laser is simple. An electrical discharge is used to excite CO_2 molecules into the 00^02 energy level, and then an externally generated sequence pump pulse transfers population from the 00^02 level to the 10^01 level. Under appropriate operating conditions, a transient population inversion and hence gain is created on the (10^01-10^00) 4.3-μm band. With an appropriate optical resonator, lasing at 4.3 μm occurs. Prior to the work of Znotins et al. [6], laser action at 4.3 μm in CO_2 had been obtained using other pumping schemes. These included bromine transfer [7], optical pumping with HF lasers [8], and pumping from optical parametric oscillators [9]. Hocker et al. [10] also observed stimulated emission at 4.3 μm from a Q-switched CO_2 laser, but the transitions involved were not clearly identified. The use of a sequence band pump laser to obtain 4.3-μm lasing in CO_2 has many advantages over these earlier techniques. A system based only on CO_2 lasers is simple to construct and operate, uses highly developed and readily available CO_2 laser components, and the inherent scalability of CO_2-based lasers offers the potential for high energy 4.3-μm pulses.

In the initial experiments of Znotins et al. [6], the 4.3-μm output energy was ~50 μJ/pulse. An output energy of 250 μJ/pulse was soon obtained from a scaled up version of the laser [11], and high repetition rate Q-switched operation, producing >100 mW average power, was reported [12]. In all of these experiments, optimum performance

occurred with CO_2 partial pressures $\leq$ 1 Torr in the discharge. A study of the various processes involved in 4.3-μm lasing [13] suggested that significant improvements in pulse energy could be obtained by increasing the sequence pump power and CO_2 partial pressure in the discharge. However, there was little quantitative data available regarding the influence of these important parameters on the performance of the 4.3-μm laser.

In this thesis, a detailed experimental and theoretical study of the 4.3-μm CO_2 laser is presented. The primary objective of the work is to provide quantitative data which can be used to optimize the performance of the laser and accurately predict scalability to higher pulse energies. The results of this investigation have led to a significant improvement in the performance of the 4.3-μm CO_2 laser, with output energies of 15 mJ/pulse and peak powers of 100 kW/pulse being obtained from an 88-cm long, 11-cm^2 aperture gain section. This output compares favourably with other types of lasers in the same wavelength region (see Sect. 7.1), and is useful for many applications. Furthermore, the experimental results of this study show that the 4.3-μm CO_2 laser is scalable to pulse energies of several hundred millijoules.

In the first half of this thesis, preliminary experiments and results are described. Preliminary work involved the characterization of discharge excited CO_2, so that quantitative comparisons with a computer model of the 4.3-μm dynamics could be made. It was also necessary to design and build a high power pulsed sequence laser to optically pump the 4.3-μm laser. In the latter half of the thesis, a detailed study of 4.3-μm laser dynamics is described. Extensive

measurements of small-signal gain and output energy over a wide range of experimental conditions are presented, and comparisons with a computer model are made. Although transversely-excited (TE) discharges were used in the experiments, the results also pertain to Q-switched operation using CW discharge excitation. A brief outline of the contents of individual chapters is given below.

Chapter 2 reviews the theory of the CO_2 molecular laser. The concepts and background information which are presented include a brief description of the molecular structure and infrared spectrum of CO_2, electrical discharge excitation and collisional relaxation of CO_2, the mode-temperature model, and the relationship between population inversion and gain. In addition, the gain dynamics of regular, sequence, and 4.3-μm CO_2 lasers are outlined.

In Chapt. 3, experimental techniques for characterizing discharge excited CO_2 laser gas mixtures are described. Measurements of small-signal gain coefficients in the 9.4- and 10.4-μm bands enable the determination of vibrational and rotational-translational temperatures, the degree of gain overlap, and collision-broadened CO_2 linewidths. Accurate values of these parameters are required for quantitative 4.3-μm computer modeling. The results of Chapt. 3 are also relevant in many other areas of CO_2 laser research. The linewidth measurements are of particular significance, as they represent the most accurate and extensive data presently available on He-broadened CO_2 linewidths as a function of temperature and rotational quantum number.

An important step in improving the performance of 4.3-μm CO_2 lasers is the development of an efficient, high power sequence pump

laser. In Chapt. 4, the design and optimization of transversely-excited atmospheric pressure (TEA) sequence lasers is discussed. Sequence output energies of 6 J/pulse are obtained, representing 40% of the regular band pulse energy. This is the best performance which has been reported to date for pulsed sequence lasers.

Chapters 5, 6, and 7 deal with the performance of the 4.3-μm laser. Extensive experimental measurements and comparisons with a rate-equation model are described. The results fall into two categories: small-signal gain and energy extraction measurements.

In Chapt. 5, small-signal gain coefficients are measured in an amplifier using low power probe pulses from a separate 4.3-μm oscillator. The measurements are used to validate a rate-equation model of the gain dynamics. The experimental conditions which optimize the gain are determined and peak gains as high as 14 %/cm are measured. The model, which uses no adjustable parameters, is found to be in good agreement with experiment over a wide range of conditions. The only discrepancy between model and experiment is the tendency of the model to overestimate the peak gain on 4.3-μm transitions which are directly coupled to the sequence pump transition by a common energy level. In Chapt. 6, it is shown that this discrepancy is due to the dynamic Stark effect; the intense sequence pump radiation causes a splitting of the 4.3-μm line and a resulting reduction in linecenter gain. Modifications to the rate-equation model are described which account for this effect, and improved agreement with experiment is obtained.

Chapter 7 deals with the energy extraction characteristics of the 4.3-μm laser. Extensive pulse energy measurements are compared with

model calculations and good agreement is obtained over a wide range of conditions. The operating parameters most strongly influencing the performance of the laser are identified. Discharge operating conditions of 60 Torr and 4 % CO_2 are found to be optimum, and result in 4.3-μm output energies of 15 mJ/pulse. Scalability predictions based on experimental results are given, and a simplified cavity arrangement for the 4.3-μm laser is described. The feasibility of obtaining 4.5-μm lasing in N_2O is also investigated.

Chapter 8 contains a summary of the important results and conclusions of this thesis. Applications for 4.3-μm lasers are discussed.

CHAPTER 2

CO_2 LASER THEORY

2.1 Introduction

This chapter gives a brief review of the theory of the CO_2 molecular laser. It is intended to introduce the concepts and background information which are necessary to understand the experimental results and calculations described in the following chapters. A brief description of CO_2 molecular structure and the selection rules governing the infrared spectrum are given, with emphasis on the regular, sequence, and 4.3-μm laser transitions. Several topics important in CO_2 laser modeling are discussed, such as electrical discharge excitation, collisional relaxation, the mode-temperature concept, and the relationship between population inversion and gain. Finally, the gain dynamics of regular, sequence, and 4.3-μm CO_2 lasers are outlined, and typical output characteristics of these three types of lasers are described.

2.2 CO_2 Molecular Structure and Infrared Spectrum ‡

The CO_2 molecule is a linear symmetric molecule which has an axis of symmetry, C_∞, and a plane of symmetry perpendicular to the C_∞ axis. There are three normal modes of vibration: symmetric stretching

‡ The principal reference for this section is Herzberg [14].

ν_1, bending ν_2, and asymmetric stretching ν_3. The ν_2 mode is doubly degenerate, as the bending vibration can be considered to occur with equal frequency in two perpendicular planes. Each vibrational energy level is denoted by (i,j^{ℓ},k), where i, j, and k are the number of quanta excited in the ν_1, ν_2, and ν_3 modes, respectively, and ℓ denotes the angular momentum associated with the bending vibration. ℓ can take on the values j, j-2, j-4, ... 1 or 0. If $j > 1$, the vibrational level is split into more than one level (for example, 02^00 and 02^20). The levels are nondegenerate if $\ell=0$, or are doubly degenerate if $\ell\neq0$. The fundamental frequencies of the three vibrational modes are ν_1=1337 cm^{-1}, ν_2=667 cm^{-1}, and ν_3=2349 cm^{-1}. Anharmonicity of the vibrations causes a slight decrease in the energy level spacings in these modes with increasing quantum number. The energies of the 10^00 and 02^00 levels (and similar levels higher in vibrational energy) are nearly equal, i.e., $\nu_1 \simeq 2\nu_2$. This perturbs the levels, causing them to repel each other (e.g., 02^00 is found at 1285 cm^{-1} and 10^00 at 1388 cm^{-1}). This phenomenon, which was first recognized by Fermi [15], also causes a strong mixing of the eigenfunctions.‡ Consequently, the levels are more appropriately represented as $[10^00,02^00]_I$ and $[10^00,02^00]_{II}$. However, this nomenclature will not be adopted in this thesis. For convenience, 10^00 is used to represent the $[10^00,02^00]_I$ level, 02^00 for the $[10^00,02^00]_{II}$ level, and similar notation for higher lying Fermi dyads (e.g., 10^01 for the $[10^01,02^01]_I$ level). Figure 2-1 shows the vibrational energy levels of CO_2 relevant to the three principal types

‡ Fermi mixing only occurs between levels of the same species. Species of various levels are defined later in this section.

FIGURE 2-1

Simplified vibrational energy level diagram of CO_2 showing the energy levels relevant to regular, sequence, and 4.3-μm lasing.

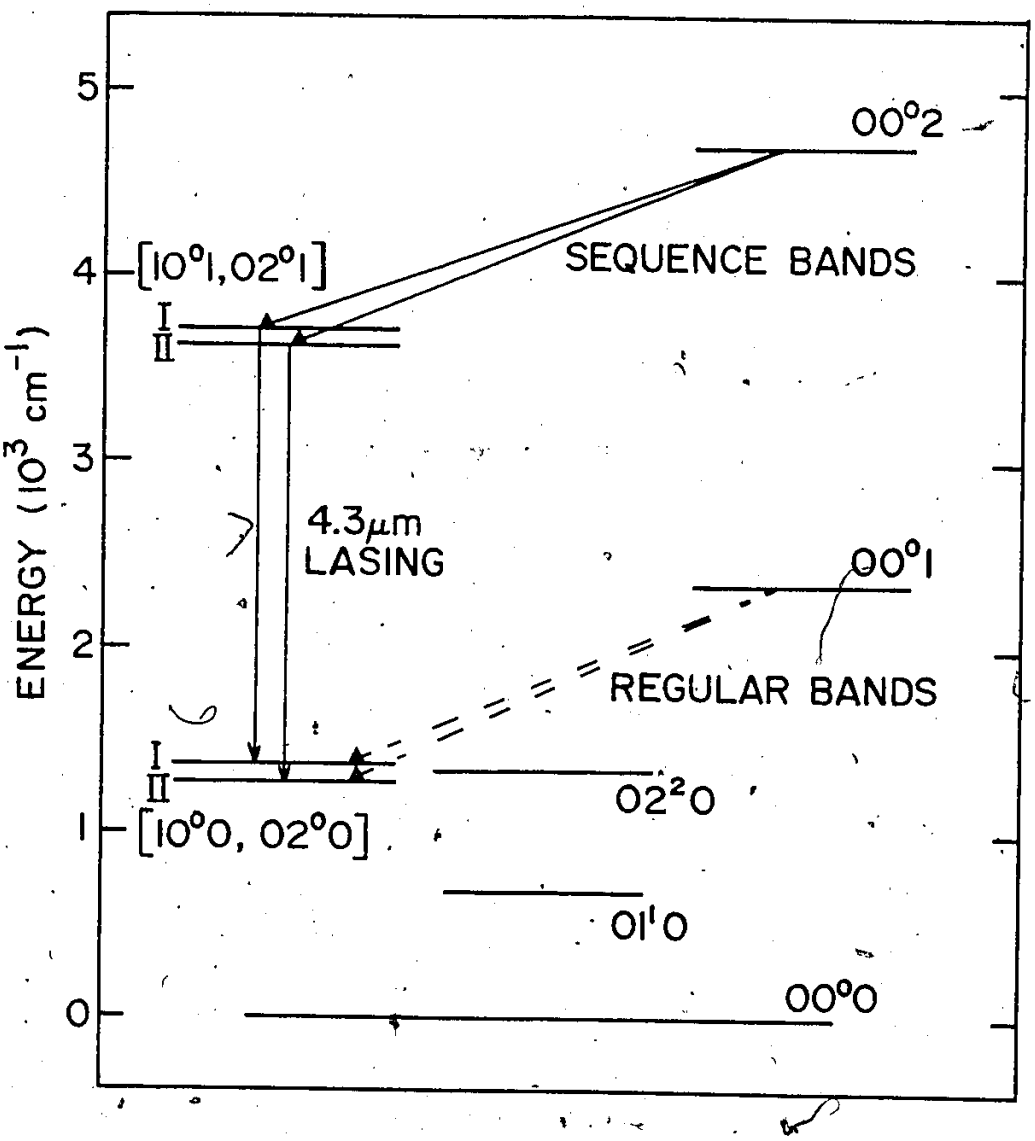
ENERGY (10^3 cm^{-1})
5
4
3
2
1
0
00^02
$[10^01, 02^01]$
SEQUENCE BANDS
I
II
4.3μm
LASING
00^01
REGULAR BANDS
I
II
02^20
$[10^00, 02^00]$
01^10
00^00

of laser transitions considered in this thesis.

The designations of species (symmetry types) for the vibrational states of the CO_2 molecule are the same as for the electronic states of homonuclear diatomic molecules [16]. Species are dependent upon the angular momentum. Levels having $\ell = 0, 1, 2, 3, \ldots$ are represented by $\Sigma, \Pi, \Delta, \Phi, \ldots$, respectively. The species of the ground state and the first excited state of each vibrational mode are Σ_g^+, Σ_g^+, Π_u, and Σ_u^+, corresponding to 00^00, 10^00, 01^10, and 00^01, respectively. The superscript of species Σ is always + for the ground electronic state of CO_2, in which all vibrational levels relevant to CO_2 lasing are found. The subscripts g and u represent the German words "gerade" meaning even, and "ungerade" meaning odd. The subscript g or u for a combination level depends upon the subscript of each of the levels combined, according to the rule: g+g → g, u+u → g, and g+u → u. For example, the level 10^01 is a combination of 10^00 and 00^01, and therefore is of species Σ_u^+. Similarly, the species of 01^11 is Π_g, and 02^20 is Δ_g, etc. A knowledge of the species of levels 10^00, 01^10, and 00^01 enables the species of any level to be determined by using the rules given above.

Superimposed upon each vibrational level is a set of rotational levels having energies given by the formula:

$$E(J) = BJ(J+1) - DJ^2(J+1)^2 + \ldots , \qquad (2\text{-}1)$$

where E is the rotational energy of the level with rotational quantum number J, and B is the rotational constant ($B \approx 0.39\ cm^{-1}$). B differs slightly for each vibrational level, becoming smaller with increasing vibrational energy because of the larger moment of inertia of the

molecule. The $DJ^2(J+1)^2$ and higher order terms enter Eq. (2-1) because of the nonrigidity of the molecule and other effects which are small compared with the first term. Figure 2-2 shows the rotational states for various species of vibrational levels. The value of ℓ defines the minimum value of J. If $\ell \neq 0$, each rotational level is split into two levels, which is known as ℓ-type doubling. The two sets of levels which result are designated c and d (or more recently e and f [17]) and have different effective rotational constants.‡ The symmetry of the rotational wavefunction with respect to inversion is indicated in Fig. 2-2 by + or −. The symmetry of the total wavefunction with respect to an exchange of identical nuclei is denoted by s or a, representing symmetric and antisymmetric. In the case of CO_2, the spins of the identical oxygen nuclei are zero. Therefore, the antisymmetric rotational energy levels are missing entirely.‡‡ This, in conjunction with ℓ-type doubling, causes the rotational-vibrational spectra of bands having $\ell \neq 0$ to exhibit frequency staggering. For those rotational levels which are allowed, the statistical weight of the level is given by $g(J)=2J+1$, which represents the number of possible orientations of J in a magnetic field (sometimes referred to as Zeeman, or M degeneracy).

The rotational-vibrational spectrum in the infrared is

---

‡ This is important when calculating line positions from spectroscopic constants. For even vibrational levels (subscript g), the rotational levels with even J are c (or e) and those with odd J are d (or f). The opposite holds for odd vibrational levels.

‡‡ In the case of nonsymmetric CO_2 molecules containing two different oxygen isotopes, both the symmetric and antisymmetric rotational levels exist.

FIGURE 2-2

Symmetry properties of the rotational levels in various species of vibrational levels of CO_2. The values in parentheses correspond to odd (subscript u) vibrational levels (from Ref. [14]).

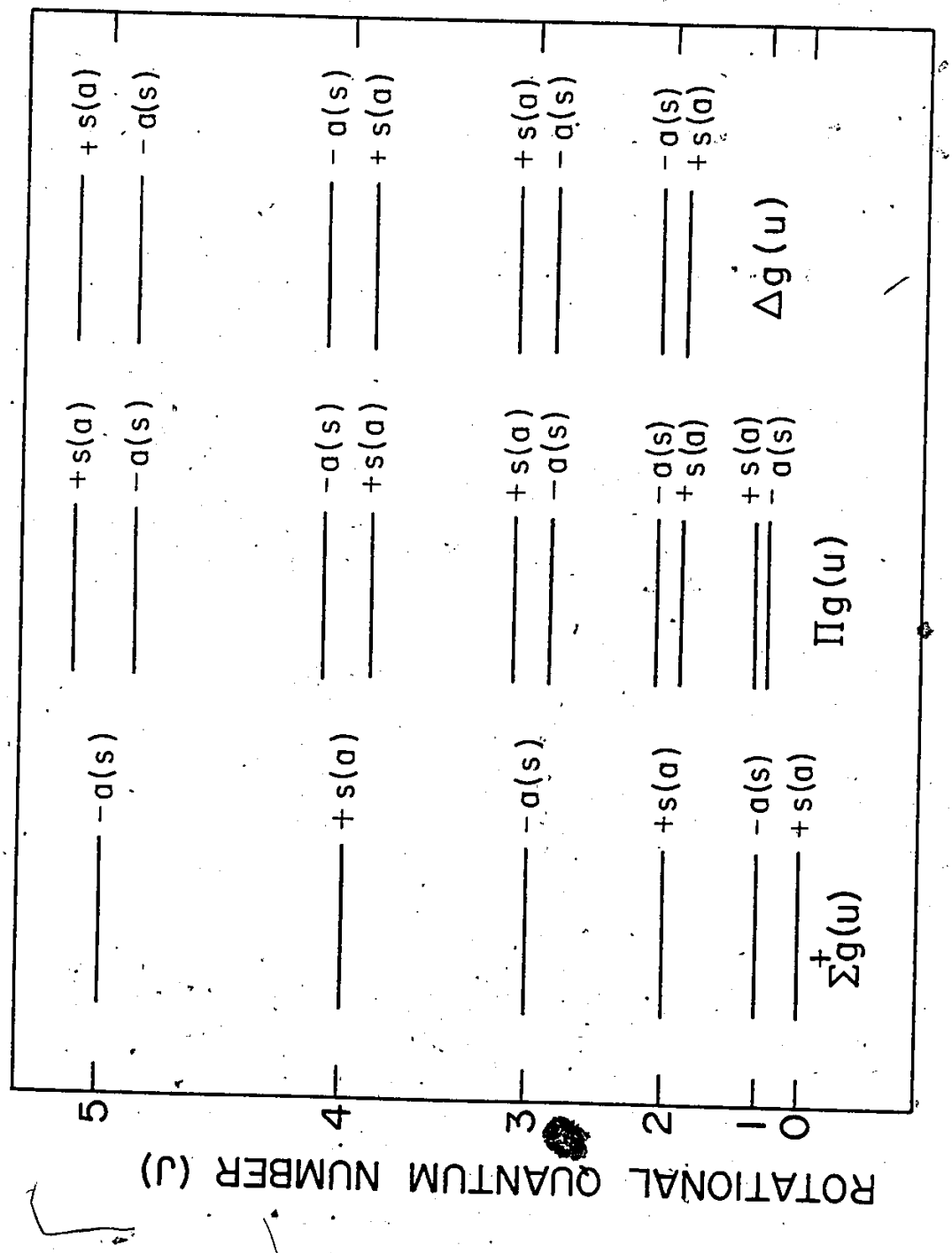
ROTATIONAL QUANTUM NUMBER (J)
0
1
2
3
4
5
$^1\Sigma_g^+(u)$
$^1\Pi_g(u)$
$^1\Delta_g(u)$
+s(a)
−a(s)
+a(s)
−s(a)

determined by the following selection rules. Only those vibrational transitions occur for which:

$$\Delta\ell = 0, \pm 1 \quad , \quad \Sigma^+ \not\leftrightarrow \Sigma^- \quad , \quad g \not\leftrightarrow g \quad , \quad u \not\leftrightarrow u, \tag{2-2}$$

and only those rotational transitions occur for which:

$$\Delta J = 0, \pm 1 \quad (J=0 \not\leftrightarrow J=0) \quad , \quad + \leftrightarrow - \quad , \quad s \not\leftrightarrow a, \tag{2-3}$$

where the symbols $\leftrightarrow$ and $\not\leftrightarrow$ represent "allowed" and "not allowed" transitions, respectively. All rotational-vibrational bands in CO_2 are comprised of a P branch ($\Delta J = -1$) and an R branch ($\Delta J = +1$). The Q branch ($\Delta J = 0$) only exists when $\ell \neq 0$ for one, or both of the vibrational levels. In parallel bands ($\Delta\ell = 0$), the Q branch is weak compared to the R and P branches, while in perpendicular bands ($\Delta\ell = \pm 1$) the Q branch is strong. The laser bands and all other bands considered in this thesis are parallel bands.

The upper and lower vibrational levels of the 10.4-μm ($00^0 1$-$10^0 0$) and 9.4-μm ($00^0 1$-$02^0 0$) regular laser bands are of species Σ_u^+ and Σ_g^+, respectively. Thus, no Q branch exists, and only the rotational states with even (odd) rotational quantum numbers exist in the lower (upper) vibrational level. Figure 2-3 is a detailed transition diagram for both the P and R branches of the 10.4- and 9.4-μm regular bands [18]. The transitions are denoted by the rotational quantum numbers of the lower level, and therefore all of the regular band transitions are denoted by even quantum numbers. The same is true for transitions of the ($10^0 1$-$10^0 0$) and ($02^0 1$-$02^0 0$) 4.3-μm laser bands, which possess the same lower levels as the regular bands. The situation reverses for the 10.4-μm ($00^0 2$-$10^0 1$) and 9.4-μm ($00^0 2$-$02^0 1$) sequence

FIGURE 2-3

Detailed transition diagram of laser oscillation in the 10.4- and 9.4-μm regular laser bands of CO_2 (from Ref. [18]).

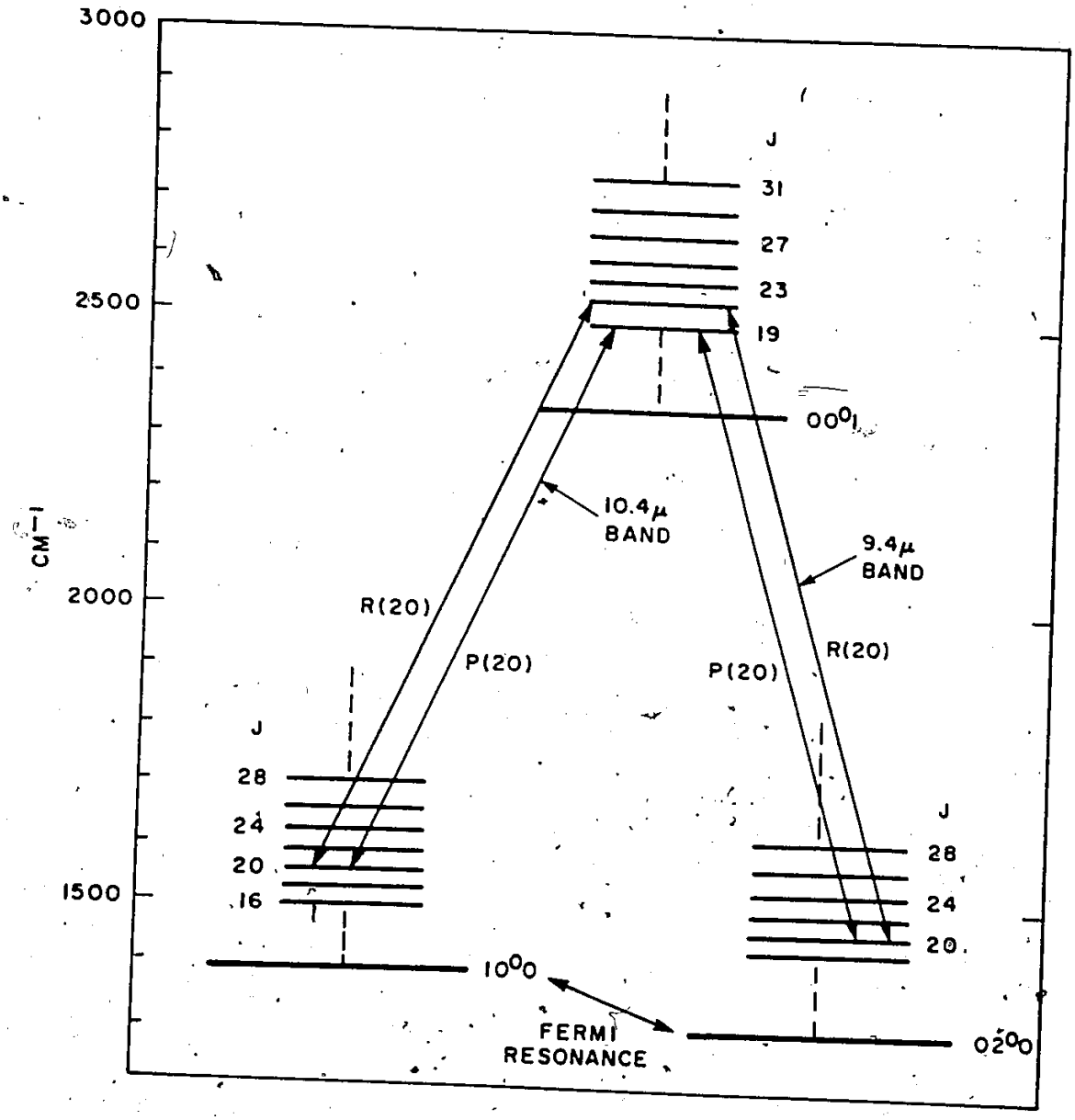
3000
2500
2000
1500
CM⁻¹
J
31
27
23
19
00⁰1
10.4μ BAND
9.4μ BAND
R(20)
P(20)
P(20)
R(20)
J
28
24
20
16
J
28
24
20
10⁰0
FERMI RESONANCE
02⁰0

bands. The sequence bands are analogous to the regular bands , with one quantum of asymmetric stretch added to each vibrational energy level. This changes the symmetry, and thus sequence transitions are represented by only odd rotational quantum numbers. A much weaker laser band which is also analogous to the 10.4-μm regular band is the $(01^{1}1\text{-}11^{1}0)$ hot band. The energy levels correspond to the regular levels plus a bending mode quantum (ν_2). Even and odd rotational states are both present in these levels because $\ell = 1$, and the observed spectra feature frequency staggering. Hot band lasing, in conjunction with regular and sequence band lasing, is important in measuring discharge parameters, as described in Chapt. 3.

There are many infrared bands in CO_2 which overlap the laser bands and contribute gain or absorption to the laser lines. The selection rules described in this section enable one to identify these bands, and the frequencies of individual rotational-vibrational transitions can be calculated from measured spectroscopic constants using standard formulae [19]. The consequences of overlaps between the laser bands and other bands in CO_2 are discussed throughout this thesis.

2.3 Electrical Discharge Excitation of CO_2

The most convenient and commonly used technique for exciting CO_2 laser gas mixtures is the self-sustained electrical discharge. This excitation method was used for the work reported in this thesis, and in particular, lasing processes in pulsed discharges were studied.

In a discharge, the energy transferred to CO_2, N_2, and He by collisions with electrons causes translational, rotational, vibrational

and electronic excitation of the atoms and molecules, as well as ionization and dissociation. For CO_2 laser operation, it is desirable to maximize the vibrational excitation of N_2 and the ν_3 mode of CO_2, while minimizing the electron energy channelled into other processes.‡ To determine the distribution of the input electrical energy transferred to the various vibrational modes requires a knowledge of electron drift velocity, electron density, electron energy distribution and elastic and inelastic collision cross-sections between electrons and all components in the gas mixture. The electron energy distribution is particularly difficult to determine experimentally and therefore a solution of the Boltzmann transport equation, utilizing measured or calculated cross-sections, is generally relied upon. Using this approach, Nighan and Bennett [21], and later Nighan [22], numerically calculated the electron energy distribution function and determined the fractional power transferred to vibrational excitation, electronic excitation, and ionization of CO_2 and N_2 molecules as a function of the ratio of applied electric field to neutral particle density E/N. These calculations were extended to include a wider range of laser gas mixtures and other experimental parameters by Lowke et al. [23] and Judd [24], who both used new, experimentally derived cross-sections for CO_2.

The results of Lowke et al. [23] are summarized in Fig. 2-4, which shows the percentage of electron energy lost to various processes

---

‡ Resonant energy transfer from vibrationally excited N_2 to the ν_3 mode of CO_2 contributes significantly to the vibrational excitation of CO_2 in a discharge [20].

FIGURE 2-4

Calculated fraction of discharge input electrical energy lost as a function of E/N to (a) elastic collisions, rotational excitation of N_2 and excitation of the ν_1 and ν_2 modes of CO_2, (b) the CO_2 00^01 level and the first eight vibrational levels of N_2, (c) electronic excitation, and (d) ionization. The predicted efficiency given by (b) increases with increasing ratio of N_2 to CO_2 (from Ref. [23]).

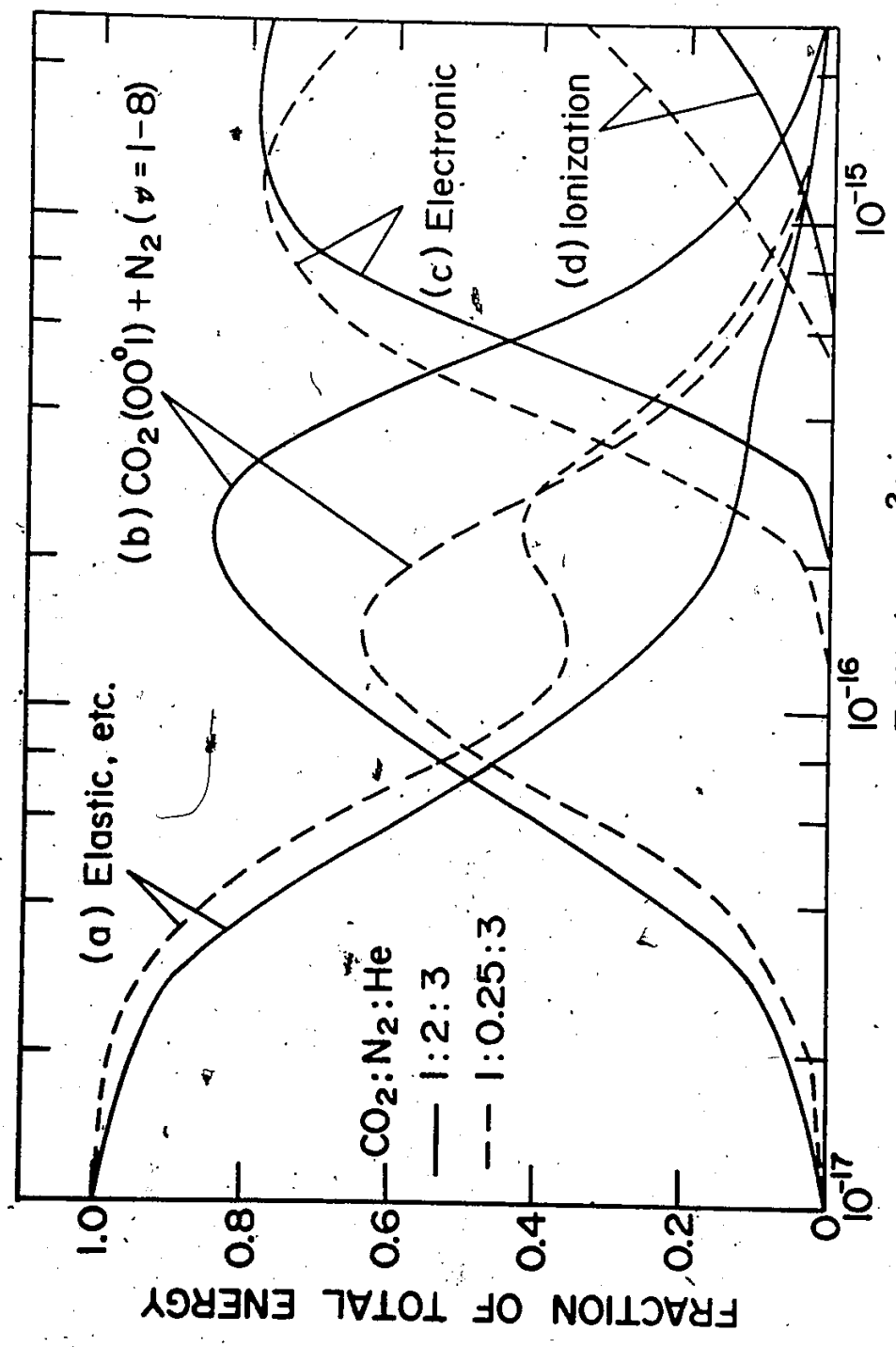
FRACTION OF TOTAL ENERGY
1.0
0.8
0.6
0.4
0.2
0
10^{-17}
10^{-16}
10^{-15}
E/N (V·cm^2)
(a) Elastic, etc.
(b) $CO_2(00^0 1) + N_2 (v = 1-8)$
(c) Electronic
(d) Ionization
CO_2:N_2:He
1:2:3
1:0.25:3

for two gas mixtures composed of CO_2, N_2, and He in the ratios 1:2:3 and 1:0.25:3. Comparison of the results indicates that much more energy is transferred into N_2 vibrations and the ν_3 mode of CO_2 when the gas mixture contains a higher concentration of N_2. This is because N_2 has a large cross-section for vibrational excitation by inelastic collisions with electrons [25]. The large N_2 cross-section, combined with the fast coupling rate between N_2 and the ν_3 mode of CO_2 (discussed in Sect. 2.4), makes N_2 an important constituent in the laser gas mixture. The results of Fig. 2-4 indicate that the optimum value of E/N for CO_2 laser operation is in the range $(1-3)\times10^{-16}$ $V\cdot cm^2$. Experimental values of E/N in self-sustained discharges range from $(2-8)\times10^{-16}$ $V\cdot cm^2$ [26,27]. Although these values are higher than optimum, they still result in a high level of vibrational excitation of N_2 and the ν_3 mode of CO_2. As indicated in Fig. 2-4, the ν_1 and ν_2 vibrational modes of CO_2 are also excited by electron collision. However, these modes are relatively quickly de-excited by molecular relaxation processes (discussed in Sect. 2.4). The favourable excitation and relaxation mechanisms in CO_2 account for the high efficiency and output power attainable on the regular laser transitions of CO_2. Calculated excitation rates into the various vibrational modes [24] have been used in the computer modeling of both regular and sequence band lasers, described in Chapt. 4.

Other authors have carried out similar calculations to those described above [28,29]. However, Lowke et al. [23] and Judd [24] used the more recent electron cross-section data. They used the data of Hake and Phelps [30] with some modification, which was largely based on

experiment; for more details, Ref. [23] should be consulted. A later measurement [31] of the excitation of the CO_2 ν_3 mode by electron collision is in agreement with Lowke et al. [23] for E/N values > $1x10^{-16}$ $V \cdot cm^2$. In a recent solution of the Boltzmann equation, Sakai et al. [32] included the effects of attachment, dissociation, and dissociative ionization by electrons. These effects seem to have little influence on the results, especially at E/N values of less than $5x10^{-16}$ $V \cdot cm^2$.

The validity of the Boltzmann equation calculations of Lowke et al. [23] and others has been examined both theoretically and experimentally. Monte Carlo simulations have been compared with Boltzmann equation solutions by Lucas and Saelee [33] and Taniguchi et al. [34], while Pitchford et al. [35] have examined the importance of higher order terms in the solution of the Boltzmann equation. It appears from these works that the two-term expansion solution used by Lowke et al. [23] and others is valid for E/N < $5x10^{-16}$ $V \cdot cm^2$. Of more significance are experimental verifications of the calculations. The calculated electron energy distribution used to predict vibrational excitation efficiency can also be used to predict many other discharge parameters. One of these parameters is discharge impedence, which was measured as a function of gas mixture by Denes and Lowke [26] and found to be in good agreement with theory. Lakshminarasimha et al. [36] have measured the ionization coefficient and the ratio of the radial diffusion coefficient to mobility of electrons, and Sierra et al. [37] have measured electron drift velocities, attachment coefficients, and ionization coefficients in gas mixtures of CO_2, N_2, and He. In both

works, good agreement was obtained with the calculations of Lowke et al. [23] over the range of E/N values relevant to CO_2 laser operation. Several additional measurements of electron drift velocities in various CO_2 laser gas mixtures have also been shown to agree with theory [38-40].

Electron de-excitation of vibrationally excited CO_2 and N_2 plays a very important role in CO_2 laser discharges [41,42]. Electron de-excitation makes a substantial contribution to the relaxation rate of the ν_3 mode of CO_2, and dominates other relaxation processes at high input electrical energy. This effect accounts for the saturation of the energy stored in the ν_3 mode observed in many previous measurements on CO_2 lasers [41-46]. Mellis and Smith [41] incorporated the de-excitation effects of superelastic electron collisions in a numerical solution of the Boltzmann equation and obtained good quantitative agreement in comparisons with measured saturation of the energy stored in the ν_3 mode. Dang et al. [42] measured the ratio of electron de-excitation to electron excitation to be ~3.5:1 in a CW discharge. Experimental evidence suggests that CO_2 has a larger cross-section for electron de-excitation than N_2. This conclusion is based on the fact that the fractional energy excited into the ν_3 mode increases as the proportion of N_2 to CO_2 in the gas mixture increases [41,45,46]. Data which illustrates this point is presented in Chapt. 3, and the implications for CO_2 laser operation are discussed. The occurrence of substantial electron de-excitation appears to be unavoidable in electrical discharge excited CO_2 lasers. The consequences of this are not as severe in CW CO_2 laser operation, as stimulated emission reduces

the population in the ν_3 mode and competes effectively with electron de-excitation. However, in pulsed lasers, the current pulse generally ends before lasing begins, and electron de-excitation severely limits the energy which can be stored in the discharge medium.

The molecular relaxation processes responsible for redistributing population among the energy levels of CO_2 are described in the next section.

2.4 Molecular Relaxation Processes

Following excitation in a pulsed discharge, many low lying vibrational energy levels of CO_2 and N_2 are populated. The processes which relax this population to the ground state are summarized in this section. The discharge operating pressures considered in this thesis are reasonably high (40 Torr to 760 Torr). Therefore, collisionally induced processes are the dominant relaxation mechanism in the absence of lasing, and de-excitation by spontaneous emission or diffusion to the walls can be neglected [42].

The collisional relaxation processes important to CO_2 laser operation are indicated by the solid lines in the energy level diagram of Fig. 2-5. Many measurements and calculations of the relaxation rates for these processes have been reported in the literature, and most of the rates are known quite accurately (within ~5-10 %). An attempt has been made to select the best available data to use in the sequence and 4.3-μm rate-equation models described in Chapts. 4 and 5. Table 2-1 lists the rate constants and also lists relaxation times for typical high pressure (sequence) and low pressure (4.3-μm) discharge conditions.

FIGURE 2-5

Summary of collisional relaxation processes relevant to CO_2 lasing. The solid lines indicate collisional processes whereas the dashed lines represent laser transitions. The relaxation times shown correspond to the low pressure 4.3-μm discharge conditions given in Table 2-1.

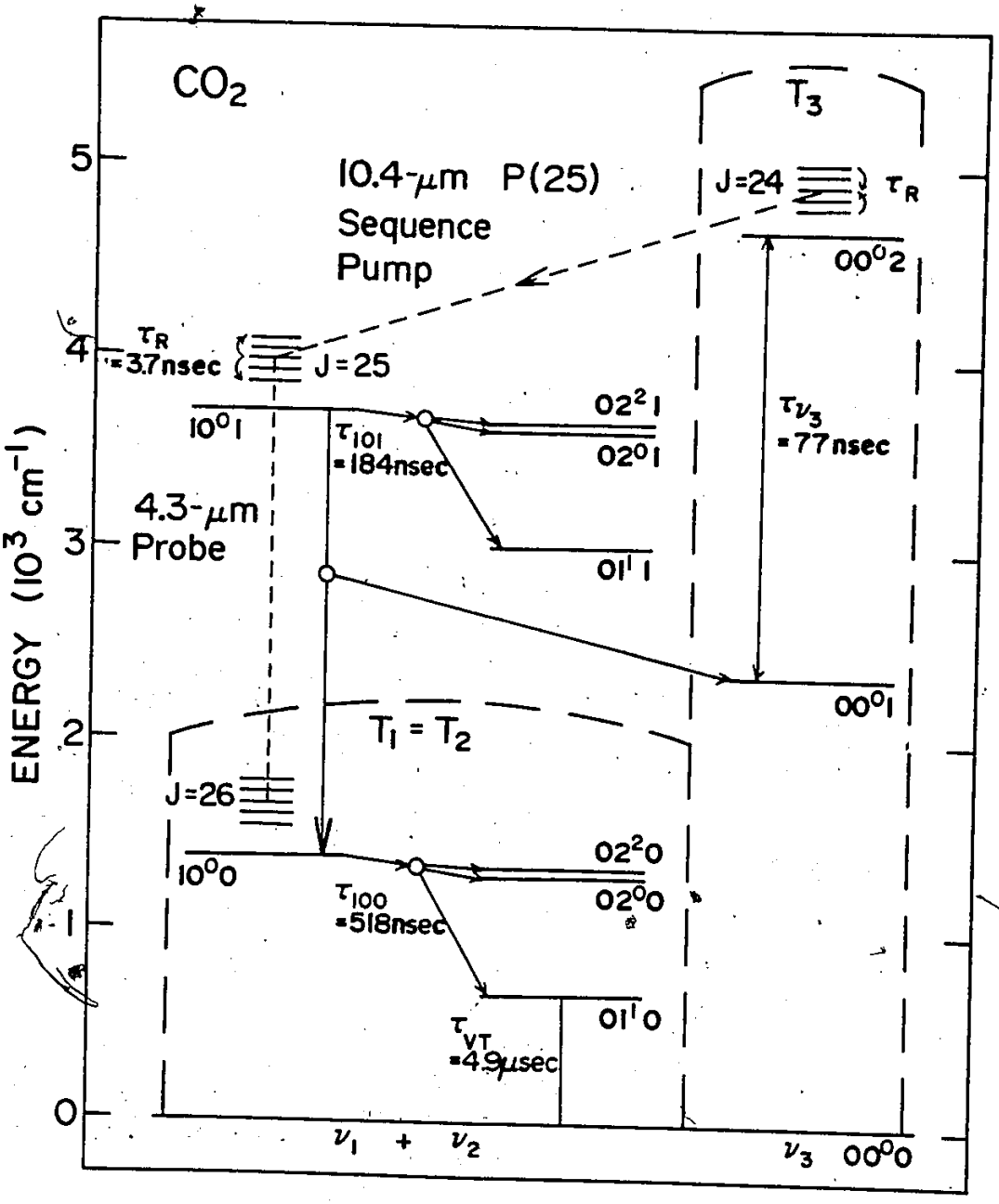
CO_2
T_3
10.4-μm P(25)
Sequence
Pump
J=24
τ_R
00^02
τ_R
=3.7nsec
J=25
10^01
τ_{101}
=184nsec
02^21
02^01
τ_{ν_3}
=77nsec
4.3-μm
Probe
01^11
00^01
ENERGY (10^3 cm^{-1})
$T_1 = T_2$
J=26
10^00
τ_{100}
=518nsec
02^20
02^00
01^10
τ_{VT}
=4.9μsec
5
4
3
2
1
0
$\nu_1 + \nu_2$
ν_3 00^00

TABLE 2-1

Summary of temperature dependent CO_2 collisional relaxation rates. k represents the rate, the subscript denotes the collision process, the molecule in brackets indicates the collision partner, and T represents the temperature (in K). Collisional lifetimes calculated from the rates are given for typical 4.3-μm and sequence laser discharge conditions.

Temperature-Dependent Relaxation Rate ($s^{-1}Torr^{-1}$) b) [a]	Reference	4.3-μm 3% CO_2:10% N_2:87% He 40 Torr, T = 360 K	Sequence 11% CO_2:16% N_2:73% He 760 Torr, T = 440 K
$k_3(CO_2) = 2.95\times10^{-5}\ T^{2.75}$, T > 400 K	[59]		
$= 94 + 0.818\ T$, 250K < T < 400K	[56]		
$k_3(N_2) = 10^{(4.44-16\ T^{-1/3})}$	[59]	τ_3 = 231 μs	τ_3 = 5.1 μs
$k_3(He) = 21.4 + 0.2\ T$	[58]		
$k_{N_2}(CO_2) = 8.60\times10^{7}\ T^{-1.5}$	[59]	τ_{N_2} = 66 μs	τ_{N_2} = 0.88 μs
$k_{VT}(CO_2) = 187\exp\{3.77\times10^{-3}(T-300)\}$	[56]		
$k_{VT}(N_2) = 115\exp\{5.98\times10^{-3}(T-300)\}$	[57]	τ_{VT} = 4.9 μs	τ_{VT} = 117 ns
$k_{VT}(He) = 3825\exp\{7.14\times10^{-3}(T-300)\}$	[58]		
$k_{100}(CO_2) = 4.3\times10^{5}$	[51]		
$k_{100}(N_2,He) = 2.5\times10^{4}(T/280)^{1.5}$	[51,53,55]	τ_{100} = 518 ns	τ_{100} = 9.8 ns
$k_{101}(CO_2) = 4.2\times10^{6}(295/T)^{1.117}$	[50,9,63]		
$k_{101}(N_2,He) = k_{100}(N_2,He)$	see text	τ_{101} = 184 ns	τ_{101} = 2.6 ns
$k_{\nu_3}(CO_2) = 13.7\times10^{6}(300/T)^{1.258}$	[63]	τ_{ν_3} = 77 ns	τ_{ν_3} = 1.0 ns
$k_R(CO_2) = 1.3\times10^{7}$	[48]		
$k_R(N_2) = 1.2\times10^{7}$	[48]	τ_R = 3.7 ns	τ_R = 0.12 ns
$k_R(He) = 0.6\times10^{7}$	[48]		

a) The temperature dependences are valid from ~300 K to ~500 K.

b) For conversion to units of cm^3/s, multiply by 1.035×10^{-19} T

The low pressure relaxation times are also indicated in Fig. 2-5. In the case of the low pressure 4.3-μm conditions, the relaxation times are calculated assuming constant pressure conditions, i.e., it is assumed that the gas in the discharge has time to expand in the period between the current pulse and the occurrence of 4.3-μm lasing.‡ In contrast, the gain risetime and the onset of lasing in a high pressure discharge occurs before the gas has time to expand. Thus, the number density remains constant and the rapid heating of the gas causes a pressure increase proportional to the temperature increase. It was necessary to include the temperature dependence of the relaxation rates to obtain good agreement between the model calculations and experiment, particularly in the 4.3-μm work. The temperature dependences shown in Table 2-1 are generally empirical fits to reported data, and the functional form has no physical significance. Each of the relaxation processes is discussed in more detail below.

Molecular collision processes can be categorized into rotational relaxation processes, vibration-to-vibration (V-V) relaxation processes, and vibration-to-translation (V-T) relaxation processes. The rotational relaxation rate, k_R, is the fastest rate and has a value close to the kinetic collision rate. This ensures thermalization of the rotational sublevels within each vibrational level, unless one of the rotational levels is perturbed by intense laser radiation. Rotational relaxation rate constants have been measured in a CO_2:N_2:He discharge at a

‡ The expansion time is determined by the speed of sound in the gas, which is independent of pressure [47].

temperature of ~400 K to be $k_R(CO_2)= 1.3\times10^7$ $s^{-1}Torr^{-1}$, $k_R(N_2)= 1.2\times10^7$ $s^{-1}Torr^{-1}$, and $k_R(He)= 0.6\times10^7$ $s^{-1}Torr^{-1}$ [48]. Other measurements made under similar conditions [49], and in pure unexcited CO_2 at 700 K [50] are in agreement, and k_R is found to be independent of temperature.

The 10^00 and 02^00 levels are the lower laser levels of both the regular and 4.3-μm CO_2 laser. Therefore, the relaxation rates of these levels are very important for accurate computer modeling. The 10^00 level is coupled to its nearby vibrational levels on a reasonably fast time scale through the V-V processes:

$$CO_2(10^00) + M \rightarrow CO_2(02^20) + M, \qquad (2\text{-}4)$$

$$CO_2(10^00) + M \rightarrow CO_2(02^00) + M, \qquad (2\text{-}5)$$

$$CO_2(10^00) + CO_2(00^00) \rightarrow 2\ CO_2(01^10), \qquad (2\text{-}6)$$

where M is the collision partner. The 02^00 level is de-excited in a similar way. The collisional relaxation rate for the 10^00 level, k_{100}, has been measured and calculated many times [51-54]. However, there is a large variation in the reported results. We have chosen to use the results of Dang et al. [51], which were measured at a temperature of ~280 K. The measured rates for the collective processes (2-4) to (2-6) are $k_{100}(CO_2)= 4.3\times10^5$ $s^{-1}Torr^{-1}$, and $k_{100}(N_2)= k_{100}(He)= 2.5\times10^4$ $s^{-1}Torr^{-1}$ [51]. Little experimental evidence is available for the temperature dependence of k_{100}. We have taken $k_{100}(CO_2)$ to be independent of temperature (two different calculations predict opposite temperature dependences [52]), while $k_{100}(He)$ and $k_{100}(N_2)$ are assumed to increase as $T^{1.5}$. This latter temperature dependence is a compromise

between the T^2 dependence calculated in [53] and the $T^{0.5}$ dependence given in [55]. The calculated 4.3-μm absorption which follows the transient gain is very sensitive to variations in k_{100}, and in Chapt. 5 it is shown that the value chosen for k_{100} gives good agreement with experimental results.

The lower levels are coupled to the ν_1 and ν_2 vibrational modes of CO_2 by processes (2-4) to (2-6). The decay of energy from the ν_1 and ν_2 modes is governed by the slower V-T process:

$$CO_2(01^10) + M \rightarrow CO_2(00^00) + M. \qquad (2\text{-}7)$$

The rate constants for this process have been accurately measured as a function of temperature. At 300 K they are: $k_{VT}(CO_2)$=187 $s^{-1}Torr^{-1}$ [56], $k_{VT}(N_2)$= 115 $s^{-1}Torr^{-1}$ [57], and $k_{VT}(He)$=3825 $s^{-1}Torr^{-1}$ [58]. It is chiefly because He is so efficient in de-exciting the 01^10 level (and hence the lower laser levels) that it is a common constituent of CO_2 laser gas mixtures.

The relaxation of the lower laser levels is rapid relative to the relaxation of the upper laser level, 00^01. This is partly responsible for the high efficiency and high output power characteristic of regular band CO_2 lasers. The de-excitation of the 00^01 level is due to the slow V-V coupling between the ν_3 mode and the ν_1 and ν_2 modes of CO_2, i.e.:

$$CO_2(00^01) + M \rightarrow CO_2(i,j^{\ell},0) + M. \qquad (2\text{-}8)$$

The rate constants for this process have been accurately measured as a function of temperature, and at 300 K they are: $k_3(CO_2)$= 339 $s^{-1}Torr^{-1}$

[56], $k_3(N_2)$= 112 $s^{-1}Torr^{-1}$ [59], and $k_3(He)$= 81 $s^{-1}Torr^{-1}$ [58].

In contrast to the slow relaxation of 00^01, there are many very fast, near-resonant V-V processes which couple energy into 00^01. The most important of these (for efficient excitation in a discharge) is the transfer of energy from vibrationally excited N_2 to $CO_2(00^01)$, i.e.:

$$CO_2(00^00) + N_2(1) \rightarrow CO_2(00^01) + N_2(0). \qquad (2\text{-}9)$$

The rate constant for this process, k_{N_2}, has been accurately measured as a function of temperature and has a value of 1.66×10^4 $s^{-1}Torr^{-1}$ at 300 K [59]. The rates for other processes which de-excite N_2 are negligible in comparison [60].

Several other near-resonant V-V processes rapidly redistribute energy within the ν_3 mode of CO_2. The rate for the process:

$$CO_2(01^11) + CO_2(00^00) \rightarrow CO_2(01^10) + CO_2(00^01), \qquad (2\text{-}10)$$

has been measured in two different experiments to be 3.7×10^6 $s^{-1}Torr^{-1}$ [61] and 5.3×10^6 $s^{-1}Torr^{-1}$ [62], both at 300 K. Two other equally fast processes are:

$$CO_2(02^01) + CO_2(00^00) \rightarrow CO_2(02^00) + CO_2(00^01), \qquad (2\text{-}11)$$

with a measured rate of 3.9×10^6 $s^{-1}Torr^{-1}$ at 295 K [9], and:

$$CO_2(10^01) + CO_2(00^00) \rightarrow CO_2(10^00) + CO_2(00^01), \qquad (2\text{-}12)$$

with a measured rate of 4.2×10^6 $s^{-1}Torr^{-1}$ at 295 K [9]. These processes are responsible for the very short lifetimes of the 10^01 and 02^01 levels, which are the 4.3-μm upper laser levels. In addition, these

processes directly populate the 4.3-μm lower laser levels, 10^00 and 02^00. The relaxation rate of the 10^01 level has also been measured at 700 K [50], confirming the temperature dependence calculated by Pack [63], as given in Table 2-1. There is a second relaxation mechanism of 10^01 which is important in the modeling of 4.3-μm lasers. It is due to collisions with N_2 and He, which transfer population from the 10^01 level to the 02^21, 02^01 and 01^11 levels, as shown in Fig. 2-5. This de-excitation mechanism is analogous to the transfer of population from 10^00 to 02^20, 02^00 and 01^10, and consequently we have assumed that $k_{101}(He,N_2) = k_{100}(He,N_2)$. A similar relaxation mechanism due to N_2 and He exists for the 02^01 level.

The fastest near-resonant V-V process is the ν_3 intra-mode relaxation, i.e.:

$$CO_2(00^01) + CO_2(00^01) \rightarrow CO_2(00^02) + CO_2(00^00). \qquad (2\text{-}13)$$

A value of $k_{\nu_3} = 18.3\times10^6$ s^{-1} $Torr^{-1}$ at 300 K has been calculated by Pack for this rate, but he suggests that this value may be too large [63]. There is one measurement (made at 700 K) which verifies Pack's calculated rate [50], however, the rates for processes (2-10) to (2-12), and other measurements of fast collisional coupling into the 00^01 level [64] are much slower ($1\text{-}5\times10^6$ $s^{-1}Torr^{-1}$). As a compromise, we have chosen to use the temperature-dependent rate calculated by Pack, reduced by a factor of 0.75 as he suggests [63].

The rapid intramode and the relatively slow intermode relaxation processes described in this section are the basis of the mode-temperature model of CO_2, which is described in the next section.

2.5 Mode-Temperature Model of CO_2

An important concept in the modeling of CO_2 lasers is that of mode temperatures. In CO_2, the transfer of energy between different vibrational modes is much slower than the redistribution of population within a mode, as described in the previous section. Therefore, in vibrationally excited CO_2, equilibrium is maintained between the energy levels within the same vibrational mode and their populations can be characterized by a single temperature, while different modes may have very different characteristic temperatures. The populations of low lying energy levels within a mode can be described by a Boltzmann distribution, although the anharmonicity of the molecule requires that a Treanor distribution be used to accurately describe the populations in high lying levels [65]. The mode-temperature model of CO_2 was first proposed by Moore et al. in 1967 [66] and Gordietz et al. in 1968 [67], and has been recently verified in several experiments [41,42,45,46,65], including the present work (see Sect. 3.6).

Each vibrational mode is characterized by a single vibrational temperature. Thus the temperatures T_1, T_2, and T_3 are associated with the modes ν_1, ν_2, and ν_3 respectively. Due to the rapid V-V coupling of the ν_1 and ν_2 modes, T_1 equals T_2 in a discharge [65]. For convenience, the exponential factors x_1, x_2, and x_3 are introduced, defined by:

$$x_n = \exp(-h\nu_n/kT_n), \tag{2-14}$$

where $h\nu_n$ is the mode spacing of the nth mode, and k is Boltzmann's constant. The population of any vibrational level can then be

calculated if the mode temperatures are known, using:

$$N(i\ell k) = \frac{N_{CO_2}\, g_i g_j g_k\, (x_1)^i\, (x_2)^j\, (x_3)^k}{Q_V}, \qquad (2\text{-}15)$$

where N_{CO_2} is the number density of CO_2 molecules, and g_i, g_j, and g_k are the statistical weights of the vibrational levels. g_i and g_k always equal one, and g_j=1 or 2, for ℓ=0 or $\ell\neq 0$, respectively (see Sect. 2.2). Q_V is the vibrational partition function and is given by $Q_V = [(1-x_1)(1-x_2)^2(1-x_3)]^{-1}$. The distribution of the vibrational population among the rotational sublevels is characterized by the rotational temperature, T. In view of the extremely fast rotational relaxation of CO_2, it is assumed that the rotational temperature is equal to the background gas temperature. The rotational population factor is given by:

$$K(J) = \frac{g(J)}{Q_R} \exp(-BJ(J+1)/kT), \qquad (2\text{-}16)$$

where Q_R is the rotational partition function. For vibrational levels which possess only even or only odd rotational levels, $Q_R = kT/2hcB$, where c is the speed of light. For vibrational levels which possess all rotational levels, Q_R is increased by a factor of 2.

The three temperatures, T, T_1, and T_3 in a discharge can be determined from gain coefficients measured in the regular, sequence, and hot bands as described in Chapt. 3. Knowledge of the discharge temperatures, gas mixture, and pressure in a discharge enables one to calculate the population in any rotational level, and hence the

population inversion for any transition. In the next section, the relationship between population inversion and gain is presented.

2.6 Relationship Between Inversion and Gain

To obtain an accurate knowledge of any laser system, it is important to be able to calculate the stimulated emission cross-section σ, which relates gain to the population inversion between two energy levels. A generalized expression is given in this section which enables the calculation of σ for all CO_2 transitions of interest in this thesis.

In a gas, the gain coefficient between two energy levels can be written [68]:

$$\alpha(\nu) = \frac{\lambda_o^2}{8\pi} A_{u\ell}\, g(\nu)\, (K_u N_u - K_\ell N_\ell\, g_u/g_\ell), \qquad (2\text{-}17)$$

where the subscripts u and ℓ denote the upper and lower levels, respectively. The population inversion, $\delta = K_u N_u - K_\ell N_\ell\, g_u/g_\ell$, can be calculated from mode temperatures as described in the previous section. The product $K_i N_i$ represents the rotational population, and g_i is the statistical weight of the level i. The remaining part of Eq. (2-17) is the gain cross-section, i.e., $\sigma(\nu) = (\lambda_o^2/8\pi)\ A_{u\ell}\, g(\nu)$, where λ_o is the wavelength at the center of the spectral line, $A_{u\ell}$ is the spontaneous transition rate, and $g(\nu)$ is the normalized lineshape function.

For the range of gas pressures considered in this thesis, a combination of Doppler and collision broadening, or collision broadening alone, are responsible for the optical linewidths. The normalized lineshape function for combined Doppler and collision broadening (the

Voigt profile) is given by :

$$g(\nu) = \frac{1}{\pi^{3/2}\,\Delta\nu_c} \int_{-\infty}^{\infty} \frac{y^2 \exp(-t^2)}{y^2 + (x-t)^2}\, dt, \qquad (2\text{-}18)$$

where $y=[\ell n(2)]^{1/2}\Delta\nu_c/\Delta\nu_D$, $x=[\ell n(2)]^{1/2}(\nu-\nu_o)/\Delta\nu_D$, and $\Delta\nu_D$ and $\Delta\nu_c$ are the Doppler and collision half widths at half maximum (HWHM). At the line center, $\nu=\nu_o$, Eq. (2-18) can be reduced to :

$$g(\nu_o) = \frac{1}{\pi^{1/2}\,\Delta\nu_c}\, y \exp(y^2)\, \mathrm{erfc}(y), \qquad (2\text{-}19)$$

where erfc is the complementary error function. If $\nu\neq\nu_o$, $g(\nu)$ can be calculated numerically for arbitrary x and y [69]. When collision broadening is the dominant broadening mechanism (i.e., y>3), $g(\nu)$ is given by :

$$g(\nu) = \frac{1}{\pi\,\Delta\nu_c}\, \frac{1}{1 + [(\nu-\nu_o)/\Delta\nu_c]^2}, \qquad (2\text{-}20)$$

which is the normalized Lorentzian lineshape function.

The Doppler-broadened linewidth is given by $\Delta\nu_D = (\nu_o/c)(2kT\,\ell n(2)/M)^{1/2}$, where M is the mass of the molecule. For 4.3-μm transitions, $\Delta\nu_D\simeq 65$ MHz and for 10.4-μm transitions, $\Delta\nu_D\simeq 27$ MHz. The collision-broadened linewidth, $\Delta\nu_c$, is proportional to the pressure of the gas, and for typical CO_2 laser conditions the broadening coefficient is ~2.5 MHz/Torr. The collision-broadened linewidth in a TE CO_2 discharge can be accurately calculated for any conditions by the expression :

$$\Delta\nu_c = P/760\ (\psi_{CO_2}\alpha_{CO_2} + \psi_{N_2}\alpha_{N_2} + \psi_{He}\alpha_{He})\ (T/300)^{0.42}, \qquad (2\text{-}21)$$

where P is the total pressure and ψ_a is the fraction of gas a in the mixture. The temperature dependence is based on measurements made as part of this work, which are described in Sect. 3.5. Equation (2-21) assumes conditions of constant number density. For constant pressure, $\Delta\nu_c$ is obtained by multiplying the temperature dependence by 300/T. The α_a coefficients represent a straight-line fit to the linewidth as a function of J for collision broadening by gas a, and are given in cm^{-1}/atm by:

$$\alpha_{CO_2} = 0.1149 - 9.2\times10^{-4}\ |m|, \qquad (2\text{-}22)$$

$$\alpha_{N_2} = 0.0794 - 4.3\times10^{-4}\ |m|, \qquad (2\text{-}23)$$

$$\alpha_{He} = 0.0598 - 2.8\times10^{-5}\ |m|, \qquad (2\text{-}24)$$

where $m = -J_\ell$ for the P branch and $m = J_\ell + 1$ for the R branch. The expression for α_{He} is based on measurements described in Sect. 3.5. The expressions for α_{CO_2} and α_{N_2} are obtained by averaging many linewidth measurements in the 9.4-μm and 10.4-μm bands [70-74] in the following way. A straight line fitted to each set of data is scaled to agree at P(20) with the measurements of Abrams [75] for CO_2-CO_2 broadening or CO_2-N_2 broadening. A weighted average of these lines then gives α_{CO_2} and α_{N_2}, the weight corresponding to the standard deviation of the fit. The data of Abrams [75] for the 10.4-μm P(20) line was considered to be the most accurate since the linewidth was directly measured by using a tunable waveguide laser, whereas all the other data were obtained from absorption coefficients measured at the line center only. For the

calculations described throughout this thesis, the same linewidth is assumed for all bands (4.3-μm, 9.4-μm, and 10.4-μm). Theoretical calculations suggest that linewidths do not vary significantly between different bands [76,77], and tunable diode laser measurements of N_2-broadened 4.3-μm [78] and 15-μm [79] CO_2 linewidths are in good agreement with Eq. (2-23). In addition, the He-broadened linewidth measurements which were made on 10.4-μm lines as part of this work are in good agreement with a linewidth measurement at 4.3 μm (see Sect. 3.5).

The spontaneous transition rate is given by:

$$A_{u\ell} = \frac{64\pi^4 \nu |R_{u\ell}|^2 S_J F_J}{3 h \lambda_o^3 g_u}, \qquad (2\text{-}25)$$

where h is Planck's constant, $|R_{u\ell}|$ and S_J are the vibrational and rotational contributions to the transition dipole moment, respectively, and F_J is the interaction factor between vibration and rotation (which is close to unity). S_J is a function of both J and ℓ (where ℓ denotes the angular momentum of the vibrational level) and equations for calculating S_J are given in Table 2-2 for P-, Q-, and R-branch transitions [80].

$R_{u\ell}$ and F_J are generally determined by fitting Eq. (2-17) to absorption coefficients measured in pure, room-temperature, CO_2. Since the rotational constants for CO_2 are accurately known and the rotational population can be accurately calculated when the gas temperature is known, the only uncertainties are $|R_{u\ell}|$, F_J, and $g(\nu_o)$. At low pressure, where Doppler broadening dominates, $g(\nu_o)$ can be calculated,

TABLE 2-2

Rotational contribution to the transition dipole moment S_J for P, Q, and R branch transitions. ℓ denotes the angular momentum of the vibrational level and J represents the rotational quantum number of the lower level.

Branch	S_J	
	$\ell = 0$	$\ell \neq 0$
P	J	$\frac{2\,(J^2-\ell^2)}{J}$
Q	0	$\frac{2\,(2J+1)\,\ell^2}{J\,(J+1)}$
R	J + 1	$\frac{2\,[(J+1)^2-\ell^2]}{J+1}$

whereas at high pressure $g(\nu_o)$ depends on $\Delta\nu_c$. In the past, $|R_{u\ell}|$, F_J, and $\Delta\nu_c$ have been deduced from linecenter absorption measurements, made at both low pressure and at high pressure [70]. However, it is difficult to separate out the effects of linewidth and linestrength using this technique, and the procedure is prone to errors [81]. Even when correctly applied, the results show surprising inconsistencies. For example, many authors measure the same small-signal absorption to within ~3 % at the line center of the 9.4-μm and 10.4-μm regular laser transitions in pure CO_2 at pressures >100 Torr [70-73]. Yet, the collision-broadened linewidths determined from these measurements vary by as much as 10 % [71,72], with similar variations in $|R_{u\ell}|$. Although the data of each author is self-consistent and correctly reproduces the measured absorption in pure CO_2, calculations of gain and absorption in CO_2:N_2:He gas mixtures may be incorrect, because both the magnitude and the J dependence of the broadening coefficient are different for each gas (see Eqs. (2-22) to (2-24)). In addition, CO_2 is generally a minor constituent of the gas mixture, and therefore an incorrect value of $|R_{u\ell}|$ can no longer be compensated for by a self-consistent, and equally incorrect value of the self-broadened linewidth.

To enable accurate gain and absorption calculations to be made in gas mixtures, α_{CO_2} of Eq. (2-22) (which had been normalized to the accurate linewidth measurements of Abrams) was used in Eq. (2-21) to obtain $\Delta\nu_c$. Consistent values of $|R_{u\ell}|$ and F_J were then obtained by using this value of $\Delta\nu_c$ in Eq. (2-17), and fitting (with an average deviation of < 3 %) to all of the reported high pressure absorption data [70-73]. Values of $|R_{u\ell}|$ and F_J were determined for the regular bands

and are given in Table 2-3.‡ The ratio $|R_{u\ell}|^2_{seq}/|R_{u\ell}|^2_{reg}$ for the sequence and regular bands has been measured to be 1.89 for the 9.4-μm band and 2.1 for the 10.4-μm band [46,82]. These values are both close to the value of two predicted by the harmonic oscillator approximation. $|R_{u\ell}|$ has also been determined for the 4.3-μm fundamental band (00^o1-00^o0) [78,83] and the 4.3-μm laser band (10^o1-10^o0) [78]. The measurements by Malathy Devi et al. [78] are based on tunable diode laser measurements and are probably the most accurate. For transitions where measurements are not available, F_J is set equal to one and the harmonic oscillator approximation is used to obtain $|R_{u\ell}|$ (i.e., $|R_{002-001}|^2 = 2\,|R_{001-000}|^2$, $|R_{003-102}|^2 = 3\,|R_{001-100}|^2$, etc.). In Table 2-3, values of F_J, $|R_{u\ell}|$, and $A_{u\ell}$ are given for several transitions relevant to the work described in this thesis. Note that the transition dipole moment in the 4.3-μm bands is very large, resulting in large gain coefficients in the 4.3-μm laser, as described in Chapt. 5.

The theory presented in this and the previous section can be used to calculate gain or absorption on any CO_2 transition of interest in a laser gas mixture, given the temperatures T, T_1, and T_3.

2.7 Gain and Output Characteristics of CO_2 Lasers

In this section, the dynamics of pulsed laser operation on the regular, sequence, and 4.3-μm bands of CO_2 are outlined. Typical

---

‡ In Sect. 3.6, it is shown that these values of $|R_{u\ell}|$ and F_J in conjunction with $\Delta\nu_c$ of Eqs. (2-21) to (2-24) correctly predict gain in a CO_2:N_2:He gas mixture.

TABLE 2-3

CO_2 linestrength constants used for gain and absorption calculations in this thesis.

Band	Band Center (μm)	F_J a)	$\lvert R_{u\ell}\rvert$ (Debye) b)	$\frac{\lvert R_{u\ell}\rvert^2}{\lvert R_{00^01}\rvert^2}$	$A_{u\ell}$ c) (s^{-1})
$00^01 - 10^00$	10.4	$1-1.8\times10^{-3}m+3.7\times10^{-5}m^2$ d)	0.0371 d)		0.20
$00^01 - 02^00$	9.4	$1-2.4\times10^{-4}m+4.1\times10^{-5}m^2$ d)	0.0339 d)		0.22
$00^02 - 10^01$	10.4	same as (00^01-10^00)		2.1 e),f)	0.41
$00^02 - 02^01$	9.4	same as (00^01-02^00)		1.89 f)	0.40
$01^11 - 11^10$	10.8	same as (00^01-10^00)		0.54 g)	0.19
$10^01 - 10^00$	4.3	1 h)	0.3116 h)		192
$00^01 - 00^00$	4.3	1 h)	0.3237 h)		213

a) $m=-J_\ell$ (P branch) or $m=J_\ell+1$ (R branch).

b) For conversion to units of $(J\cdot m^3)^{1/2}$, multiply by 3.162×10^{-25}.

c) Calculated for the P branch, $J\approx20$.

d) Present study, see text.

e) Siemsen et al. [46].

f) Reid et al. [82].

g) Cousin et al. [73].

h) Malathy Devi et al. [78].

small-signal gain values and output pulse characteristics are also given.

2.7.1 Regular Laser Bands

Gain on the regular laser transitions in CO_2 arises as a result of the combined effects of the electron excitation and collisional relaxation processes detailed in Sects. 2.3 and 2.4. The generally accepted model for regular CO_2 laser dynamics is outlined below [84]. The same processes are also responsible for lasing in both the sequence and 4.3-μm bands.

Consider a CO_2:N_2:He laser gas mixture which is excited in a pulsed electrical discharge. As a result of direct excitation by electrons and collisional transfer from excited N_2 molecules, all the low lying vibrational levels in CO_2 are populated. The population in the tightly coupled $\nu_1 + \nu_2$ mode decays away rapidly relative to the population in the ν_3 mode. Consequently, after a period of time (several V-T relaxation times), the levels in the $\nu_1 + \nu_2$ mode are effectively empty, whereas a substantial population still exists in the ν_3 mode. In particular, an inversion has been created between the 00^01 level and the 10^00 and 02^00 levels. This inversion results in gain on the 10.4- and 9.4-μm regular laser bands. The risetime and falltime of the gain reflect the lifetimes of the lower and upper laser levels respectively, while the peak gain can be obtained from the values of the mode temperatures at that time. For a typical atmospheric pressure gas mixture of 20% CO_2: 20% N_2: 60% He, discharge temperatures of approximately T=490 K, T_1=520 K, and T_3=1800 K at the peak of the gain

can be obtained (see Sect. 3.4). This corresponds to a fractional population of ~9 % in the $00^0 1$ level and ~1.3 % in the $10^0 0$ level. Substituting these values into the small-signal gain expression of Sect. 2.6 gives a value of ~2.4 %/cm for the peak small-signal gain. If an 88-cm long, 11-cm^2 aperture discharge is placed in an optical resonator, a typical output pulse has an energy of ~15 J and a peak power of ~40 MW under these conditions.

2.7.2 Sequence Laser Bands

It is apparent from the previous section that gain will exist on other transitions in addition to the regular laser bands. In particular, there will be appreciable gain on those transitions having upper levels belonging to the ν_3 mode, i.e., transitions of the type $(00^0 n \rightarrow 10^0 n-1)$.‡ Although this fact was recognized in earlier studies of CO_2 lasers [85] it was not until 1976 that Reid and Siemsen [4] constructed a laser operating on the $(00^0 2-10^0 1)$ and $(00^0 2-02^0 1)$ sequence bands. The difficulty in achieving sequence oscillation arises because the population of the $00^0 2$ level is less than that of the $00^0 1$ level, which lies lower in vibrational energy. (For T_3 = 2100 K, the fractional population in $00^0 2$ is only ~2.4 %, whereas it is ~12 % in $00^0 1$.) Therefore the gain on the sequence transitions is also lower (~40 % of the regular gain). Consequently, CO_2 lasers operate solely on the regular transitions unless regular laser operation is selectively suppressed in some manner.

---

‡ Using tunable diode lasers, gain has been experimentally observed on transitions up to n = 4 (i.e., $00^0 4-10^0 3$) [46].

The sequence bands are very similar to the regular laser bands. However, the small anharmonicity of the CO_2 molecule results in sequence band frequencies which are slightly different from those of the regular bands. In general, the differences are so small that the wavelength discrimination of a typical grating-tuned laser cavity is not sufficient to obtain sequence oscillation. An efficient means of achieving sequence oscillation is to use the absorption properties of hot CO_2. This technique is based on the fact that the lower levels of the regular CO_2 laser bands lie only ~1300 cm^{-1} above the ground state and are thermally populated much more easily than the lower levels of the sequence bands, which have energies of ~3700 cm^{-1}. Consequently, the regular laser lines experience considerable absorption in hot (~550 K) CO_2, while the absorption on the sequence lines remains small. Therefore, by placing a hot CO_2 cell inside the optical cavity of a conventional CO_2 laser, the regular lines can be suppressed and lasing will only take place on the sequence lines.

Using an intracavity hot cell, Reid and Siemsen [5] were able to achieve CW laser oscillation on more than 80 lines in the 00^o2 9.4-μm and 10.4-μm sequence bands, with output powers up to 50% of the power levels available on the regular lines from the same laser. Reference [5] provides a comprehensive discussion of sequence lasing in CW CO_2 lasers. A detailed description of sequence lasing in TEA CO_2 lasers is given in Chapt. 4, where it is shown that the hot cell technique is also an efficient means of achieving high power sequence band oscillation from a conventional TEA CO_2 laser. A typical atmospheric pressure sequence laser gas mixture consists of 11% CO_2: 16% N_2: 73% He.

Discharge temperatures of approximately T=440 K, T_1=470 K, and T_3=2100 K at the peak of the gain can be obtained under these conditions. Peak small-signal gain coefficients are ~0.9 %/cm and pulse energies and peak intensities are approximately one-third to one-half of that available on the regular bands.

The use of sequence lasers to produce 4.3-μm lasing in CO_2 is described in the next section.

2.7.3 4.3-μm Laser Bands

As described in Chapt. 1, the use of sequence laser radiation to optically pump discharge excited CO_2 and produce 4.3-μm laser oscillation was first reported by Znotins et al. in 1979 [6]. The principle of operation can be understood by referring to Fig. 2-1. A CO_2 laser gas mixture is excited in a pulsed electrical discharge. This results in significant population of the low lying vibrational levels of CO_2. The ν_1 and ν_2 mode populations decay away rapidly, producing gain on both the regular and sequence band transitions. When the sequence gain reaches its peak, the gas mixture is optically pumped with an intense, saturating pulse of sequence radiation. This results in significant population transfer from the 00^02 level to the 10^01 level by stimulated emission (i.e., the pump pulse is amplified). The 10^00 level is nearly empty however, and under proper operating conditions, a population inversion and hence gain is created in the (10^01-10^00) band. In a suitable cavity, lasing can then take place at a wavelength near 4.3 μm.

The 4.3-μm CO_2 laser, typically operates with a low pressure gas

mixture and a low CO_2 content (~60 Torr and ~4 % CO_2). Small-signal gain coefficients are generally quite large, ~10 %/cm, because of the large 4.3-μm transition dipole moment. The gain dynamics are described in detail in Chapts. 5 and 6. The maximum 4.3-μm pulse energy that has been obtained to date is 15 mJ, and the corresponding peak power is 100 kW. This performance was achieved as part of the present study, and was obtained from an 88-cm long by 11-cm^2 aperture discharge. The optimization of 4.3-μm pulse energy is discussed in Chapt. 7.

2.8 Summary

This chapter has presented a review of CO_2 laser theory with emphasis on the aspects which are relevant to this thesis. It is intended that the information presented here serve as a background for the discussion of the following chapters, which are concerned primarily with optimizing the performance of sequence and 4.3-μm lasers. In the next chapter, optimization of discharge operating conditions and discharge characterization in terms of mode temperatures are discussed.

CHAPTER 3

EXPERIMENTAL TECHNIQUES FOR DISCHARGE CHARACTERIZATION

3.1 Introduction

In this chapter, experimental techniques for characterizing discharge excited CO_2 laser gas mixtures are described. Measurements are made of the temperatures T, T_1, and T_3, the collision-broadened linewidths of several 10.4-μm laser lines, and the degree of gain overlap on the 9.4- and 10.4-μm regular and sequence band laser lines. All of these parameters are important for accurate computer modeling of the laser dynamics. The experimental technique is based on measuring gain coefficients in the 9.4- and 10.4-μm bands. The next section explains the theoretical relationship between measured gain coefficients and discharge temperatures, and Sect. 3.3 gives a description of the experimental apparatus. In Sect. 3.4, measured discharge temperatures are used to monitor and optimize the excitation of the gas mixture. Section 3.5 describes accurate measurements of collision-broadened linewidths obtained by a new technique, and Sect. 3.6 compares measurements and calculations of anomalous gain coefficients due to overlaps on the laser lines. The effect of linewidth and overlapping gain on the accuracy of measured discharge temperatures is discussed. Comparisons between the measured and calculated gain coefficients are shown to validate the mode-temperature model described in Sect. 2.5, and confirm the accuracy of the measured linewidths and discharge

temperatures.

3.2 Relationship Between Gain and Temperatures

The three temperatures, T, T_1, and T_3 in a discharge can be determined experimentally by making gain measurements on the regular, sequence, and hot bands of CO_2. In this section, the relationship between the measured gain coefficients and the temperatures is given.

At the peak of the gain in a pulsed discharge, the inversion ratio is typically large (i.e., $N_u \gg N_\ell$ [65,86]). Therefore, the gain coefficient at the line center of a collision-broadened line is given by Eqs. (2-17), (2-20) and (2-25) to be:

$$\alpha(\nu_o) = \frac{G\,|R_{u\ell}|^2\,S_J\,F_J\,K_u\,N_u}{\lambda_o\,g_u\,\Delta\nu_c}, \qquad (3\text{-}1)$$

where G is a constant and N_u and K_u are given by Eqs. (2-15) and (2-16), respectively. Equation (3-1) can be used to calculate the relative rotational gain distribution in a vibrational band, in which case N_u and $|R_{u\ell}|^2$ are absorbed by the constant G. The shape of the distribution is determined by the J dependence of the remaining variables and the dependence of K_u upon temperature, T. If all of the J dependences are known, the value of T in a discharge can be obtained by comparing the calculated rotational gain distribution to the measured distribution, and varying T to obtain the best fit [68,87-89]. Errors in the fitted temperature are most likely to occur as a result of using the wrong J dependence for $\Delta\nu_c$, or neglecting the effects of gain overlaps which may create anomalously large gain coefficients on some lines. The influence

of these two factors is discussed in Sects. 3.5.3 and 3.6.3, respectively. By properly taking account of these factors, T can be determined to within ± 10 K.

The vibrational temperatures T_3 and T_1 are obtained by measuring gain ratios between the sequence and regular bands, and the hot and regular bands, respectively [5,46]. For the lines having the highest gain in the sequence and regular bands (i.e., for the lines with J ≈ 18), all of the variables in Eq. (3-1) are approximately equal, except for $|R_{u\ell}|$ and N_u. To a first approximation, the ratio of the gain in the 00^02 sequence bands to that in the 00^01 regular bands is given by

$$\alpha_{seq}/\alpha_{reg} = \frac{|R_{u\ell}|^2_{seq}\ x_3^2}{|R_{u\ell}|^2_{reg}\ x_3} \approx 2\ \exp(-h\nu_3/kT_3). \tag{3-2}$$

A more exact expression accounts for the minor differences in the 9.4- and 10.4-μm transition dipole moments (see Table 2-3), and gives:

$$(\alpha_{seq}/\alpha_{reg})_{9.4} = 1.89\ \exp(-h\nu_3/kT_3),$$
$$(\alpha_{seq}/\alpha_{reg})_{10.4} = 2.1\ \exp(-h\nu_3/kT_3). \tag{3-3}$$

In a similar fashion, gain measurements on the 10.4-μm 00^01 regular band and the 10.8-μm 01^11 hot band are used to determine T_2 (which equals T_1). In this case, $|R_{u\ell}|^2$, S_J, K_u and the degeneracy of N_u differ by factors of approximately two for each band. However, these factors of two cancel each other, and T_2 can be determined from:

$$\alpha_{hot}/\alpha_{reg} = 0.96\ \exp(-h\nu_2/kT_2). \tag{3-4}$$

The factor of 0.96 arises because of the difference in wavelength of the transitions in each band. As in the determination of T, care must be taken to avoid lines with overlapping gain or to properly account for the overlap, if accurate values of T_1 and T_3 are to be obtained. If this is done, T_1 and T_3 can be determined to within ±4 %.

The use of Eq. (3-1) and the other simplifications described in this section give the discharge temperatures to a very good approximation. However, a more exact approach is to fit Eq. (2-17) to the gain measurements, which is the method used for the work described in this thesis. Although Eq. (2-17) depends on more than one temperature simultaneously, the interdependence is very weak and the approximate equations given in this section can be used for the other temperatures not being fitted. A computer program based on Eq. (2-17) was developed which could be used to calculate either relative or absolute gain as a function of the input temperatures. The gain due to overlaps from other bands could also be accounted for.

As mentioned in Chapt. 1, an examination was made of the feasibility of obtaining 4.5-μm laser oscillation in N_2O through the use of the same pumping scheme as is used in the 4.3-μm CO_2 laser. N_2O is a linear molecule similar to CO_2, except that it is nonsymmetric [14]. There are three normal modes of vibration and a set of vibrational energy levels analogous to those of CO_2. N_2O possesses a $(00^01\text{-}10^00)$ regular laser band [90,91] and a $(00^02\text{-}10^01)$ sequence laser band [92]; both bands are centered at 10.7 μm. The possibility exists for laser oscillation on the $(10^01\text{-}10^00)$ 4.5-μm band by optically pumping discharge excited N_2O with a sequence band pulse. A necessary parameter

for predicting the performance of a 4.5-μm N_2O laser is the value of T_3 which can be attained in a discharge. Thus, T_3 was determined from measured gain ratios on the sequence and regular bands of N_2O by using Eq. (3-2) and setting ν_3 equal to 2224 cm^{-1}. A comparison between T_3 values in CO_2 and in N_2O is presented in Sect. 3.4. In the next section, the experimental apparatus which was used to measure T, T_1, and T_3 in CO_2, and T_3 in N_2O is described.

3.3 Experimental Apparatus

Nearly all of the experimental results presented in this thesis were obtained by using the TE discharge described in this section. To obtain the results of this chapter, the experimental configuration included a CW laser which was used to measure small-signal gain coefficients in the TE discharge. The apparatus and measurement technique are described below.

Figure 3-1 is a photograph of the Lumonics K-902-2 TE discharge used throughout the work described in this thesis. The discharge can be operated at any pressure up to 760 Torr. The pressure is monitored with a calibrated, barometrically compensated vacuum gauge, and a mercury manometer. The gas mixture is controlled by calibrated flow meters and the flow rate is varied between 3 and 15 ℓ/min, according to the pressure, to prevent the build up of dissociation products. The discharge module consists of two equivalent sections, each having an active volume of 3.3 x 3.5 x 44 cm^3, with the 3.3 cm dimension representing the gap between the solid brass electrodes. A row of seven spark plugs on each side of the electrodes provides a source of UV

FIGURE 3-1

Photograph of the Lumonics K-902-2 UV-preionized TE discharge module used for the work described in this thesis. The gain length is 88 cm (44 cm in each section), and the overall length is 145 cm.

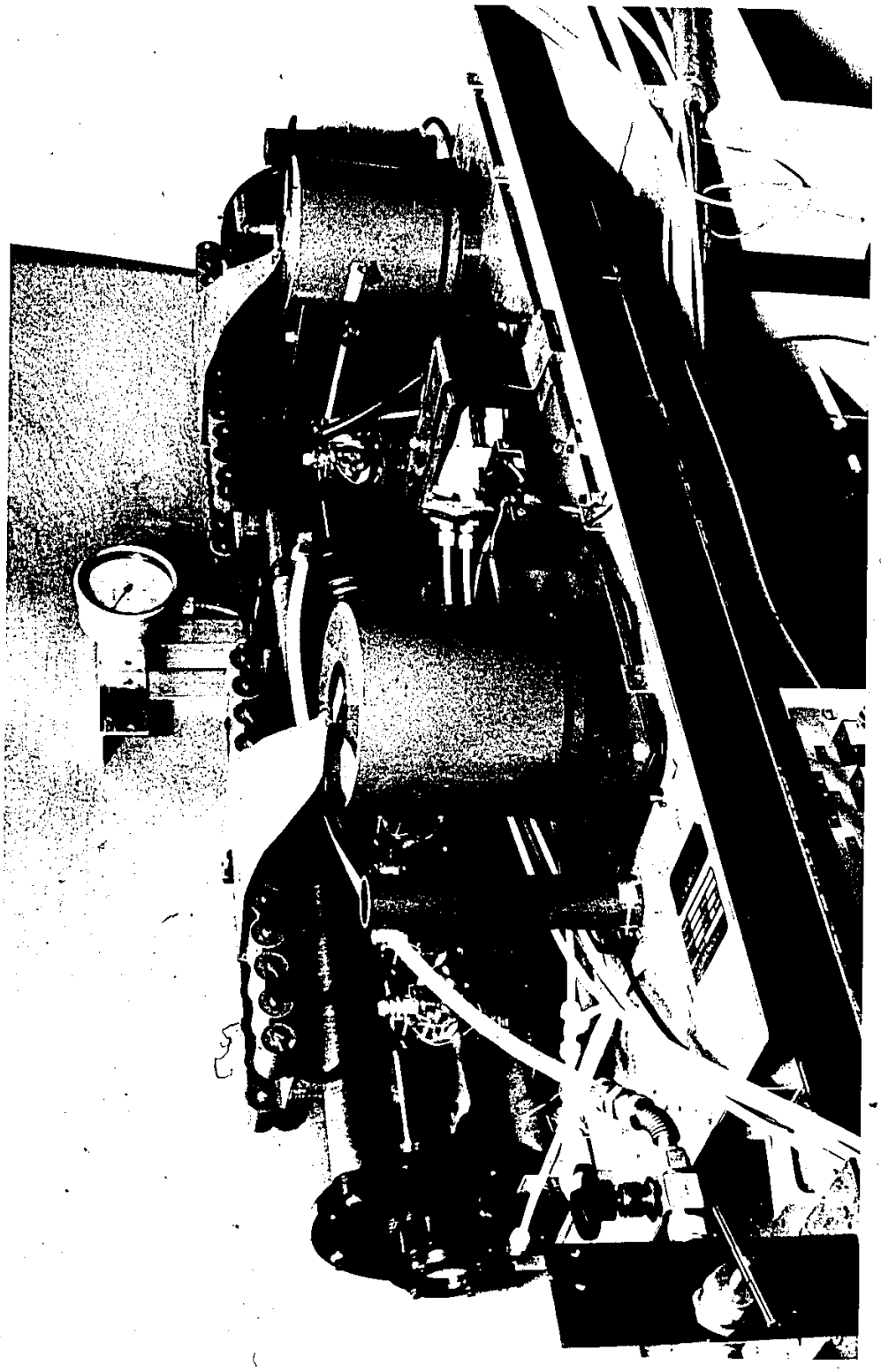

photons which preionize the laser gas mixture, resulting in uniform excitation of the gas volume by the main discharge. Each section has a separate discharge excitation circuit. The circuit is shown schematically in Fig. 3-2. A single spark gap is used to simultaneously trigger each section at repetition rates up to 1 Hz. The main discharge capacitor and charging voltage are varied over the ranges shown in Fig. 3-2, according to the discharge pressure. Typical voltage and current pulses are shown in Fig. 3-3. These were measured with a Tektronix voltage probe and a Pearson current probe at the points indicated in Fig. 3-2. The experimental conditions are given in the caption to Fig. 3-3. The integrated product of voltage and current corresponds to the energy deposited into the gas. For most of the work described in this thesis, it was necessary to maximize the energy deposition into the gas. In order to do this and still maintain a uniform discharge, the electrodes were carefully filed and sanded to remove high spots,‡ and then the spacing between electrodes was shimmed to within ± 0.03 mm along the length. This improved the performance of the discharge, allowing higher input energies to be used. The voltage and current pulses of Fig. 3-3 correspond to an input energy of ~220 J/ℓ·atm. Comparison of this to the energy stored in the main discharge capacitor (225 J/ℓ·atm) indicates the efficiency of the discharge circuit, which in this case is very high. For this discharge module, the efficiency is typically > 90 % over the range of operating

‡ The final finish recommended for the electrodes is bead blasting, a process similar to sand blasting where glass beads are used instead of sand [93].

FIGURE 3-2

Schematic diagram of the excitation circuit used with the Lumonics TE discharge. The ranges of values for the various parameters are shown in their correct respective order (i.e., the first value of the range corresponds to low pressure operation).

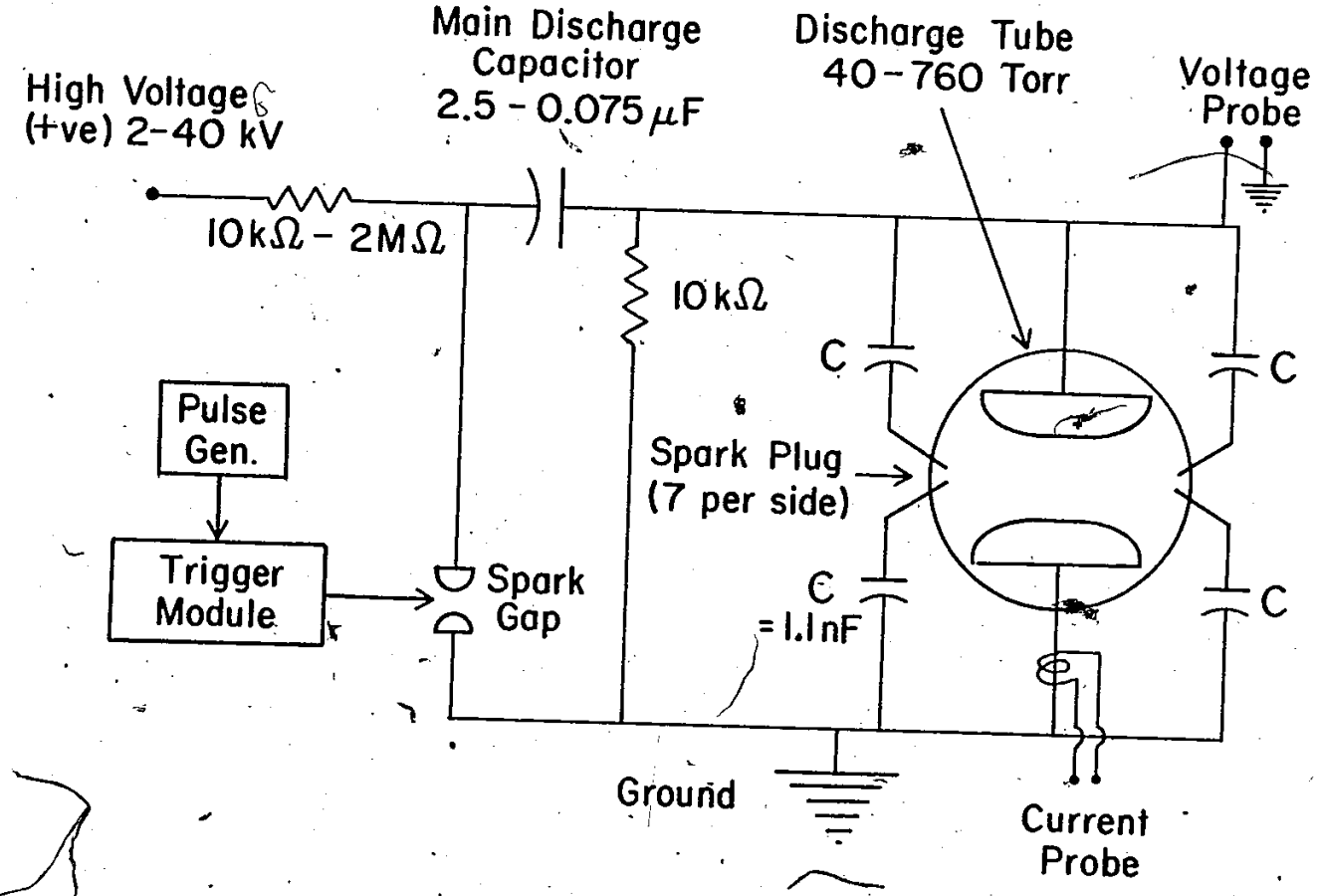
High Voltage
(+ve) 2-40 kV
Main Discharge
Capacitor
2.5 - 0.075 μF
Discharge Tube
40 - 760 Torr
Voltage
Probe
10kΩ - 2MΩ
10kΩ
C
C
Pulse
Gen.
Spark Plug
(7 per side)
Trigger
Module
Spark
Gap
C
= 1.1nF
C
Ground
Current
Probe

FIGURE 3-3

Voltage and current pulses measured for the discharge circuit of Fig. 3-2, corresponding to a single discharge section having a 1.5-μF capacitor charged to 4 kV. A gas mixture of 5% CO_2: 10% N_2: 85% He at 80 Torr was used. Note that the voltage pulse is negative with respect to ground.

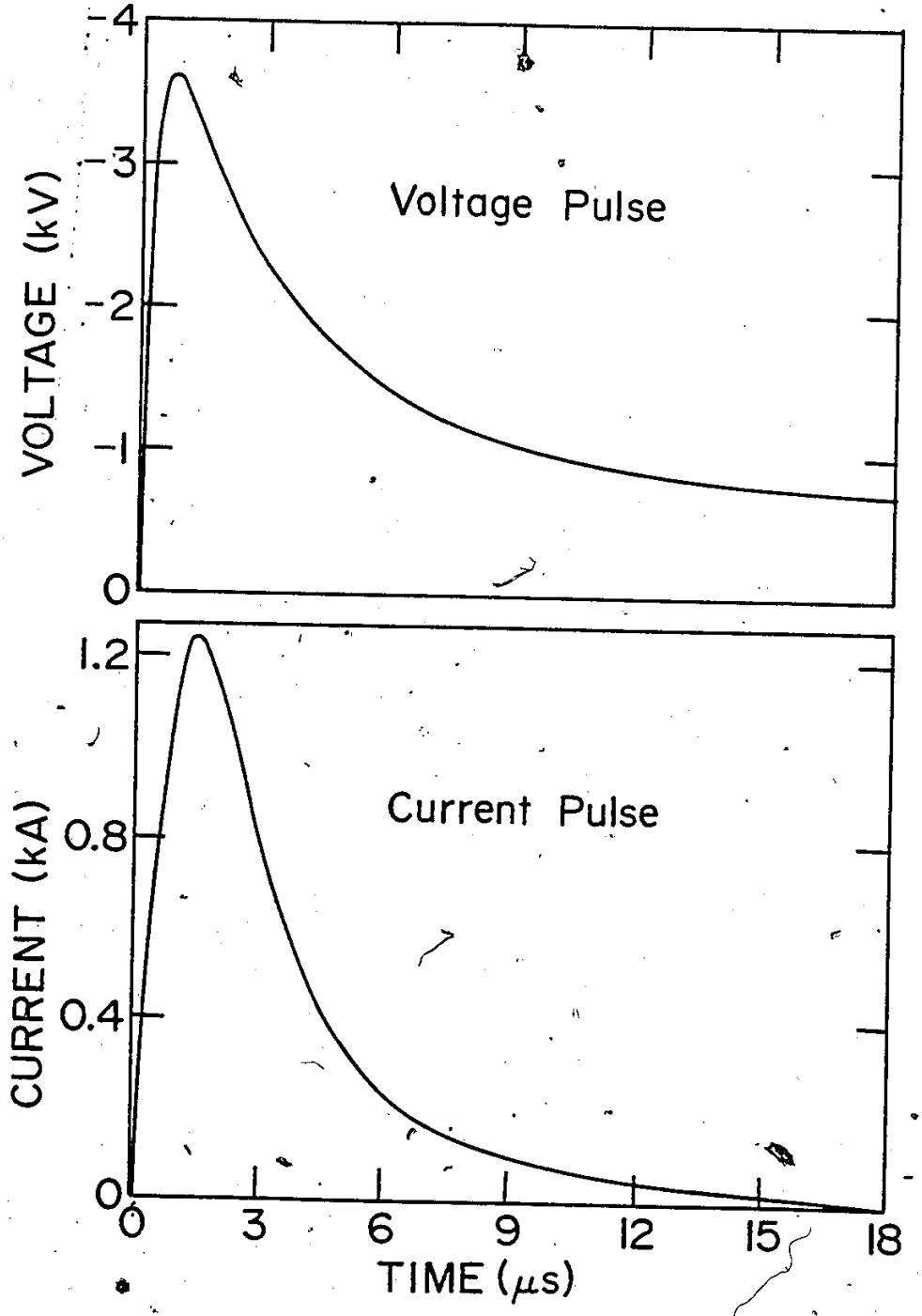
-4
-3
-2
-1
0
VOLTAGE (kV)
Voltage Pulse
1.2
0.8
0.4
0
CURRENT (kA)
Current Pulse
0
3
6
9
12
15
18
TIME (μs)

conditions described in this thesis.

Figure 3-4 is a schematic diagram of the experimental apparatus used to measure 9.4- and 10.4-μm small-signal gain coefficients in the TE discharge. The CW laser cavity consisted of a 98-% reflectivity output coupler mounted on a piezoelectric translator (PZT), and a PTR ML-304 original grating (135 lines/mm) with a measured reflectivity of >95 % mounted in Littrow. The cavity length was 298 cm, to allow for the 185-cm long discharge and a 65-cm long hot cell [94]. Intracavity apertures at each end restricted oscillation to the fundamental TEM_{oo} transverse mode. The flowing gas mixture in the discharge could be changed to contain either CO_2 or N_2O. With the hot cell evacuated, many lines in the regular bands of N_2O and CO_2 could be made to lase. N_2O lasers generally perform poorly compared to CO_2 lasers [95,96]. Therefore, discharge conditions were chosen to maximize the N_2O laser performance. A gas mixture of 8% N_2O: ~~20% N_2:~~ 72% He at 5 Torr, and a discharge current of ~14 mA resulted in maximum output powers of ~0.5 W. When the laser was operated under the same conditions with CO_2 instead of N_2O in the discharge, the maximum output power was ~1.1 W. Lasing was also obtained on several 10.8-μm $(01^11^{-1}0)$ CO_2 hot band lines near the peak of the P branch. Output powers were much lower than on the regular lines, and were optimized by increasing the discharge current and the CO_2 content in the gas mixture. By operating the hot cell at a temperature of ~550 K with 10 Torr of pure CO_2, lasing on many CO_2 sequence band transitions was obtained with output powers of ~0.5 W on the strongest lines. Lasing on the sequence bands of N_2O is very difficult to obtain because of the low gain [92]. However, the high-

FIGURE 3-4

Schematic diagram of the apparatus used for measuring 9.4- and 10.4-μm small-signal gain coefficients.

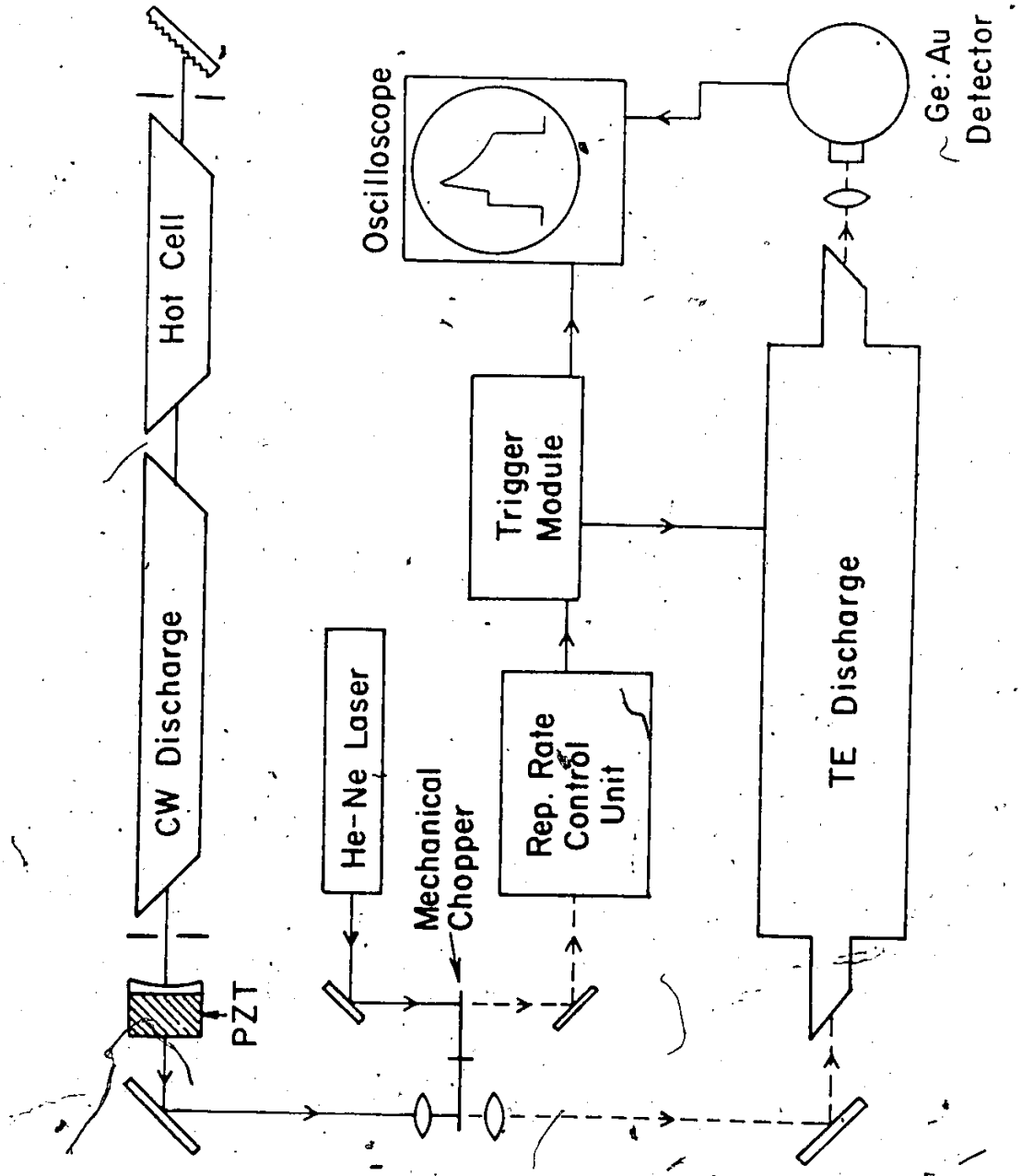
Hot Cell
CW Discharge
PZT
He-Ne Laser
Mechanical Chopper
Rep. Rate Control Unit
Trigger Module
Oscilloscope
Ge: Au Detector
TE Discharge

reflectivity cavity in conjunction with the long discharge resulted in lasing on many sequence band N_2O lines. The hot cell was filled with 10 Torr of pure N_2O at a temperature of ~400 K. A discharge gas mixture slightly leaner in N_2O optimized the output power, which was very low (<50 mW).‡ Laser emission was observed from P(12) to P(24) in the N_2O sequence band, and from P(3) to P(40) in the regular band. The full range in the R branch was not examined.

The output from the CW laser was directed through the center of the TE discharge with a maximum beam diameter of ~1 cm. A mechanical chopper, He-Ne laser and repetition rate control unit were used to synchronize the firing of the TE discharge and superimpose the time dependent gain on the chopped CW beam, as shown in Fig. 3-5. This allowed simultaneous measurements of optical zero, baseline, and peak gain coefficient. Further details are given in Ref. [44]. Care was taken to eliminate any systematic errors in the gain measurements. The Ge:Au detector was checked for linearity of response and the probe laser intensities were attenuated as necessary to prevent gain saturation. Effects due to unexcited CO_2 and dissociation of CO_2 in the discharge module were found to be negligible. Gain coefficients on different lines were always measured at the same time delay from discharge excitation, which generally corresponded to the peak of the gain.

The output power of the probe laser was maximized by adjusting the cavity length with the PZT before each gain measurement. Great care was taken to stabilize the output power of the probe laser. This was

---

‡ Improved performance can be obtained by using a shorter hot cell [92].

FIGURE 3-5

Typical gain signal synchronized with the chopped probe laser beam. The oscilloscope photograph superimposes 10 shots taken over a 30 s period. Note the excellent reproducibility of the measurement from shot to shot. The discharge gas mixture is 3% CO_2: 10% N_2: 87% He at a total pressure of 80 Torr, and gain is measured on the P(18) 10.4-μm line.

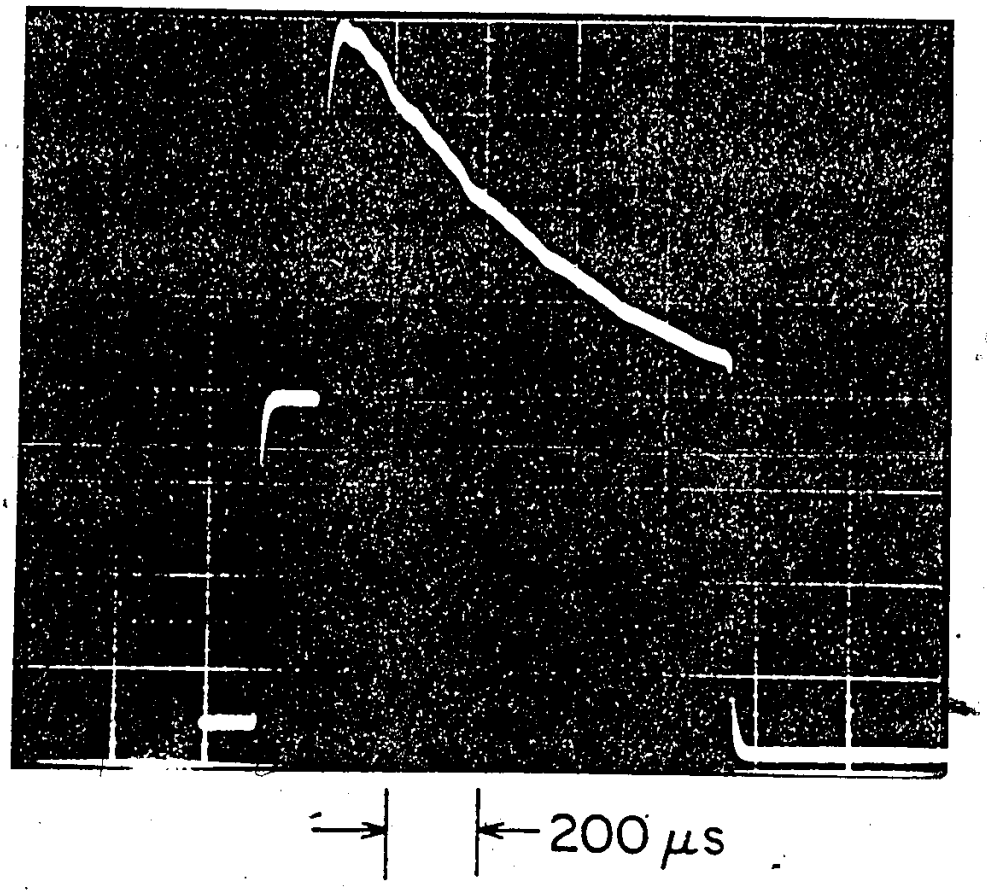
200 μs

accomplished by enclosing the intracavity beam path to eliminate air currents, by using a large (4-μF) filter capacitor and large (1.6-MΩ) ballast resistance in the CW laser discharge circuit, and by ensuring that all mounts were fastened solidly to the optical table. As a result, the power remained very stable over the time interval required for the measurement. This can be seen from Fig. 3-5, which is a photograph of 10 oscilloscope traces taken over a 30 s period. Since slight long term drifts in the operating conditions of the TE discharge were possible, the gain coefficient on a particular line was measured at regular intervals between other gain measurements to monitor any changes. The pulse-to-pulse reproducibility of the measurements was ±1 % and the day-to-day reproducibility was ±3 %.

The experimental apparatus described above was used to obtain the results presented in the following sections.

3.4 Optimization of Discharge Excitation

The use of measured gain coefficients to experimentally determine discharge temperatures is a powerful technique for monitoring and optimizing the performance of the discharge excitation circuit. The optimum operating conditions are those which maximize the excitation of population into the ν_3 mode of CO_2 (i.e., maximize T_3). Clearly, this is beneficial to the performance of any CO_2 laser, and it is especially important in sequence and 4.3-μm CO_2 lasers (see Chapts. 4, 5, and 7).

The excitation of the ν_3 mode is a function of both the total energy deposited into the gas, and the electron energy distribution in the discharge. The latter is characterized by E/N. In Sect. 2.3 it was

shown that the optimum value of E/N ranges from $(1-3)\times10^{-16}$ V·cm^2, and that such low values cannot be attained in a self-sustained discharge. For the TE discharge used in this study, the value of E/N is defined by the charging voltage. For example, in Fig. 3-3 the peak of the voltage pulse is nearly equal to the 4-kV charging voltage. The peak voltage of 3.6 kV corresponds to an E/N of $\sim4.2\times10^{-16}$ V·cm^2. As indicated by the duration of the current pulse, most of the energy is deposited into the gas while E/N is near its peak value. Therefore, the effective value of E/N can be minimized by keeping the charging voltage as low as possible. It is observed experimentally that higher values of T_3 can be obtained for a given input energy by reducing the charging voltage and increasing the capacitance, while still maintaining a uniform, arc-free discharge. This is illustrated in Fig. 3-6, which shows measured values of T_3 as a function of stored input energy for various combinations of capacitance and charging voltage. For the smallest capacitance, and hence largest charging voltage and E/N, T_3 is the lowest. As the capacitance is increased and E/N reduced, T_3 increases. Optimum performance is obtained with the lowest possible value of E/N ($\sim4.4\times10^{-16}$ V·cm^2), which is kept constant while the input energy is varied by changing the capacitance. Under these optimum excitation conditions, T_3 increases almost linearly with input energy until discharge degradation (arcing) occurs.‡ The results of Fig. 3-6 indicate that the maximum T_3 is obtained by minimizing E/N while maximizing the input energy to the

‡ Since arcing occurs at relatively low input energies for the low E/N data, saturation of T_3 with input energy due to electron de-excitation is not observed (see Sect. 2.3).

FIGURE 3-6

Measured vibrational temperature T_3 as a function of (stored) input electrical energy to the discharge. The input energy was changed by varying either the charging voltage or the main discharge capacitance, C. Peak E/N values are indicated. Increased excitation efficiency is clearly obtained by reducing E/N.

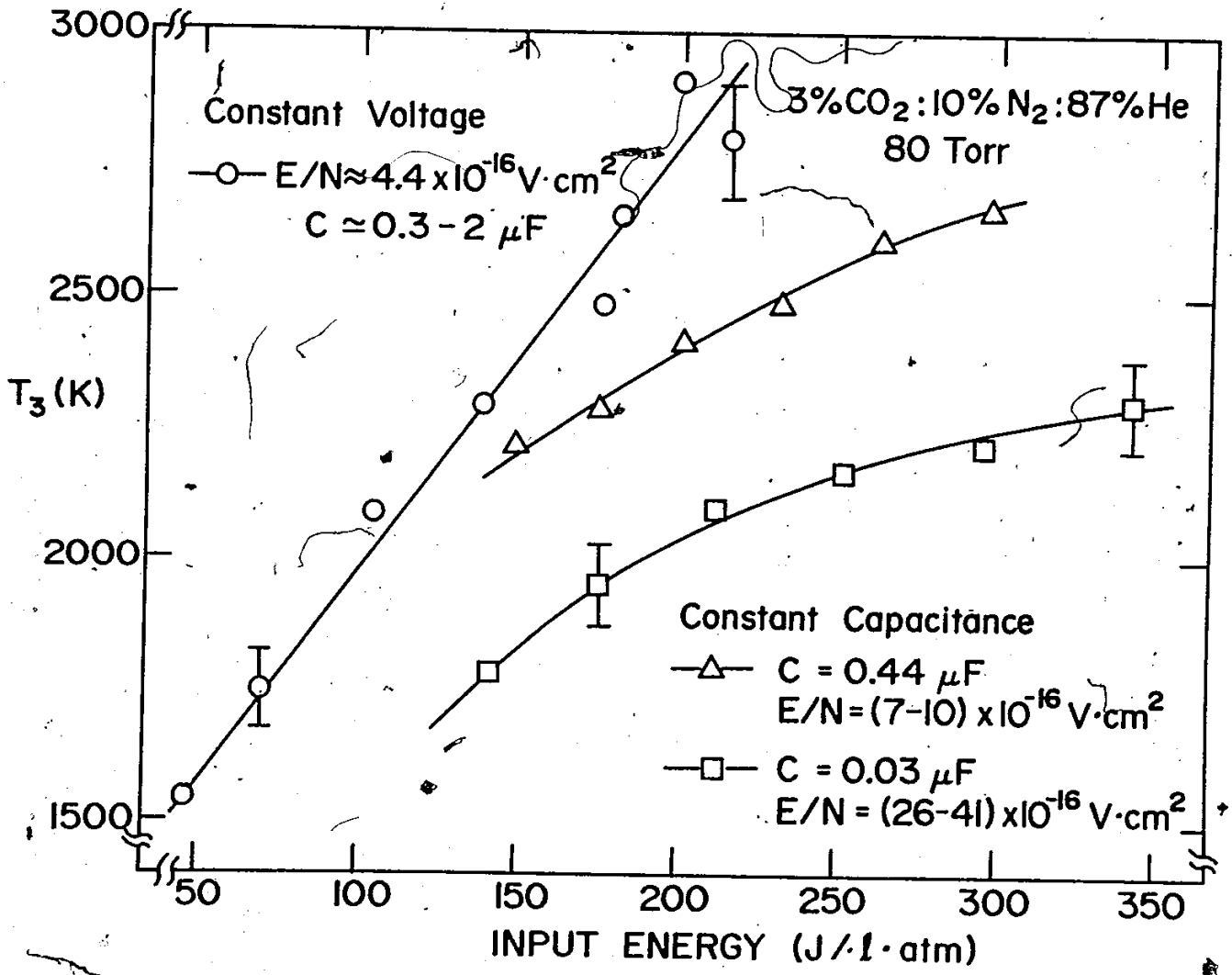
3000
2500
2000
1500
T_3 (K)
Constant Voltage
E/N≈4.4 x10^{-16} V·cm^2
C ≃0.3 - 2 μF
3%CO$_2$: 10% N$_2$: 87% He
80 Torr
Constant Capacitance
C = 0.44 μF
E/N = (7-10) x10^{-16} V·cm^2
C = 0.03 μF
E/N = (26-41) x10^{-16} V·cm^2
50
100
150
200
250
300
350
INPUT ENERGY (J/ℓ·atm)

discharge.

The dependence of T_3 upon gas mixture was also examined. The procedure outlined above was followed to maximize T_3 for each gas mixture and pressure. The results are plotted in Fig. 3-7, which shows T_3 as a function of CO_2 content in the gas mixture. Data points taken from several other sources [41,42,45,46,65] are also shown, to illustrate the generality of the results. Note that the highest value of T_3 is always obtained for gas mixtures with low CO_2 content, independent of the total discharge pressure. As pointed out in Sect. 2.3, these results suggest that CO_2 molecules have a much larger cross-section for electron de-excitation than do N_2 molecules. Thus, mixtures with a high N_2 to CO_2 ratio attain the highest values of T_3. Figure 3-7 also shows the values of T_1 measured when the discharge excitation is optimized for high T_3 values. T_1 increases with increasing CO_2 concentration. Measured values of T are not shown in Fig. 3-7, but T is generally 20 to 40 K less than T_1.

It is instructive at this point to compare the T_3 values plotted in Fig. 3-7 for CO_2 with T_3 measurements made in N_2O. Figure 3-8 shows T_3 as a function of N_2O content in the gas mixture. The pulsed discharge data was measured in the Lumonics module operating at 80 Torr with the excitation optimized. A 0.5-μF capacitor charged to 5 kV (for each discharge section) gave an input electrical energy of ~115 J/ℓ·atm. Arc formation in the discharge prevented the use of lower E/N values or higher input energy [97]. Also shown in Fig. 3-8 are much more extensive measurements of T_3 made in a CW discharge [95]. As in CO_2, the limiting value of T_3 in N_2O is independent of the type of excitation

FIGURE 3-7

Measured vibrational temperatures T_1 and T_3 as a function of CO_2 content of a discharge. The values of T_3 correspond to the maximum attainable in a self-sustained discharge due to the effects of electron de-excitation. See text for further details.

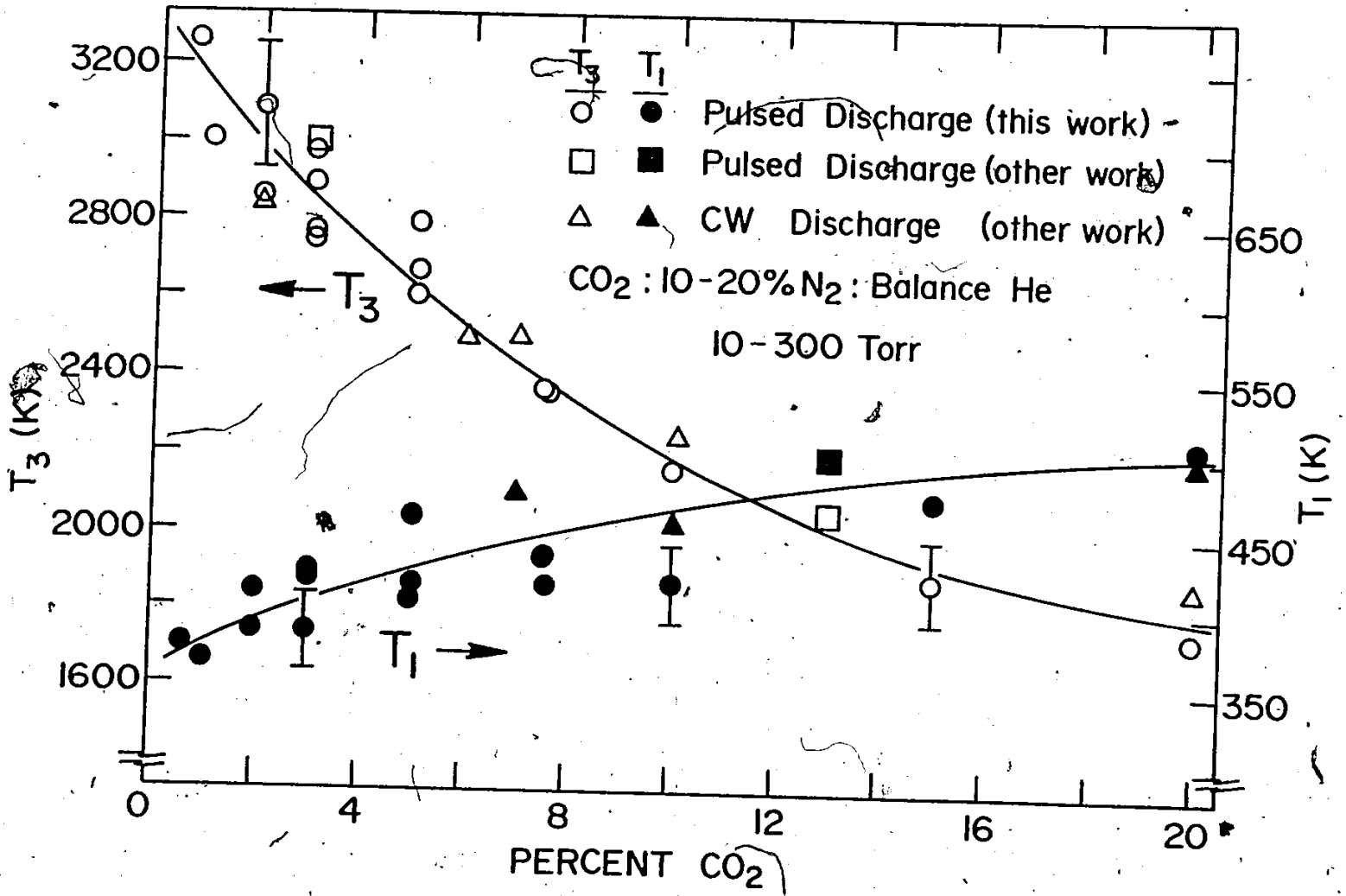
3200
2800
2400
2000
1600
650
550
450
350
T_3 (K)
T_1 (K)
T_3
T_1
Pulsed Discharge (this work)
Pulsed Discharge (other work)
CW Discharge (other work)
CO_2 : 10-20% N_2 : Balance He
10-300 Torr
T_3
T_1
0
4
8
12
16
20
PERCENT CO_2

FIGURE 3-8

Measured vibrational temperature T_3 and rotational temperature T as a function of N_2O content in a discharge. The values of T_3 correspond to the maximum attainable in a self-sustained discharge due to the effects of electron de-excitation. The CW discharge data are taken from Fox and Reid [95], where it is noted that T_1 typically equals T. Effective percent N_2O refers to the N_2O remaining in the gas mixture after dissociation is taken into account. See text for further details.

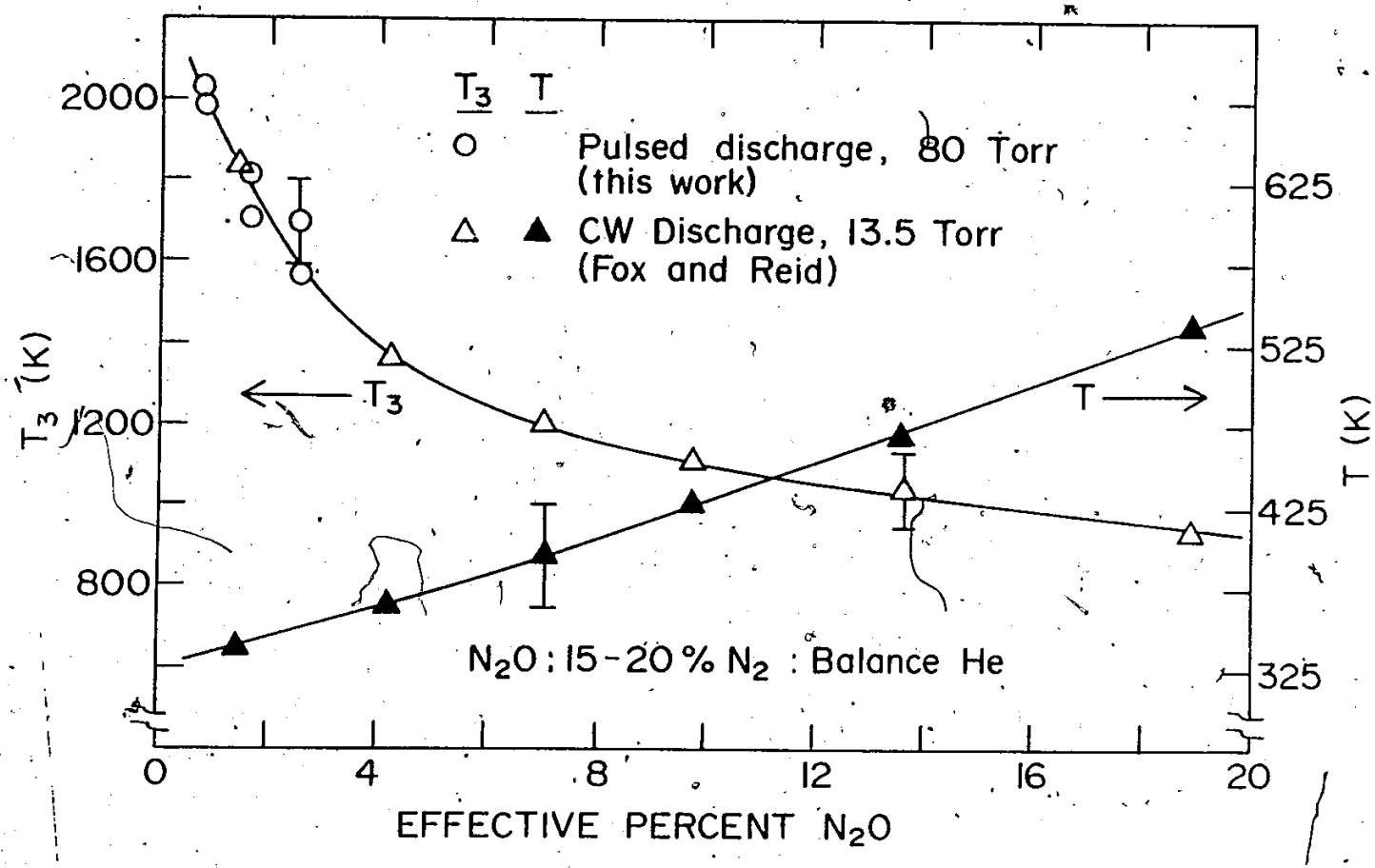
T_3 T
Pulsed discharge, 80 Torr (this work)
CW Discharge, 13.5 Torr (Fox and Reid)
T_3
T
N_2O : 15-20 % N_2 : Balance He
T_3 (K)
T (K)
2000
1600
1200
800
625
525
425
325
0
4
8
12
16
20
EFFECTIVE PERCENT N_2O

(CW or pulsed), independent of pressure, and is a decreasing function of the N_2O content. However, a significant difference in the absolute value of T_3 between the two molecules is evident by comparing Figs. 3-7 and 3-8. On average, T_3 is lower in N_2O by 1200 K, which suggests that N_2O has a much larger cross-section for electron de-excitation than does CO_2. This low value of T_3 is largely responsible for the poor performance of 10.7-μm N_2O lasers relative to 10.4-μm CO_2 lasers [95]. In addition, the low values of T_3 explain why an attempt to produce 4.5-μm lasing in N_2O (made as part of the present study) was unsuccessful. The topic of 4.5-μm lasing in N_2O is discussed in more detail in Sect. 7.7.

The Lumonics TE discharge used in this study was characterized in terms of T, T_1, and T_3 with the excitation optimized over a range of gas mixtures from < 1% CO_2 to 10% CO_2, and pressures ranging from 40 to 400 Torr. These conditions pertain to 4.3-μm operation, and the measured discharge temperatures were used as input to computer models of the 4.3-μm dynamics described in Chapts. 5 to 7. In the next two sections of this chapter, measurements of 10.4-μm linewidths, and 9.4- and 10.4-μm overlapping gain coefficients are described.

3.5 Accurate Measurements of Pressure-Broadened Linewidths

The small-signal gain in CO_2 laser systems depends strongly upon the pressure-broadened widths of the rotational-vibrational lines in CO_2: N_2: He gas mixtures. These mixtures are typically dominated by He, however, few experimental measurements have been made of CO_2-He pressure-broadening coefficients. This point is expanded upon in a

recent paper by Pack [76], who calculates CO_2-He broadening coefficients as a function of rotational quantum number J and temperature T, but can only compare his calculations with two accurate experimental results for P(20) in the (00^01-10^00) 10.4-μm band [78] and R(20) in the (00^01-00^00) 4.3-μm band [98].

Accurate CO_2-He pressure-broadening coefficients are required for the work described in this thesis. The fitting of T to rotational gain distributions is very sensitive to the J dependence of the pressure-broadened linewidth, and accurate measurements of T, T_1, and T_3 require that account be taken of gain overlaps, which are also sensitive to the exact linewidth. Accurate linewidths are required for calculations of overlapping absorption in the 4.3-μm wavelength region. These calculations are necessary when predicting the performance of 4.3-μm CO_2 lasers, as described in Chapt. 7. Several other areas of CO_2 laser dynamics also require accurate CO_2-He pressure-broadening coefficients. At pressures of several atmospheres, the gain of individual rotational-vibrational lines merges into one broad band. Taylor et al. [99] calculate that a 4 % increase in linewidth causes a 5 % increase in predicted gain under these conditions. He-broadened linewidths are also important in determining the width of mode-locked pulses in TE CO_2 oscillators [100,101].

In view of these factors, detailed measurements of He-broadened CO_2 linewidths in the Lumonics TE discharge were made as a function of J and T, using a novel technique which is capable of high accuracy [102]. These measurements are described below, and the influence of the J dependence on the fitted rotational temperature is discussed.

3.5.1 Linewidth Measurement Technique

The linewidth measurement technique is based on small-signal gain measurements and the key to the method is that the CW probe laser can be operated on either CO_2 or N_2O transitions. The use of an N_2O probe laser allows gain on the CO_2 transition to be measured at a fixed frequency offset, in addition to the gain measurement at the line center. The method relies on chance occurrences of CO_2 lines and regular band N_2O lines having a suitable frequency separation. Therefore, this study is restricted to nine transitions of the 10.4-μm P branch.‡ Since the frequency differences between CO_2 and N_2O transitions are very well known [103], the linewidth can easily be calculated from the gain ratio by assuming a Lorentzian lineshape (Eq. (2-20)). The gain at the offset is given by:

$$g(\nu) = \frac{g(\nu_o)}{1 + [(\nu-\nu_o)/\Delta\nu_c]^2}, \tag{3-5}$$

where $g(\nu_o)$ is the gain at the line center, $\nu-\nu_o$ is the offset, and $\Delta\nu_c$ is the pressure-broadened linewidth (HWHM). Equation (3-5) can be rearranged to give the linewidth as:

$$\Delta\nu_c = \frac{\nu-\nu_o}{[g(\nu_o)/g(\nu) - 1]^{1/2}}. \tag{3-6}$$

---

‡ An attempt was made to access more lines by operating the probe laser on the N_2O sequence band. However, the output was too weak to accurately measure the low values of gain at offsets from CO_2 lines. The measurement technique could be extended by using isotopic forms of CO_2 in the probe laser instead of N_2O.

By varying the pressure in the CO_2 discharge, the linewidth can be "tuned" through the fixed offset and determined very accurately as a function of pressure. At a given pressure, the effects of slow changes in the TE discharge conditions are minimized by measuring the gain at the line center and at the offset alternately, four times each, within a period of ~20 min. The uncertainties in the averaged gains are ±1 % for gains > 0.3 %/cm, while gains as small as 0.02 %/cm can be measured to accuracies of ±10 %. Each measurement of linewidth at a fixed pressure has an uncertainty ranging from ±2 % to ±6 %, and a least-squares fit to linewidth versus pressure data results in the broadening coefficients having accuracies of ±2 %.

This technique for measuring linewidth has several advantages. The use of a gain ratio eliminates any requirement to know the exact length of the discharge. Data reduction is very simple and gives the linewidth directly. This simple data reduction should be compared with that used in previous measurements of CO_2 linewidths made by measuring absorption in thermal CO_2 mixtures at the line center only (see Sect. 2.6). The data reduction in these previous measurements involved separating out linewidth and linestrength effects, whereas the present technique is independent of the value of the linestrength. There are also many advantages associated with a method based on pulsed gain measurements. Most importantly, these linewidth measurements are the first to be made under the exact operating conditions of TE CO_2 lasers. Also, the pulsed discharge produces high gain in gas mixtures containing > 90% He, whereas absorption in such an unexcited gas mixture is low. The difficulties associated with measuring such small absorptions

increase the problems in obtaining CO_2-He broadening coefficients by absorption techniques. Another drawback of absorption measurements is the problem of determining optical zero, whereas pulsed gain measurements provide a simultaneous picture of the probe laser intensity in the absence of gain and at the peak gain (see Fig. 3-5).

3.5.2 Linewidth Measurements as a Function of J

The He-broadened linewidths of nine transitions in the 10.4-μm P branch from P(2) to P(46) were measured. A discharge gas mixture of 3% CO_2: 2% N_2: 95% He was chosen to provide the maximum He content while still producing enough gain for accurate measurements. The excitation of the gas was kept as low as possible (~15 J/ℓ·atm) to minimize temperature increases. From measurements of the rotational gain distribution, T was found to increase by only ~6 K.

The linewidth of P(32) was measured initially, as it has the smallest available offset from an N_2O line (587 MHz from P(7) N_2O [103]). At a fixed pressure, the gain was measured at the line center and at the offset by operating the probe laser on either the P(32) line of CO_2 or the P(7) line of N_2O. The linewidth was calculated from the ratio of these gains using Eq. (3-6). The same procedure was repeated at several pressures ranging from approximately 80 Torr to 760 Torr. The lowest pressure was chosen such that the line remained in the pressure-broadened regime, while 760 Torr was the maximum operating pressure of the discharge.

Figure 3-9 shows the results of these measurements. The error bars are calculated by combining the uncertainty in the measured gain

FIGURE 3-9

Linewidth (HWHM) as a function of pressure for the P(32) 10.4-μm transition in a gas mixture of 3% CO_2: 2% N_2: 95% He at a temperature of 304 ± 5 K. The straight-line fit is constrained to pass through the origin and gives a broadening coefficient of 0.0611 ± 0.0009 cm^{-1}/atm.

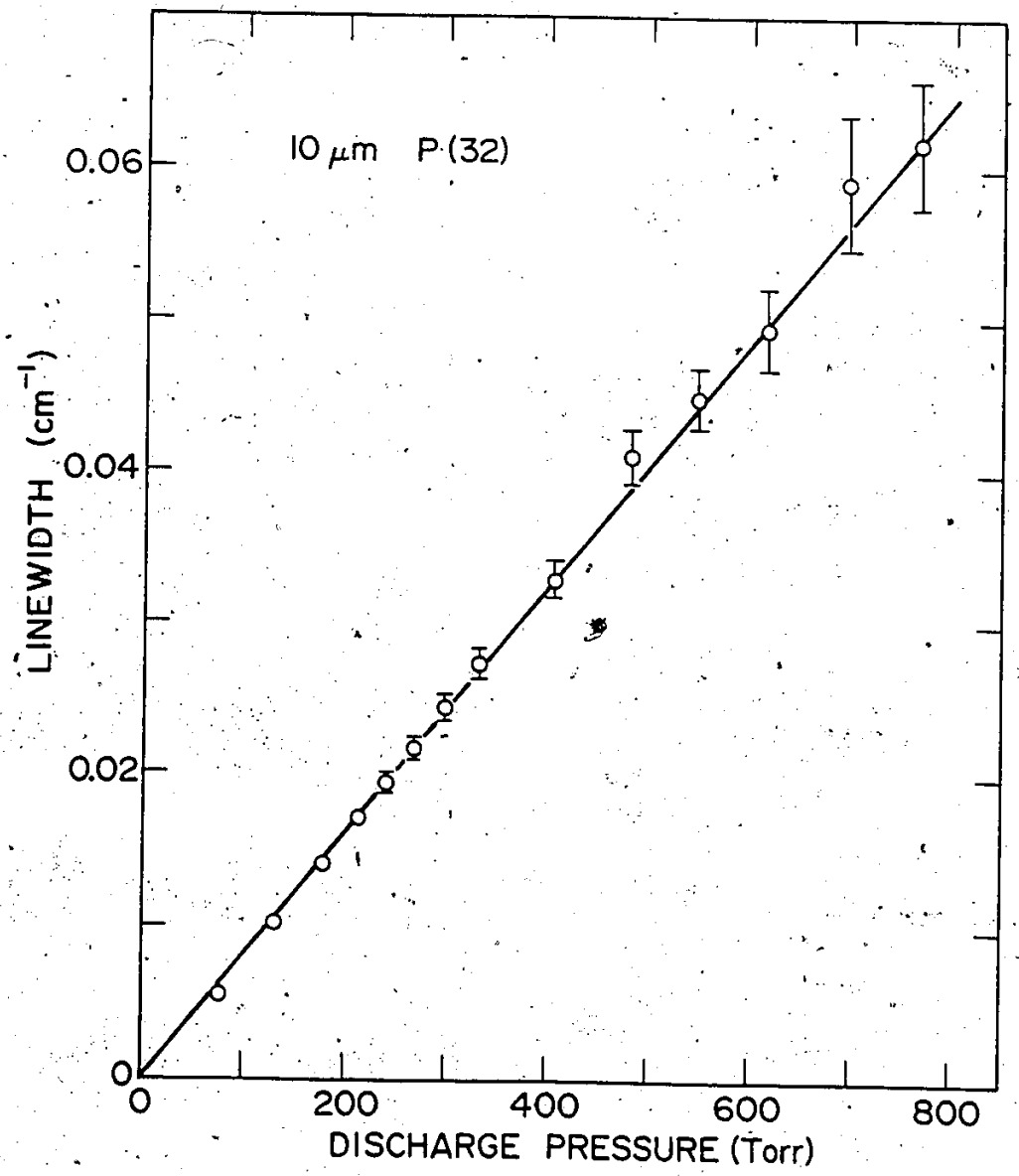
10 μm P(32)
0.06
0.04
0.02
0
LINEWIDTH (cm⁻¹)
0
200
400
600
800
DISCHARGE PRESSURE (Torr)

ratio with the uncertainty in the frequency difference between the two probe lines. Even though this frequency difference is known very accurately, the possibility of the probe laser operating off line center is taken into account by assuming the exact frequency difference is only known to ± 7.5 MHz. This has a minor effect on the accuracy of the results. The smallest relative errors in linewidth occur at pressures where the line center to offset gain ratio is ~2. At higher pressures, the gains become similar which adds to the uncertainty in their ratio, while at lower pressures, the offset gain becomes small, thereby decreasing the accuracy of its measurement. Note that the weighted least-squares fit which is constrained to pass through the origin has a standard deviation of < 2 %, confirming the accuracy of the measurement technique.

Similar results are shown in Fig. 3-10 for the P(14) line of CO_2, which is offset from the R(12) line of N_2O by 2623 MHz [103]. In this case, the linewidth could not be measured very accurately at pressures below 200 Torr, due to the small gain at the N_2O transition which was then more than 5 halfwidths from the line center of P(14). Also shown in Fig. 3-10 are corrections to the linewidth for the effect of overlapping gain. The data points without error bars represent the linewidths calculated from the ratio of the measured gains. The measured gain however, is due not only to P(14) but includes contributions from nearby sequence and hot band transitions. This is unlike the case of P(32), where there are negligible contributions from nearby lines. In general, the overlapping gain is significant and must be taken into account, particularly at high pressure. The fraction of

FIGURE 3-10

Linewidth (HWHM) as a function of pressure for the P(14) 10.4-μm transition under the same conditions as given in the caption to Fig. 3-9. The straight line which is constrained to pass through the origin is fitted to the corrected data and gives a broadening coefficient of 0.0613 ± 0.0008 cm^{-1}/atm.

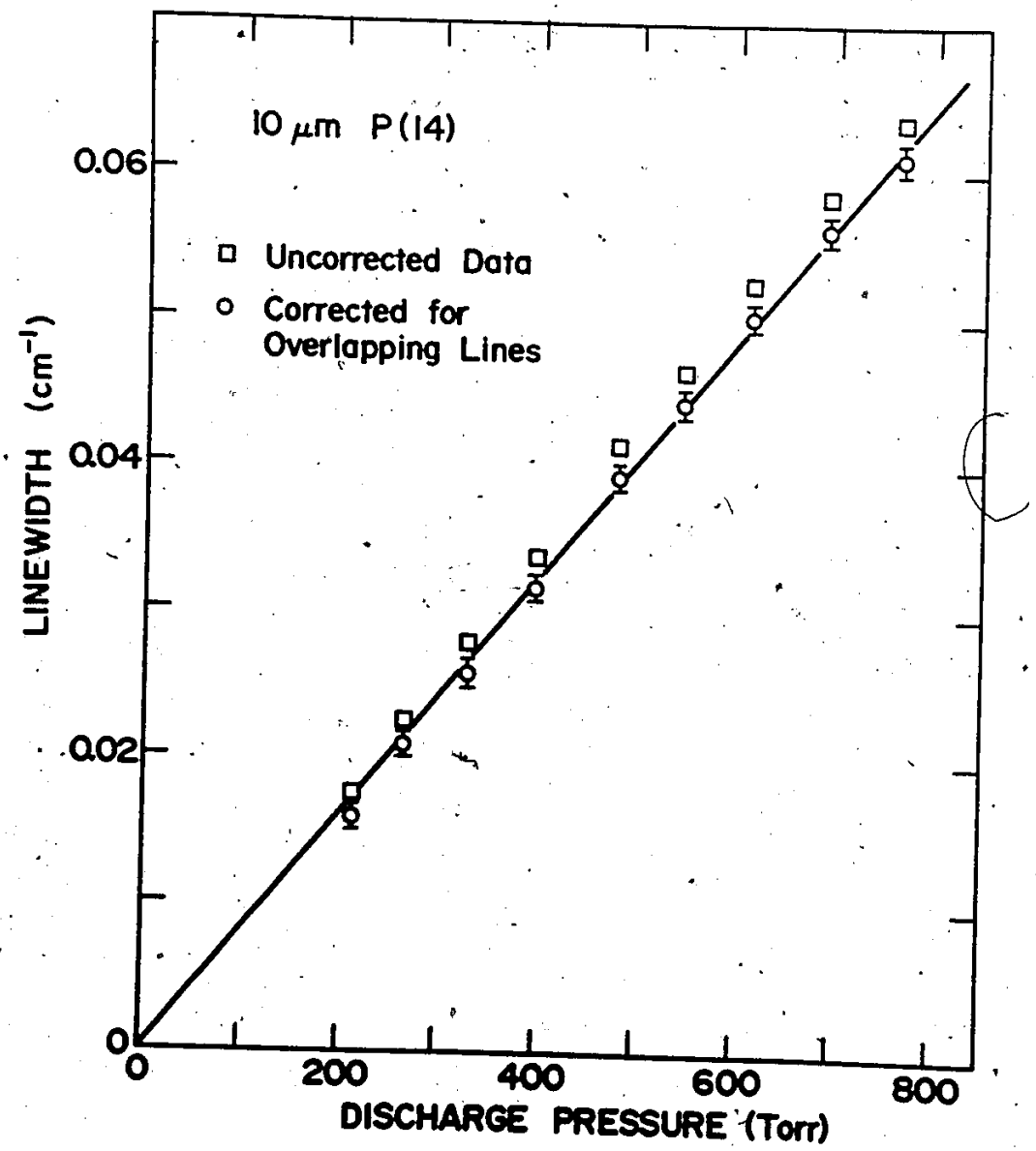
10 μm P(14)
Uncorrected Data
Corrected for Overlapping Lines
LINEWIDTH (cm⁻¹)
0.06
0.04
0.02
0
0
200
400
600
800
DISCHARGE PRESSURE (Torr)

the gain due to overlaps is calculated using accurately known CO_2 line positions, the measured linewidths, and measured vibrational temperatures (see Sect. 3.6). These calculations are done in a self-consistent manner, and have an accuracy which is probably much better than ±30 %. However, this uncertainty is used, along with the other uncertainties, to determine the error bars on the corrected linewidth values shown in Fig. 3-10. Since the overlapping gain can be calculated quite accurately and the effect on the linewidth is minor, these corrections do not significantly affect the accuracy of the results. The corrected linewidth data for P(14) are fitted with a straight line constrained to pass through the origin, as shown in Fig. 3-10. Once again, the standard deviation of the fit is < 2 %.

The broadening coefficients of the nine CO_2 transitions listed in Table 3-1 were determined in such a manner. These were the only lines that had both a sufficiently small frequency offset from an N_2O line and a sufficiently large gain coefficient to enable linewidth measurements to be made. The relevant N_2O transitions are also listed in Table 3-1 with the frequency offset from the nearby CO_2 line. The fourth column of the table shows the He-broadening coefficients for the 3% CO_2: 2% N_2: 95% He gas mixture at a temperature of 304 ± 5 K. To scale the data back to a temperature of 300 K, they are multiplied by a factor of $(304/300)^{-0.42}$. This temperature relationship is justified in Sect. 3.5.4. The linewidths are then corrected for the effects of CO_2 and N_2 broadening. The CO_2- and N_2-broadening coefficients of Eqs. (2-22) and (2-23) were used. The linewidths which represent pure He broadening at 300 K are shown in the last column of Table 3-1.

TABLE 3-1

Broadening coefficients in the 10.4-μm P branch of CO_2. The N_2O line was used to measure gain at the listed offset from the line center of the CO_2 transition.

CO_2 Line	N_2O Line	Offset [a] CO_2-N_2O (MHz)	Broadening Coefficient (cm^{-1}/atm)	
			3% CO_2:2% N_2:95% He Mixture at 304 ±5 K	Pure He at 300 K [b]
P(2)	R(25)	1347	0.0666	0.0645 ± 0.0015
P(4)	R(23)	-1594	0.0621	0.0599 ± 0.0010
P(6)	R(21)	-4844	0.0607	0.0585 ± 0.0014
P(14)	R(12)	2623	0.0613	0.0594 ± 0.0008
P(16)	R(10)	-1986	0.0602	0.0584 ± 0.0007
P(32)	P(7)	587	0.0611	0.0599 ± 0.0009
P(38)	P(14)	4343	0.0567	0.0555 ± 0.0022
P(40)	P(16)	-3686	0.0622	0.0614 ± 0.0019
P(46)	P(23)	-2729	0.0577	0.0569 ± 0.0027

a) Ref. [103].

b) The uncertainties in the fit represent one standard deviation.

The He-broadening results are presented in graphical form in Fig. 3-11 (Eq. (2-24) gives a straight-line fit to the data). Also shown are the experimental results of Abrams [75] and Oodate and Fujioka [98], which are both in good agreement with the present results. It should be noted that the measurement by Oodate and Fujioka was made in the 4.3-μm fundamental band of CO_2, which supports the assumption of Sect. 2.6 that the broadening coefficients are band independent. Meyer et al. [104] have also measured He-broadening coefficients on the 9.4- and 10.4-μm bands of CO_2. However, their data seems to have the wrong J dependence and shows large scatter. The solid line in Fig. 3-11 shows the calculated He-broadened linewidths of Pack [76]. These calculations agree well with the measured J dependence, although the magnitude of the calculated linewidths is somewhat large. Also shown in Fig. 3-11 are the self-broadened and N_2-broadened linewidths of CO_2, which are given by Eqs. (2-22) and (2-23).

3.5.3 The Influence of Linewidth on Rotational Temperature Determination

The measurements of He-broadened linewidths described above were partly motivated by the results of fitting rotational temperatures to measured rotational gain distributions. In the past, it was found that at very low excitation the fitted temperature was significantly below room temperature. This discrepancy was caused by using the J dependence of CO_2-broadened linewidths to determine T in a laser gas mixture which was dominated by He-broadening. However, no detailed measurements of the J dependence of He-broadened linewidths existed and thus the present

FIGURE 3-11

Broadening coefficients, α, as a function of $|m|$ for CO_2 at 300 K. $m = -J$ for the P branch and $m = J+1$ for the R branch. The He-broadening data of the present study is compared to measurements by Abrams [75] and Oodate and Fujioka [98] and to the calculation of Pack [76]. Also shown are CO_2-CO_2 and CO_2-N_2 linewidths (- - -), which represent straight-line fits to measurements by others (see Eqs. (2-22) and (2-23)).

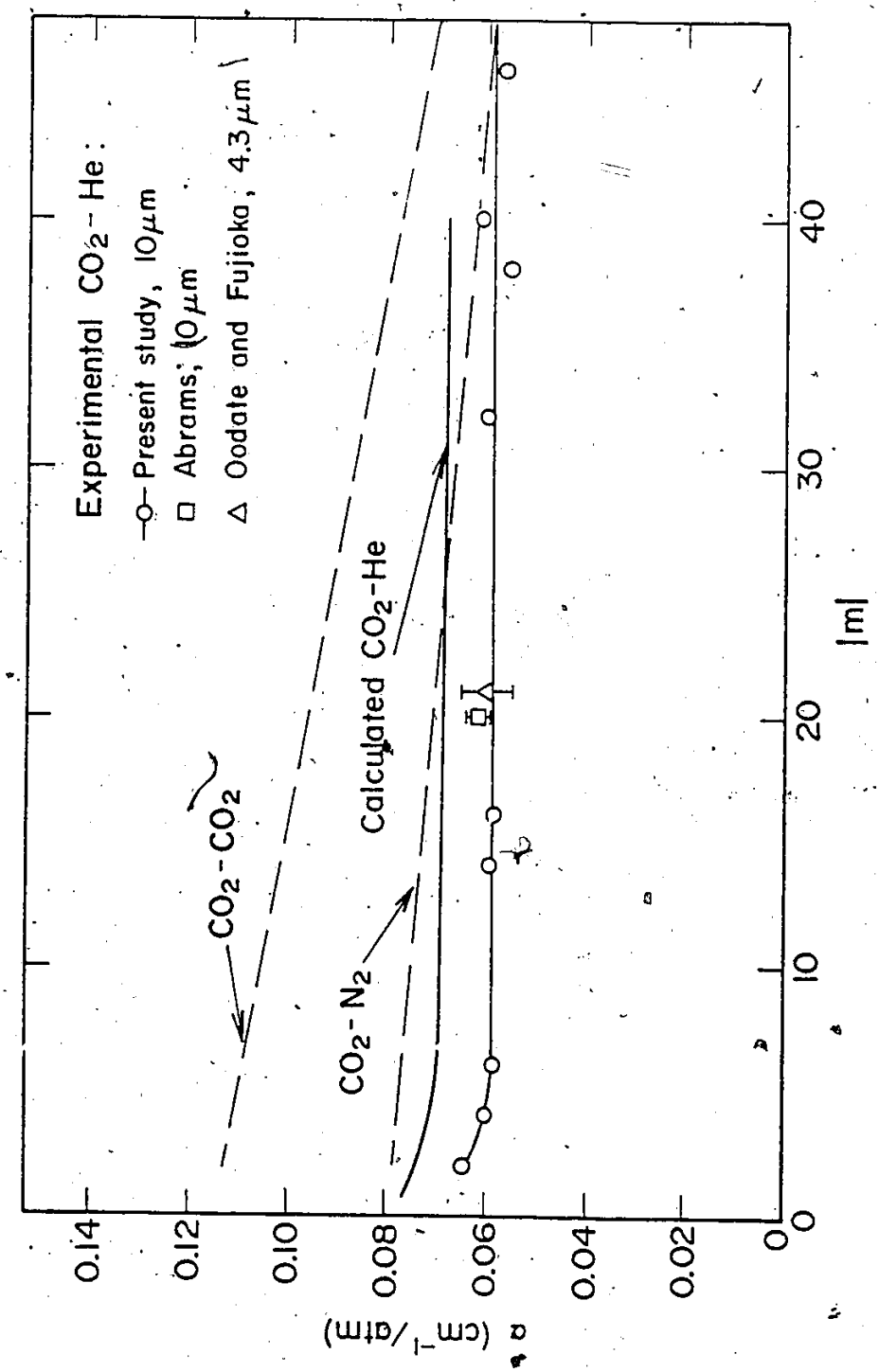
Experimental CO_2 - He:
Present study, 10 μm
Abrams; 10 μm
Oodate and Fujioka, 4.3 μm
CO_2 - CO_2
Calculated CO_2-He
CO_2 - N_2
α (cm⁻¹/atm)
0.14
0.12
0.10
0.08
0.06
0.04
0.02
0
0
10
20
30
40
|m|

study was undertaken. The measured He-broadening coefficients of this study enable one to determine the correct J dependence of the linewidth and obtain a reasonable value for T.

Figure 3-12 shows the measured rotational gain distribution in the 10.4-μm P branch of CO_2 for a gas mixture of 5% CO_2: 10% N_2: 85% He at 80 Torr total pressure. The discharge excitation was kept low so that T would not rise much above room temperature. The fit to the gain distribution excluded P(12) and P(20) since these lines are known to have anomalously large gains even at low pressure and low excitation (see Sect. 3.6). Two separate fits were carried out, each using a different J dependence for the linewidth. In one fit, only CO_2-broadening data was used (Eq. (2-22)), while the second fit used a combination of CO_2 broadening, N_2 broadening, and He broadening in proportion to the gas mixture (Eqs. (2-22) to (2-24)). Both fits were equally good and are represented by the single solid line in Fig. 3-12. However, the fitted temperature in the two cases was 272 ± 10 K (CO_2 broadening) and 297 ± 10 K (exact CO_2: N_2: He broadening). As the true discharge temperature must be slightly above room temperature (~298 K), it is clear that the exact CO_2: N_2: He linewidth must be used for accurate determinations of T.[∓] Thus, the use of CO_2 self-broadened linewidths has led to an underestimate of T by ~25 K in previous work.

[∓] As the J dependence of the linewidth can be compensated for by adjusting T in the gain equation, incorrect linewidths result in the wrong temperature, even though a good fit is obtained.

FIGURE 3-12

Measured rotational gain distribution in the 10.4-μm P branch of CO_2 for a mixture of 5% CO_2: 10% N_2: 85% He at 80 Torr. Low discharge excitation is used (~43 J/ℓ·atm). The solid line represents a fit to the data from which the rotational temperature is determined. Fitted temperatures range from 272 ± 10 to 297 ± 10 K depending on the choice of linewidth, as explained in the text.

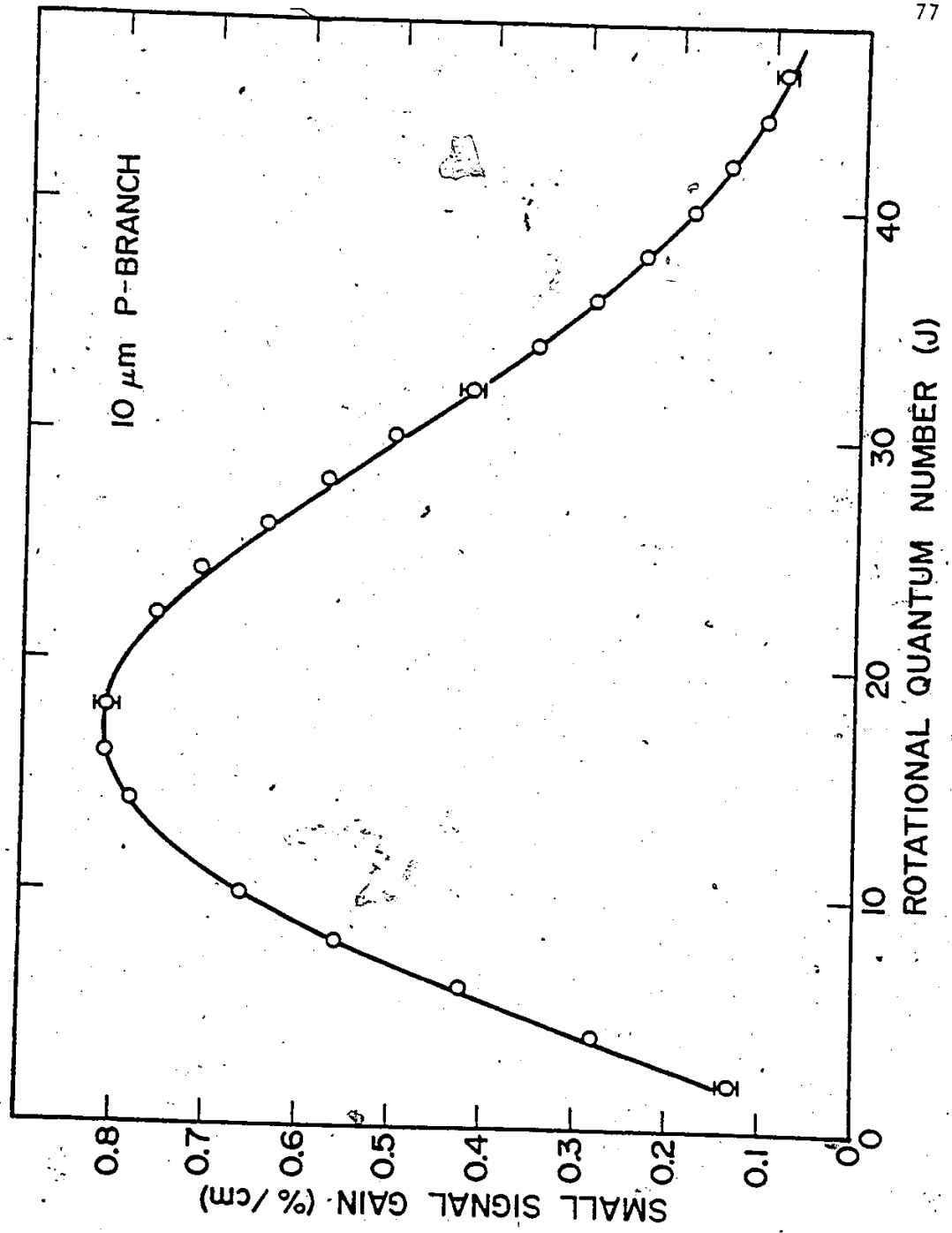
10 μm P-BRANCH
SMALL SIGNAL GAIN (%/cm)
0.8
0.7
0.6
0.5
0.4
0.3
0.2
0.1
0
0
10
20
30
40
ROTATIONAL QUANTUM NUMBER (J)

3.5.4 Temperature Dependence of Linewidth

In this section the results of linewidth measurements as a function of temperature are described. The linewidth was measured using the two-frequency probe technique, and from measurements of the rotational gain distribution T was determined. For discharge conditions of fixed pressure and mixture, the excitation of the gas was varied to produce values of T ranging from 300 to 508 K. This range represents the extremes which could be obtained in the TE CO_2 discharge.

Several measurements have previously been made of the temperature dependence of CO_2 linewidths using absorption techniques under conditions of constant pressure [79,105-107]. It is generally agreed that the linewidth decreases as T^{-n}, where measurements of n vary from ~0.5 [105], which corresponds to the limit of hard sphere collisions, to > 1 [79,106]. All of these values correspond to either CO_2- or N_2-broadened linewidths. The temperature dependence of He-broadened linewidths is expected to be similar. Pack [76] has calculated a value of $n \approx 0.62$ for He broadening in the 300 to 400 K region. In the present study, measurements of linewidth versus temperature are made in He-dominated gas mixtures, and are the first to be made under conditions of constant number density.‡ Thus, the linewidth is expected to increase with temperature as $T^{1-n} = T^r$. The measurements of n at constant pressure suggest that r should lie in the range from < 0 to ~0.5, and the calculation by Pack [76] predicts that $r \approx 0.38$ for He broadening.

---

‡ As explained in Sect. 2.4, the gain peak occurs in a high pressure pulsed discharge before the gas has time to expand.

The linewidths of both P(16) and P(32) were measured as a function of temperature over a range of pressures and gas mixtures. The results for P(16) are shown in Fig. 3-13. The gas mixture consists of 20% CO_2: 10% N_2: 70% He at a total pressure of 402 Torr. The natural log of the broadening coefficient normalized by its value at 300 K is plotted versus $\ell n(T/300)$. A least-squares fit of a straight line to the data results in a slope of $r = 0.38 \pm 0.07$. The error bars in Fig. 3-13 represent an accuracy of ±2\5 % in each linewidth measurement.

Results similar to those shown in Fig. 3-13 were obtained for the linewidth of P(32). Table 3-2 summarizes all of the results on the temperature dependence of the linewidth. Of interest is the last column which shows the best-fit slope to the data for each of the different conditions. The scatter in the results and the large uncertainties are attributed to the difficulty of accurately measuring the small increases in linewidth. A weighted average of the slopes reduces the uncertainty somewhat, and gives $r = 0.42 \pm 0.06$. Thus, based on these measurements the linewidth in a TE CO_2 laser increases as $T^{0.42\pm0.06}$, which is in good agreement with the value of $T^{0.38}$ predicted by Pack's calculation.

The He-broadened linewidth results described in this section and the available data for self broadening and N_2 broadening of CO_2 were combined to give Eqs. (2-21) to (2-24), enabling linewidths to be calculated in a CO_2 discharge under any conditions. These equations are used in calculations of 4.3- and 10.4-μm gain and absorption coefficients in Chapts. 4 to 7, and in calculations of gain overlaps in the 9.4- and 10.4-μm bands of CO_2. The measurements and calculations of overlapping gain are described below.

FIGURE 3-13

Temperature dependence of the collision-broadening coefficient, α, for the 10.4-μm P(16) transition from 312 to 508 K in a gas mixture of 20% CO_2: 10% N_2: 70% He at 402 Torr. The linewidth varies as $T^{0.38}$.

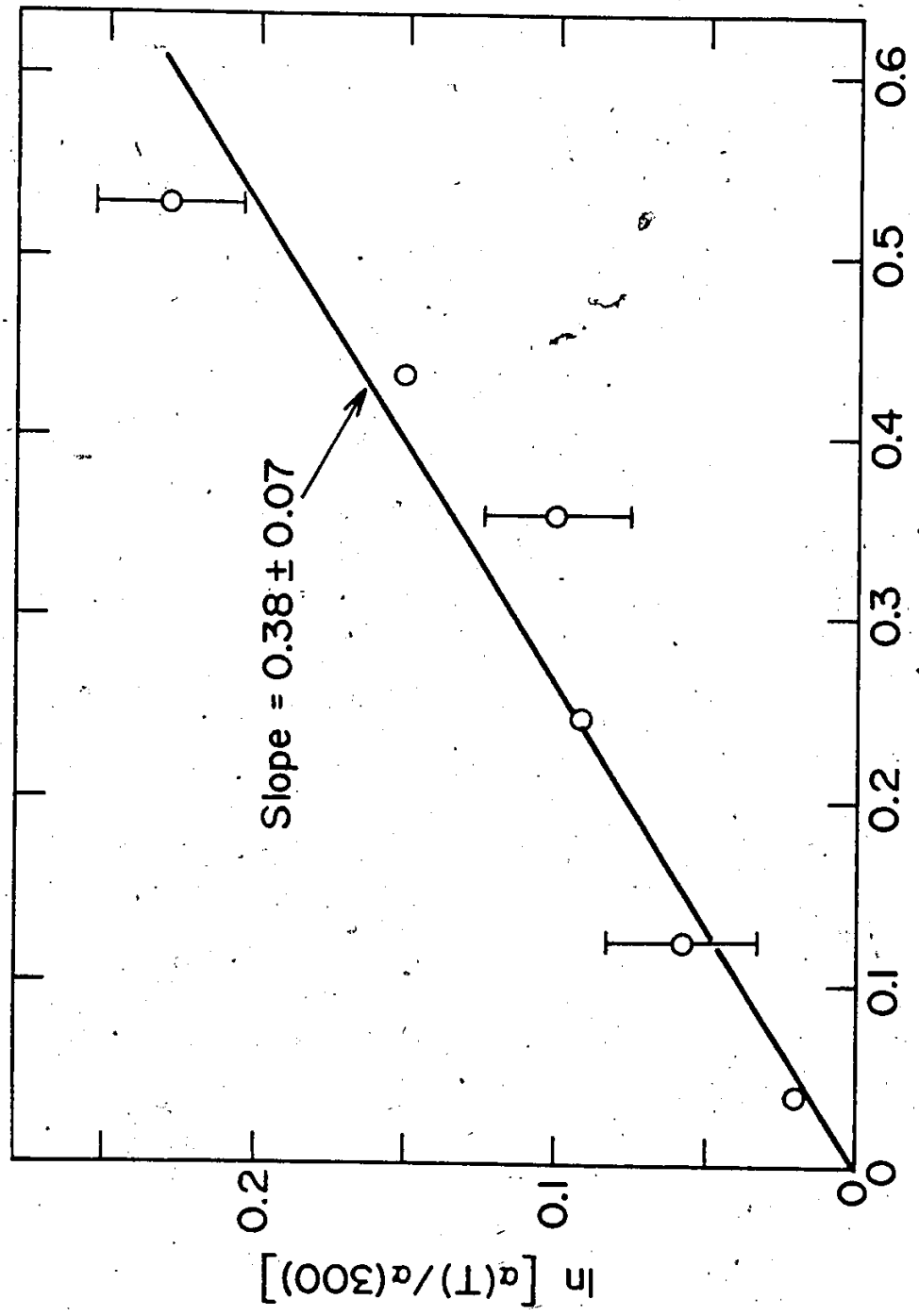
Slope = 0.38 ± 0.07
ln [α(T)/α(300)]
ln (T/300)
0
0.1
0.2
0.3
0.4
0.5
0.6

TABLE 3-2

Temperature dependence of the linewidth of P(16) and P(32) over a range of conditions. The linewidth is proportional to T^r where r is the slope of a line fitted to data such as in Fig. 3-13. The weighted average of r is 0.42 ± 0.06.

10.4-μm CO_2 Line	Mixture CO_2:N_2:He	Pressure (Torr)	Temperature Range (K)	r a)
P(16)	20:10:70	402	312 → 508	0.38 ± 0.07
P(32)	15:10:75	98	316 → 470	0.43 ± 0.10
P(32)	5:10:85	210	319 → 409	0.50 ± 0.11
P(32)	3:2:95	210	325 → 366	0.37 ± 0.37

a) The uncertainties in the fit represent one standard deviation.

3.6 Anomalous Gain Coefficients

It has long been recognized that a few CO_2 laser lines have anomalously high gain coefficients. In particular, the 10.4-μm P(20), P(28), and P(34) lines, and the 9.4-μm P(22) line, all have extra gain due to chance overlaps with lines in the 01^11 hot bands [88,89,108,109]. However, it was not generally recognized that many more lines have extra gain until Reid and Siemsen [110] calculated the effect of the sequence bands on the gain of high pressure CO_2 lasers. Their prediction that the majority of the laser lines have significant gain contributions are confirmed by the experimental results described in this section [111]. The present results are also in agreement with the observations made by Goldstein et al. [112] in an 1800-Torr amplifier. Extra gain due to overlaps affects many lines at high pressure and a few lines at low pressure. If this fact is neglected, erroneous rotational and vibrational temperatures may be determined from measured gain coefficients.

In this section, detailed measurements are presented of gain coefficients on a total of 153 different laser lines in the 9.4- and 10.4-μm regular and sequence bands. High excitation conditions and a gas mixture containing only 5 % CO_2 are chosen for the TE discharge, which results in a T_3 of ~2500 K (see Fig. 3-7). At this value of T_3, the 00^on sequence bands have gain which is $\sim[(n)(0.25)^{n-1}]$ times the regular gain, and the effects of chance overlaps with sequence lines are enhanced. Measurements are made at discharge pressures of 80 and 425 Torr, and the effect of increasing linewidth can be clearly observed. The accuracy and reproducibility of the gain measurements enable

detection of all anomalies > 3%.

3.6.1 80-Torr Measurements

The initial series of measurements were made with a TE discharge pressure of 80 Torr. This low pressure minimizes the anomalies in the gain coefficients, but still results in pressure-broadened linewidths. A gas mixture of 5% CO_2: 10% N_2: 85% He was used.

Figure 3-14 shows the results of the 80-Torr gain measurements in the regular and sequence bands. In the 10.4-μm P branch, the smooth curve in the regular band indicates the best fit of the calculated relative gain to the measured gain coefficients. This fit was obtained by simultaneously varying T and a normalization factor to give the least-square deviation for all but the anomalous gain lines (P(6), P(12), P(20), and P(48)). Figure 3-14 shows a total of 153 measured gain coefficients in the regular and sequence, 9.4- and 10.4-μm bands. A simultaneous fit to all regular band lines (excluding the anomalies) was made with T = 362 ± 9 K,‡ while varying each normalization factor separately. The same value of T was then used in a fit to the sequence bands where only the normalization factor was varied. The overall fit is excellent, with an average deviation of < 2% on all 8 branches, and no serious discrepancies other than the anomalous lines. These results justify the assumption that the linewidths are the same for all bands. In addition to fitting the relative gain in each band, the absolute gain coefficients have also been calculated using the theory of Sects. 2.5

---

‡ The uncertainty reflects the variation in temperature which is obtained when each gain distribution is fitted separately.

FIGURE 3-14

Rotational gain distribution in the 9.4- and 10.4-μm, regular and sequence bands. The discharge was operated with a 5% CO_2: 10% N_2: 85% He gas mixture at 80 Torr total pressure. The smooth curves show the best fit of the calculated relative gain with T = 362 K, while the triangles show the calculated absolute gain. Crosses are used to indicate the gain coefficients calculated for the anomalous lines. The measured vibrational temperatures were T_2 = 388 ± 15 K, and T_3 = 2460 ± 50 K.

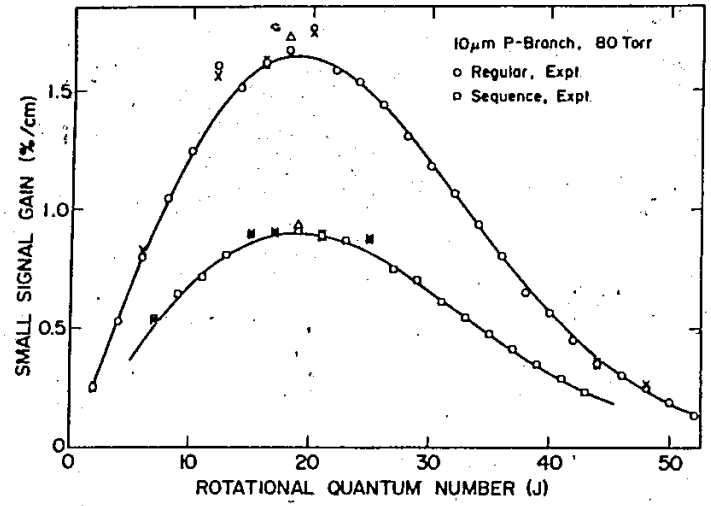
10μm P-Branch, 80 Torr
o Regular, Expt
□ Sequence, Expt
SMALL SIGNAL GAIN (%/cm)
ROTATIONAL QUANTUM NUMBER (J)

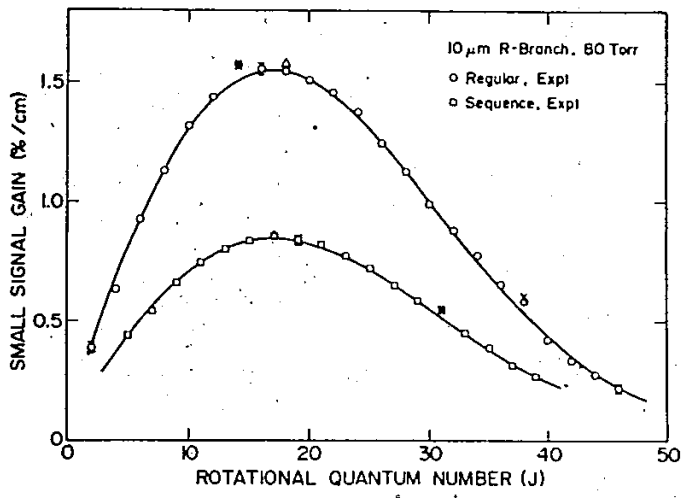
10μm R-Branch, 80 Torr
o Regular, Expt
□ Sequence, Expt
SMALL SIGNAL GAIN (%/cm)
ROTATIONAL QUANTUM NUMBER (J)

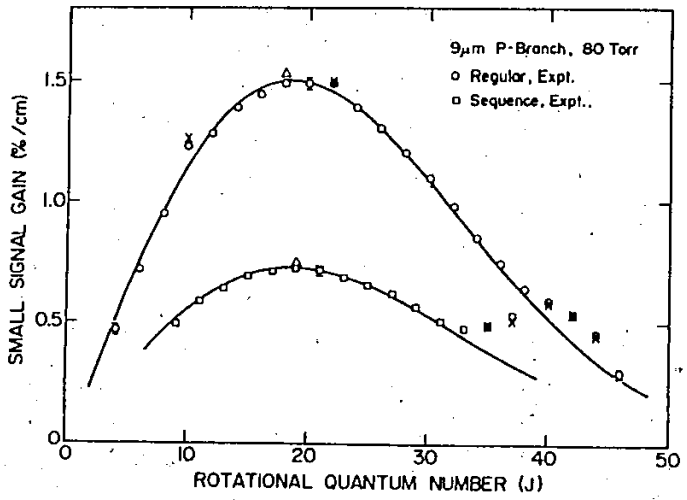
9μm P-Branch, 80 Torr
o Regular, Expt.
□ Sequence, Expt..
SMALL SIGNAL GAIN (%/cm)
ROTATIONAL QUANTUM NUMBER (J)

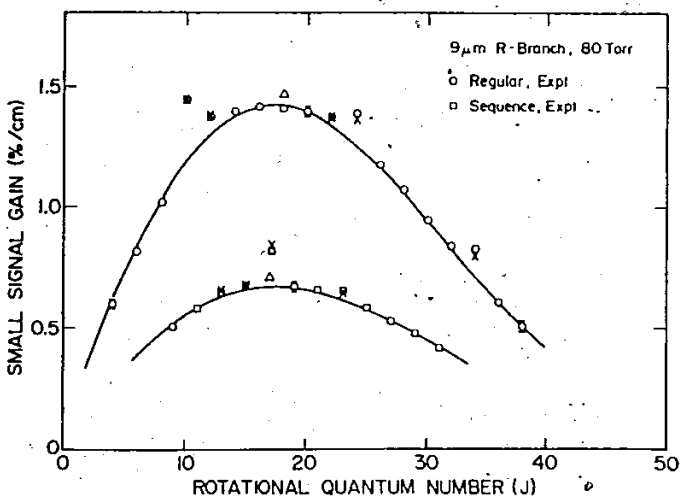
9μm R-Branch, 80 Torr
o Regular, Expt
□ Sequence, Expt
SMALL SIGNAL GAIN (%/cm)
ROTATIONAL QUANTUM NUMBER (J)

and 2.6, and the measured values of T, T_1, and T_3. The results of these calculations are indicated by triangles in Fig. 3-14. Only one calculated gain coefficient is shown for each branch, since the variation with J is identical to that of the solid line. There is very good agreement between calculation and experiment in all branches. The degree of gain overlap for each line is indicated by the crosses in Fig. 3-14. To accurately calculate the effect of overlapping gain, contributions from 15 bands in the 9.4- and 10.4-μm wavelength region are considered. These bands are listed in Table 3-3. The line positions of most of these transitions have been measured to very high accuracy by Bailly and Rossetti [113], Whitford et al. [114], and Dupre-Maquaire and Pinson [115], and for the remaining lines the constants given in Ref. [19] are used. Once the frequency separation of two lines is known, the gain contribution due to overlap is calculated by using the theory of Sects. 2.5 and 2.6, and assuming a Lorentzian lineshape. Only those calculations which predict additional gain of > 0.015 %/cm are shown. All of the calculated anomalies agree with experiment within experimental error.

3.6.2 425-Torr Measurements

For the next series of measurements, the discharge pressure was raised to 425 Torr. This substantially increased the degree of line overlap and the number of lines with anomalously high gain.

Figure 3-15 shows the results of measurements of gain coefficients on the regular and sequence bands at 425 Torr. Almost all the lines were anomalous to some degree, making it difficult to

TABLE 3-3

CO_2 9.4- and 10.4-μm bands which are included in the calculation of overlapping gain.

9.4-μm Bands			10.4-μm Bands		
Vibrational Levels		Constants	Vibrational Levels		Constants
Upper	Lower	From:	Upper	Lower	From:
00^01	02^00	[113]	00^01	10^00	[113]
00^02	02^01	[113]	00^02	10^01	[113]
00^03	02^02	[113]	00^03	10^02	[113]
00^04	02^03	[113]	00^04	10^03	[113]
01^11	03^10	[115]	01^11	11^10	[114]
02^01	04^00	[115]	02^21	12^20	[19]
02^21	04^20	[19]	01^12	11^11	[19]
01^12	03^11	[19]			

FIGURE 3-15

Rotational gain distribution in the 9.4- and 10.4-μm, regular and sequence bands. The discharge was operated with a 5% CO_2: 10% N_2: 85% He gas mixture at 425 Torr total pressure. The smooth curves show the best fit of the calculated relative gain with T = 381 K, while the triangles show the calculated absolute gain. Crosses are used to indicate the gain coefficients calculated for the anomalous lines. The measured vibrational temperatures were T_2 = 411 ± 15 K, and T_3 = 2325 ± 50 K.

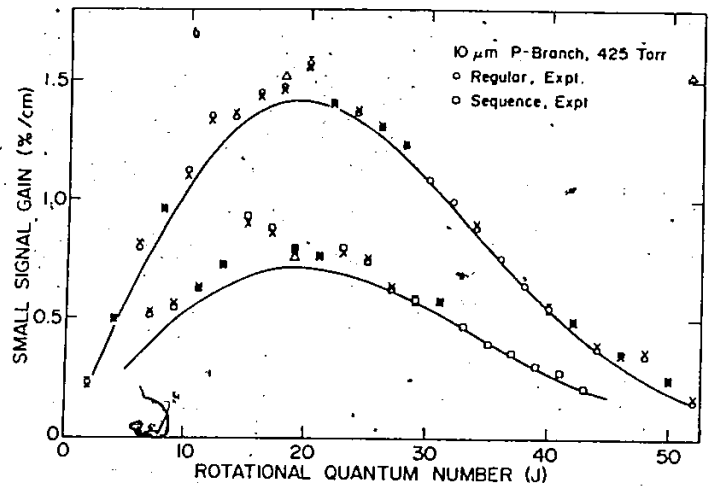
10 μm P-Branch, 425 Torr
o Regular, Expt.
o Sequence, Expt
SMALL SIGNAL GAIN (%/cm)
ROTATIONAL QUANTUM NUMBER (J)

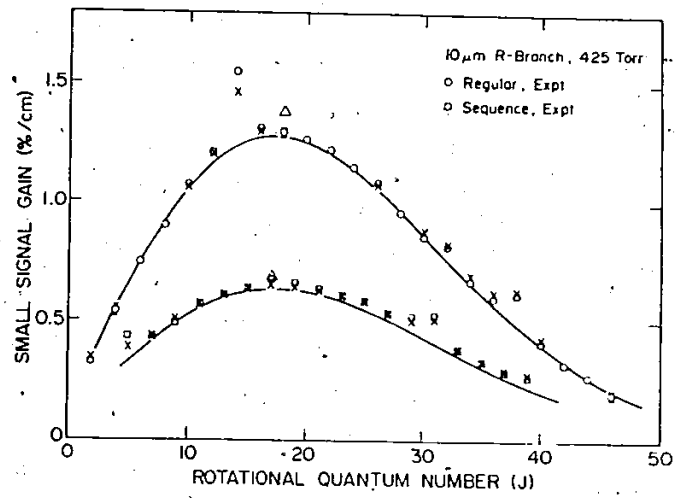
10μm R-Branch, 425 Torr
o Regular, Expt
o Sequence, Expt
SMALL SIGNAL GAIN (%/cm)
ROTATIONAL QUANTUM NUMBER (J)

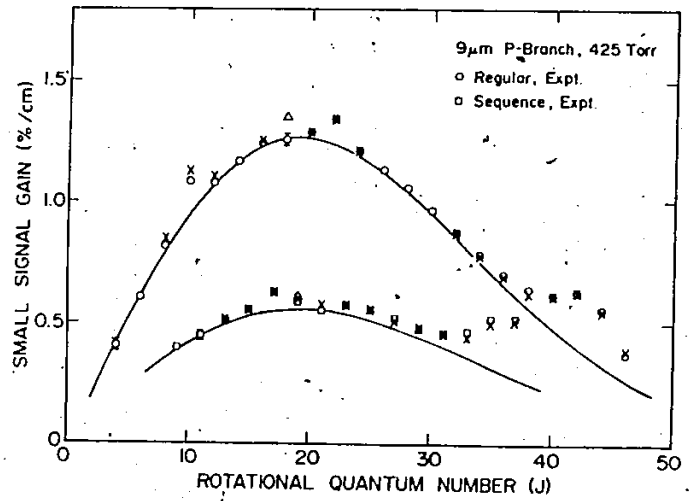
9μm P-Branch, 425 Torr
o Regular, Expt.
o Sequence, Expt.
SMALL SIGNAL GAIN (%/cm)
ROTATIONAL QUANTUM NUMBER (J)

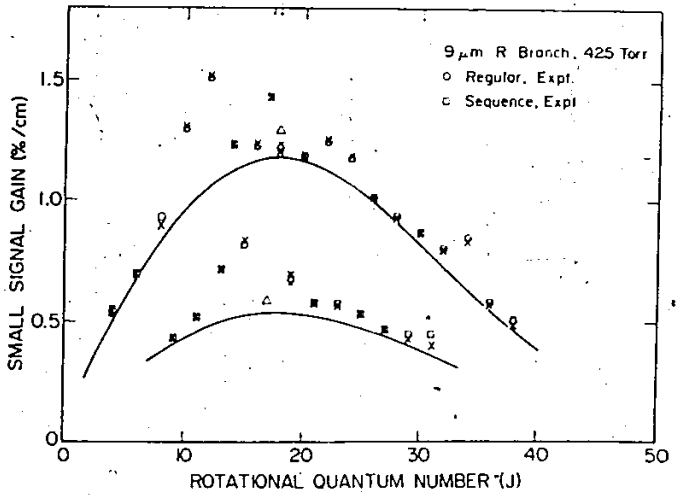
9 μm R Branch, 425 Torr
o Regular, Expt.
o Sequence, Expt
SMALL SIGNAL GAIN (%/cm)
ROTATIONAL QUANTUM NUMBER (J)

accurately fit a rotational temperature. Therefore, the relative gain due to overlaps was first calculated and the measured gain coefficients were reduced by this factor. The smooth curves in Fig. 3-15 represent the best fit to the corrected gain coefficients. The correction for overlap and the rotational temperature fit were performed in a self-consistent manner. A simultaneous fit to the four regular branches gave T = 381 ± 7 K. This value was then used in the fit to the sequence band gain coefficients. The overall fit is very good, with an average deviation of < 2 %.

As expected, many more lines have anomalously high gain at 425 Torr than at 80 Torr. The crosses in Fig. 3-15 show the calculated gain coefficients including overlaps. Once again, all of the calculated values are in good agreement with the measured gain coefficients. The effect of overlapping gain is particularly noticeable in the 9.4-μm R branch, where the $00^{0}1$ and $00^{0}2$ lines lie close together. Lavigne et al. [116] reported anomalously high gains on both regular and sequence lines in this region, but it is surprising that there appear to be no other reports of these large anomalous gains. Once again, the calculated values of the absolute gain are shown in Fig. 3-15. On average, the calculated gain is ~8 % higher than the measured gain. This discrepancy is not regarded as significant in view of the remaining uncertainties in CO_2-broadened linewidths, and hence the CO_2 transition dipole moment (see Sect. 2.6).

3.6.3 Significance of Overlapping Gain

The results shown in Figs. 3-14 and 3-15 confirm that there are

many more transitions with anomalous gain coefficients in the TE CO_2 laser than has been generally realized. If these results are extrapolated to an atmospheric pressure discharge, calculations indicate that > 75 %of the 10.4-μm lines have significant anomalies.‡ Neglect of these overlaps in the P branch of the 10.4-μm band, where rotational temperatures are generally determined, can result in an underestimation of T by ~20 K.‡‡ When this error is combined with a further underestimation of ~25 K due to the incorrect J dependence of the linewidth (see Sect. 3.5.3), significant errors in rotational temperature measurements can occur.

The situation in the 9.4-μm R branch is of particular interest in atmospheric pressure discharges. Calculations indicate that for T_3 > 2400 K, the combined R(12) 00^01 and R(17) 00^02 transitions will have a gain coefficient which exceeds that on any other transition, including the 10.4-μm P(20) transition. This prediction was confirmed experimentally by operating the TE discharge at atmospheric pressure in a nonselective laser cavity formed by a concave copper mirror and an uncoated Ge flat. As the CO_2 content in the gas mixture was reduced from 5 % to 3 %, T_3 increased to ~2400 K, and the laser switched from oscillation on only the 10.4-μm P(20) line to oscillation on both 10.4-μm P(20) and 9.4-μm R(12). The Ge flat was then replaced by a 65-%

---

‡ This calculation is based on the vibrational temperatures given in Fig. 3-15, and anomalies of > 5 % extra gain are considered to be significant.

‡‡ The gain overlaps in the 10.4-μm P branch tend to increase the gain coefficients for low-J transitions relative to high-J transitions, thus simulating the conditions of a lower temperature if overlap is neglected.

reflectivity output coupler. With oscillation occurring about equally on P(20) and R(12), an output pulse energy of 13 J was measured using a Gen Tec ED-500 joulemeter. The discharge contained a gas mixture of 3% CO_2: 10% N_2: 87% He, and the input energy density was ~175 J/ℓ·atm. Such a multiline oscillator may prove useful in obtaining maximum energy extraction from an amplifier chain [117].

The excellent agreement between experiment and calculation shown in Figs. 3-14 and 3-15 confirms the accuracy of the mode-temperature model described in Sect. 2.5 and used throughout this thesis. In addition, the use of the same linewidths for the 9.4- and 10.4-μm sequence and regular bands is found to be accurate. The results presented in this section are helpful in understanding the operation of the TEA sequence laser described in the next chapter.

3.7 Summary

This chapter presents a detailed account of how a CO_2 laser discharge can be characterized in terms of the temperatures T, T_1, and T_3, and how discharge excitation is optimized. In particular, optimization of the TE discharge used throughout this thesis is described. Accurate measurements of linewidths and anomalous gain coefficients are also presented, and the influence of these results on the accuracy of measured discharge temperatures is discussed. All of these topics provide the background necessary for the discussions concerning optimization of sequence and 4.3-μm laser performance found in the following chapters.

CHAPTER 4

DESIGN OF EFFICIENT TEA SEQUENCE LASERS

4.1 Introduction

One of the key elements in the production of high power 4.3-μm CO_2 laser pulses is an efficient, high power sequence pump laser. However, at the time this research was undertaken such a pump laser source had not been developed. Therefore, the design and optimization of TEA sequence lasers was investigated [118,119], and is the subject of this chapter. The high power sequence laser technology developed as a result of this work was then utilized in the experiments described in Chapts. 5, 6, and 7, to produce high gain, high power 4.3-μm lasers.

Laser emission on the $(00^02\text{-}10^01)$ and $(00^02\text{-}02^01)$ sequence bands of CO_2 was first reported by Reid and Siemsen in 1976 [4,5]. They employed an intracavity hot CO_2 cell to convert a conventional CW CO_2 laser to operation on the sequence lines, and were able to obtain CW output powers equivalent to ~50 % of the regular output power from the same laser. In general, the sequence bands are very similar to the regular laser bands, but the small anharmonicity of the CO_2 molecule causes the frequencies of the sequence laser lines to lie between those of the regular lines. Consequently, CW sequence lasers found immediate use in frequency-dependent applications such as optical pumping of molecular gases to produce far-infrared lasers [120]. In principle, the sequence bands also provide a simple means of translating the inherent

advantages of regular band TE CO_2 lasers to a new set of frequencies, with corresponding applications to optical pumping, laser isotope separation, laser photochemistry, atmospheric monitoring, and nonlinear optics.

Recently, several other groups have produced sequence laser pulses from TE CO_2 oscillators. The initial investigations [121-123] were not very successful, with maximum output energies ranging from 100 to 185 mJ/pulse (< 0.1 to 1.7 J/ℓ·atm energy extraction). In a later experiment [124], increased pulse energy (1 J/pulse) and energy extraction (2.5 J/ℓ·atm) were reported. However, all of these values were much less than the energy extraction of ~15 J/ℓ·atm that could be obtained from an optimized regular band CO_2 laser. It seemed very probable that the performance of TE sequence lasers could be significantly improved upon, in light of the successful conversion of CW CO_2 lasers to sequence band operation [5]. Thus, a re-examination of the possibility of obtaining efficient pulsed sequence operation from a conventional TE CO_2 laser was undertaken. Through the use of an intracavity hot CO_2 cell and the 88-cm long Lumonics TE discharge, sequence pulses with energies as high as 6 J (5.9 J/ℓ·atm energy extraction) were obtained. In addition, lasing on 54 sequence lines was observed from a grating-tuned cavity, with 30 lines having output energies greater than 2 J/pulse. These results represent a significant improvement over the previous studies, as the comparison in Table 4-1 shows. Since the sequence lines differ in frequency from the regular CO_2 laser lines, sequence band operation greatly increases the line tunability of a TE CO_2 laser. Furthermore, any conventional TE CO_2

TABLE 4-1

Comparison of pulsed sequence CO_2 lasers.

Institute	Maximum Energy (J/pulse)	Maximum Energy Extraction (J/ℓ·atm)	Number of Lines Observed
Los Alamos [a] U.S.A., 1977	0.1	< 0.1	9
DREV [b] Canada, 1978	0.185	1.7	1
Minsk [c] U.S.S.R., 1978	0.18	0.45	28
Minsk [d] U.S.S.R., 1980	1.0	2.5	1
McMaster [e] Canada, 1981	6.0	5.9	54

a) Ref. [121].
b) Ref. [122].
c) Ref. [123].
d) Ref. [124].
e) This work and Ref. [118].

laser can be converted to operation on the sequence lines simply by incorporating a hot CO_2 cell inside the optical cavity.

The purpose of this chapter is to outline the design criteria for construction of high energy TE sequence CO_2 lasers. Although the use of an intracavity hot cell is a simple technique to implement, certain considerations must be taken into account if efficient sequence operation is to be achieved. Otherwise, output energies are low as can be seen from the values shown in Table 4-1. In the next section, the experimental apparatus is described. In Sects. 4.3 to 4.5, a theoretical model suitable for both regular and sequence operation of TE CO_2 lasers is presented, and the importance of the various gain and loss mechanisms is discussed. Factors such as hot cell length, hot cell pressure, degree of discharge excitation, and output coupling are shown to be important considerations. It is demonstrated that intracavity hot CO_2 cells are an effective means of achieving efficient TE sequence lasing, contrary to the conclusions of Ref. [122]. Finally, several applications of high power sequence lasers are described in Sect. 4.6.

4.2 Experimental Apparatus

Figure 4-1 is a schematic diagram of the experimental apparatus used to generate and observe sequence band CO_2 laser pulses. The sequence laser cavity was 350 cm long to accommodate the TE discharge and hot cell, which were ~50 % longer overall than the active length which is indicated in Fig. 4-1. The Cu mirror could be replaced by an original (PTR, ML-304) grating to make the laser line tunable. The 65-% reflectivity output coupler was used for sequence operation, and was

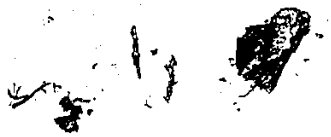

FIGURE 4-1

Schematic diagram of the apparatus employed to generate and observe sequence band CO_2 laser pulses.

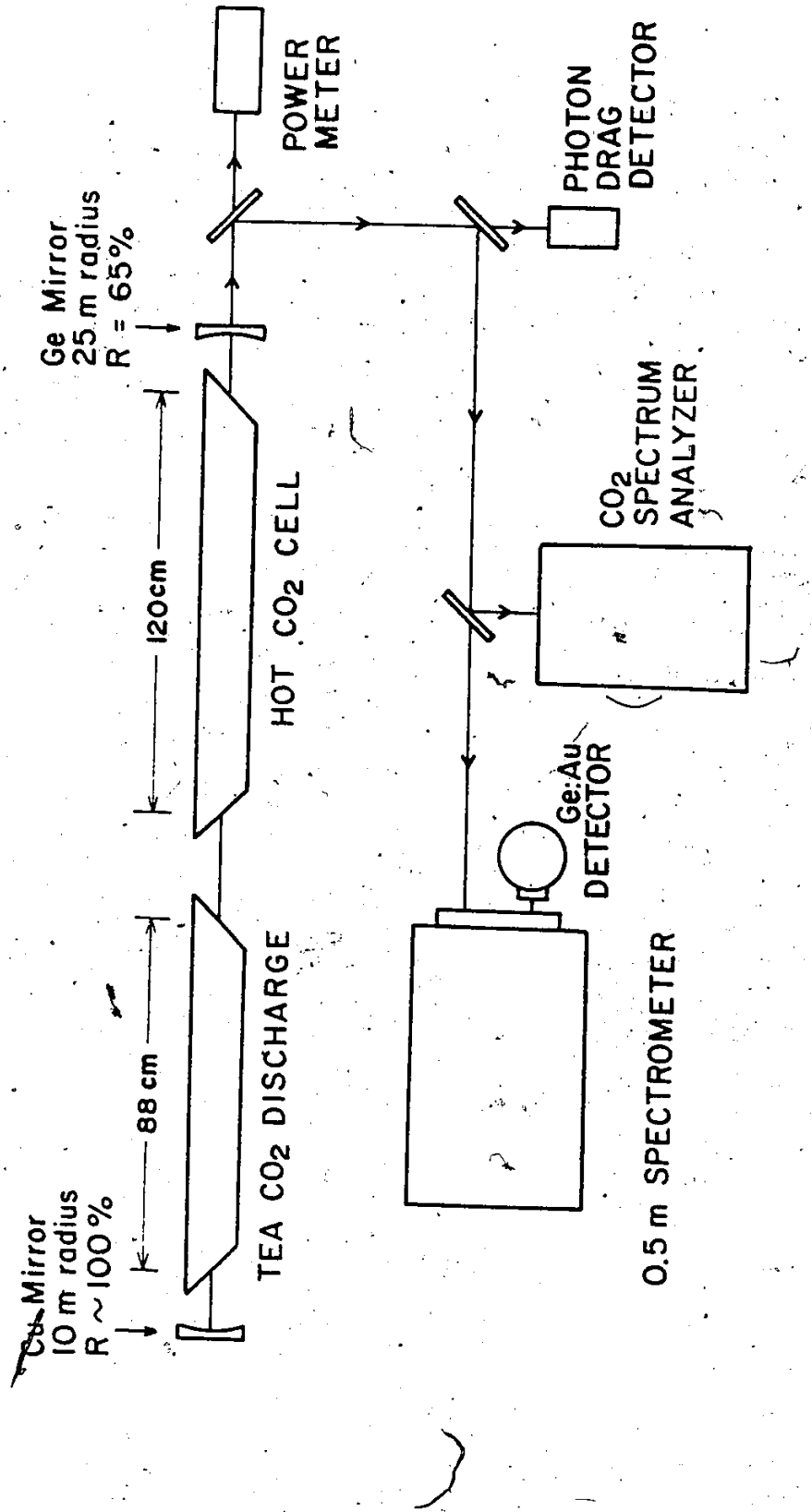
POWER METER
PHOTON DRAG DETECTOR
Ge Mirror
25 m radius
R = 65%
120cm
HOT CO_2 CELL
CO_2 SPECTRUM ANALYZER
Ge:Au DETECTOR
88 cm
TEA CO_2 DISCHARGE
Cu Mirror
10 m radius
R ~ 100 %
0.5 m SPECTROMETER

replaced by a flat uncoated Ge reflector (R = 36 %) if the laser was operated on the regular bands. The discharge was the Lumonics K-902-2 module which is described in detail in Sect. 3.3. It was operated at atmospheric pressure, with gas mixtures typically containing 10-15% CO_2, 15-20% N_2, and the balance He. In initial experiments, a discharge excitation of ~115 J/ℓ·atm was used, which was obtained by charging a 0.075-μF capacitor to 40 kV. This excitation was the standard value at which the discharge was designed to operate. However, it was necessary to increase the excitation, as described in Sect. 4.5. Therefore, the capacitance was increased to 0.135 μF, resulting in an input energy of ~210 J/ℓ·atm. The increased excitation necessitated an increase in the gas flow rate from 10 ℓ/min to 15 ℓ/min to obtain arc-free operation at repetition rates of ~0.5 Hz.

The hot cell used in this work was of a very simple design. It consisted of a 5-cm ID stainless steel tube sealed at both ends with NaCl Brewster windows, and it could operate at pressures up to 760 Torr. A single winding of nicrhome wire around the tube (5-cm pitch) was used to heat the cell. Asbestos tape was used for thermal and electrical insulation, and the windings were surrounded by a 12-cm diameter aluminum heat shield. A photograph of the hot cell is shown in Fig. 4-2. The total length was 180 cm but the measured temperature profile, obtained using a thermocouple, indicated a central hot region ~120 cm long which was surrounded by cooler end regions. The hot cell was operated with ~500 W input power, which resulted in the central hot region having a temperature of ~600 K and the windows being at ~400 K. An improved design for a hot cell, which has the nichrome heater coil

FIGURE 4-2

Photograph of the hot cell used in the TEA sequence laser. Total cell length is 180 cm.

wound inside a pyrex tube, was used for the sequence laser described in Chapts. 5 to 7 (see Fig. 5.4). A very efficient vacuum-insulated hot cell is described in Ref. [94].

The arrangement of the experimental apparatus shown in Fig. 4-1 enabled measurements of several important parameters: Total pulse energy was measured using a Scientech model 36-0001 calorimeter and a Gen Tec ED-500 joulemeter, and pulse shape was monitored with a photon drag detector. A CO_2 spectrum analyser gave the approximate lasing frequencies and the number of lines lasing, while a 0.5-m spectrometer provided enough frequency resolution to separate nearby sequence and regular lines. The results obtained with this experimental setup are presented in the rest of this chapter. First however, a rate-equation model of the sequence laser is described, which gives a better understanding of the gain dynamics and is useful in optimizing the performance of the laser.

4.3 Rate-Equation Model

To obtain a better understanding of the gain dynamics of a TE CO_2 laser operating on either the regular or sequence bands, a rate-equation model of the system was developed. The model is similar to those used by Manes and Seguin [125] and Smith and Thomson [126], except that separate equations are used to explicitly describe the populations of the upper and lower laser levels, using the formalism of Garside et al. [127]. The sequence laser model is described in detail below. The model describing operation on the regular bands is similar, but the equations are adjusted to account for the different levels involved (see

Appendix A).

The seven differential equations governing sequence operation of a TE CO_2 laser on the 10.4-μm (00^02-10^01) band are as follows:

$$\frac{dE_3}{dt} = N_e(t)N_{CO_2}h\nu_3\Sigma_3 + \frac{E_4 - E_4^e(T_3)}{\tau_{N_2}} - \frac{E_3}{\tau_3} - h\nu_3 G_{ov}\sigma_s\delta_s\rho_s c, \quad (4\text{-}1)$$

$$\frac{dE_{12}}{dt} = N_e(t)N_{CO_2}h\nu_{12}\Sigma_{12} + \frac{E_3}{\tau_3} - \frac{E_{12} - E^e{}_{12}(T)}{\tau_{VT}} + h\nu_1 G_{ov}\sigma_s\delta_s\rho_s c, \quad (4\text{-}2)$$

$$\frac{dE_4}{dt} = N_e(t)N_{N_2}h\nu_3\Sigma_4 - \frac{E_4 - E_4^e(T_3)}{\tau_{N_2}}, \quad (4\text{-}3)$$

$$\frac{dN_{002}}{dt} = -G_{ov}\sigma_s\delta_s\rho_s c - \frac{N_{002} - N^e{}_{002}(T_3)}{2\tau_{\nu_3}} - \frac{2N_{002}}{\tau_3}, \quad (4\text{-}4)$$

$$\frac{dN_{101}}{dt} = G_{ov}\sigma_s\delta_s\rho_s c - \frac{N_{101} - N^e{}_{101}(T_1,T_3)}{\tau_{101}}, \quad (4\text{-}5)$$

$$\frac{d\delta_s}{dt} = -2G_{ov}\sigma_s\delta_s\rho_s c - \frac{\delta_s - (K_{002}N_{002} - K_{101}N_{101}\, g_{002}/g_{101})}{\tau_R}, \quad (4\text{-}6)$$

$$\frac{d\rho_s}{dt} = FG_{ov}\sigma_s\delta_s\rho_s c - \frac{\rho_s}{\tau_c} + FG_{ov}\beta K_{002}N_{002}. \quad (4\text{-}7)$$

E_3 and E_{12} are the stored energies in the ν_3 and combined $\nu_1 + \nu_2$ vibrational modes of CO_2 respectively, and E_4 is the vibrational energy stored in the N_2 molecules. Variables denoted by the subscripts 002 and 101 pertain to the corresponding vibrational levels. N_{002} and N_{101} are

vibrational populations and N_{CO_2} and N_{N_2} are the total number densities of CO_2 and N_2. δ_s is the population inversion on the sequence transition and is given by $\delta_s = n_{002} - n_{101}g_{002}/g_{101}$, where $g = 2J + 1$ represents the statistical weight of the rotational level with rotational quantum number J, and n_{002} and n_{101} are the populations of the upper and lower rotational levels of the sequence transition. σ_s is the sequence gain cross-section calculated from Eq. (2-17), such that the product $\sigma_s\delta_s$ gives the small-signal gain coefficient. G_{ov} is a factor having a value > 1 which accounts for overlapping gain contributions, and is discussed further in Sect. 4.5. G_{ov} and σ_s are calculated by assuming a Lorentzian lineshape (Eq. (2-20)). $h\nu_1$ and $h\nu_3$ are the fundamental energy intervals of the ν_1 and ν_3 modes, and $h\nu_{12}$ is the energy of one average $\nu_1 + \nu_2$ quantum ($h\nu_{12}=h(\nu_1+\nu_2)/2$). The sequence photon density is given by ρ_s, and c is the speed of light. K_{002} and K_{101} are the rotational population factors for the particular rotational levels connected by the sequence transition, and have values of ~0.05 calculated from Eq. (2-16). Thus, the products $K_{002}N_{002}$ and $K_{101}N_{101}$ represent the equilibrium populations of the sequence transition upper and lower rotational levels. F is the cavity filling factor (ie: ratio of discharge length to total cavity length), and $\beta K_{002}N_{002}$ is the spontaneous emission term as given in Ref. [128]. The various molecular relaxation times are defined in Sect. 2.4, where the corresponding relaxation rates are also given. The relaxation times are calculated from the rates by assuming constant number density conditions. Typical values of the relaxation times are given in Table 2-1 for an atmospheric pressure gas mixture of 11% CO_2: 16% N_2: 73% He.

The derivation of the relaxation terms in Eqs. (4-1) to (4-7) from the relaxation processes described in Sect. 2.4 is given in Appendix B. In particular, the origin of the factor of two in the second term on the right hand side of Eq. (4-4) is discussed.

The three-temperature model of Sect. 2.5 is used to describe the unperturbed populations in the discharge. Variables denoted with the superscript e represent the equilibrium value of that variable at the temperature indicated in brackets. At each step of the calculation, new values of T_1 and T_3 are determined from the current values of E_{12} and E_3. Vibrational energy and vibrational temperature are related by the following expression [125]:

$$E_n = N_{CO_2} h\nu_n g_n \frac{x_n}{1-x_n}, \tag{4-8}$$

where E_n is the energy stored in the vibrational mode with frequency ν_n, x_n is a function of T_n and is defined by Eq. (2-14), and g_n is the degeneracy factor. g_1 and g_3 equal one, while g_2 equals two. Equation (4-8) gives the stored energy in the vibrational mode of N_2 to a good approximation if N_{CO_2} is replaced by N_{N_2}, and the other variables have values which correspond to the ν_3 mode of CO_2 (i.e., $h\nu_3$, g_3, and T_3). An expression for T_1 can be obtained by adding $E_1 + E_2$ to give E_{12}, and rearranging to give:

$$T_1 = \frac{h\nu_1}{2k\ \ln[2(2+a)/\{(1-4a(2+a))^{-1/2} - 1\}]}, \tag{4-9}$$

where $a = E_{12}/(N_{CO_2} h\nu_1)$. Similarly, Eq. (4-8) can be solved for T_3

giving:

$$T_3 = \frac{h\nu_3}{k \ln[N_{CO_2} h\nu_3/E_3 + 1]}. \qquad (4\text{-}10)$$

The rotational-translational temperature T is assumed to remain constant in the model, and the input value of T corresponds to the value at the peak of the gain.

The instantaneous value of the electron density $N_e(t)$ is obtained from the relation [126]:

$$N_e(t) = \frac{i(t)}{e\, v_d\, A}, \qquad (4\text{-}11)$$

where i(t) is the value of the discharge current at time t obtained from measured current pulses, e is the electronic charge, v_d is the electron drift velocity, and A is the area of cross-section of the discharge (308 cm^2). The Σ_i's in Eqs. (4-1) to (4-3), are the effective electron-vibration excitation rates for the vibrational modes. Values for the Σ_i's and v_d are taken from [24] and are based on E/N values obtained from measured voltage pulses.

The cavity decay time τ_c is composed of two terms and is given by $\tau_c=(1/\tau_{refl} + 1/\tau_{loss})^{-1}$. τ_{refl} is the photon lifetime in the cavity due to output coupling losses, i.e., $\tau_{refl}= - 2L/[c \ln(R)]$, where L is the cavity length and R is the reflectivity of the output coupler. τ_{loss} is the photon lifetime due to all losses in the cavity other than output coupling, and is an important term in the modeling of sequence lasers. τ_{loss} is given by $\tau_{loss}= - L/[c \ln(1-\bar{L})]$, where $\bar{L}$ is the total

loss per pass in the cavity. $\bar{L}$ is defined as the sum of the internal optical losses $\bar{L}_{opt}$, due to Brewster windows and diffraction losses, etc., and the loss introduced by the hot CO_2 cell. The hot cell loss is given by $\alpha_{hot}L_{hot}$, where L_{hot} is the length and α_{hot} is the absorption coefficient in the hot cell. (α_{hot} is a function of position along the hot cell axis due to the temperature variation over the length.)

The relative magnitudes of τ_{refl} and τ_{loss} determine the fraction of available optical energy that is coupled out of the cavity. The total rate of loss of photons from the cavity is $1/\tau_c$, and the rate of loss through the output coupler is $1/\tau_{refl}$. Therefore, the fraction coupled out as useful energy is given by:

$$F_{out} = \frac{\tau_c}{\tau_{refl}} \qquad (4\text{-}12)$$

This simple method of determining F_{out} is based on the assumption that the output coupling loss per pass can be averaged over the cavity length. Since this loss is only ~15 %/pass in the case of sequence lasers and is comparable to the other cavity losses of ~10 %/pass, the assumption should be valid. The output pulse energy is determined by integrating the stimulated emission term $G_{ov}\sigma_s\delta_s\rho_s c$ over time, and multiplying by $h\nu_{laser}$ and F_{out}, where ν_{laser} is the laser radiation frequency.

The model is implemented in the following manner. Initial energies and populations in Eqs. (4-1) to (4-7) are calculated by setting T, T_1, and T_3 equal to 300 K. Successive values of $N_e(t)$ are determined from Eq. (4-11) and the measured current pulse, and the

equations are solved beginning at a time corresponding to the start of the current pulse. The numerical technique used is the Hamming 2/3 predictor-corrector method [129] and the solutions are obtained using a DEC PDP-11/44 computer. Preliminary calculations using the model indicate that the gain dynamics of sequence lasers and regular lasers are similar. The differences in laser output are primarily due to the relative magnitudes of the gain in the discharge and the loss in the hot cell. Thus, the effects of gain and loss in the cavity are discussed in detail in the next section.

4.4 Intracavity Gain and Loss Considerations

It is reasonably simple to convert a regular band CO_2 laser to operation on the sequence bands by using an intracavity hot CO_2 cell. However, care must be taken when determining the hot cell operating parameters if efficient sequence lasing is to be obtained. The most critical parameter is that of hot cell pressure. While the sequence transitions themselves are too high in vibrational energy to produce any significant absorption at a temperature of 600 K, absorption at the sequence frequencies can arise due to pressure broadening of nearby absorption lines, and this becomes appreciable at pressures in excess of a few hundred Torr. The result is a substantial decrease in sequence output energy, as noted in Ref. [122].

To determine the absorption at the sequence frequencies in the hot cell, measurements were made of absorption as a function of CO_2 pressure using a CW CO_2 probe laser similar to that described in Sect. 3.3, which was capable of operation on both the sequence and

regular transitions. Results are shown in Figs. 4-3 and 4-4 for two pairs of lines. As expected, the regular transitions experience an order of magnitude more absorption in hot CO_2, but absorption on the sequence transitions becomes appreciable at atmospheric pressure. The sequence absorption increases approximately as the square of the pressure due to the Lorentzian nature of the overlapping lines (see Eq. (2-20)). Also shown in Figs. 4-3 and 4-4 is the absorption calculated for both the regular and sequence lines. The calculation was carried out using the theory of Sects. 2.5 and 2.6 and the gas temperature was determined from the measured temperature profile in the hot cell. The same overlapping bands were included in the calculation as were used for the overlapping gain calculations of Sect. 3.6 (see Table 3-3). However, in the hot cell it is mainly the regular and hot bands which contribute to the absorption at the sequence frequencies. The overall agreement between calculation and experiment shown in Figs. 4-3 and 4-4 is good, and the small discrepancies observable on the sequence transitions are attributed to uncertainties in the exact CO_2 self-broadened linewidths.

The most important conclusion that can be drawn from the results shown in Figs. 4-3 and 4-4 is that the hot cell pressure should be kept as low as possible. However, if one is to convert an atmospheric pressure ~~TE~~ CO_2 laser to operation on the sequence lines, the hot cell pressure cannot be reduced below a certain minimum value. Although 100 Torr of CO_2 in the hot cell produces optimum absorption at the line center of the regular transitions, the large gain bandwidth of an atmospheric pressure discharge enables regular lasing to continue at an

FIGURE 4-3

Measured and calculated hot cell absorption as a function of CO_2 pressure for the P(18) regular and P(15) sequence 10.4-μm lines. $\alpha_{hot}L_{hot}=\ell n(I_o/I)$ where I is the transmitted probe laser power with CO_2 in the hot cell and I_o is the transmitted power for the hot cell evacuated. See text for details of the calculation.

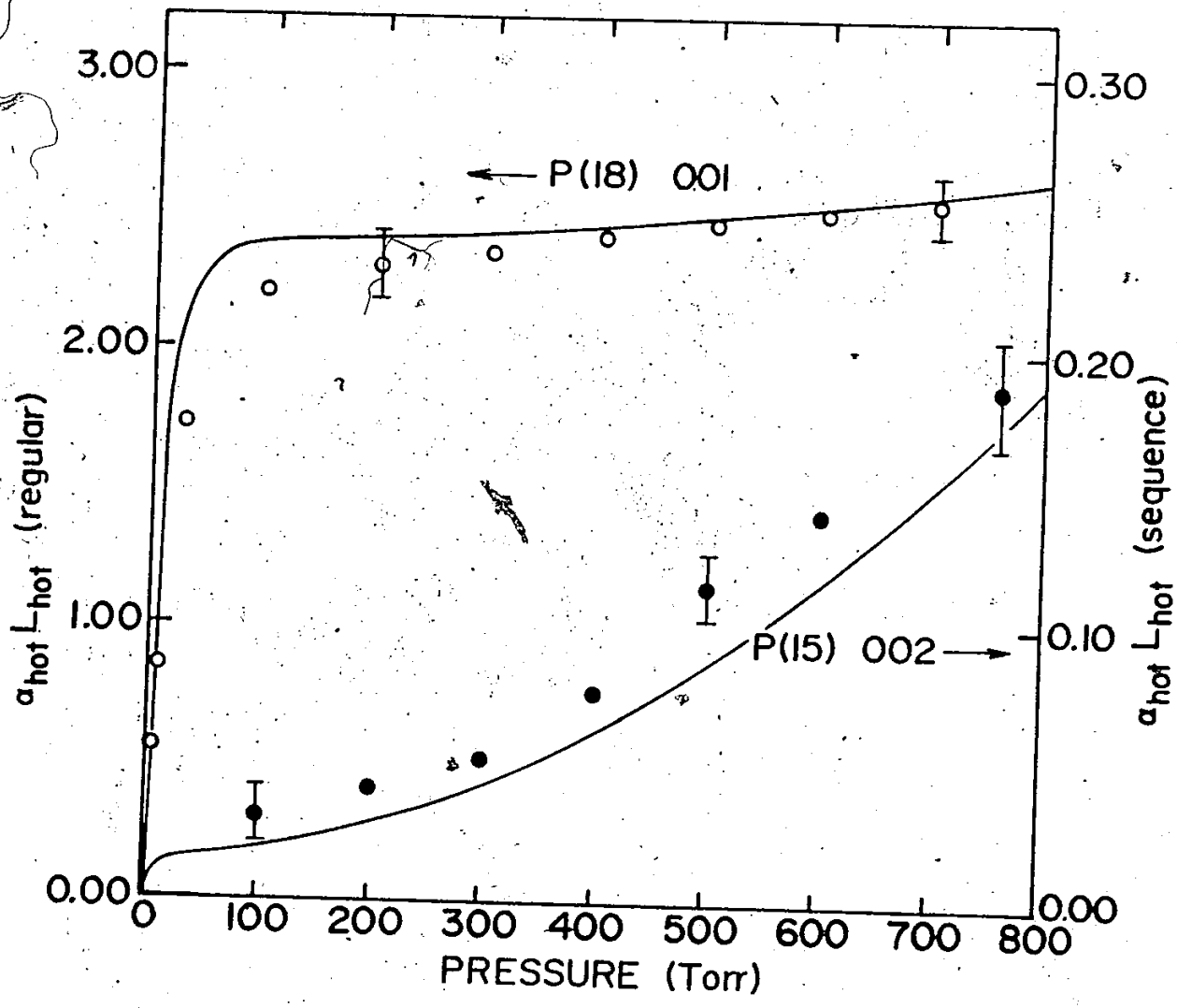
3.00
2.00
1.00
0.00
0.30
0.20
0.10
0.00
P(18) 001
P(15) 002
$a_{hot} L_{hot}$ (regular)
$a_{hot} L_{hot}$ (sequence)
0
100
200
300
400
500
600
700
800
PRESSURE (Torr)

FIGURE 4-4

Measured and calculated hot cell absorption as a function of CO_2 pressure for the P(20) regular and P(17) sequence 10.4-μm lines. Further detail is given in the caption to Fig. 4-3.

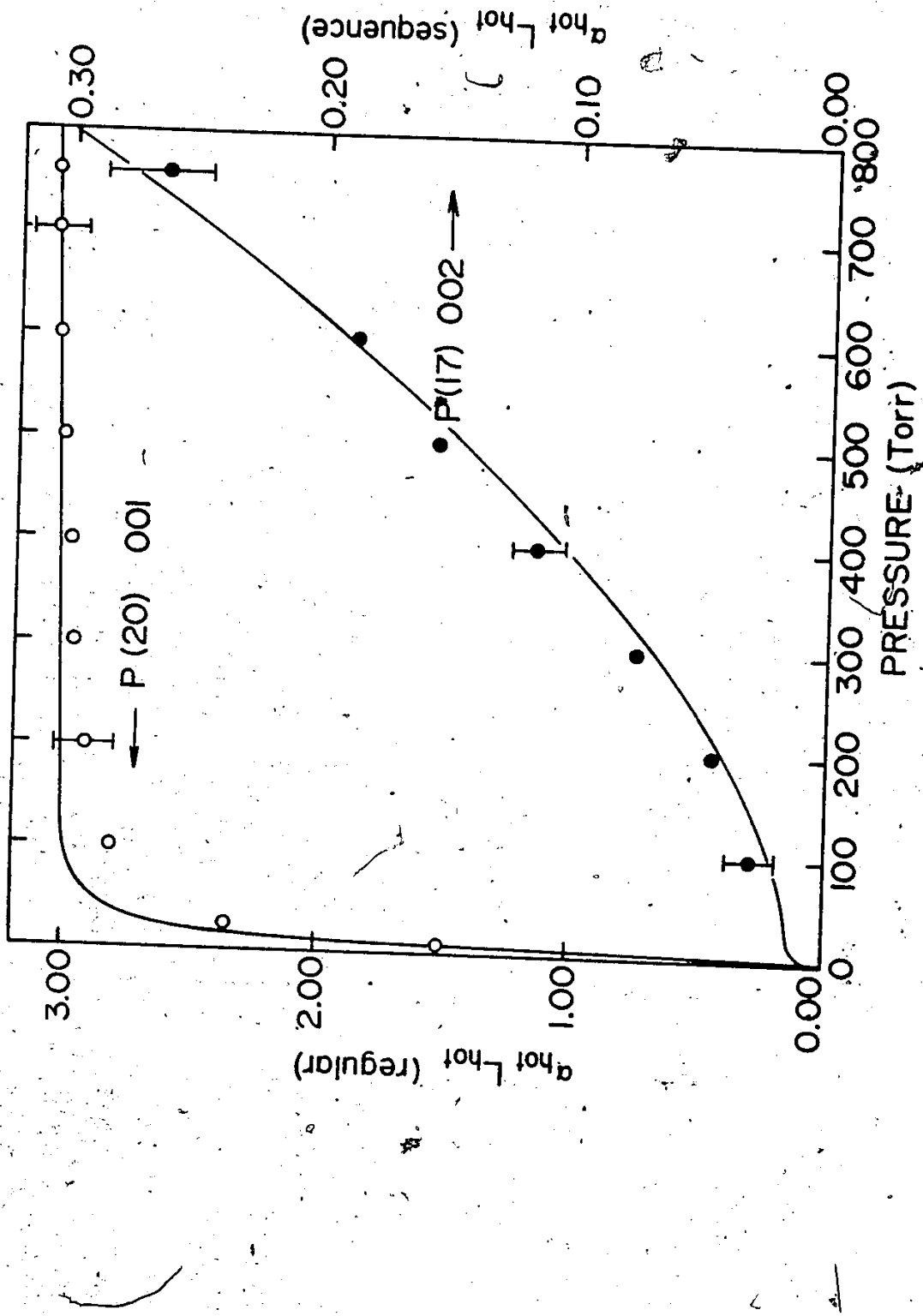
$\alpha_{hot} L_{hot}$ (sequence)
0.30
0.20
0.10
0.00
P(17) 002
P (20) 001
3.00
2.00
1.00
0.00
$\alpha_{hot} L_{hot}$ (regular)
0
100
200
300
400
500
600
700
800
PRESSURE (Torr)

offset from the line center [130]. The hot cell pressure must be increased until regular lasing is suppressed over a major portion of the gain profile, and all calculations of net gain must consider the effects of line overlap and pressure broadening in both the discharge and the hot cell.

In Sect. 3.6, detailed calculations of linecenter gain overlaps were verified by experiment at subatmospheric pressure. These calculations have been extrapolated to atmospheric pressure and the Lorentzian lineshape function of Eq. (2-20) was used to calculate the gain profile as a function of frequency. A typical gain profile is shown in Fig. 4-5(a). The significance of overlapping gain contributions on the sequence lines can be seen by referring to Fig. 3-15 of Sect. 3.6, which shows measured rotational gain distributions in a 425-Torr amplifier. Clearly, many sequence lines possess large gain overlaps. Calculations at atmospheric pressure indicate that ~35 % of the gain on the P(15) ($00^0 2$-$10^0 1$) transition is contributed by overlapping lines. The presence of this substantial additional gain permits increased output coupling and a corresponding increase in the output energies available on the sequence transitions.

Using the gain profiles as shown in Fig. 4-5(a) and calculating hot cell absorption profiles in a similar fashion, one can determine the net gain which would exist inside the sequence laser cavity of Fig. 4-1 as the hot cell pressure is increased. Typical curves are shown in Figs. 4-5(b) and 4-5(c) for hot cell pressures of 450 and 760 Torr. The effect of different linewidths in the hot cell and the discharge is evident, especially at 450 Torr. The hot cell pressure must be

FIGURE 4-5

Net gain per pass on the P(18) regular and P(15) sequence 10.4-μm lines in the laser cavity of Fig. 4-1. Traces (a), (b), and (c) are plotted for pressures of 0, 450, and 760 Torr of CO_2, respectively, in the hot cell.

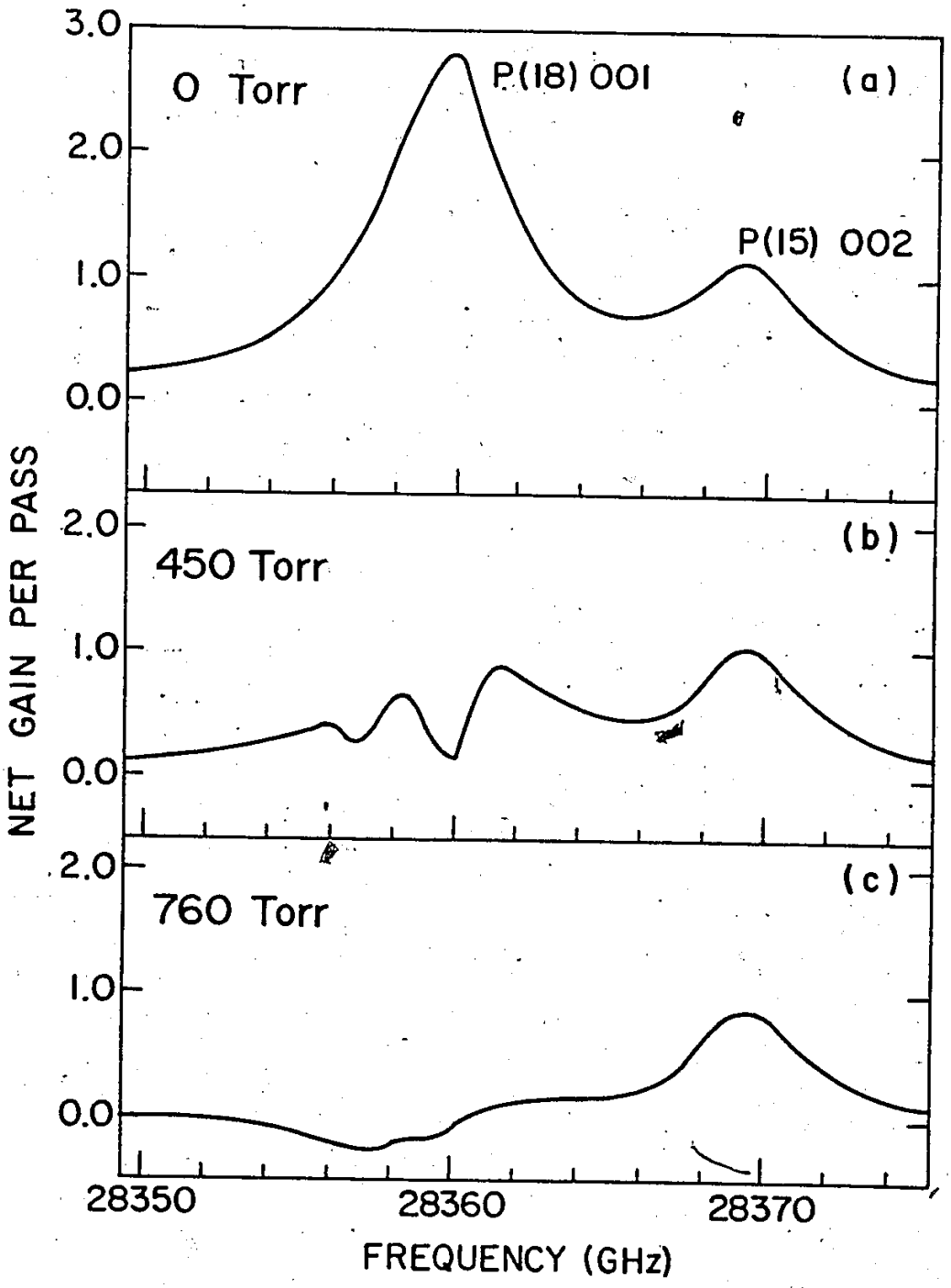
3.0
2.0
1.0
0.0
0 Torr
P(18) 001
(a)
P(15) 002
2.0
1.0
0.0
450 Torr
(b)
2.0
1.0
0.0
760 Torr
(c)
NET GAIN PER PASS
28350
28360
28370
FREQUENCY (GHz)

sufficient to reduce the net gain in the wings of the regular transition to less than the net sequence gain. At this point the laser will switch from oscillation on the regular transition to oscillation on the sequence transition. In fact the situation is somewhat more complex due to the J dependence of gain and absorption. What is actually observed in a nonselective cavity as the hot cell pressure is increased from 350 to 450 Torr is that the laser switches from oscillation on the P(18) 10.4-μm transition to simultaneous lasing on the P(12), P(14), and P(16) 10.4-μm lines plus the R(10) and R(12) 9.4-μm lines, and then finally to oscillation on the P(15) 10.4-μm sequence line with some contribution from sequence P(17). The line switching behavior can be understood by again referring to the rotational gain distribution of Fig. 3-15. The low-J transitions in the 9.4-μm R branch possess large overlapping gain contributions, as does the 10.4-μm P(15) sequence line. The effect of these overlaps is even greater in the atmospheric pressure sequence laser discharge because of the increased linewidth. In the hot cell, line broadening not only reduces the net gain in the wings of the regular transition, but also increases the absorption at the sequence frequency as Figs. 4-3 and 4-4 show. Thus, increasing the hot cell pressure beyond the minimum value which is required to suppress regular lasing simply introduces additional loss on the sequence transition, with a corresponding reduction in output power. This point is discussed in greater detail in the next section.

4.5 Optimization of Pulse Energy

The results of the previous section can now be incorporated into

the rate-equation model described in Sect. 4.3. A hot cell loss of 8 %/pass (corresponding to a hot cell pressure of ~450 Torr, see Fig. 4-3) is included in the sequence modeling, in addition to an optical loss of 4 %/pass present in both the sequence and the regular models. In the model, it is assumed that additional gain due to overlapping bands can be accounted for by the factor G_{ov} in the stimulated emission term of the rate equations. This assumption is based on the rapid ν_3 intramode relaxation time (see Sect. 2.4) and eliminates the need for additional rate equations. Figure 4-6 shows experimental and theoretical laser output pulse shapes for the 10.4-μm P(15) sequence and P(20) regular lines. The output coupling is optimized in each case and the time delays are measured from the start of the current pulse. The cavity configuration is the same as that shown in Fig. 4-1. The experimental P(20) pulse was observed with the hot cell evacuated, while the P(15) pulse was obtained with 450 Torr of CO_2 in the hot cell. The discharge was operated with a gas mixture of 11% CO_2: 16% N_2: 73% He at atmospheric pressure and an input electrical energy of 115 J/ℓ·atm. The measured sequence output energy was 3 J/pulse. The agreement between theory and experiment is good, confirming the validity of the model. It is apparent from the model calculations that there is no fundamental limitation to the extraction of energy on the sequence lines as compared with that on the regular lines. This is a direct consequence of the rapid intramode relaxation rates in CO_2, particularly within the ν_3 mode. However, it must again be stressed that proper cavity design is essential if efficient sequence operation is to be achieved. This can best be seen by considering three

FIGURE 4-6

Comparison of theoretical and experimental pulse shapes for both the P(15) sequence and P(20) regular 10.4-μm lines. Time delays are measured from the start of the current pulse, which has a peak value of 8 kA (corresponding to the total current in both discharge sections). The output coupler has a reflectivity of 65 % for sequence operation and 36 % for regular operation. The gas mixture is 11% CO_2: 16% N_2: 73% He and the discharge excitation energy is 115 J/ℓ·atm.

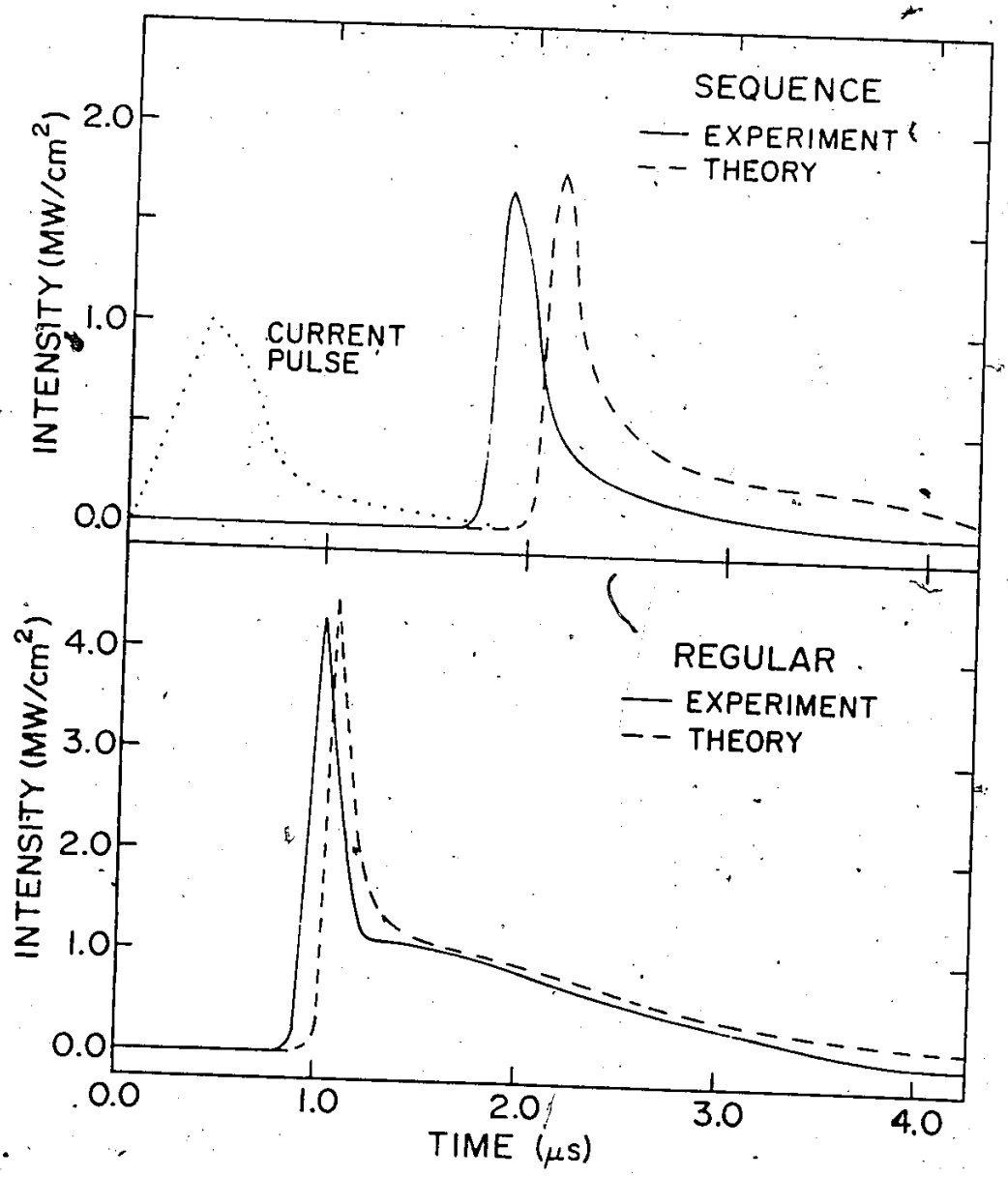
SEQUENCE
EXPERIMENT
THEORY
CURRENT PULSE
INTENSITY (MW/cm²)
2.0
1.0
0.0
REGULAR
EXPERIMENT
THEORY
INTENSITY (MW/cm²)
4.0
3.0
2.0
1.0
0.0
0.0
1.0
2.0
3.0
4.0
TIME (μs)

interrelated factors: hot cell losses, output coupling, and degree of excitation in the discharge.

The origin of the hot cell losses at the sequence frequencies was described above. In order to quantitatively determine the effect of substantial hot cell loss on sequence output, the sequence model calculations were performed for a wide range of hot cell losses. The results are presented in Fig. 4-7. Also shown are experimental data points corresponding to the range of losses which could be realized using the present apparatus. The calculated loss per pass includes a 4 % contribution from optical losses but excludes the 35 % transmission of the output coupler. The other experimental conditions are the same as those described in the preceding paragraph, although similar curves were obtained for a wide range of operating conditions. The arrow indicates the point corresponding to the minimum hot cell loss that could be achieved experimentally,‡ and shows that the output energies obtained are within 30 % of the maximum energy which could be extracted in the ideal case (i.e., no hot cell loss). This is a considerable improvement over the laser described in Ref. [122], in which the hot cell loss was 45 %/pass. It would certainly be desirable to eliminate hot cell losses altogether, however this is not physically possible. By applying the gain and loss calculations described in Sect. 4.4, it was determined that a hot cell loss of ~6 %/pass is close to the minimum which can be achieved. The optimum hot cell temperature was found to be

---

‡ This minimum hot cell loss corresponds to an operating pressure of ~400 Torr. However, under these conditions regular lasing ocurred intermittently. Thus, the hot cell was generally operated at ~450 Torr.

FIGURE 4-7

The effect of cavity loss $\bar{L}$ on sequence output energy. $\bar{L} = \bar{L}_{opt} + \alpha_{hot}L_{hot}$ where $\bar{L}_{opt}$ is the optical loss per pass and $\alpha_{hot}L_{hot}$ is the hot cell loss per pass. The data points correspond to the loss introduced on the 10.4-μm P(15) sequence transition for hot cell pressures ranging from 400 to 760 Torr. See text for further details.

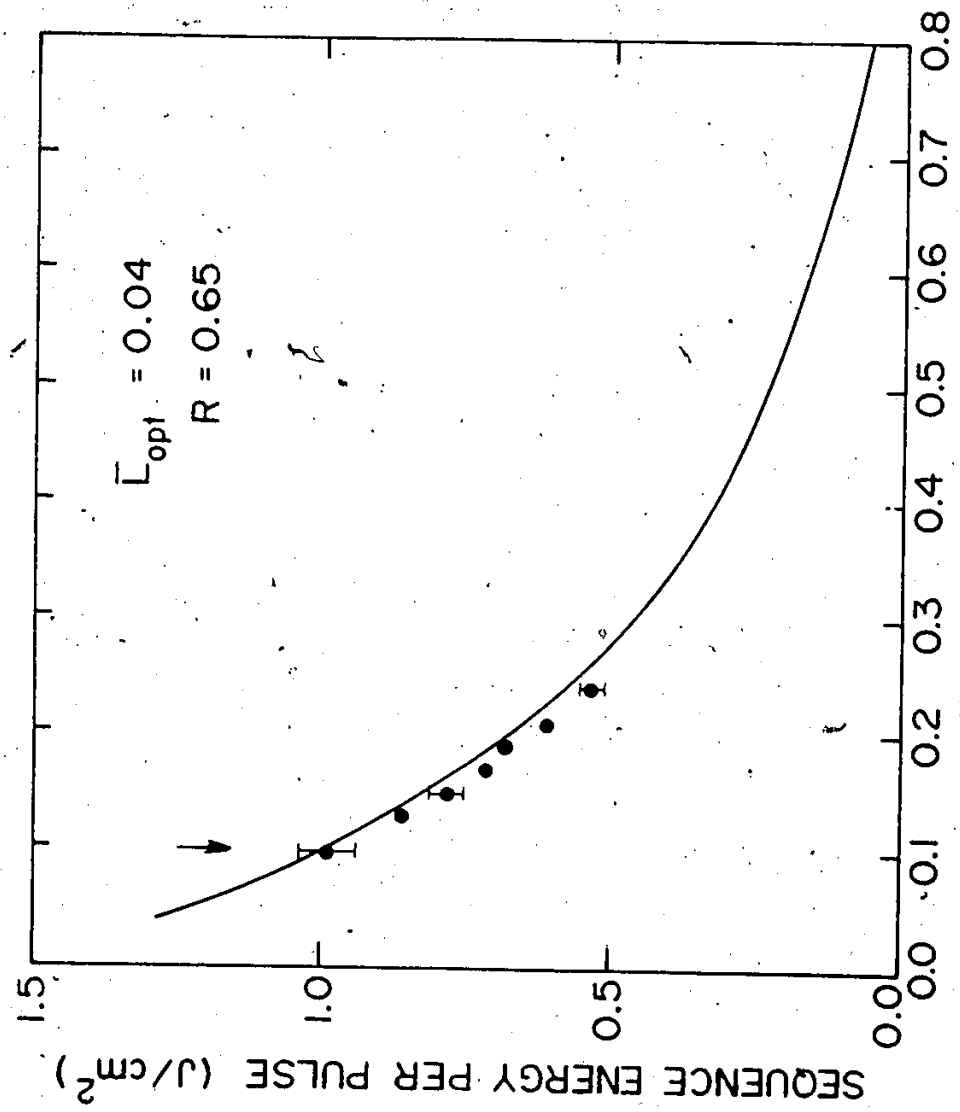
SEQUENCE ENERGY PER PULSE (J/cm²)
1.5
1.0
0.5
0.0
0.0
0.1
0.2
0.3
0.4
0.5
0.6
0.7
0.8
L̄ (total loss per pass)
L̄opt = 0.04
R = 0.65

in the range 550 to 600 K, while the optimum length corresponded to an active region equal to or slightly greater than the discharge length.‡ However, the most critical factor affecting hot cell loss remains that of pressure, and the lowest pressure needed to achieve sequence lasing should always be used.

Another major factor in the design of sequence lasers is that of optimum output coupling. Even in the presence of substantial gain contributions from overlapping bands, the sequence gain will still be equal to only ~40 % of the regular gain. Thus, the high-transmission output couplers used in regular CO_2 lasers are not suitable for sequence operation. The effect of output coupling on pulse energies and intensities is shown in Fig. 4-8 for both the P(20) regular and P(15) sequence 10.4-μm transitions. These curves were obtained using model calculations and confirmed by experiment with selected output couplers. Optimum output coupling is in the range 20 to 40 % for the sequence laser used in this study.

The final factor to be considered is that of the degree of excitation in the discharge. In general, the optimum excitation energy for sequence lasers will be greater than for regular lasers because efficient sequence laser operation requires a higher value of T_3. The need for maximizing T_3 arises as a result of two factors. First, the small-signal sequence gain is strongly dependent upon the value of T_3 in the discharge (e.g., sequence gain doubles as T_3 is increased from 1700

‡ In CW sequence CO_2 lasers, the optimum hot cell length is < 1/3 of the discharge length due to the lower value of regular band small-signal gain in these lasers [94].

FIGURE 4-8

Calculated output energy (solid curve) and intensity (dashed curve) as a function of cavity reflectivity for both sequence and regular operation. The gas mixture was 11% CO_2: 16% N_2: 73% He, and the excitation energy was 115 J/ℓ·atm. The optical loss was taken as 4 %/pass in both cases.

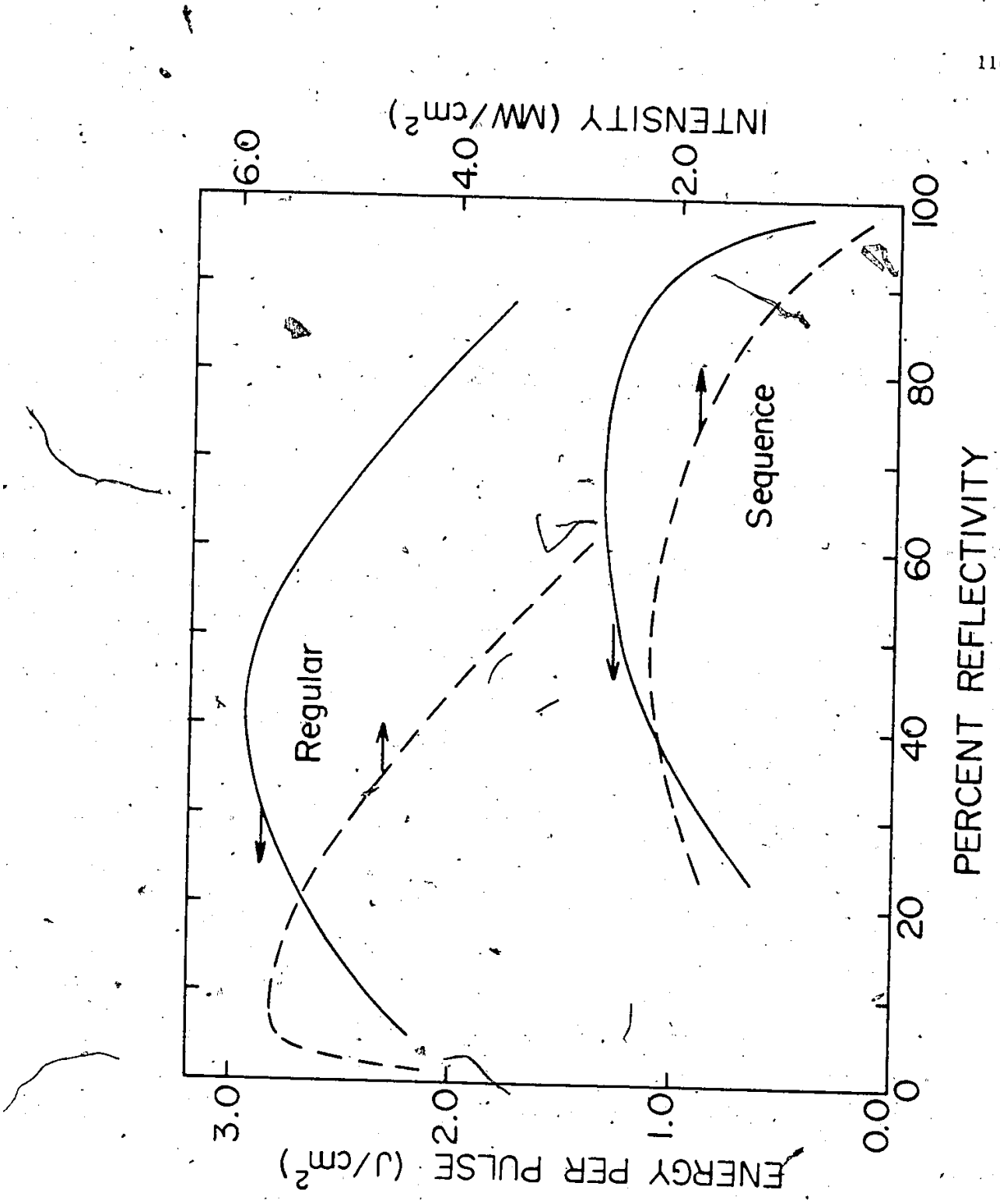
INTENSITY (MW/cm²)
6.0
4.0
2.0
Regular
Sequence
ENERGY PER PULSE (J/cm²)
3.0
2.0
1.0
0.0
0
20
40
60
80
100
PERCENT REFLECTIVITY

to 2100 K, whereas the regular gain increases by only 35%). Consequently, use of low excitation causes the sequence laser to operate near threshold resulting in low output energies. Second, laser action on the sequence transitions will terminate once T_3 is reduced to the point where gain equals cavity loss. For the calculated sequence pulse shown in Fig. 4-6, the model predicts that lasing ceases when T_3 = 1300 K, and as a result a substantial portion of the energy initially stored in the upper laser levels and in the vibrationally excited N_2 cannot be extracted. This is a direct result of the reduced gain values present on the sequence transitions and the increased cavity loss due to the hot cell. The effect of this residual energy can only be minimized by ensuring that the initial value of T_3 is as large as possible.

The importance of maximizing the initial value of T_3 can be readily seen in the following analysis. The energy stored in the ν_3 mode of CO_2 and in the vibrationally excited N_2 can be determined from Eq. (4-8) and is given to a good approximation by:

$$E_{stored} = (N_{CO_2}+N_{N_2})\, h\nu_3 \frac{x_{3i}}{1-x_{3i}}, \qquad (4\text{-}13)$$

where the subscript i denotes the initial value before lasing commences. The maximum optical energy which can be extracted is the difference between this quantity and the energy stored at the completion of lasing (denoted by the subscript f) multiplied by the quantum efficiency of the CO_2 laser transition. Hence:

$$E^{max}_{optical} = 0.41\,(N_{CO_2}+N_{N_2})\, h\nu_3 \left[\frac{x_{3i}}{1-x_{3i}} - \frac{x_{3f}}{1-x_{3f}}\right]. \qquad (4\text{-}14)$$

In a lossless cavity (i.e., no losses other than output coupling losses), the optical energy extracted would be equal to this value. In the more realistic case of a cavity possessing some loss per pass L, only the fraction F_{out} of $E_{optical}^{max}$ can be extracted, where F_{out} is given by Eq. (4-12). Figure 4-9 shows a plot of percent energy extracted as a function of T_{3i} for both regular and sequence transitions. Percent energy extracted is defined as $(F_{out} E_{optical}^{max})/(0.41 E_{stored})$, i.e., the ratio of the extracted optical energy to the maximum energy one could theoretically extract from an ideal system. The two curves are very similar in that no energy is extracted until the small-signal gain exceeds the cavity loss (T_{3i} = 900 K for regular lasing and 1300 K for sequence lasing). As T_{3i} is further increased the residual energy term in Eq. (4-14) becomes less important and the curves asymptotically approach a final value given by F_{out}. While Fig. 4-9 gives some indication of the importance of high values of T_{3i}, one must also remember that the available energy increases dramatically with T_{3i}, as can be seen by examining Eq. (4-13). For these reasons the discharge excitation was increased from 115 J/ℓ·atm to 210 J/ℓ·atm, as described in Sect. 4.2. The increased excitation caused T_{3i} to increase from ~1750 K to ~2100 K,‡ and as a consequence the measured sequence output energy increased substantially, from 3 J/pulse to nearly 6 J/pulse. This near doubling of the output energy is in agreement with calculations using Eq. (4-14).

---

‡ The T_3 value of 1750 K was obtained from small-signal gain data provided by Lumonics [illegible], and is consistent with T_3 measurements made under similar excitation conditions but at lower pressure. The T_3 value of 2100 K was obtained from Fig. 3-7.

FIGURE 4-9

Percent energy extracted as a function of T_{3i} for both regular and sequence transitions. Details of the calculation are given in the text.

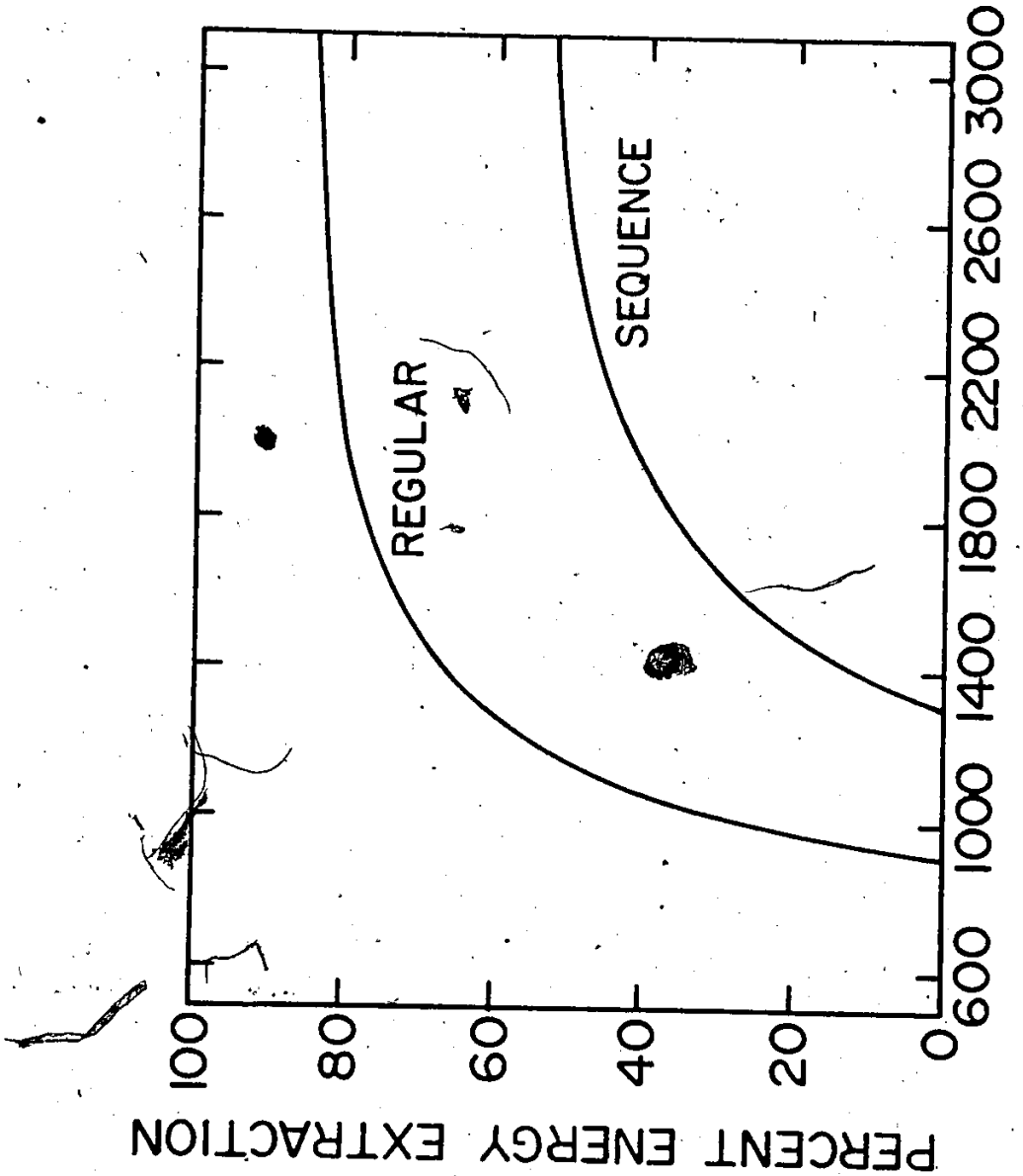
PERCENT ENERGY EXTRACTION
0
20
40
60
80
100
600
1000
1400
1800
2200
2600
3000
T_{3i}
REGULAR
SEQUENCE

The gas mixture dependence of sequence laser operation is also related to the interdependence of gain and T_3. The data plotted in Fig. 3-7 shows that high values of T_3 can only be obtained in gas mixtures having a low concentration of CO_2. The dependence of T_3 upon CO_2 content explains why optimum sequence laser gas mixtures contain approximately one-half the CO_2 content of regular laser gas mixtures [5,131]. Optimum gas mixtures for the TE sequence laser in this study contained 10-15 % CO_2, 15-20 % N_2, and the balance He. The dependence of sequence laser performance on gas mixture variations within the optimum range was observed to be weak. This result is a consequence of the trade off between enhanced gain due to increased T_3 and decreased gain due to reduced CO_2 number density, as the fraction of CO_2 is varied. The maximum measured sequence laser output energy of 6 J/pulse was obtained with a gas mixture of 12% CO_2: 20% N_2: 68% He, although a gas mixture of 11% CO_2: 16% N_2: 73% He resulted in more stable discharge operation and only slightly lower pulse energies. This output energy compares favourably with the maximum 15 J/pulse that was obtained on the regular transitions for a similar level of excitation.

As a final step in characterizing the sequence laser, the Cu mirror was replaced with an original grating and the laser was tuned over a wide range of sequence lines, optimizing the hot cell pressure in each case. Results are given in Fig. 4-10 and show that an output energy > 2 J/pulse can be obtained on more than 30 sequence lines. Since the sequence lines lie between the regular laser lines, this result represents a significant improvement in the line tunability available from a TE CO_2 laser.

FIGURE 4-10

Measured output energy on the 10.4- and 9.4-μm sequence band lines for the grating-tuned cavity. The 65-% reflector was used for all measurements and the discharge excitation was 210 J/ℓ·atm.

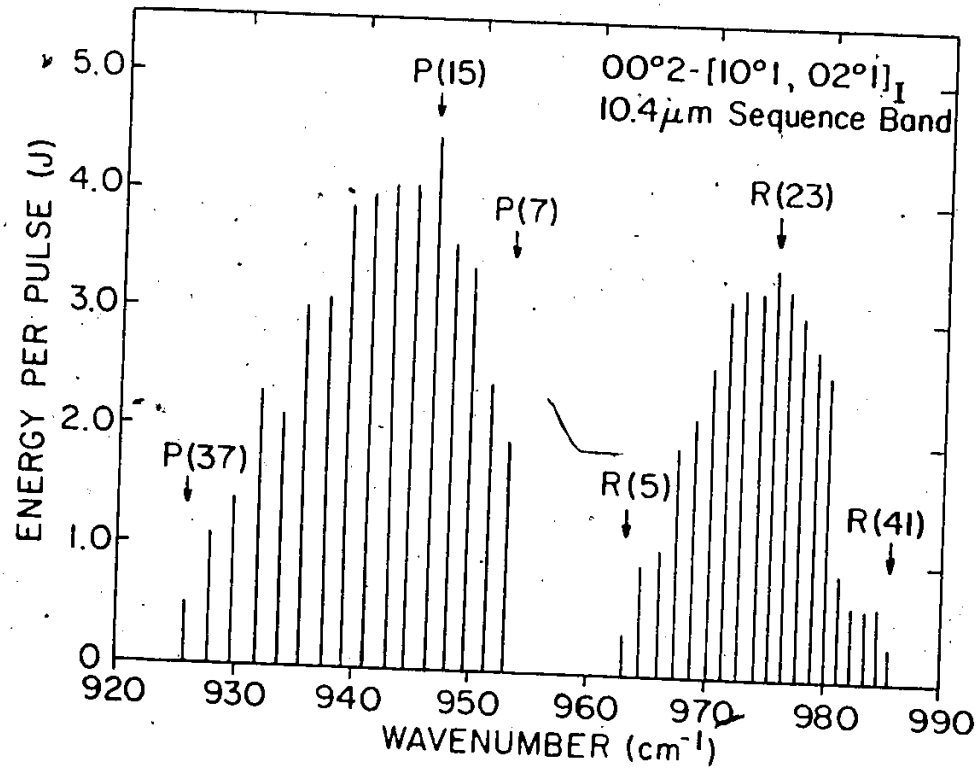
P(15)
00°2-[10°1, 02°1]I
10.4μm Sequence Band
P(7)
R(23)
P(37)
R(5)
R(41)
ENERGY PER PULSE (J)
5.0
4.0
3.0
2.0
1.0
0
920
930
940
950
960
970
980
990
WAVENUMBER (cm-1)

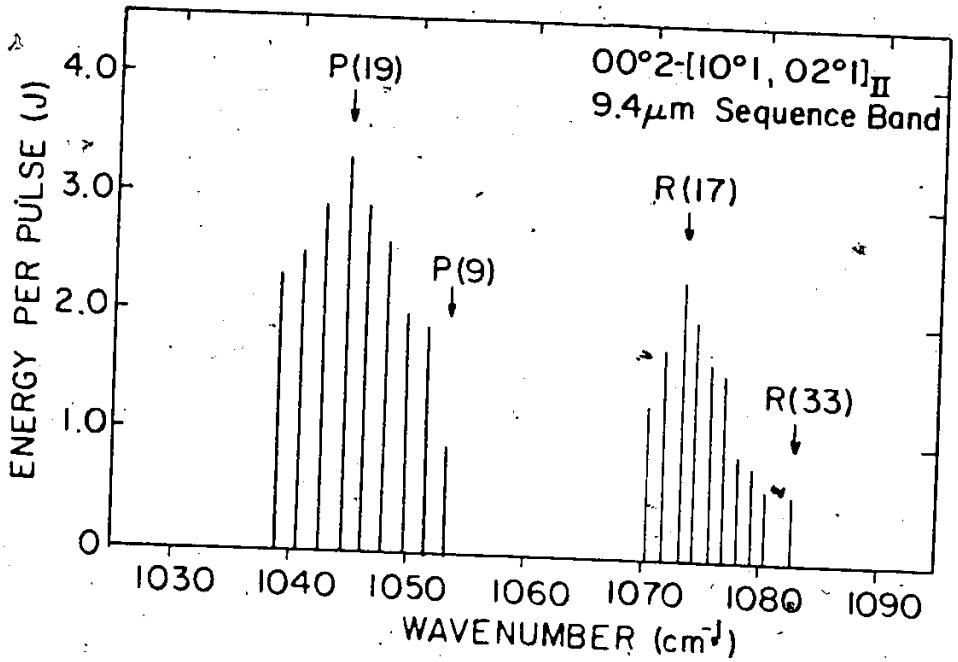
P(19)
00°2-[10°1, 02°1]II
9.4μm Sequence Band
R(17)
P(9)
R(33)
ENERGY PER PULSE (J)
4.0
3.0
2.0
1.0
0
1030
1040
1050
1060
1070
1080
1090
WAVENUMBER (cm-1)

4.6 Applications of High Power Sequence Lasers

The work described in this chapter was motivated by the need for a convenient high power sequence laser to use as the optical pump source in the development of high power 4.3-μm CO_2 lasers. A detailed experimental study of 4.3-μm laser operation is described in the next three chapters. It is the purpose of this section to outline the importance of high power TE sequence lasers, and describe other uses for the high energy sequence pulses now available.

Regular CO_2 lasers have excellent output characteristics and high efficiencies and consequently have found widespread use in applications such as laser isotope separation, laser photochemistry and optical pumping of molecular gases. In many of these applications, effective use of the laser is limited to a few chance coincidences between the regular laser frequencies and the absorption lines in the gas under investigation. The use of a hot cell in a grating-tuned cavity results in a near doubling of the number of laser lines which can be obtained from a TE CO_2 laser, as shown by Fig. 4-10. The improved tunability can clearly increase the utility of the TE CO_2 laser in any frequency-dependent application. One example is the recent use of a sequence CO_2 laser to produce 12-μm lasing in NH_3 [132]. The P(7) and P(17) 9.4-μm sequence lines have closer coincidences with NH_3 absorption lines than any of the regular lines. Consequently, for identical pumping powers, higher output powers are obtained when using these sequence lines rather than the R(30) 9.4-μm regular line.

Another application of a high power sequence laser is in the area of atmospheric monitoring. Since the sequence lines experience

negligible absorption in atmospheric CO_2, they will have significantly better transmission through the atmosphere than will the regular CO_2 laser lines, particularly under conditions of low humidity [133]. By comparing atmospheric absorption on the sequence and regular lines, one can accurately determine CO_2 concentrations over long path lengths. Similarly, sequence lasers may extend the range of laser Doppler lidar devices currently employing TE CO_2 lasers to determine wind velocities [134].

4.7 Summary

In this chapter, it was demonstrated that conventional TE CO_2 lasers can be converted to efficient, high energy operation on the sequence transitions by utilizing a simple intracavity hot CO_2 cell. However, proper design of the laser is essential and factors such as hot cell length and pressure, and discharge length and degree of excitation must be considered. Implementation of the hot cell technique to produce sequence lasing greatly improves the line tunability of TE CO_2 lasers and the significance of this result to several areas of application has been discussed. One particular application of high power sequence lasers, i.e., as optical pump sources in 4.3-μm CO_2 lasers, is discussed in detail in the following chapters, beginning with a detailed investigation of the gain dynamics of the 4.3-μm laser.

CHAPTER 5

GAIN DYNAMICS OF THE 4.3-μm CO_2 LASER

5.1 Introduction

Soon after the initial report [6] of a 4.3-μm CO_2 laser optically pumped by a 10.4-μm sequence band CO_2 laser, significant improvements in pulse energy [11,135] and repetition rate [12] were attained. The 4.3-μm CO_2 laser is relatively simple to construct and operate as it uses only conventional CO_2 laser technology, and it operates in a wavelength region where few other lasers are available. These attributes and the potential for scalability to higher output energies motivated the detailed investigation of 4.3-μm laser dynamics which is the topic of this thesis. As a result of the present study, 4.3-μm output energies of 15 mJ/pulse and peak powers of 100 kW/pulse have been obtained [136], representing the best performance reported to date.

The study of the 4.3-μm CO_2 laser has involved extensive experimental measurements and the development of a rate-equation model [135-142]. The experimental results fall into two categories: small-signal gain measurements and energy extraction measurements. Detailed measurements of small-signal gain coefficients are used in this chapter to validate the 4.3-μm rate-equation model. This is the most logical first step in developing an accurate model of a new laser system; any model which cannot correctly predict small-signal gain in an

amplifier is unlikely to accurately model the behaviour of an oscillator. In Chapt. 6, the influence of coherent effects on the gain measurements is discussed and modifications to the model to account for these effects are described. Chapter 7 deals with the energy extraction characteristics of the laser; extensive measurements of 4.3-μm pulse energies are compared with model calculations, and the operating parameters which most strongly influence the performance of the laser are identified.

The small-signal gain coefficients reported in this chapter were measured in a 4.3-μm amplifier by using low power pulses from a 4.3-μm probe laser. Gain coefficients as high as 14 %/cm were measured. The measurements are compared with a rate-equation model and good quantitative agreement is obtained over a wide range of conditions. This agreement is particularly significant as all of the input parameters for the model are determined separately and no adjustable parameters are required. The rate-equation model is described fully in the next section. In Sect. 5.3, the experimental apparatus and technique used to measure 4.3-μm small-signal gain coefficients are described. The measured and calculated gain coefficients are compared in Sect. 5.4 as a function of several parameters. These parameters include the time dependence and the rotational transition dependence of the gain, and the effects of variations in discharge excitation, gas mixture, gas pressure, and sequence pump intensity. Finally, in Sect. 5.5 optimization of the 4.3-μm gain is discussed.

5.2 Rate-Equation Model of the Gain Dynamics

The gain dynamics of the 4.3-μm CO_2 laser are discussed in Sect. 2.7, and are reviewed here briefly. A pulsed electrical discharge containing a mixture of CO_2, N_2, and He excites significant population into the 00^02 level of CO_2. A population inversion occurs between the 00^02 and 10^01 levels, and transient gain is created in the 10.4-μm (00^02-10^01) sequence band (see Fig. 2-1). An externally generated 10.4-μm P(25) sequence pump pulse is timed to arrive at the peak of this gain, and the optical pulse transfers population from the 00^02 level to the 10^01 level (the pump pulse is amplified in the process). Under appropriate operating conditions, a transient population inversion and hence gain is created in the (10^01-10^00) 4.3-μm band.‡ As Table 2.3 shows, transitions in CO_2 involving the change of one ν_3 mode quantum possess a strong transition dipole moment. Thus, the transient inversion results in large gain coefficients at 4.3 μm. The rate-equation model given below simulates the chain of events in the discharge, beginning with the arrival of the pump pulse.

The seven-equation model used here has been adapted from an existing 4.3-μm CO_2 laser model [13], and is similar to the sequence laser model described in Sect. 4.3. The present model is only designed to calculate 4.3-μm small-signal gain, and thus a 4.3-μm photon density equation is not required. The set of coupled differential equations

---

‡ The use of a 9.4-μm sequence pump pulse will generate gain in the (02^01-02^00) 4.3-μm band.

which model gain on the $(10^{0}1\text{-}10^{0}0)$ 4.3-μm band‡ is as follows:

$$\frac{dE_3}{dt} = - h\nu_3\sigma_s\delta_s\rho_s c, \tag{5-1}$$

$$\frac{dE_{12}}{dt} = - \frac{E_{12} - E^{e}_{12}(T)}{\tau_{VT}} + h\nu_1\sigma_s\delta_s\rho_s c, \tag{5-2}$$

$$\frac{dN_{002}}{dt} = - \sigma_s\delta_s\rho_s c + \frac{N^{e}_{002}(T_3) - N_{002}}{2\tau_{\nu_3}}, \tag{5-3}$$

$$\frac{dn_{002}}{dt} = - \sigma_s\delta_s\rho_s c + \frac{K_{002}N_{002} - n_{002}}{\tau_R}, \tag{5-4}$$

$$\frac{dN_{101}}{dt} = \sigma_s\delta_s\rho_s c - \frac{N_{101} - N^{e}_{101}(T_1,T_3)}{\tau_{101}}, \tag{5-5}$$

$$\frac{dn_{101}}{dt} = \sigma_s\delta_s\rho_s c + \frac{K_{101}N_{101} - n_{101}}{\tau_R}, \tag{5-6}$$

$$\frac{dN_{100}}{dt} = \frac{N_{101} - N^{e}_{101}(T_1,T_3)}{\tau'_{101}} - \frac{N_{100} - N^{e}_{100}(T_1)}{\tau_{100}}. \tag{5-7}$$

E_3 is the stored energy in the ν_3 mode and E_{12} is the stored energy in the combined $\nu_1+\nu_2$ mode. Variables denoted by the subscripts 002, 101, and 100 pertain to the corresponding vibrational levels. N_{002}, N_{101},

‡ Modeling of operation on the $(02^{0}1\text{-}02^{0}0)$ 4.3-μm band can be achieved by modifying the equations to account for the different levels involved.

and N_{100} are vibrational populations, while n_{002} and n_{101} are the rotational populations of the levels having rotational quantum numbers $J_{002}=24$ and $J_{101}=25$ (corresponding to the 10.4-μm P(25) sequence pump transition). δ_s is the inversion on the sequence transition given by $\delta_s=n_{002}-n_{101}g_{002}/g_{101}$, where $g=2J+1$ is the statistical weight of the rotational level. σ_s is the sequence gain cross-section calculated from Eq. (2-17) such that the product $\sigma_s\delta_s$ is the small-signal gain coefficient. The lineshapes of both the sequence and 4.3-μm transitions are represented by Voigt profiles in the model. $h\nu_1$ and $h\nu_3$ are the fundamental energy intervals of the ν_1 and ν_3 modes, and c is the speed of light. The photon density of the sequence pump pulse is given by ρ_s. K_{002} and K_{101} are the rotational population factors for $J_{002}=24$ and $J_{101}=25$ and have values of ~0.05, calculated from Eq. (2-16). Thus, the products $K_{002}N_{002}$ and $K_{101}N_{101}$ represent the equilibrium populations of the pump transition upper and lower rotational levels. The three-temperature model of Sect. 2.5 is used to describe the unperturbed populations in the discharge. Variables denoted with the superscript e represent the equilibrium value of that variable at the temperature indicated in brackets. At each step of the calculation, new values of T_1 and T_3 are determined from the current values of E_{12} and E_3 as described in Sect. 4.3, and T is assumed to remain constant.

The various molecular relaxation times are denoted by τ and are defined in Sect. 2.4, where the corresponding relaxation rates are also given. The relaxation times are calculated from the rates by assuming constant pressure conditions in the discharge. Typical values of the relaxation times are given in Table 2-1 for a 40-Torr gas mixture of

3% CO_2: 10% N_2: 87% He. Another assumption present in the model is that intermode relaxation of the ν_3 mode (Eq. (2-8)), and energy transfer from the N_2 molecules (Eq. (2-9)) can be ignored. This assumption is justified as these relaxation times (τ_3 and τ_{N_2}, respectively) are more than an order of magnitude slower than τ_{VT}, which is the slowest relaxation time included in the model (see Table 2-1).‡

The model is implemented in the following manner. The initial values of T, T_1, and T_3 (i.e., the values at the time of peak sequence gain in the pulsed discharge) are input to the program and are used to calculate initial values for the populations and energies in Eqs. (5-1) to (5-7). These initial temperatures are determined experimentally using techniques described in Chapt. 3. The measured pump pulse profile is used to determine the successive values of ρ_s, and the differential equations are solved beginning at a time corresponding to the start of the sequence pump pulse. The model assumes uniform excitation and pump intensity throughout the discharge volume, which is a good approximation for the experimental conditions.

Once Eqs. (5-1) to (5-7) have been solved, the 4.3-μm small-signal gain can be calculated from the populations of the $10^0 1$ and $10^0 0$ levels. The 4.3-μm population inversion is given by $\delta_4 = n_{101}(J_{101}) - n_{100}(J_{100}) g_{101}/g_{100}$ where $n_{101}(J_{101})$ and $n_{100}(J_{100})$ are the rotational populations of the levels indicated in brackets. $n_{100}(J_{100})$ is given by the product $K_{100}(J_{100})N_{100}$. $n_{101}(J_{101})$ is given

‡ The slow ν_3 mode energy transfer terms were included in preliminary modeling, however it was found that they had a negligible effect on the calculations.

by the product $K_{101}(J_{101})N_{101}$, unless $J_{101}=25$ (the pump transition lower level), in which case n_{101} is given by Eq. (5-6). These two cases correspond to collisionally-pumped and directly-pumped 4.3-μm transitions, respectively. The 4.3-μm small-signal gain is calculated from the product $\sigma_4\delta_4$, where σ_4 is the 4.3-μm gain cross-section. σ_4 is calculated from Eq. (2-17) using the appropriate transition dipole moment [78], and spectroscopic constants [143].

At this point it is instructive to use the model predictions to examine some of the qualitative aspects of the gain dynamics. Figure 5-1 shows a typical P(25) sequence pump pulse, the calculated time-dependent populations of the relevant 00^02, 10^01, and 10^00 rotational energy levels (J=24, 25, and 26 respectively) and the resulting directly-pumped 4.3-μm small-signal gain. The calculation is carried out for typical 4.3-μm discharge conditions. Note that the population inversion, and therefore the gain, on the 4.3-μm transition is short lived compared to the pump pulse. This transient behaviour arises because of the very fast relaxation of the 10^01 level, and the fact that the lifetime of the 10^01 level is ~3 times shorter than that of the 10^00 level (see Table 2-1). The collisional relaxation mechanism responsible for this behaviour, which is given by Eq. (2-12), plays an important role in the dynamics of 4.3-μm laser operation. Another characteristic of 4.3-μm laser dynamics shown in Fig. 5-1 is the strong absorption on the 4.3-μm transition which follows the gain. This absorption occurs because most of the population de-excited from the 10^01 level goes directly to the 10^00 level (see Fig. 2-5). The magnitude and time dependence of the predicted absorption is very

FIGURE 5-1

Calculated values of the 00^02, 10^01, and 10^00 rotational energy level populations as a function of time for a discharge gas mixture of 3% CO_2: 10% N_2: 87% He at 40 Torr total pressure and initial temperatures: T=360 K, T_1=385 K, and T_3=2750 K. The resulting 4.3-μm gain is also shown, as is the sequence pump pulse used in the calculation.

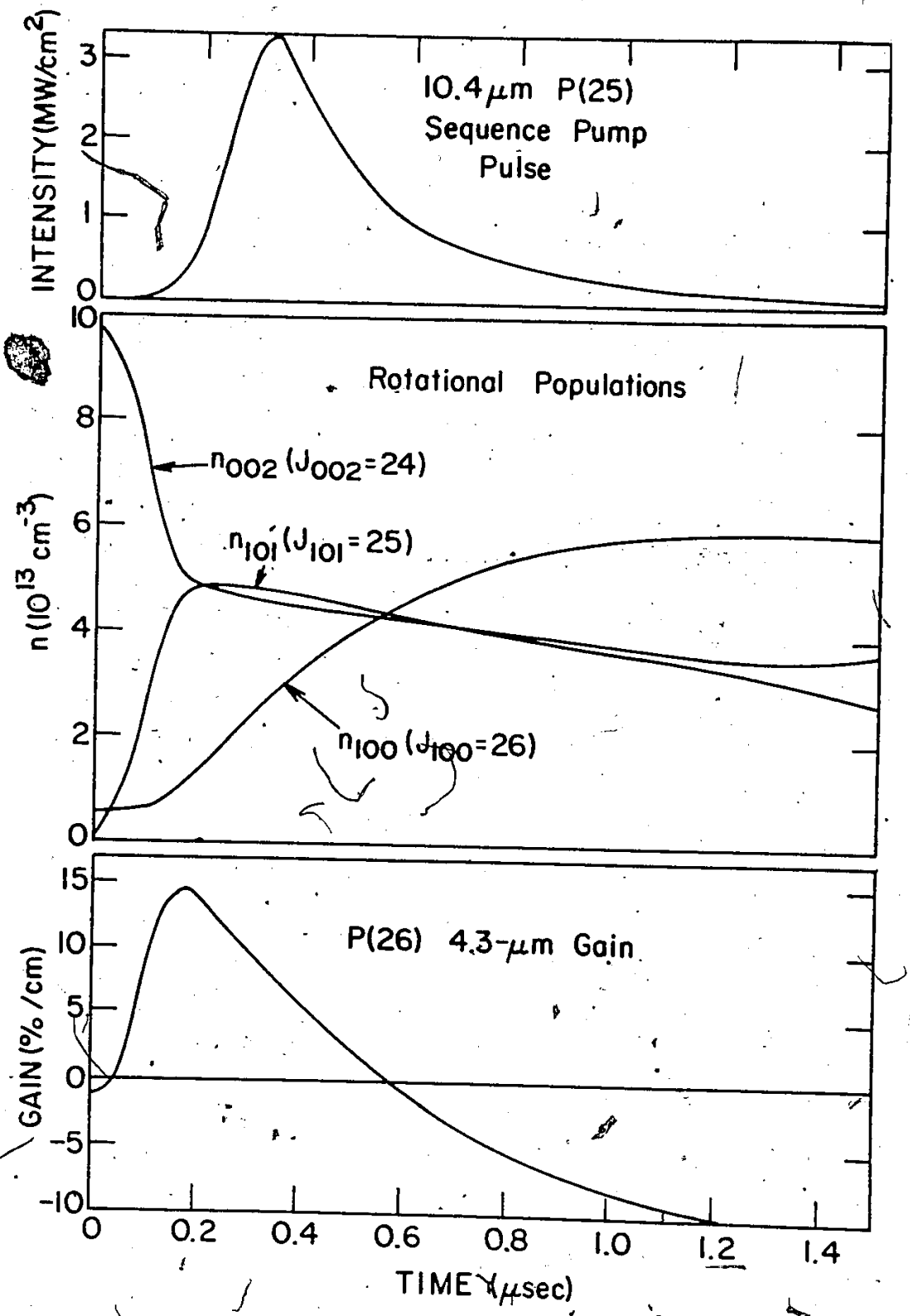
INTENSITY(MW/cm²)
10.4 μm P(25)
Sequence Pump
Pulse
Rotational Populations
n(10¹³ cm⁻³)
n002 (J002=24)
n101 (J101=25)
n100 (J100=26)
GAIN (%/cm)
P(26) 4.3-μm Gain
TIME (μsec)

sensitive to k_{100}, the rate constant for collisional de-excitation of the 10^00 level. As discussed in Sect. 2.4, k_{100} has been measured many times, and there is poor agreement among the results. In Fig. 5-2, 4.3-μm absorption profiles calculated for various values of τ_{100} are compared with measured absorption coefficients (the measurement technique is described in the next section). Note that the value for τ_{100} listed in Table 2-1 gives a much better fit to the experimental data than either the constants of Jacobs et al. [52] or Stark [54]. This comparison confirms that the appropriate value for τ_{100} is being used in the model.

5.3 Experimental Apparatus and Technique

Figure 5-3 is a schematic diagram of the experimental apparatus used to measure 4.3-μm gain coefficients. The 4.3-μm probe laser and the 4.3-μm amplifier are optically pumped by separate, independently operated sequence lasers. The 4.3-μm amplifier is a Lumonics TE discharge identical to the one described in Sect. 3.3, except that the gain length is only 44 cm and the overall length is 76 cm (i.e., one-half of the module shown in Fig. 3-1). The 4.3-μm amplifier is operated at pressures from 40 to 120 Torr.

The sequence pump lasers also contain Lumonics discharge modules with 44 cm of gain. These discharges are operated at repetition rates of 0.5 Hz with a 10% CO_2: 15% N_2: 75% He gas mixture at atmospheric pressure, and an input excitation energy of ~100 J/ℓ·atm. The intracavity hot cells used in the sequence lasers consist of 5-cm ID pyrex tubes sealed with NaCl Brewster windows. A photograph of one of

FIGURE 5-2

Measured and calculated time-dependent gain on the directly-pumped 4.3-μm P(26) line. The discharge temperatures are given in the caption to Fig. 5-1. The variation of the calculated absorption as a function of τ_{100} is shown. The influence of coherent effects is explained in Sect. 5.4.

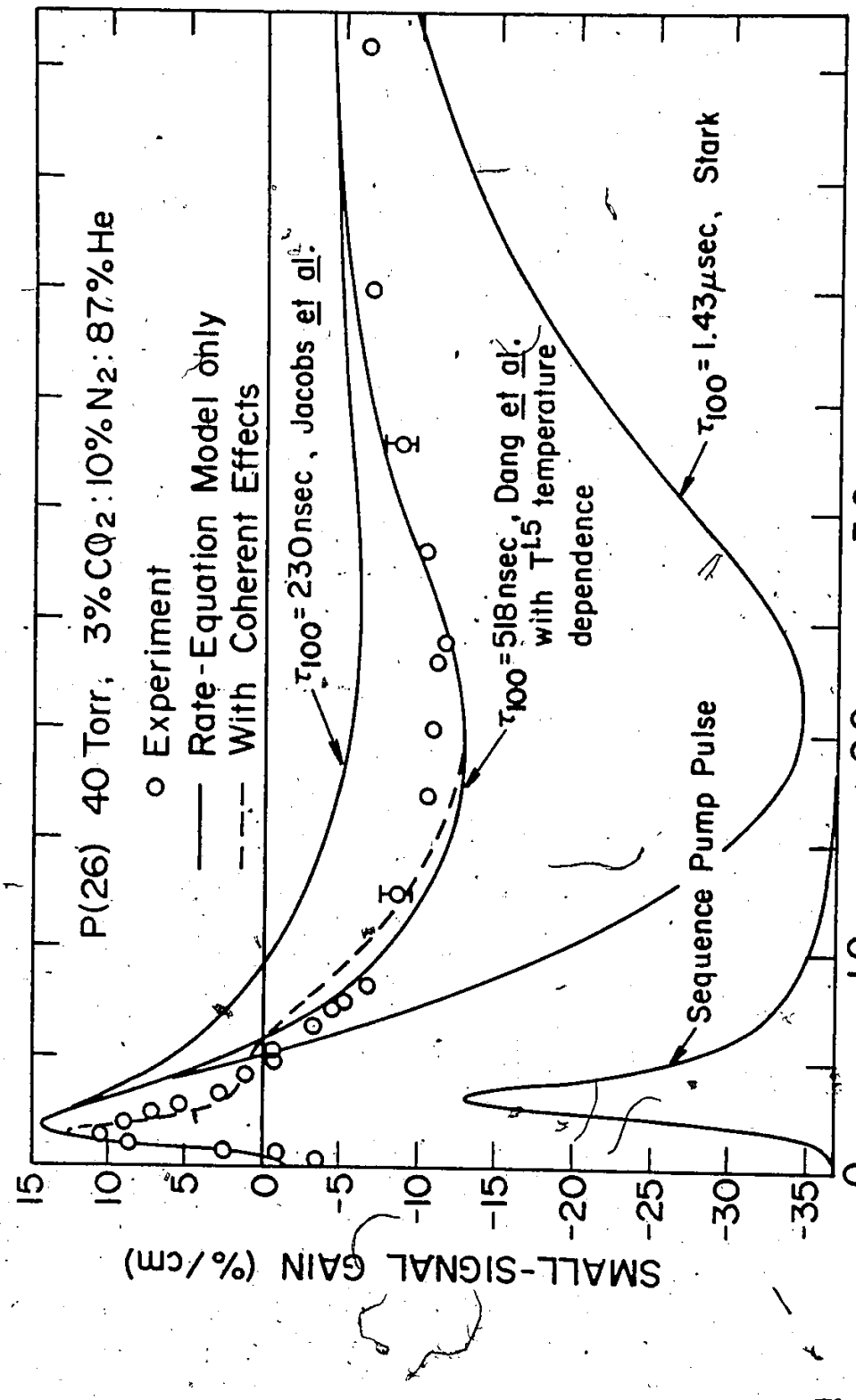
P(26) 40 Torr; 3% CO2 : 10% N2 : 87% He
o Experiment
Rate-Equation Model only
With Coherent Effects
τ100 = 230nsec, Jacobs et al.
τ100 = 518nsec, Dang et al. with T^1.5 temperature dependence
τ100 = 1.43μsec, Stark
Sequence Pump Pulse
SMALL-SIGNAL GAIN (%/cm)
TIME (μsec)
15
10
5
0
-5
-10
-15
-20
-25
-30
-35
0
1.0
2.0
3.0
4.0
5.0

FIGURE 5-3

Schematic diagram of the experimental apparatus used to measure 4.3-μm small-signal gain coefficients. The NaCl windows on the 4.3-μm amplifier were tilted to prevent parasitic oscillation.

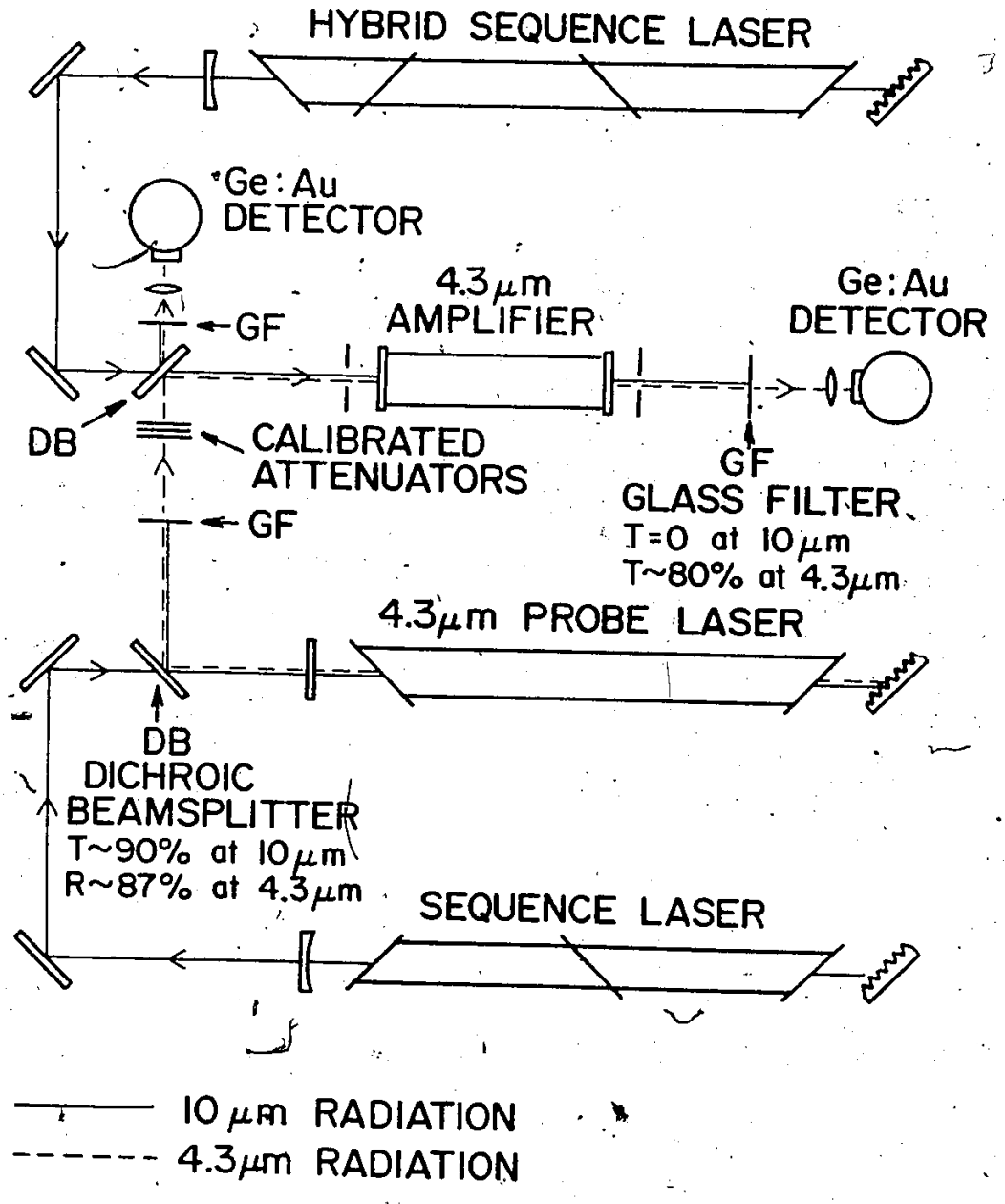
HYBRID SEQUENCE LASER
*Ge:Au DETECTOR
4.3μm AMPLIFIER
Ge:Au DETECTOR
GF
DB
CALIBRATED ATTENUATORS
GF
GF
GLASS FILTER
T=0 at 10μm
T~80% at 4.3μm
4.3μm PROBE LASER
DB
DICHROIC BEAMSPLITTER
T~90% at 10μm
R~87% at 4.3μm
SEQUENCE LASER
10μm RADIATION
4.3μm RADIATION

the hot cells is shown in Fig. 5-4. The cell has an overall length of 60 cm, and a nichrome wire heating coil 50 cm long is wound inside. Aluminum foil provides a heat shield, and an input power of ~200 W results in a temperature at the center of the cell of ~575 K. Note in Fig. 5-4 that the cavity length and optical loss in the sequence laser have been minimized by utilizing a single NaCl window between the hot cell and the other cavity components. To the left of the hot cell in Fig. 5-4 is the TEA discharge, and to the right is a 25-cm long low pressure discharge which operates with a 5% CO_2: 10% N_2: 85% He gas mixture at 20 Torr. The low pressure gain section makes the sequence laser a hybrid laser, and as Fig. 5-3 shows, this pertains only to the sequence laser which optically pumps the 4.3-μm amplifier. A hybrid laser is required in this case to match the spectral linewidth of the pump radiation to the linewidth in the low pressure 4.3-μm amplifier [144]. The hybrid pump laser is grating tuned to the 10.4-μm P(25) transition, and a 65-% reflectivity output coupler is used. An output energy of 1 J is typically obtained in a pulse having a FWHM of ~300 ns. This pump pulse is gently focussed down the center of the 4.3-μm amplifier to a minimum beam diameter of ~1 cm. The pulse shape and energy are monitored with a photon drag detector and a calibrated Gentec ED-500 joulemeter. The pump intensity profile determined in this manner is used as input to the rate-equation model.

The 4.3-μm probe laser in Fig. 5.3 is grating tunable over many 4.3-μm lines and produces probe pulses of ~150 ns FWHM. The sequence laser which optically pumps the 4.3-μm probe laser is also grating tuned to directly pump the desired 4.3-μm transition. An 80-% reflectivity

FIGURE 5-4

Photograph of the hot cell used in the hybrid sequence laser of Fig. 5-3. The hot cell is 60 cm long overall. To the left of the hot cell is a TEA discharge with 44 cm of gain, and to the right is a low pressure discharge with 25 cm of gain.

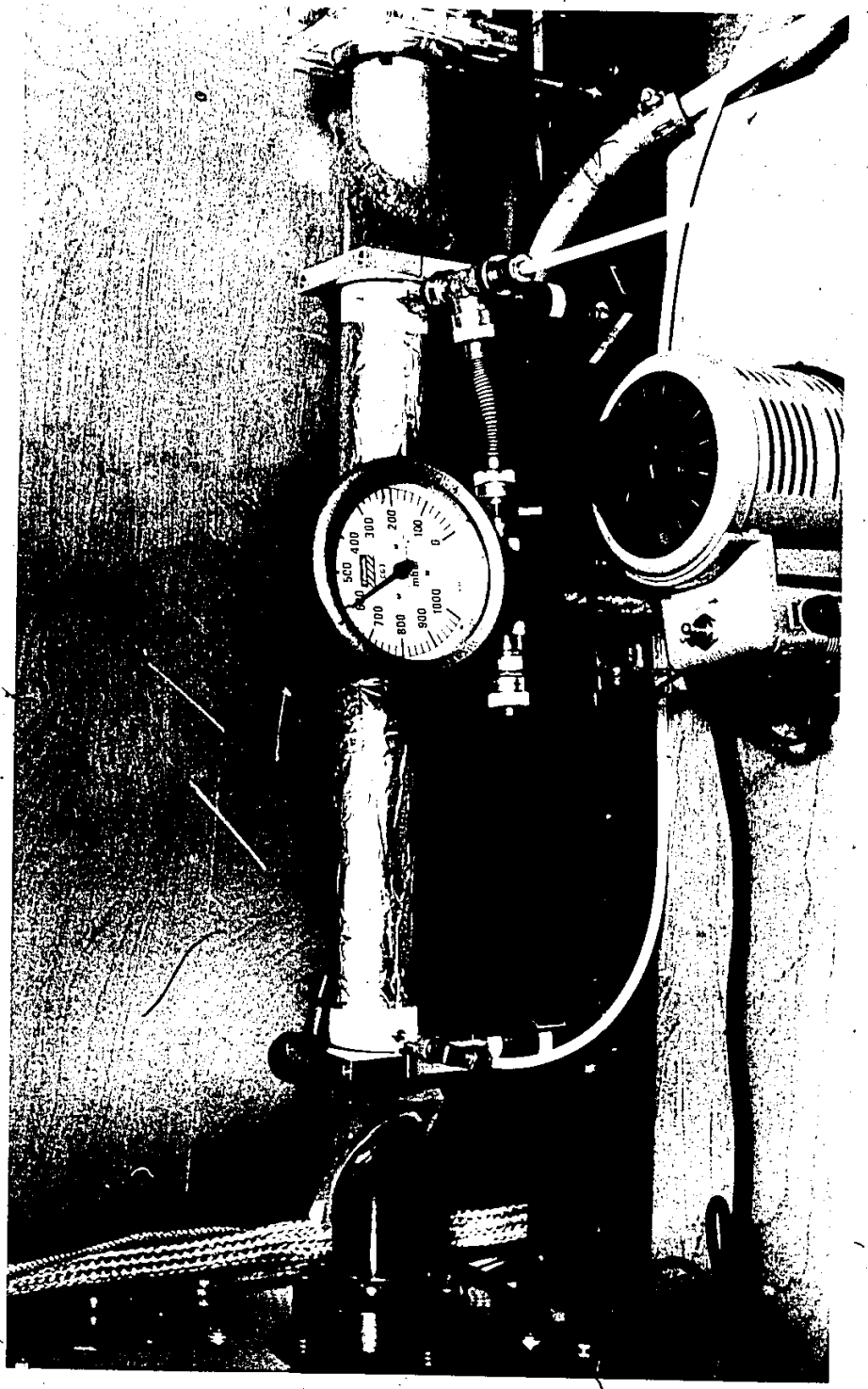
0
100
200
300
400
500
600
700
800
900
1000
mm

output coupler is used in this sequence laser to enhance the line tunability, and since maximum efficiency is not a concern in producing the low power probe pulses, the sequence laser is not a hybrid laser. The 4.3-μm probe pulses are focussed into the 4.3-μm amplifier to a maximum beam diameter of ~0.5 cm to ensure that they do not pass through unpumped regions of the discharge. Two Ge:Au detectors are used to monitor the 4.3-μm probe pulses before and after passage through the amplifier, and the two detector signals are displayed simultaneously on a dual-beam oscilloscope to reduce errors caused by pulse-to-pulse variability of the probe power. Gain is measured at the peak of the probe pulse, which can be controlled in time relative to the arrival of the pump pulse in the amplifier. Calibrated attenuators (microscope slides) are used to ensure that measurements are made in the small-signal regime, and that the signal intensity at each detector is approximately constant (~10 W/cm^2 peak). This technique minimizes problems with detector linearity and saturation even when measuring gain coefficients as large as 14 %/cm. Typical gain and absorption coefficients can be measured with a pulse-to-pulse reproducibility of better than ±5 % and a day-to-day reproducibility of ±10 %.

The operating parameters of the 4.3-μm amplifier were measured using the techniques described in Chapt. 3 so that the measured parameters could be used as input to the rate-equation model. Once the discharge in the 4.3-μm amplifier had been characterized in terms of T_3, T_1, and T, experiments were performed to measure 4.3-μm gain coefficients as a function of sequence pump intensity, gas mixture, gas pressure, etc. The experimental results were compared with the

predictions of the rate-equation model, and these comparisons are described in the next section.

5.4 Validation of the Rate-Equation Model

In initial experiments the time delay between the sequence pump pulse and the 4.3-μm probe pulse was varied and the time dependence of the 4.3-μm gain was determined. The 4.3-μm laser was grating tuned to probe a range of different 4.3-μm transitions. Results are shown in Figs. 5-2, 5-5, and 5-6. Figure 5-5 displays the measured and calculated time dependence of the 4.3-μm gain coefficient for two different transitions. The gain coefficient calculated for P(24) is in excellent agreement with experiment. However, the peak gain calculated by the rate-equation model for P(26) is ~35 % too large. This discrepancy is mostly caused by power broadening and splitting of the 4.3-μm lineshape by the intense 10.4-μm pump radiation. These effects reduce the 4.3-μm gain at the line center, but only occur when the pump and 4.3-μm transition are connected by a common level (the J_{101}=25 rotational level in this case). The density matrix formalism of Panock and Temkin [145] has been used to modify the rate-equation model and account for these effects. These modifications and further examples of coherent effects in the 4.3-μm laser are discussed in detail in Chapt. 6. As shown in Fig. 5-5, better agreement is obtained between the calculated and measured gain on P(26) when coherent effects are included in the model, although the peak gain is still overestimated. The influence of coherent effects on a longer time scale is shown in Fig. 5-2. The time dependence of the calculated gain in Fig. 5-5 is in

FIGURE 5-5

Time dependence of the measured and calculated 4.3-μm gain on the directly-pumped P(26) line and the collisionally-pumped P(24) line. The 10.4-μm P(25) sequence pump pulse has a peak intensity of ~3.5 MW/cm^2. The discharge temperatures are given in the caption to Fig. 5-1 and details of the model calculations are given in the text.

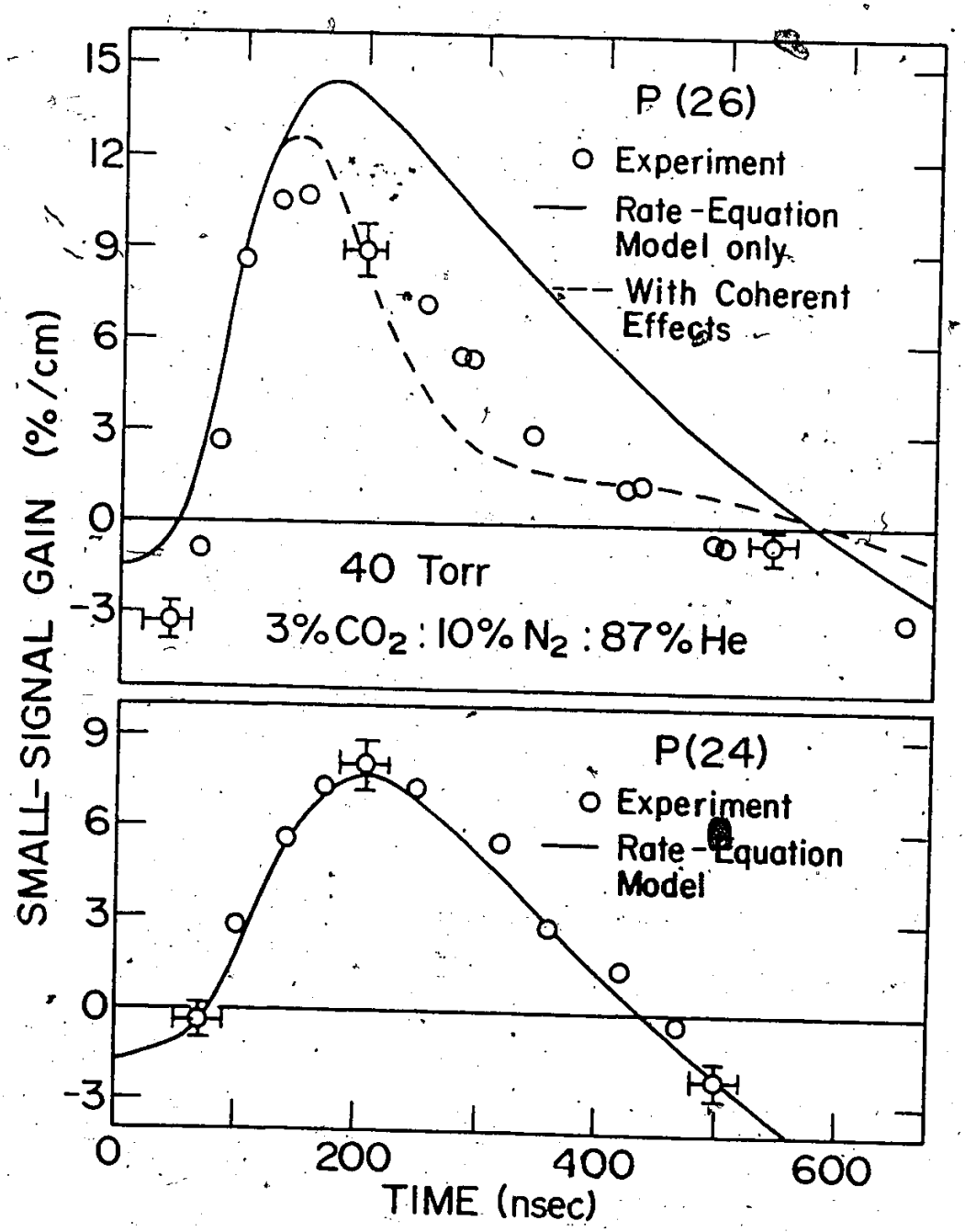
P (26)
Experiment
Rate-Equation Model only
With Coherent Effects
40 Torr
3%CO2 : 10% N2 : 87% He
P(24)
Experiment
Rate-Equation Model
SMALL-SIGNAL GAIN (%/cm)
TIME (nsec)
15
12
9
6
3
0
-3
200
400
600

FIGURE 5-6

P-branch rotational distribution of 4.3-μm gain obtained by pumping with a 10.4-μm P(25) sequence pulse of ~3.5 MW/cm^2 peak intensity. The two sets of symbols represent the measured gain, and the gain which has been corrected by using measured overlapping absorption coefficients. The P(26) line is directly pumped and thus has much higher gain than the other lines, which are collisionally pumped and correspond to the model calculation shown. At 80 Torr, the initial discharge temperatures are T=392 K, T_1=420 K, and T_3=2900 K. The 40 Torr discharge temperatures are the same as those of Fig. 5-1.

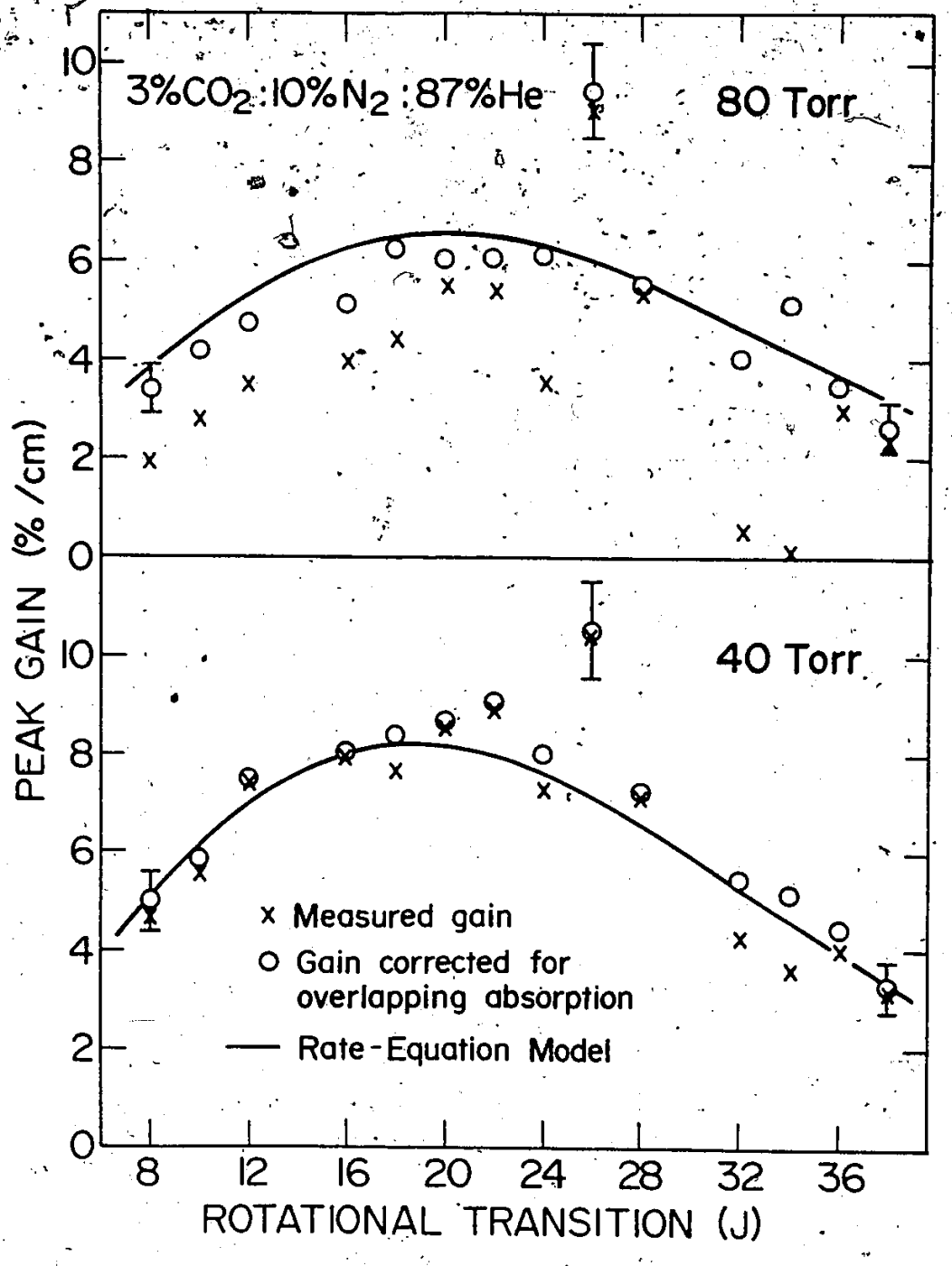
3%CO2:10%N2:87%He
80 Torr
40 Torr
PEAK GAIN (% /cm)
ROTATIONAL TRANSITION (J)
x Measured gain
o Gain corrected for overlapping absorption
Rate-Equation Model
0
2
4
6
8
10
8
12
16
20
24
28
32
36

good agreement with experiment for both P(24) and P(26). On both transitions the gain lifetime is shorter than the duration of the pump pulse (see Fig. 5-1 for a typical pump pulse) due to the short collisional lifetime of the $10^0 1$ level.

Fast rotational transfer in the $10^0 1$ level ensures that the entire ($10^0 1$-$10^0 0$) band is inverted. Figure 5-6 shows typical gain distributions measured at the time of peak gain by grating tuning the probe laser. The measured gain coefficients are corrected for overlapping absorption bands, and the corrected results form a smooth, thermalized distribution with an anomalous peak on the directly-pumped P(26) transition. The calculated gain distribution is in very good agreement with experiment at both 40 and 80 Torr, and similar agreement is obtained at a discharge pressure of 120 Torr. This agreement confirms the accuracy of the rate-equation model, particularly the J-dependence of the collision-broadened linewidths (Eqs. (2-22) to (2-24)), and the value of T measured in the 10.4-μm bands.

The results displayed in Fig. 5-6 can be used to assess the line tunability of the 4.3-μm laser. Clearly, significant tunability can be attained with a single pump transition, although optimum performance always occurs by directly pumping the required transition. The P(14) and P(30) lines are missing from the rotational gain distribution as they suffer severe overlapping absorption from other 4.3-μm bands, and as a consequence do not lase in the probe laser. In a discharge, population is excited into many CO_2 energy levels, each of which has an associated 4.3-μm absorption band. The individual lines of these absorption bands are pressure broadened and overlap nearby 4.3-μm laser

transitions. Overlapping absorption occurs to some extent on all 4.3-μm laser transitions. Thus, the measured gain consists of the actual gain on the laser transition, reduced by the overlapping absorption. In Fig. 5-6, both the measured and corrected gain are shown, the difference being the measured overlapping absorption.‡ In most cases this absorption is small relative to the gain. However, the absorption is nonsaturable and can create significant losses in a 4.3-μm laser. The effect of overlapping absorption on the output energy from a 4.3-μm oscillator is treated in detail in Chapt. 7, where measurements and calculations of overlapping absorption are also discussed.

5.5 Optimization of 4.3-μm Gain

An important step in optimizing any laser system is to determine the operating conditions which maximize the small-signal gain. Therefore, a study was carried out of the 4.3-μm system to determine those parameters which most strongly influence the small-signal gain. As a first step, the variation of small-signal gain with T_3 was investigated. Results are shown in Fig. 5-7. T_3 in the amplifier section was varied by changing the storage capacitor and charging voltage, and for each data point T_3, T_1, and T were measured by the techniques described in Chapt. 3. The gain lifetime, defined as the time for which the gain is positive (see Fig. 5-5), has only a minor dependence upon T_3, as the lifetime is dominated by the collisional

---

‡ All of the measured 4.3-μm gain coefficients presented in Figs. 5-2, 5-5 to 5-9, 6-4, and 6-5 have been corrected for overlapping absorption. In general, this is a very small correction, particularly for the directly-pumped P(26) line.

FIGURE 5-7

Peak gain and gain lifetime as a function of T_3. The 10.4-μm P(25) sequence pump pulse has a peak intensity of ~3.5 MW/cm^2. The measured values of T and T_1 range from 313 and 335 K (at T_3=1540 K) to 392 and 420 K (at T_3=2900 K). The calculated peak gain coefficients have been scaled by a factor of 0.85 (see text).

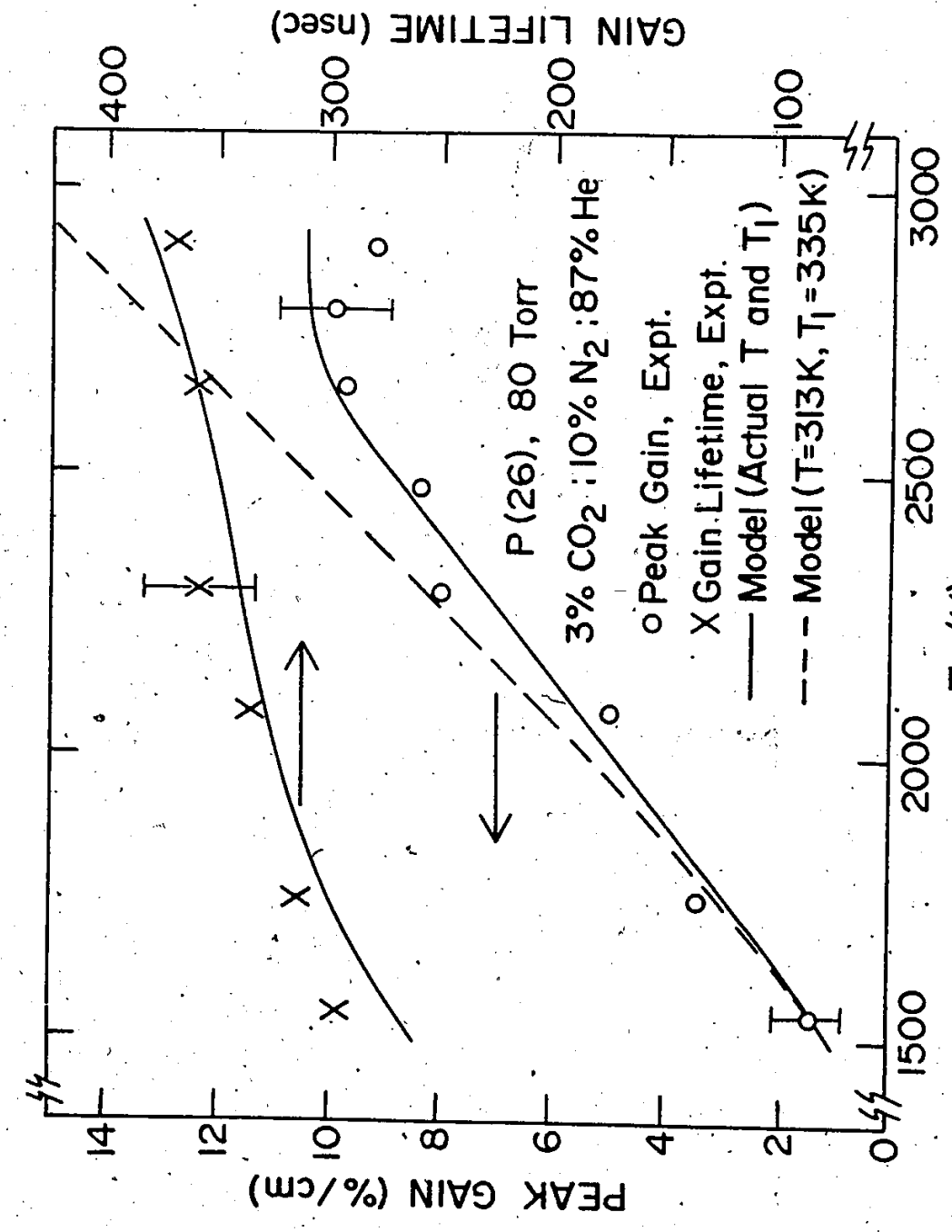
GAIN LIFETIME (nsec)
400
300
200
100
PEAK GAIN (%/cm)
14
12
10
8
6
4
2
0
1500
2000
2500
3000
T_3 (K)
P(26), 80 Torr
3% CO_2 : 10% N_2 : 87% He
o Peak Gain, Expt.
X Gain Lifetime, Expt.
— Model (Actual T and T_1)
– – – Model (T=313K, T_1=335K)

relaxation of the $10^0 1$ level. However, the peak gain increases dramatically as T_3 increases. The results shown in Fig. 5-7 clearly demonstrate the importance of creating as high a value of T_3 as possible. To further illustrate this point the dashed line in Fig. 5-7 is calculated for fixed values of T_1 and T, rather than the experimentally measured values. It is clearly important to design a discharge circuit which maximizes the excitation of the ν_3 mode of CO_2, and minimizes heating of the ν_1 and ν_2 modes and thermal heating of the gas. The gain coefficients calculated by the model for the directly-pumped P(26) line overestimate the gain, even with the inclusion of coherent effects. Therefore, all of the calculated values have been scaled by a factor of 0.85 before plotting the results in Fig. 5-7. Except for this minor discrepancy, the experimental dependence of gain magnitude and lifetime upon T_3 is very well reproduced by the model.

Recalling Fig. 3-7, which shows the variation of the vibrational temperatures T_1 and T_3 with CO_2 content, it is clear that the high T_3 and low T and T_1 conditions required for optimum 4.3-μm performance can be obtained by using low CO_2 concentrations in the discharge. However, as the CO_2 content is progressively reduced, the 4.3-μm gain will eventually decrease due to the reduced number density of CO_2 molecules. The combined effect of these processes is illustrated in Fig. 5-8, where peak gain is plotted as a function of CO_2 content in the gas mixture. These measurements were made on the directly-pumped P(26) transition and once again the calculated peak gain was scaled by a factor of 0.85. The model accurately predicts the variation in peak gain with CO_2 content.

FIGURE 5-8

Peak gain and gain lifetime as a function of CO_2 content in the discharge. The gas mixture contains 10 % N_2 with the balance He. The calculated peak gain coefficients have been scaled by a factor of 0.85 (see text).

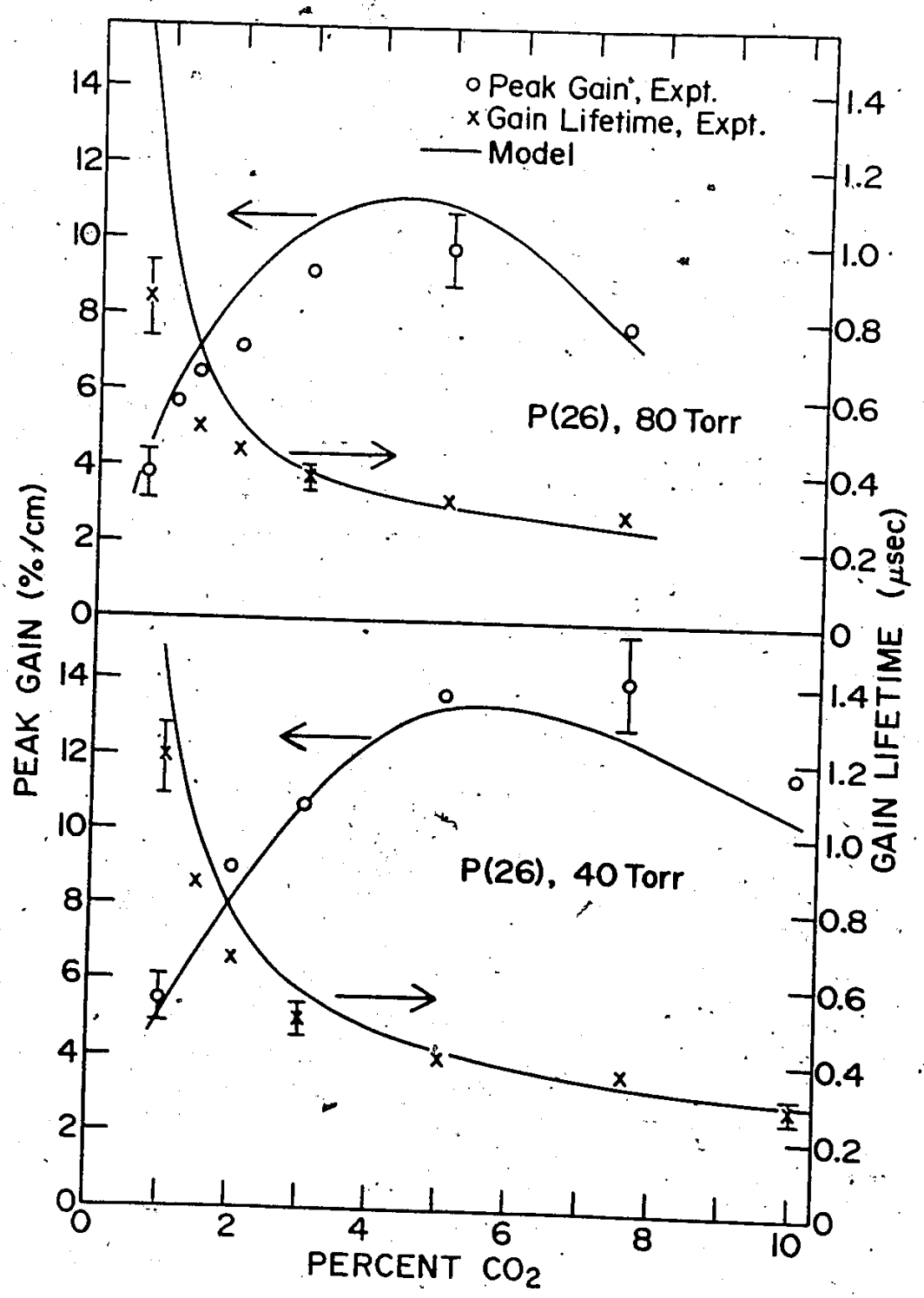
o Peak Gain, Expt.
x Gain Lifetime, Expt.
— Model
P(26), 80 Torr
P(26), 40 Torr
PEAK GAIN (%/cm)
GAIN LIFETIME (μsec)
PERCENT CO_2
0
2
4
6
8
10
12
14
0.2
0.4
0.6
0.8
1.0
1.2
1.4

The largest measured gain coefficient was ~14 %/cm at 40 Torr and 7.6% CO_2.

The data displayed in Fig. 5-8 can be used to determine the optimum discharge mixture and pressure for a 4.3-μm laser. The energy stored in the $10^0 1$ level is approximately proportional to the product of small-signal gain (fractional inversion) and pressure (number density). Thus the stored energy is maximized for a 5% CO_2 mixture at 80 Torr. However, the gain lifetime is inversely proportional to the CO_2 partial pressure due to the rapid de-excitation of the $10^0 1$ level by near-resonant collisions (see Eq. (2-12)). As the CO_2 partial pressure is increased the gain lifetime becomes much shorter than the duration of the sequence pump pulse, reducing the efficiency of the system. In addition, the nonsaturable absorption due to overlaps by the Lorentzian wings of nearby pressure-broadened lines increases with the square of the total pressure, resulting in very inefficient extraction of the stored energy at higher pressures. Consequently, 4.3-μm lasers are found to give optimum performance with a 4% CO_2 mixture at 60 Torr total pressure, as is described in Chapt. 7.

As a final stage in optimizing the 4.3-μm performance, gain coefficients were measured as a function of sequence pump intensity. Figure 5-9 shows results obtained at a discharge pressure of 40 Torr. As with the other calculations of directly-pumped gain, the model slightly overestimates the magnitude of the gain but accurately predicts the pump intensity dependence of the gain, and the time taken to reach the peak gain. Note that the peak gain in Fig. 5-9 remains approximately constant at pump intensities > 100 kW/cm^2. A similar

FIGURE 5-9

Peak gain as a function of the 10.4-μm P(25) sequence pump intensity. Also shown is the time delay between the start of the pump pulse and the peak 4.3-μm gain. Discharge temperatures are given in the caption to Fig. 5-1.

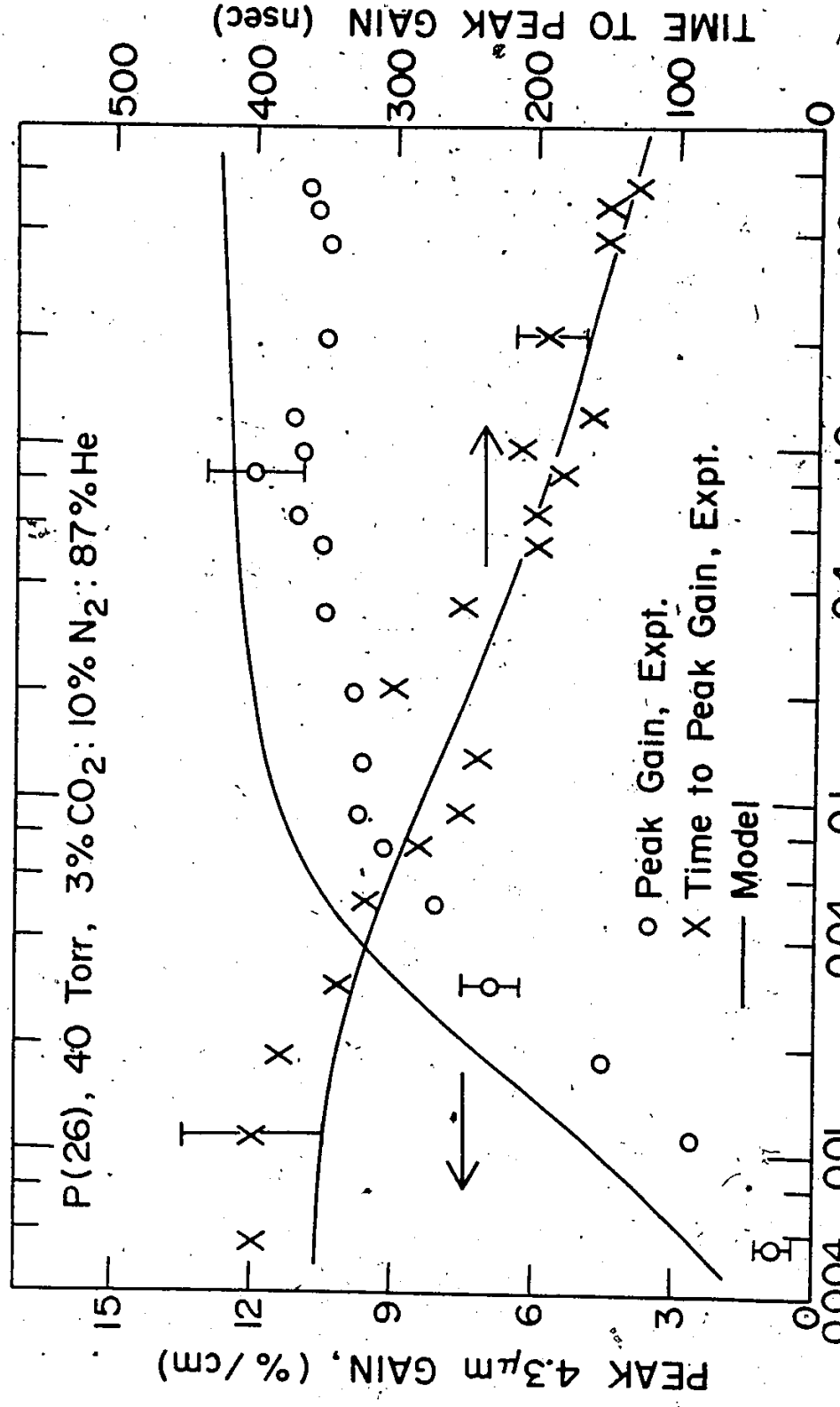
P(26), 40 Torr, 3% CO_2: 10% N_2: 87% He
PEAK 4.3μm GAIN, (%/cm)
TIME TO PEAK GAIN (nsec)
PEAK SEQUENCE INTENSITY (MW/cm²)
o Peak Gain, Expt.
X Time to Peak Gain, Expt.
— Model
0.004
0.01
0.04
0.1
0.4
1.0
4.0
0
3
6
9
12
15
100
200
300
400
500

result was obtained at 80 Torr with pump intensities >200 kW/cm^2. These results show that for most efficient operation, the pump beam used in the present experiments should be expanded and used to pump a large-aperture 4.3-μm laser.

5.6 Summary

This chapter presents a detailed experimental and theoretical study of the gain dynamics of the 4.3-μm CO_2 laser. The measured gain coefficients are typically of the order of 10 %/cm, but the gain is generally short-lived (a few hundred ns). A rate-equation model is developed which gives good agreement with experiment over a wide range of operating conditions. There are no adjustable parameters in the model as all the input constants are determined by experiment. The parameters which significantly influence the gain have been examined and the optimum operating conditions identified for the 4.3-μm amplifier. Discharge excitation is most important, with high values of T_3 being necessary to obtain the maximum gain. Discharge pressure and CO_2 content should be kept low (<100 Torr and ~5% CO_2). Otherwise, the 4.3-μm upper level lifetime becomes much shorter than the duration of the sequence pump pulse and the overlapping absorptions increase, leading to less efficient operation. It is shown that the inclusion of coherent effects improves the agreement between theory and experiment for the directly-pumped 4.3-μm transition. The influence of coherent effects on 4.3-μm gain is discussed in detail in the next chapter.

CHAPTER 6

INFLUENCE OF THE DYNAMIC STARK EFFECT ON THE SMALL-SIGNAL GAIN OF 4.3-μm CO_2 LASERS

6.1. Introduction

In the previous chapter, measured 4.3-μm small-signal gain coefficients were compared with the predictions of a rate-equation model. It was shown that the measurements and calculations were in good agreement for 4.3-μm lines that obtained a population inversion through collisional coupling from nearby rotational levels. However, the model always overestimated the magnitude of the gain on directly-pumped 4.3-μm lines (i.e., lines having a rotational energy level in common with the sequence pump transition). In this chapter, experimental results are presented which show that the dynamic Stark effect is responsible for the reduced gain which is observed on directly-pumped lines.

It has long been recognized that coherent effects play an important role in the dynamics of optically-pumped infrared lasers. The presence of an intense pump field connecting two energy levels of a molecule results in a level splitting giving rise to the Autler-Townes effect or dynamic Stark effect [146]. This splitting can be observed by monitoring a probe transition which has one level in common with the pumped transition [147], or by monitoring the fluorescence from the pump transition itself [148]. CW far-infrared lasers often operate with one common level connecting the pump and laser fields (inverted-vee

configuration), and dynamic Stark splitting has been observed in oscillator-amplifier experiments with far-infrared lasers [149,150]. However, in most experiments involving the dynamic Stark effect, the intense field which causes the splitting also produces significant population transfer between the pumped levels. This population transfer can obscure the dynamic Stark splitting, and makes it more difficult to carry out comparisons between theory and experiment.

In this chapter, a double-resonance infrared experiment is described in which dynamic Stark shifts in CO_2 are examined in the absence of population transfer. Figure 6-1 is a simplified energy level diagram of CO_2 showing the transitions used in the measurements. An intense 10.4-μm sequence band CO_2 laser pulse optically pumps a room-temperature CO_2 gas mixture. The vibrational levels which are connected by the pump transition, 10^01 and 00^02, lie > 3700 cm^{-1} above the ground state, and hence have no significant population at room temperature. The intense 10.4-μm field simply splits the specific rotational-vibrational levels connected by the pump, but has negligible effect on the populations in the low lying levels of CO_2. As shown in Fig. 6-1, the dynamic Stark splitting is monitored by measuring small-signal absorption on the $(10^00 - 10^01)$ 4.3-μm band with low power 4.3-μm probe laser pulses. Experimentally, it is observed that the 4.3-μm absorption at the line center can decrease by more than a factor of five in the presence of the intense 10.4-μm pump. (Note that population transferred out of the 10^01 level would result in an increase in absorption.) The measured decrease in absorption is in good agreement with theoretical calculations if the pump intensity is used as

FIGURE 6-1

Simplified energy level diagram of CO_2 showing the pump and probe transitions used in the double-resonance measurements.

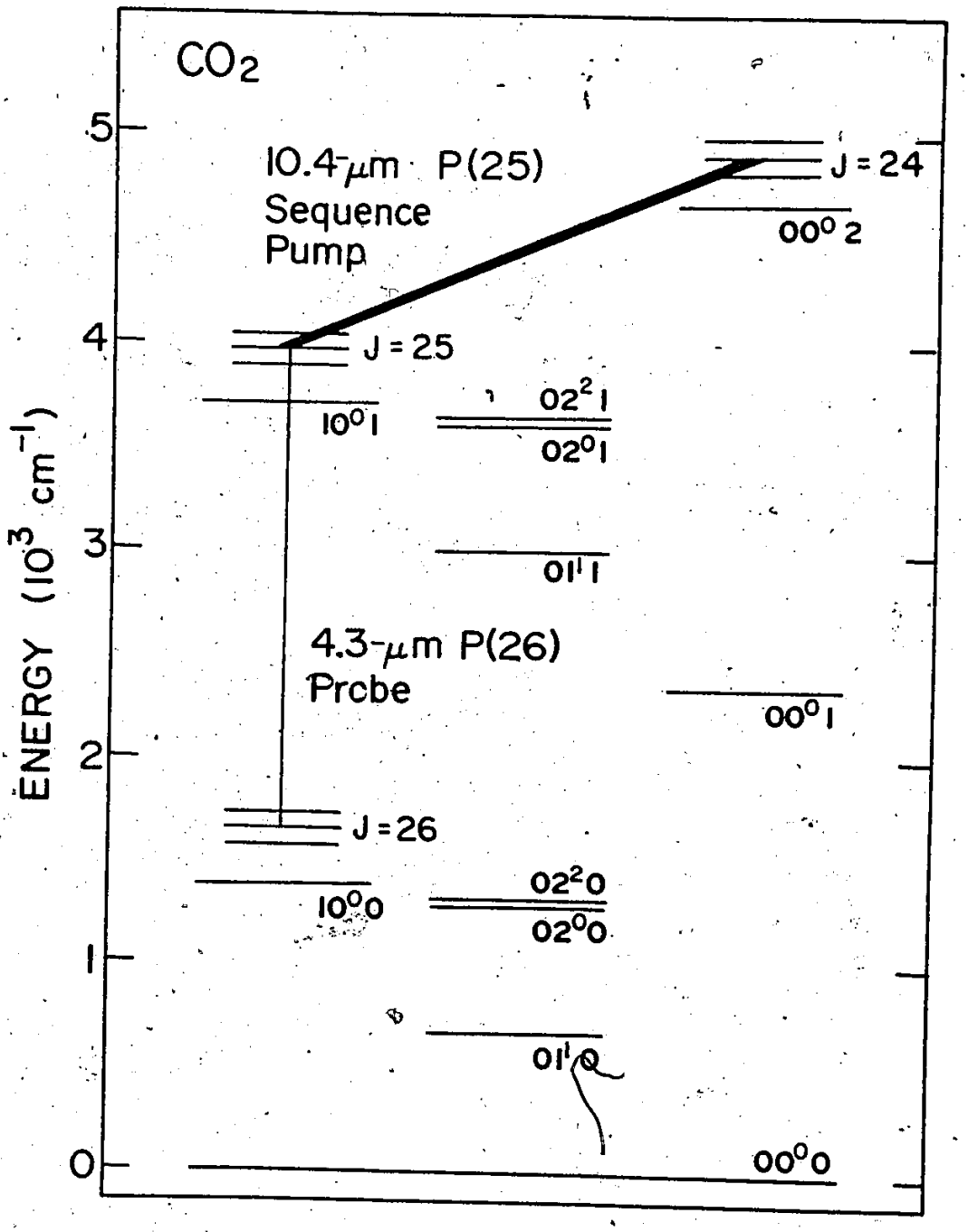
CO2
10.4-μm P(25)
Sequence
Pump
J = 24
00⁰2
J = 25
10⁰1
02²1
02⁰1
01¹1
4.3-μm P(26)
Probe
00⁰1
J = 26
10⁰0
02²0
02⁰0
01¹0
00⁰0
ENERGY (10³ cm⁻¹)
0
1
2
3
4
5

an adjustable parameter.

In addition to providing a clear and unambiguous demonstration of dynamic Stark splitting, the measurements made in room-temperature CO_2 can be used to develop a more accurate model for predicting small-signal gain on directly-pumped 4.3-μm lines. The production of gain in the 4.3-μm laser depends upon population transfer from the 00^02 level to the 10^01 level by the sequence pump pulse. Of course, the sequence pump pulse will also produce Stark splitting of the upper rotational level belonging to the directly-pumped 4.3-μm transition. The purpose of this chapter is to account for the influence of coherent effects on the 4.3-μm gain. It is shown that much better agreement with experiment is obtained if the rate-equation model of the 4.3-μm gain dynamics (described in Chapt. 5) is modified to include these effects. The next section describes the theoretical model used to predict the influence of the intense 10.4-μm radiation on the 4.3-μm absorption in room-temperature CO_2. These predictions are shown to be in good agreement with experiment. Section 6.3 deals with the influence of coherent effects on 4.3-μm gain under conditions typical of 4.3-μm lasers, and modifications to the rate-equation model are described.

6.2 Double-Resonance Experiments in Unexcited CO_2

Several theories have been developed describing the interaction of two laser fields with a three-level molecular system [145,150,151]. The model used in the present work is identical to that of Heppner et al. [150], and assumes that the rate of change of pump intensity is slow compared with the relaxation times (steady-state assumption). The

presence of degenerate M components of the rotational levels is handled by neglecting M-changing collisions and summing over a superposition of nondegenerate three-level systems. As negligible population transfer occurs in unexcited CO_2, this is a good approximation for the experimental conditions. The M dependence of the transition dipole moment [152] can be modified in the model to account for linearly-polarized pump and probe beams with polarizations which are parallel or perpendicular to each other.

Figure 6-2 illustrates how the calculated 4.3-μm lineshapes are changed by the presence of intense sequence pump radiation. The gas mixture and pressure chosen for the calculation are similar to those used in 4.3-μm CO_2 lasers. Table 6-1 lists the input data for the model [78,102,111]. At zero pump intensity, the lineshape is simply a Voigt profile. (The collision- and Doppler-broadened linewidths (HWHM) are 100 MHz and 65 MHz respectively.) With a resonant pump intensity of 2.8 MW/cm^2 the average Rabi frequency is ~250 MHz and significant splitting of the lineshape occurs for both combinations of polarization. The minor differences in the two lineshapes are caused by the M dependence and polarization dependence of the transition dipole moment [152].

It is clear from Fig. 6-2 that a significant decrease in absorption at the line center should be observable at high pump intensities. To measure this decrease, the experimental apparatus described in the previous chapter (Sect. 5.3) was used. An intense 10.4-μm sequence pulse and a weak 4.3-μm probe pulse were combined at a dichroic beam splitter and propagated through a 76-cm long absorption cell (i.e., the unexcited 4.3-μm amplifier shown in Fig. 5-3), which

FIGURE 6-2

Calculated lineshape of the 4.3-μm transition in a room-temperature CO_2 gas mixture as a function of the sequence pump intensity (I_{seq}) and the relative linear polarization of the pump and probe radiation. The calculated linecenter absorption with $I_{seq}=0$ is 2.9 %/cm.

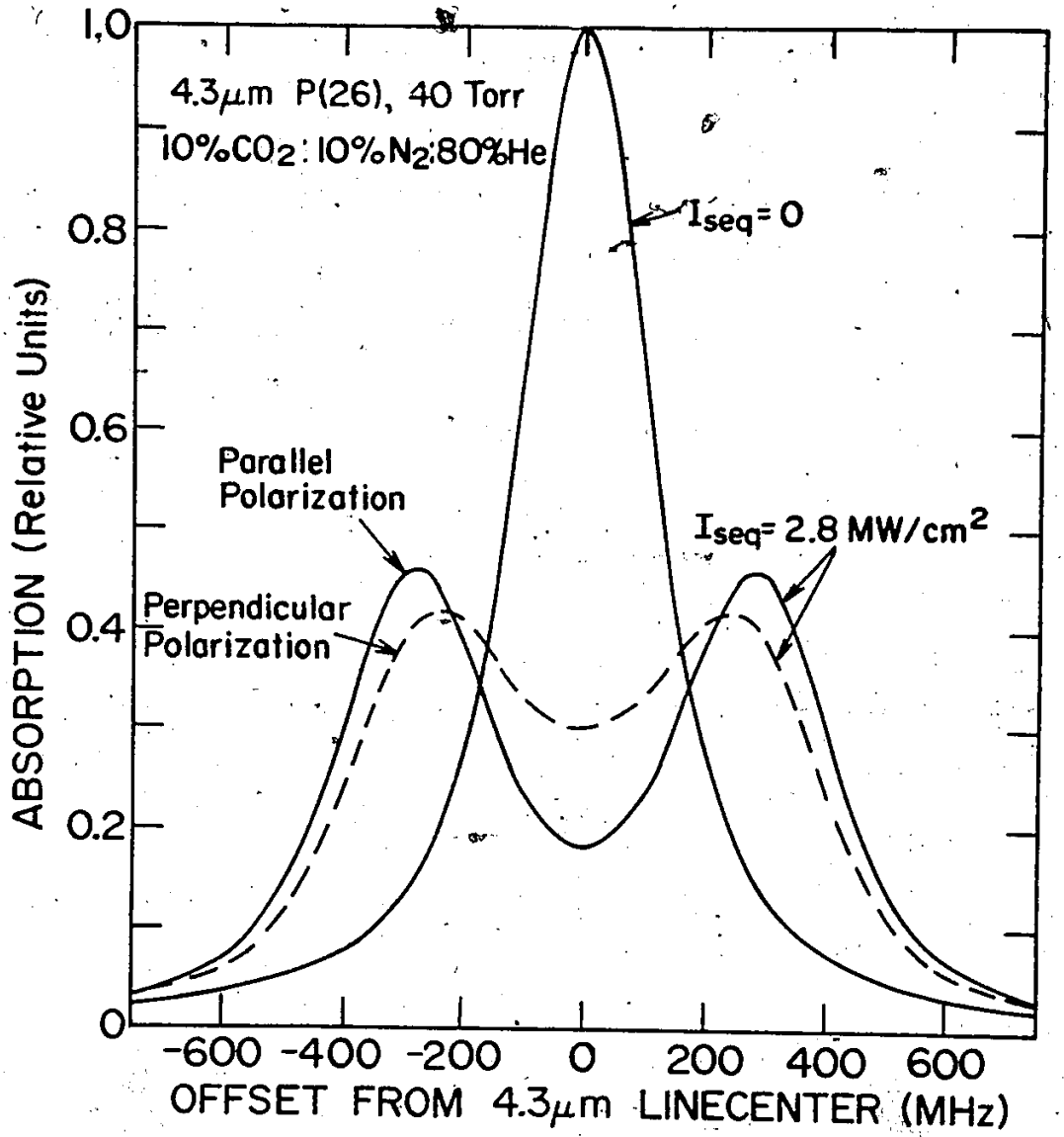
4.3μm P(26), 40 Torr
10%CO2:10%N2:80%He
Iseq= 0
Parallel Polarization
Perpendicular Polarization
Iseq= 2.8 MW/cm2
ABSORPTION (Relative Units)
1.0
0.8
0.6
0.4
0.2
0
-600 -400 -200 0 200 400 600
OFFSET FROM 4.3μm LINECENTER (MHz)

TABLE 6-1

CO_2 molecular data for the model described in Sect. 6.2. The decay rates and fractional populations correspond to a 10% CO_2: 10% N_2: 80% He gas mixture at 300 K.

Transition	Frequency (cm^{-1})	Transition Dipole Moment (Debye)
$10^0 1 - 00^0 2$, P(25)	937.393	0.0556 a)
$10^0 0 - 10^0 1$, P(26)	2304.285	0.3116 b)

Rotational Level	Fractional Population	Decay Rate c) ($s^{-1}Torr^{-1}$)
$J_{002} = 24$	1.02×10^{-12}	1.57×10^{7}
$J_{101} = 25$	9.58×10^{-11}	1.57×10^{7}
$J_{100} = 26$	6.34×10^{-6}	1.57×10^{7}

a) Ref. [111].

b) Ref. [78].

c) The decay rate is given by $2\pi\Delta\nu$, where $\Delta\nu$ is the collision-broadened linewidth (HWHM), taken from Ref. [102].

contained a 10% CO_2: 10% N_2: 80% He gas mixture at 40 Torr. Absorption coefficients were measured at the peak of the 4.3-μm probe pulse, which was varied in time relative to the pump pulse. Figure 6-3 displays the time-dependent 4.3-μm absorption measured during the pump pulse. Note that at the peak of the pump pulse the measured absorption coefficient decreases to 0.18 of the unperturbed value, in agreement with the calculation shown in Fig. 6-2. It should be emphasized that this decrease in absorption was only observed with the 4.3-μm probe laser tuned to the connected P(26) transition; no change in absorption was observed with the probe laser tuned to the nearby P(22), P(24), or P(28) lines. When the pump laser was operated on the P(23) ($10^0 1$-$00^0 2$) transition, then the decrease in 4.3-μm absorption was only observed on the connected P(24) ($10^0 0$-$10^0 1$) transition. These results confirm that coherent effects rather than population transfer are responsible for the decrease in absorption.

Also shown in Fig. 6-3 is the calculated absorption determined at the line center of the 4.3-μm transition. A complete calculation including integration over velocity classes is represented by the solid line. The sequence pump intensity was chosen as the only variable parameter in making this calculation. The agreement with experiment shown in Fig. 6-3 was obtained with a fitted pump intensity of 2.8 MW/cm^2. The fitted intensity is a factor of 0.55 less than the measured intensity. This is attributed to the fact that the calculations are carried out assuming that both pump and probe radiation are ideal monochromatic fields, whereas the experimental laser pulses have a frequency spectrum corresponding to a few longitudinal modes (spacing

FIGURE 6-3

Time dependence of the sequence pump pulse and the 4.3-μm small-signal absorption in a room-temperature CO_2 gas mixture. The sequence pump pulse has a measured peak intensity of 5 MW/cm^2 and the pump and probe beams have parallel linear polarizations. The 4.3-μm absorption coefficient, α, is normalized to the unpumped value α_o (measured as $\alpha_o = 2.6 \pm 0.3$ %/cm). See text for details of the calculation.

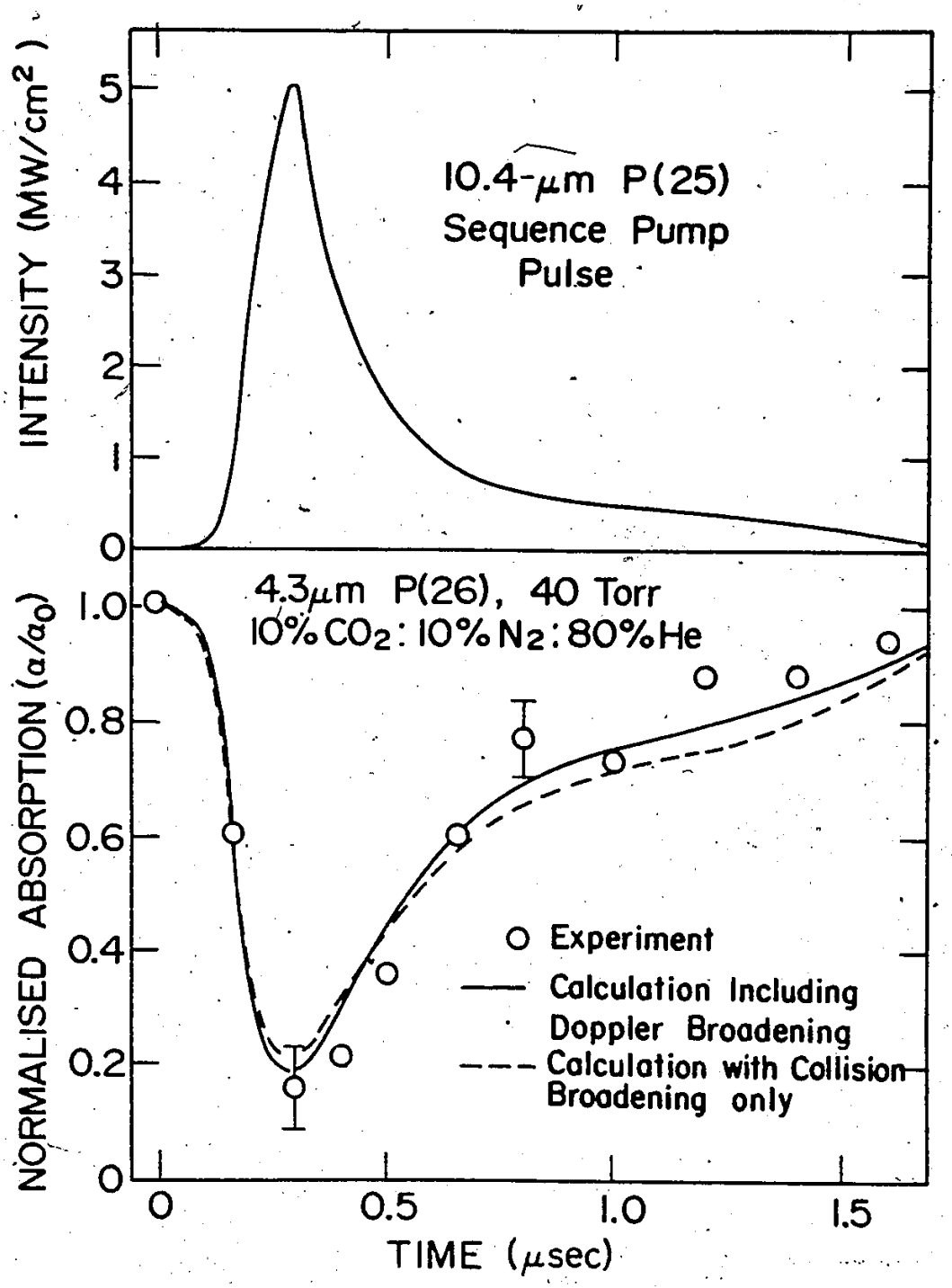
INTENSITY (MW/cm²)
10.4-μm P(25)
Sequence Pump
Pulse
4.3μm P(26), 40 Torr
10% CO₂: 10% N₂: 80% He
NORMALISED ABSORPTION (α/α₀)
Experiment
Calculation Including
Doppler Broadening
Calculation with Collision
Broadening only
TIME (μsec)

~65 MHz) and a few transverse modes. The finite frequency spectrum is probably also responsible for the fact that it was impossible to experimentally observe any significant dependence of absorption upon relative polarization.

While the results shown in Fig. 6-3 provide a very clear demonstration of coherent effects in a coupled three-level system, an exact comparison with the present theory [150] would require the use of single-frequency pump and probe lasers. However, the motivation in carrying out this work was to account for the effect of coherence on small-signal gain measurements made in a 4.3-μm amplifier. As described in Chapt. 5, the gain measurements were made with pump and probe pulses identical to those employed here. Hence, the scaling factor of 0.55 used for Fig. 6-3 is entirely appropriate for the calculations involving small-signal gain. With this motivation in mind, a further simplification can be made by neglecting Doppler broadening effects in the calculation and scaling the measured pump intensity by a factor of 0.3 to give the dashed line shown in Fig. 6-3. Once again the agreement with experiment is very good, and justifies the assumption that integration over velocity classes can be ignored in carrying out the calculations on 4.3-μm gain which are described in the next section.

6.3 Influence of Coherent Effects on 4.3-μm Gain

In the experiments described in the previous section, the pump pulse caused negligible population transfer, and it was possible to determine how coherent effects influenced the measurements made with the 4.3-μm probe laser. Now one can tackle the more difficult case of a

4.3-μm amplifier, in which CO_2 molecules are first excited into the 00^02 level by an electrical discharge, and then transferred to the 10^01 level by an intense sequence pulse. The 4.3-μm probe laser monitors the time-dependent population inversion between the 10^01 and 10^00 levels. Provided the 4.3-μm probe is not tuned to the transition directly connected to the pump, the rate-equation model described in Chapt. 5 accounts for all the dynamics of population transfer. However, if the 4.3-μm probe is tuned to the directly-pumped transition, population transfer and dynamic Stark splitting must be considered simultaneously.

It is worth taking an initial qualitative look at some results before considering the details of the calculation. Figure 6-4 shows measured and calculated 4.3-μm gain coefficients for a 1% CO_2 gas mixture at 40 Torr. (This mixture was chosen to give a relatively long lived 4.3-μm inversion.) Note that the rate-equation model overestimates the measured 4.3-μm gain, particularly at the time of the peak sequence intensity. Just as the presence of the pump pulse reduced the absorption at the line center in Figs. 6-2 and 6-3, the same dynamic Stark shifts reduce the measured gain.

In order to include coherent effects in the calculated gain, the time-dependent population of each M component must be known. However, all of the M components within a rotational level perturbed by the pump may not have the same population, because the transition dipole moment is M dependent [152]. In initial calculations, the degree of nonequilibrium between M-component populations was estimated by including an extra rate equation in the model of the gain dynamics to describe the population of a single M component in each of the

FIGURE 6-4

Time dependence of the measured and calculated 4.3-μm small-signal gain for a discharge gas mixture containing 1 % CO_2. The sequence pump pulse has a peak intensity of ~3.5 MW/cm^2. Note the improved agreement with experiment when the calculation includes coherent effects. Both experiment and calculation are for parallel polarization of the probe radiation relative to the pump radiation.

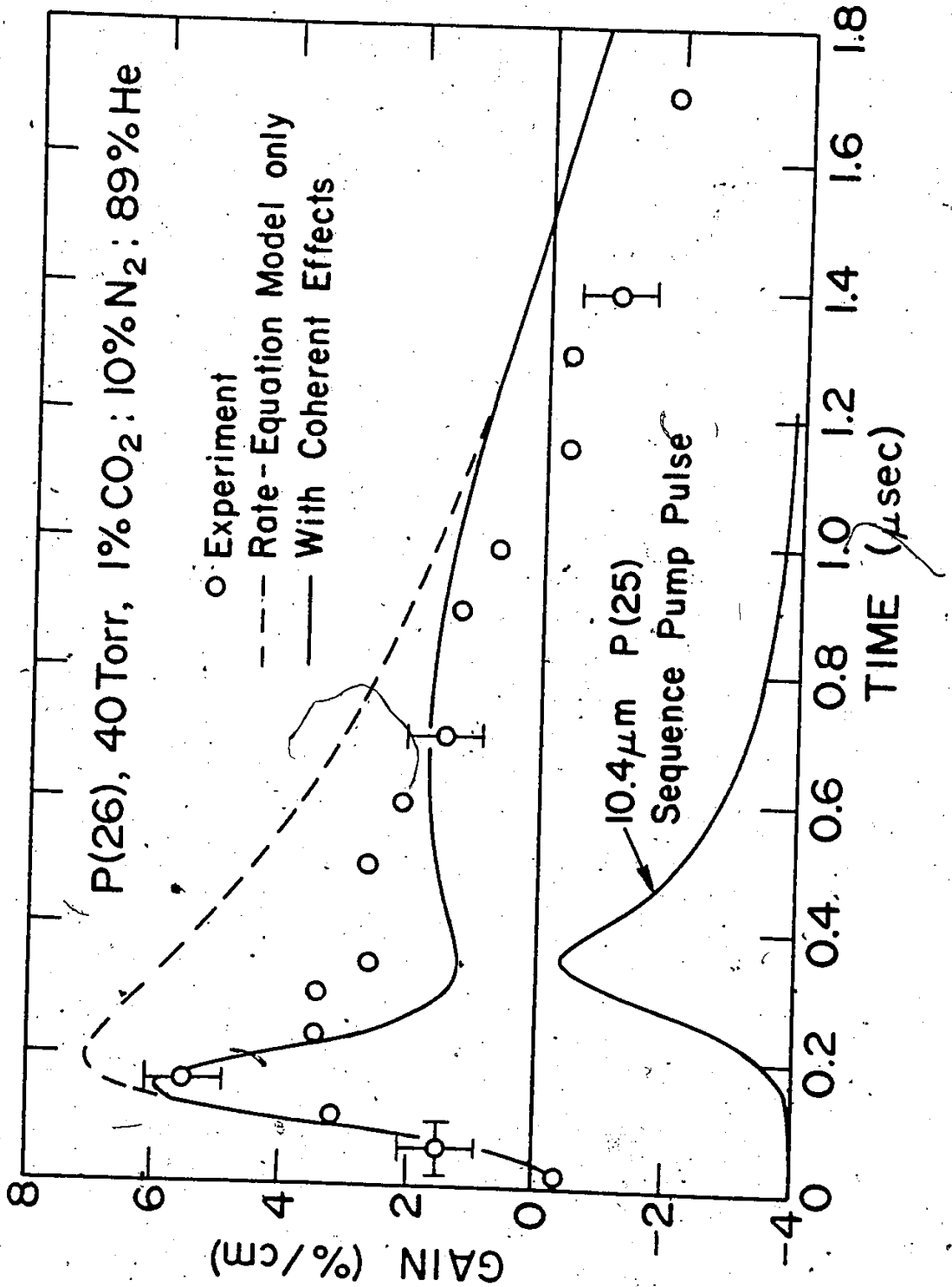
P(26), 40 Torr, 1% CO_2: 10% N_2: 89% He
Experiment
Rate-Equation Model only
With Coherent Effects
10.4μm P(25)
Sequence Pump Pulse
GAIN (%/cm)
TIME (μsec)
8
6
4
2
0
-2
-4
0
0.2
0.4
0.6
0.8
1.0
1.2
1.4
1.6
1.8

rotational levels connected by the pump transition. It was found that very fast collisional coupling from nearby rotational levels tended to equalize the M-component populations. This thermalization occurred because the collisional coupling did not conserve M in the model, an assumption which is supported by experimental evidence presented later. Consequently, in subsequent calculations it has been assumed that the populations of all M components within each rotational level are equal. This assumption greatly simplifies the calculation and is justified by the good agreement obtained between the calculations and experiment.

The time-dependent populations of the M components in the J=24 rotational level of $00^0 2$ and in the J=25 rotational level of $10^0 1$ are given by $m_{002}(M)=n_{002}/g_{002}$ and $m_{101}(M)=n_{101}/g_{101}$, respectively. The 4.3-μm lower levels are not perturbed by the sequence pulse, and hence the M-component populations in the J=26 rotational level of $10^0 0$ are given by $m_{100}(M)=K_{100}N_{100}/g_{100}$. The subscript denotes the vibrational level, N represents the vibrational population, n is the rotational population, K is the rotational population factor, and g is the degeneracy. All populations are calculated using the rate-equation model described in Chapt. 5. The 4.3-μm gain at the line center is calculated from Eq. (9) of Panock and Temkin [145], and the gain as a function of M is given by:

$$g_4^{\circ}(M) = \sigma_4(M)\,[\,m_{101}(M) - m_{100}(M)\,]\,\left[\,1 - \frac{(\beta(M)\tau)^2}{1+(\beta(M)\tau)^2}\,\right]$$

$$+ \sigma_4(M)\,[\,m_{002}(M) - m_{101}(M)\,]\,\left[\,\frac{(\beta(M)\tau)^2}{1+(\beta(M)\tau)^2}\,\right]. \qquad (6\text{-}1)$$

The 4.3-μm gain cross-section $\sigma_4(M)$ is calculated as in Chapt. 5 with a transition dipole moment that is both M dependent and polarization dependent [152]. $\beta(M)$ is the Rabi frequency on the sequence transition and is given in MHz by $\beta(M)=6.91\mu_M I^{1/2}$, where μ_M is the M-dependent transition dipole moment in Debye and I is the intensity of the radiation in W/cm^2. The relaxation time τ is given by $\tau = 1/(2\pi\Delta\nu)$, where $\Delta\nu$ is the collision-broadened linewidth (HWHM). The first term in Eq. (6-1) represents the reduction in 4.3-μm gain due to the intense 10.4-μm pump field ($\beta\tau > 1$), while the second term is related to a small Raman contribution to the gain. The total 4.3-μm gain is given by summing $g_4(M)$ over all M. Complications due to Doppler broadening and the nonmonochromatic nature of the radiation fields are accounted for in an empirical fashion by scaling the measured sequence intensity by a factor of 0.3, as explained in Sect. 6.2.‡

The 4.3-μm gain calculated using Eq. (6-1) is shown in Figs. 6-4 and 6-5 for two different gas mixtures. Note that significantly better agreement is obtained between theory and experiment when the coherent effects are included in the gain calculation. Also shown in Fig. 6-5 is the gain calculated for perpendicular polarization of the pump and probe fields. Careful measurements with both parallel and perpendicular polarizations failed to detect any significant differences in the experimental gain coefficients. This result is not surprising in view

---

‡ Note that the intensity scaling factor of 0.3 is only valid for a discharge pressure of 40 Torr. As the discharge pressure increases, Doppler broadening effects become less significant and the scaling factor increases.

FIGURE 6-5

Time dependence of the measured and calculated 4.3-μm small-signal gain for a discharge gas mixture containing 3 % CO_2. The sequence pump pulse is the same as that of Fig. 6-4. The experimental results are obtained with parallel polarization of the probe radiation relative to the pump radiation.

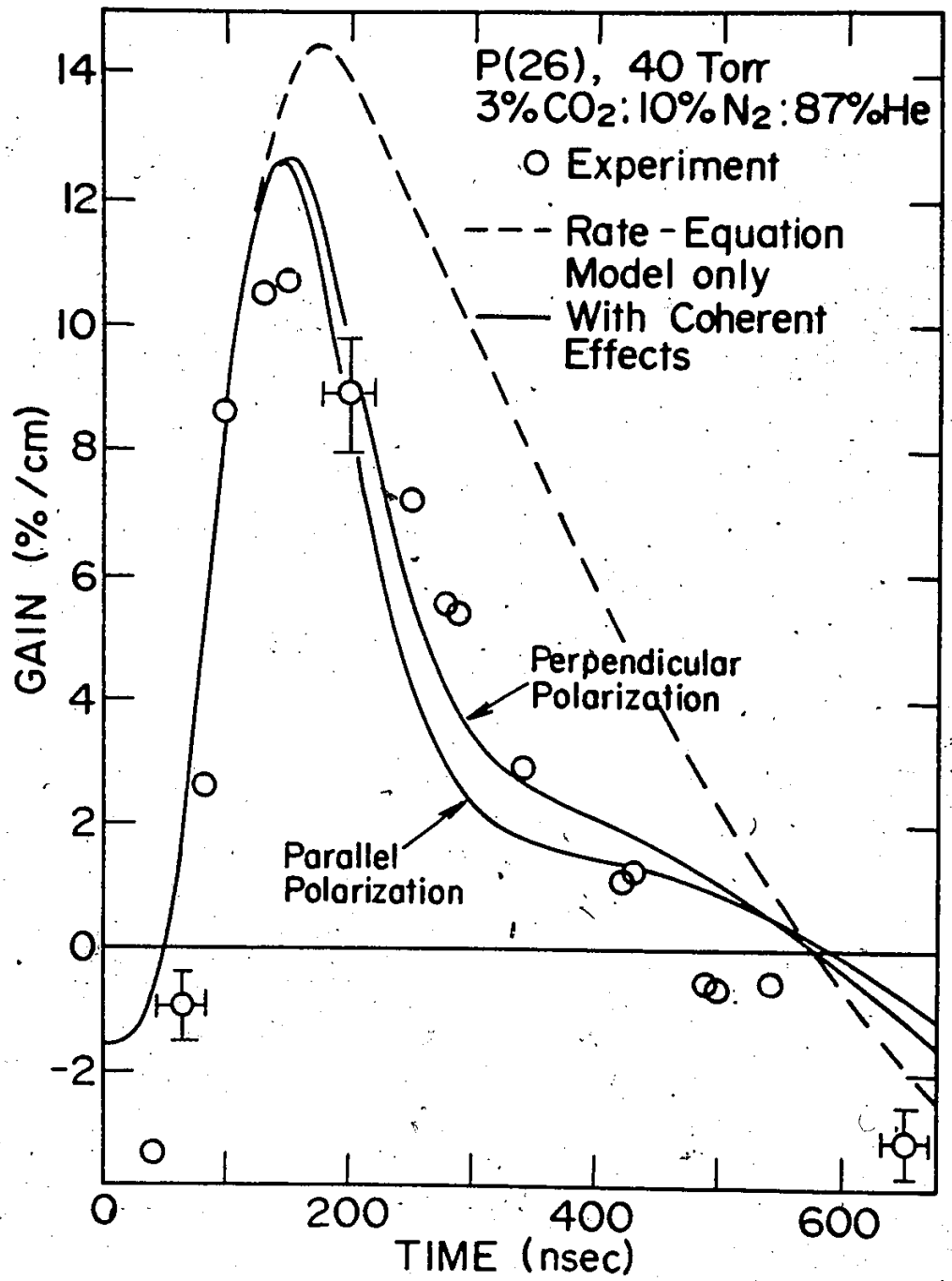
P(26), 40 Torr
3%CO2:10%N2:87%He
O Experiment
Rate-Equation Model only
With Coherent Effects
Perpendicular Polarization
Parallel Polarization
GAIN (%/cm)
TIME (nsec)
14
12
10
8
6
4
2
0
-2
0
200
400
600

of the typical error bars shown in Fig. 6-5 and the fact that no polarization dependence could be observed in absorption measurements (see Sect. 6.2). A much more sensitive measure of relative gain is to place the 4.3-μm amplifier in a polarization-insensitive optical resonator. The 4.3-μm radiation with the maximum net gain will dominate the observed output. Experimental measurements confirmed that for a variety of directly-pumped transitions, the 4.3-μm output pulses were always polarized parallel to the 10.4-μm pump radiation. As the polarization of the pump radiation was rotated, the 4.3-μm polarization followed suit. This behaviour was very different from that of the collisionally-pumped lines. These transitions obtain inversion by collisional transfer, do not have gain that is sensitive to polarization, and always give randomly polarized 4.3-μm pulses from a polarization-insensitive cavity. This is strong evidence in support of the earlier assumption that collisional population transfer between rotational levels does not conserve M. The polarization characteristics of both types of transitions provide another indication of the importance of coherent effects in 4.3-μm lasers.

6.4 Summary

The results presented in this chapter clearly demonstrate that coherent two-photon effects must be included in an accurate calculation of the small-signal gain in a 4.3-μm CO_2 laser. The dynamic Stark effect causes the 4.3-μm lineshape to split and reduces the gain at the line center. The inclusion of coherent effects in the rate-equation model is reasonably simple, and good agreement is obtained between

theory and experiment. The theoretical treatment described in this chapter can be applied to other optically-pumped pulsed laser systems, and this work has demonstrated the importance of including coherent effects in considerations of directly-pumped transitions.

CHAPTER 7

OPTIMIZATION OF PULSE ENERGY FROM 4.3-μm CO_2 LASERS

7.1 Introduction

The 4.3-μm CO_2 laser first reported by Znotins et al. [6] produced output energies of ~50 μJ/pulse. The laser appeared to be scalable, and increased output energies of 250 μJ/pulse [11] and one mJ/pulse [135] were soon reported. In the present study, the performance of the 4.3-μm CO_2 laser has been optimized, and output energies of 15 mJ/pulse and peak powers of 100 kW/pulse have been obtained from an 88-cm long by 11-cm^2 aperture discharge. This represents the highest output energy reported to date from a 4.3-μm CO_2 laser [136].

There are several other laser systems which operate in the 4.3-μm wavelength region. As mentioned in Chapt. 1, other excitation schemes have been used to obtain 4.3-μm lasing in CO_2. These include bromine transfer lasers [7], optical pumping with HF lasers [8,153], and pumping from optical parametric oscillators [9]. Among these, the highest pulse energy was 0.5 mJ/pulse and was produced by the bromine transfer laser. Bromine transfer pumping has also been used with HCN to obtain 2-mJ pulses at 3.85 μm [7]. Frequency doubling of 9.4- and 10.4-μm CO_2 laser radiation results in pulse energies of up to 8 mJ/pulse [154-156]. Several hydrogen halide lasers operate in the 3- to 5-μm wavelength region, and include DF, HCl, and HBr lasers [157]. HCl

and HBr lasers operate from 3.6 to 4.5 μm, and produce up to 30 mJ/pulse on a single line from a 3x3x50 cm^3 discharge volume [158]. Scaled up HBr lasers in multiline operation have produced pulse energies ranging from several hundred mJ [159,160] to as high as 1.4 J [158]. Energies of up to 800 μJ/pulse, which are wavelength tunable from 3.6 to 5.4 μm, can be obtained by difference frequency generation [161]. The performance of the sequence laser pumped 4.3-μm CO_2 laser compares favourably with these other sources. This 4.3-μm laser is based entirely on well-established CO_2 laser technology, and therefore has the advantage of relatively simple construction and operation. In addition, scalability of the pulse energy to several hundred mJ using existing pump pulse energies is shown in this chapter to be feasible. The 4.3-μm CO_2 laser should prove useful in applications such as laser photochemistry, optical pumping, and atmospheric monitoring.

In this chapter, a detailed study of the output energy characteristics of the 4.3-μm CO_2 laser is described. The rate-equation model which was validated in Chapt. 5 by comparison with small-signal gain measurements is used to predict output energies. The model is found to be in good agreement with experiment over a wide range of operating conditions. With the aid of the model, the three factors which most strongly influence the performance of the laser are identified. These factors are: the short lifetime of the upper laser level due to collisions with CO_2, the degree of electrical excitation of the discharge, and the existence of interfering absorptions in the discharge. As a consequence of these factors, optimum performance of the laser is obtained for low CO_2 content gas mixtures at relatively low

pressure (4 % CO_2 at 60 Torr). The implications for scalability to high pulse energies are discussed and the ultimate performance limits of the 4.3-μm laser are presented.

In the next section, a rate-equation model is presented which is similar to the gain model of Chapt. 5, except for the appropriate modifications which enable pulse energies to be calculated. The model is used to illustrate the major energy transfer kinetics involved in 4.3-μm operation. The experimental apparatus is described in Sect. 7.3. In Sect. 7.4, comparisions between the model and experiment are made, and optimization of the operating conditions is discussed. Section 7.5 deals with scalability to higher pulse energies, and Sect. 7.6 describes a simplified cavity design which incorporates the sequence and 4.3-μm lasers in the same optical resonator. Finally, Sect. 7.7 discusses the feasibility of translating the 4.3-μm CO_2 laser pumping scheme to N_2O, with the aim of producing 4.5-μm lasing.

7.2 Rate-Equation Model for Energy Extraction

To obtain a better understanding of the energy extraction characteristics of the 4.3-μm CO_2 laser, the small-signal gain rate-equation model of Chapt. 5 was modified to calculate pulse energies. One additional equation was included to describe the 4.3-μm photon density in the cavity, and extra terms were added to the appropriate equations to account for population transfer by 4.3-μm stimulated emission. In particular, the perturbation of the rotational population in the 10^00 level was included in the model. The eight differential equations governing laser action on the (10^01-10^00) 4.3-μm

band‡ of CO_2 are:

$$\frac{dE_3}{dt} = -h\nu_3(\sigma_s\delta_s\rho_s c + \sigma_4\delta_4\rho_4 c), \tag{7-1}$$

$$\frac{dE_{12}}{dt} = -\frac{E_{12} - E^e{}_{12}(T)}{\tau_{VT}} + h\nu_1\sigma_s\delta_s\rho_s c, \tag{7-2}$$

$$\frac{dN_{002}}{dt} = -\sigma_s\delta_s\rho_s c + \frac{N^e{}_{002}(T_3) - N_{002}}{2\tau_{\nu_3}}, \tag{7-3}$$

$$\frac{dN_{101}}{dt} = \sigma_s\delta_s\rho_s c - \sigma_4\delta_4\rho_4 c - \frac{N_{101} - N^e{}_{101}(T_1,T_3)}{\tau_{101}}, \tag{7-4}$$

$$\frac{dN_{100}}{dt} = \sigma_4\delta_4\rho_4 c + \frac{N_{101} - N^e{}_{101}(T_1,T_3)}{\tau_{101}} - \frac{N_{100} - N^e{}_{100}(T_1)}{\tau_{100}}, \tag{7-5}$$

$$\frac{d\delta_s}{dt} = -2\sigma_s\delta_s\rho_s c + \sigma_4\delta_4\rho_4 c - \frac{\delta_s - (K_{002}N_{002} - K_{101}N_{101}\, g_{002}/g_{101})}{\tau_R}, \tag{7-6}$$

$$\frac{d\delta_4}{dt} = \sigma_s\delta_s\rho_s c - 2\sigma_4\delta_4\rho_4 c - \frac{\delta_4 - (K_{101}N_{101} - K_{100}N_{100}\, g_{101}/g_{100})}{\tau_R}, \tag{7-7}$$

$$\frac{d\rho_4}{dt} = F\sigma_4\delta_4\rho_4 c - \frac{\rho_4}{\tau_c} + F\beta K_{101}N_{101}. \tag{7-8}$$

The notation used in Eqs. (7-1) to (7-8) is identical to that used in

‡ Modeling of operation on the $(02^01\text{-}02^00)$ 4.3-μm band is achieved by modifying the equations to account for the different levels involved.

the rate-equation model of the gain dynamics, and thus most of the variables are defined in Sect. 5.2. The remaining variables are defined as follows. The 4.3-μm photon density is given by ρ_4. F is the cavity filling factor (i.e., ratio of discharge length to total cavity length), and $\beta K_{101} N_{101}$ is the 4.3-μm spontaneous emission term, as defined in Ref. [128]. The cavity decay time τ_c is composed of two terms and is given by $\tau_c=(1/\tau_{refl} + 1/\tau_{abs})^{-1}$. τ_{refl} is the photon lifetime in the cavity due to output coupling losses, i.e., $\tau_{refl} = -2L/[c\ \ell n(R)]$, where L is the cavity length and R is the cavity reflectivity. τ_{abs} is the photon lifetime due to interfering absorptions in the discharge, which are in general nonsaturable. τ_{abs} is given by $\tau_{abs}=1/(Fc\alpha)$, where α is the nonsaturable absorption coefficient in the discharge. Other losses (such as diffraction losses) are generally much smaller than this absorption loss, and are neglected. The influence of the nonsaturable absorption on the calculation of energy extraction from the oscillator is treated in Sect. 7.4.2.

The model is implemented in the same manner as the gain dynamics model of Sect. 5.2. The initial values of T, T_1, and T_3 (i.e., the values at the time of peak sequence gain in the pulsed discharge) are input to the model and are used to calculate initial values for the populations and energies in Eqs. (7-1) to (7-8). These initial temperatures are determined experimentally using techniques described in Chapt. 3. The measured pump pulse profile is used to determine the successive values of the sequence photon density ρ_s, and the differential equations are solved beginning at a time corresponding to the start of the sequence pump pulse.

The model described by Eqs. (7-1) to (7-8) considers the directly-pumped 4.3-μm transition (i.e., the 4.3-μm transition having a rotational energy level in common with the pump transition). This transition was shown in Chapt. 5 to have the maximum small-signal gain, and lasing generally takes place only on the directly-pumped transition. Minor modification to the equations is required to account for line-tunable 4.3-μm operation on nondirectly-pumped transitions in a wavelength selective cavity, but only the directly-pumped transition will be considered here. Coherent effects play a significant role in the dynamics of the directly-pumped transition as the results of Chapt. 6 show, and cause a reduction in the small-signal gain at the line center of the 4.3-μm transition. Nevertheless, the influence of coherence has been neglected in the present work on energy extraction. This simplification enables one to avoid the complexities of dealing with two intense fields interacting with a degenerate three-level system [145], and can be justified on the basis that population transfer by stimulated emission is the dominant saturation mechanism in the 4.3-μm laser. The rate-equation model accurately computes population transfer, and hence calculates output pulse energies which are in good agreement with experiment, as described in Sect. 7.4.

The rate-equation model gives an overview of the energy transfer dynamics of 4.3-μm operation. Figure 7-1 shows a sequence pump pulse and the calculated output pulse from a 4.3-μm laser under typical operating conditions. Also shown is the time dependence of several energy transfer and energy storage mechanisms. In each case, the number density of CO_2 molecules involved has been multiplied by $h\nu_3$ and the

FIGURE 7-1

Calculated energy transfer mechanisms in the 4.3-μm laser for a gas mixture of 4% CO_2: 10% N_2: 86% He at 60 Torr, and initial discharge temperatures of T=400 K, T_1=425 K, and T_3=2870 K. The dashed lines represent the stored energy in the vibrational levels and the solid lines represent energy transfer into and out of the 4.3-μm upper laser level. Also shown is the 30-mJ/cm^2 sequence pump pulse used as input to the model and the calculated 4.3-μm output pulse. See text for further details.

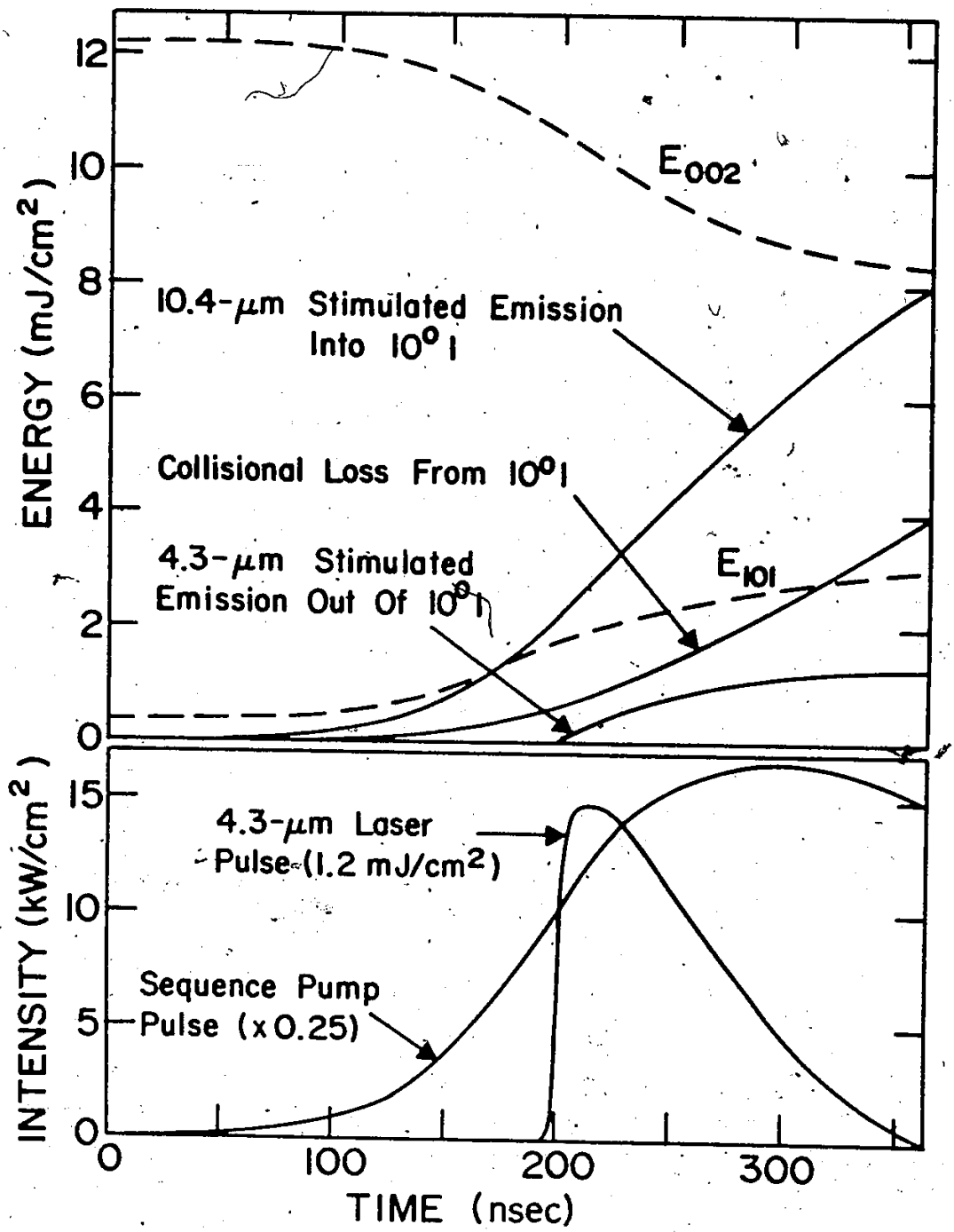
ENERGY (mJ/cm²)
12
10
8
6
4
2
0
E002
10.4-μm Stimulated Emission
Into 10⁰1
Collisional Loss From 10⁰1
4.3-μm Stimulated
Emission Out Of 10⁰1
E101
INTENSITY (kW/cm²)
15
10
5
0
4.3-μm Laser
Pulse (1.2 mJ/cm²)
Sequence Pump
Pulse (x 0.25)
0
100
200
300
TIME (nsec)

discharge length (88 cm) to give the equivalent 4.3-μm energy per unit area. The most striking result of the calculation shown in Fig. 7-1 is that only 1.2 mJ/cm^2 appears as useful output energy, even though 8 mJ/cm^2 is transferred to the 10^01 level by the pump pulse. One-half of this transferred energy is lost as a consequence of the very fast de-excitation of the upper laser level 10^01 by near-resonant collisions with CO_2 (see Eq. (2-12)). This process directly populates the relatively long lived lower laser level 10^00, and causes 4.3-μm laser action to end approximately halfway through the pump pulse. As a result, mixtures with a high partial pressure of CO_2 give short 4.3-μm pulses, poor energy extraction, and reduced efficiency. Figure 7-1 also shows the importance to 4.3-μm operation of the fast ν_3 intra-mode coupling rate. Note that the energy stored in the 00^02 level was reduced by only 4 mJ/cm^2, even though 8 mJ/cm^2 was transferred by the pump pulse. The additional 4 mJ/cm^2 was obtained as a result of collisional coupling into 00^02 from the rest of the ν_3 vibrational mode. The results of Fig. 7-1 illustrate one of the dominant characteristics of 4.3-μm CO_2 lasers: the competition between collisional de-excitation and stimulated emission de-excitation of the 10^01 level.

In the sections which follow, experimental results are presented which are used to validate the rate-equation model, and to identify the parameters which are important in optimizing 4.3-μm laser performance.

7.3 Experimental Apparatus

Figure 7-2 is a schematic diagram of the experimental apparatus used to study the output energy characteristics of the 4.3-μm CO_2 laser.

FIGURE 7-2

Schematic diagram of the experimental apparatus used to measure 4.3-μm energy extraction. The SF_6 is used to absorb the residual 10.4-μm pump radiation. The inset oscilloscope photograph shows the time dependence of the 4.3-μm pulse relative to the 10.4-μm pump pulse.

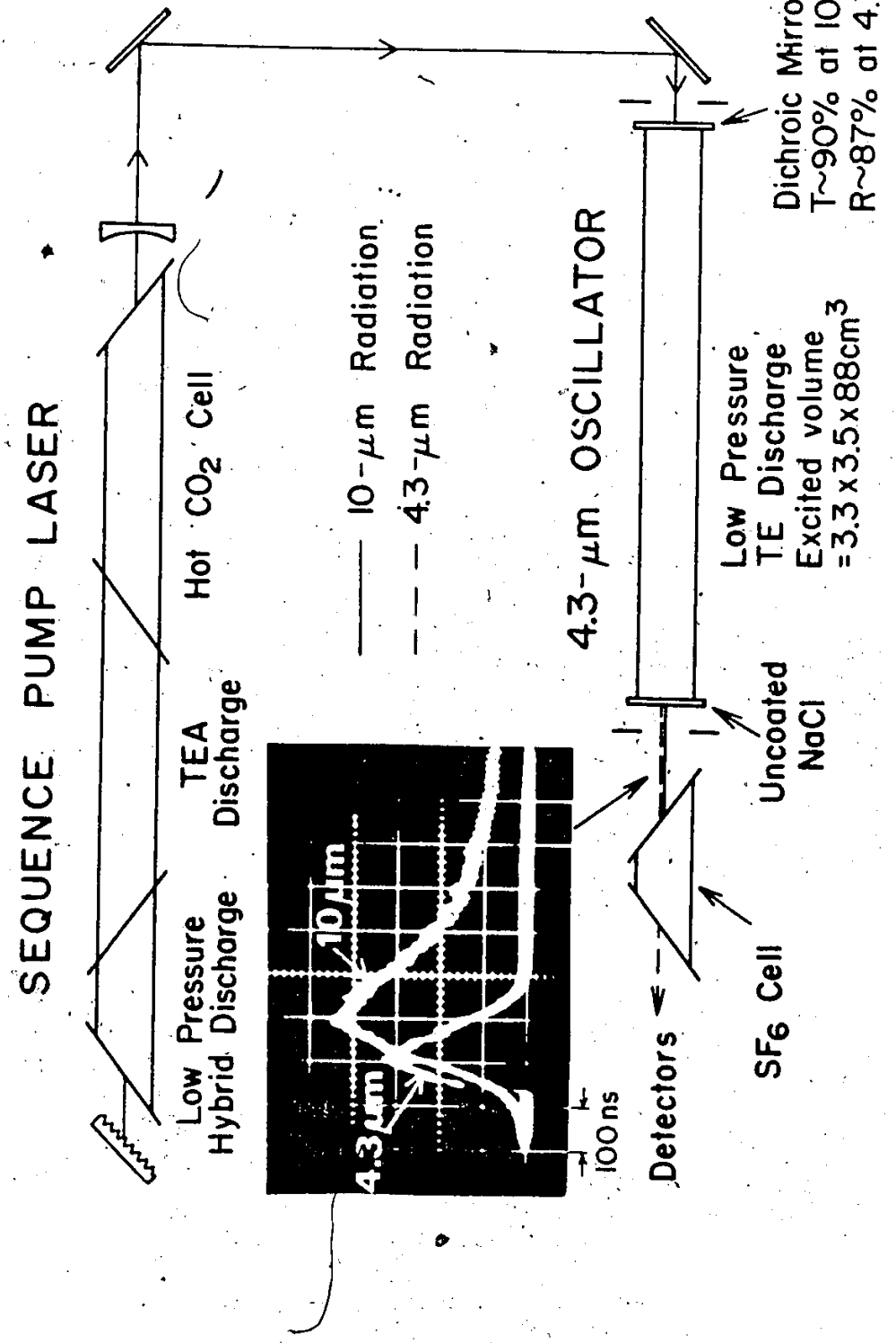
SEQUENCE PUMP LASER
Low Pressure Hybrid Discharge
TEA Discharge
Hot CO_2 Cell
10-μm Radiation
4.3-μm Radiation
4.3-μm OSCILLATOR
Low Pressure TE Discharge Excited volume =3.3x3.5x88cm³
Dichroic Mirror T~90% at 10μm R~87% at 4.3μm
Uncoated NaCl
SF_6 Cell
Detectors
10 μm
4.3 μm
100 ns

The pump pulse is derived from a grating-tunable hybrid sequence laser which is described fully in Sect. 5.3. The pump radiation is coupled into the 4.3-μm oscillator through the dichroic mirror, and the pump beam can be focussed or expanded. Pump energy and pulse shape are monitored with a calibrated Gentec ED-500 joulemeter and a photon drag detector. The 4.3-μm oscillator contains the full-length (i.e., 88 cm of gain) Lumonics discharge module which is described in detail in Sect. 3.3. This discharge is operated with CO_2: N_2: He gas mixtures at pressures from 40 to 120 Torr. The measured experimental parameters such as pressure, gas mixture, discharge temperatures (T, T_1, and T_3), and pump intensity profile are used as input to the rate-equation model. The output from the 4.3-μm oscillator, which consists of both the pump pulse and the 4.3-μm pulse, is passed through a short cell (15 cm) containing SF_6 in N_2 to totally absorb the 10.4-μm pulse. The 4.3-μm pulse shape and energy are monitored by a Ge:Au detector (~8 ns risetime) and a Scientech model 36-0001 calorimeter. The day-to-day reproducibility of the measured pulse energies is better than ± 10 %.

The experimental arrangement is used to measure 4.3-μm pulse energy as a function of pressure, gas mixture, discharge excitation, pump energy, etc. Since all of the parameters required as input to the rate-equation model are obtained experimentally, quantitative comparisons can be made between the measured and calculated 4.3-μm pulse energies. These comparisons are described in the next section.

4 Optimization of Output Energy

Comparisons between measured and calculated 4.3-μm output pulses

are presented in this section. Most of the experimental results were obtained by gently focussing the pump pulses down the center of the 4.3-μm oscillator and observing the 4.3-μm output only from the central region of the discharge (~1 cm^2). In this manner, pump energy densities as high as 350 mJ/cm^2 could be utilized while maintaining a reasonably uniform spatial pump intensity profile, and 4.3-μm oscillation occurred in a region of the discharge which was uniformly excited. This resulted in a more accurate comparison with the rate-equation model, which assumes uniform discharge excitation and pump intensity.

Initially, it was verified that the model predicts the correct 4.3-μm pulse shape. Figure 7-3 shows an oscilloscope photograph of a typical sequence pump pulse and 4.3-μm output pulse. The structure on the 4.3-μm pulse is due to transverse mode beating. The lower portion of Fig. 7-3 is the pulse shape predicted by the model, which is in good agreement with experiment. The fast risetime of the pulse is a result of the high peak gain which occurs in the 4.3-μm laser (~10 %/cm, see Chapt. 5). The gain is short lived, however, and is quickly replaced by strong absorption, causing laser action to stop abruptly before the pump pulse ends. As discussed in Sect. 7.2, this behaviour limits efficient 4.3-μm operation to gas mixtures with a low partial pressure of CO_2. It has been found experimentally that the maximum 4.3-μm pulse energy is obtained with a gas mixture of 4% CO_2: 10% N_2: 86% He at 60 Torr, and a discharge excitation circuit which maximizes T_3. The importance of maximizing T_3 and the effect on the optimum gas mixture are discussed in the following section.

FIGURE 7-3

Time dependence of the measured and calculated 4.3-μm output pulse. The measured P(26) 4.3-μm pulse is shown in the oscilloscope photograph together with the P(25) 10.4-μm pump pulse. The discharge conditions and the sequence pump energy are given in the caption to Fig. 7-1. The measured and calculated 4.3-μm pulse energies are 1.17 ± 0.1 and 1.2 mJ/cm^2, respectively.

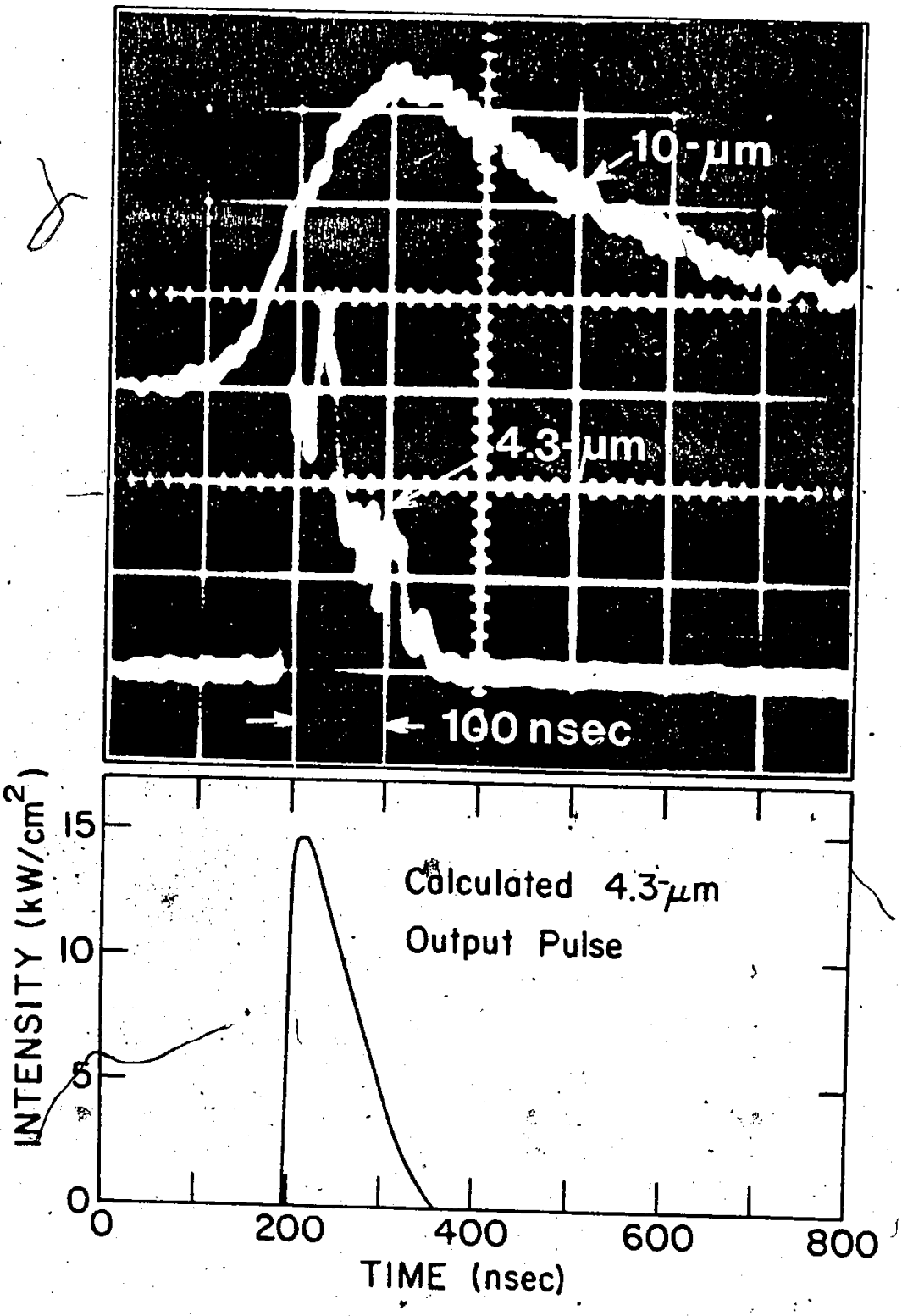
10-μm
4.3-μm
100 nsec
INTENSITY (kW/cm²)
15
10
5
0
Calculated 4.3-μm
Output Pulse
0
200
400
600
800
TIME (nsec)

7.4.1 Discharge Excitation

The performance of the 4.3-μm laser can clearly be improved by increasing the population of the 00^02 level of CO_2 in the discharge (i.e., by increasing T_3). To demonstrate this experimentally, T_3 was varied by changing the input electrical excitation energy to the discharge. The temperatures T, T_1, and T_3 were determined for each set of conditions. The 4.3-μm pulse energy was then measured as a function of T_3. The results are plotted in Fig. 7-4 for a 3% CO_2: 10% N_2: 87% He gas mixture at 80 Torr. Note the dramatic increase in 4.3-μm pulse energy with increasing value of T_3. Similar results are obtained at a discharge pressure of 40 Torr. Also shown in Fig. 7-4 is the pulse energy predicted by the model. The solid line was calculated by using the measured discharge temperatures and is in good agreement with experiment. The dashed line, which was calculated with fixed values of T and T_1, shows that the pulse energy continues to increase linearly with T_3 if T and T_1 remain constant. Unfortunately, heating of the combined $\nu_1 + \nu_2$ vibrational mode and heating of the gas are a consequence of the increased discharge excitation necessary to maximize T_3. The optimum discharge conditions for 4.3-μm operation are clearly those which maximize T_3 while minimizing T and T_1. Such conditions can be obtained, independent of total pressure, by reducing the CO_2 content of the discharge gas mixture (see Fig. 3-7). However, this also reduces the number density of CO_2 molecules and the stored laser energy. The trade off between these two factors is shown in Fig. 7-5. The output energy from the 4.3-μm oscillator was measured as a function of CO_2 content in the gas mixture for a discharge pressure of 60 Torr. The

FIGURE 7-4

Measured and calculated 4.3-μm pulse energies as a function of T_3. The values of T and T_1 range from 328 and 350 K (at T_3=2080 K) to 390 and 420 K (at T_3=2900 K). See text for details of the calculation.

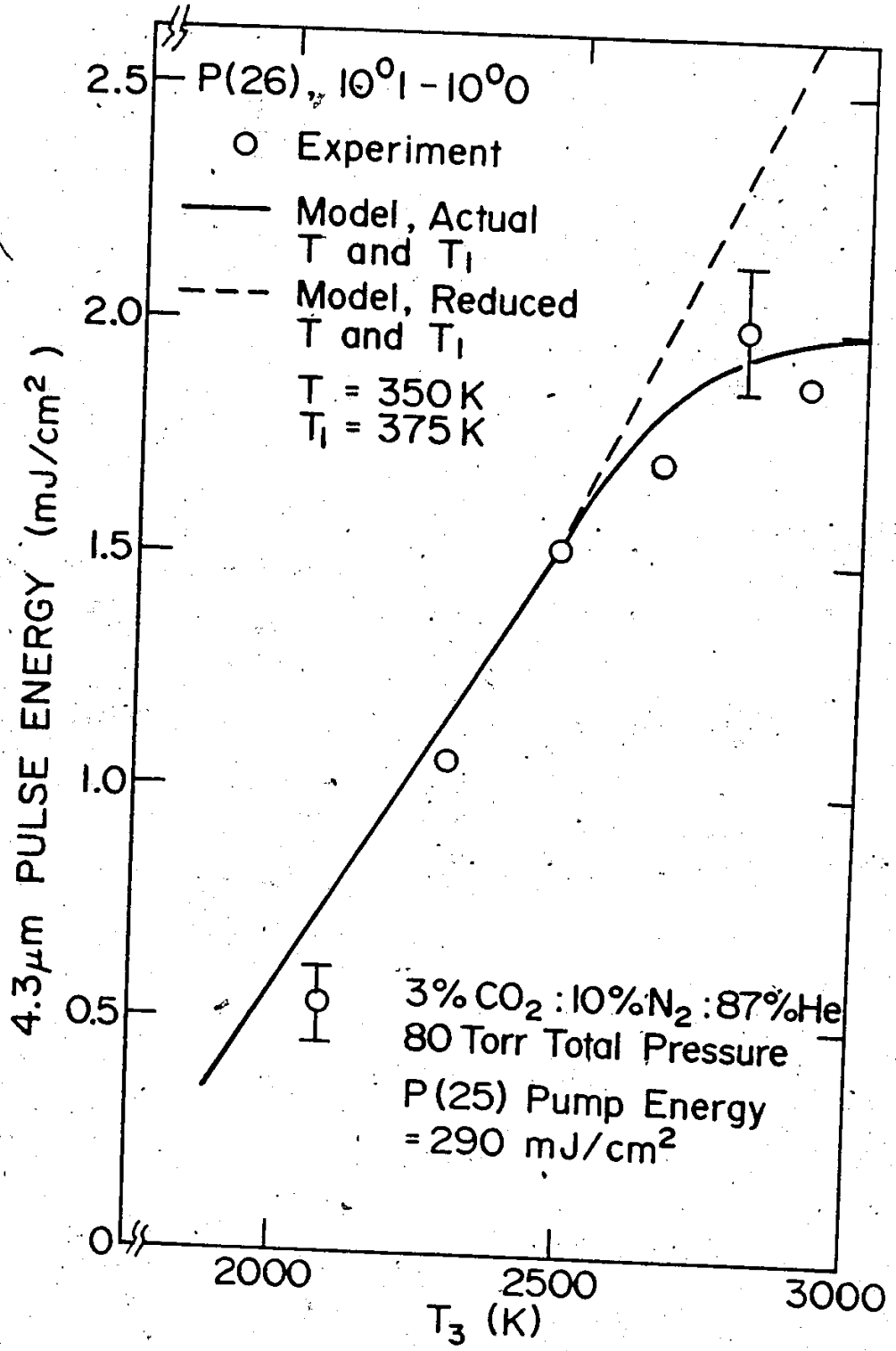
P(26), $10^0 1 - 10^0 0$
Experiment
Model, Actual T and T_1
Model, Reduced T and T_1
T = 350 K
T_1 = 375 K
3% CO_2 : 10% N_2 : 87% He
80 Torr Total Pressure
P(25) Pump Energy
= 290 mJ/cm²
4.3μm PULSE ENERGY (mJ/cm²)
T_3 (K)
0
0.5
1.0
1.5
2.0
2.5
2000
2500
3000

FIGURE 7-5

Measured and calculated 4.3-μm pulse energy as a function of CO_2 content of the discharge. See text for details of the calculation.

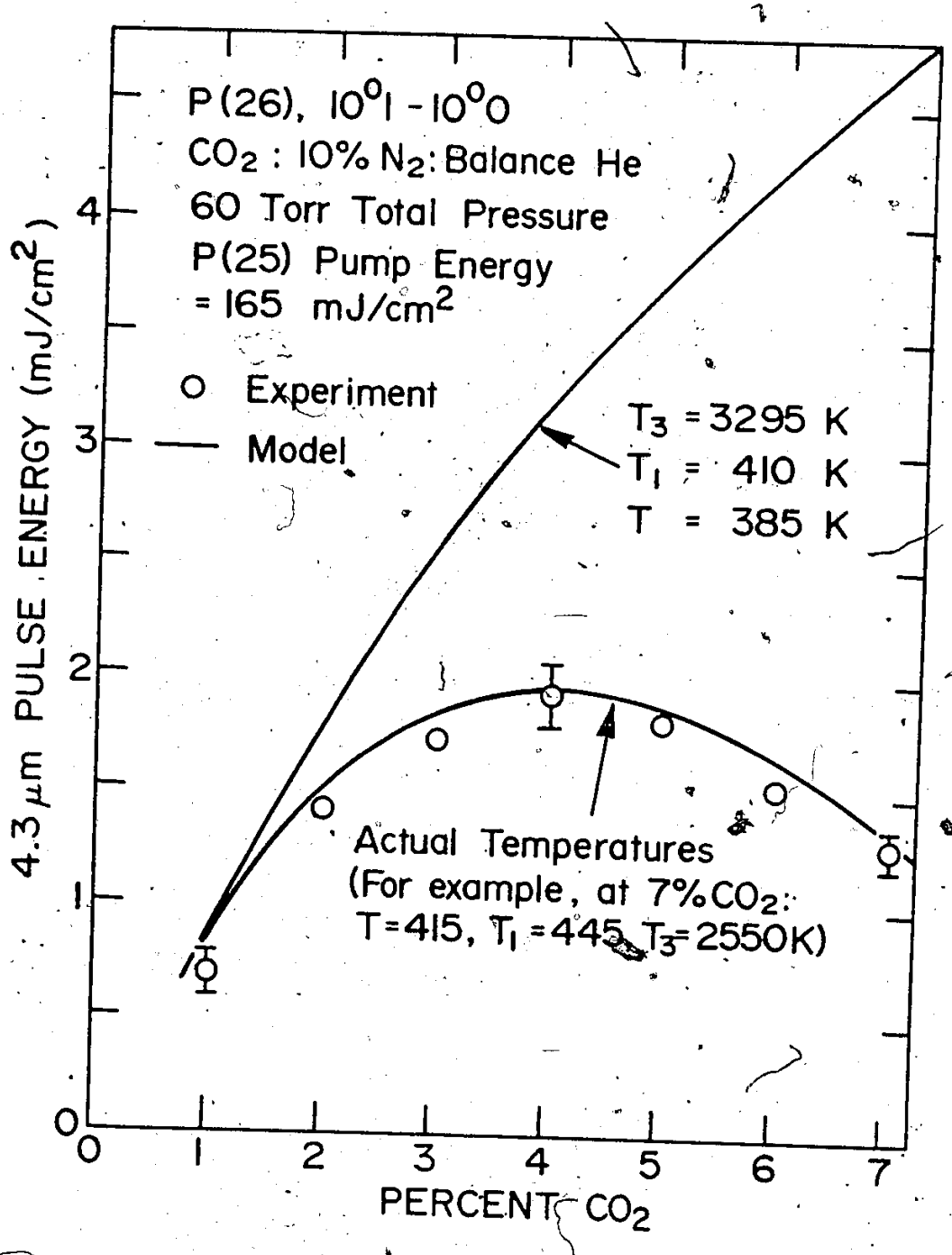
P(26), $10^0 1 - 10^0 0$
CO_2 : 10% N_2: Balance He
60 Torr Total Pressure
P(25) Pump Energy
= 165 mJ/cm^2
O Experiment
— Model
T_3 = 3295 K
T_1 = 410 K
T = 385 K
Actual Temperatures
(For example, at 7% CO_2:
T=415, T_1 = 445, T_3 = 2550K)
4.3 μm PULSE ENERGY (mJ/cm^2)
PERCENT CO_2
0
1
2
3
4
5
6
7

measured discharge temperatures were used as input to the model, and as Fig. 7-5 shows, very good agreement was obtained between calculation and experiment. In constrast, the upper curve in Fig. 7-5 is calculated for fixed discharge temperatures corresponding to the conditions measured for 1 % CO_2. The difference between the two calculated curves clearly illustrates the limitations in energy extraction which occur due to the decrease in T_3 associated with increasing CO_2 content. If this decrease in T_3 could be avoided, optimum mixtures would contain >10 % CO_2. However, the saturation of T_3 imposed by electron de-excitation in self-sustained discharges (see Sect. 2.3) results in maximum experimental 4.3-μm energy occurring for a CO_2 content of 4%.

Another factor which limits the energy available from a 4.3-μm laser is the presence of interfering absorptions in the CO_2 discharge. These are discussed in the next section.

7.4.2 Interfering Absorptions

The experimental results presented so far were obtained by operating the 4.3-μm laser on the ($10^0 1$-$10^0 0$) P(26) line. Operation on other 4.3-μm laser lines always produces lower output energy. The lower energy is primarily a result of interfering absorptions which are caused by the CO_2 in the discharge gas mixture. Every vibrational energy level of CO_2 has an associated absorption band in the 4.3-μm region. In unexcited CO_2, only the lowest energy levels are significantly populated. However, in discharge excited CO_2 many higher lying levels become populated, resulting in many additional absorption lines. This effect is illustrated in the inset of Fig. 7-6, which shows a tunable

FIGURE 7-6

Pressure dependence of measured and calculated absorption coefficients for the P(24) and P(26) 4.3-μm laser lines in a discharge. The experimental discharge temperatures were approximately T=410 K, T_1=450 K, and T_3=2700 K (the temperatures varied with pressure). Details of the calculation are given in the text. The inset shows a tunable diode laser scan of the region around P(26) in a low pressure CO_2 gas mixture.

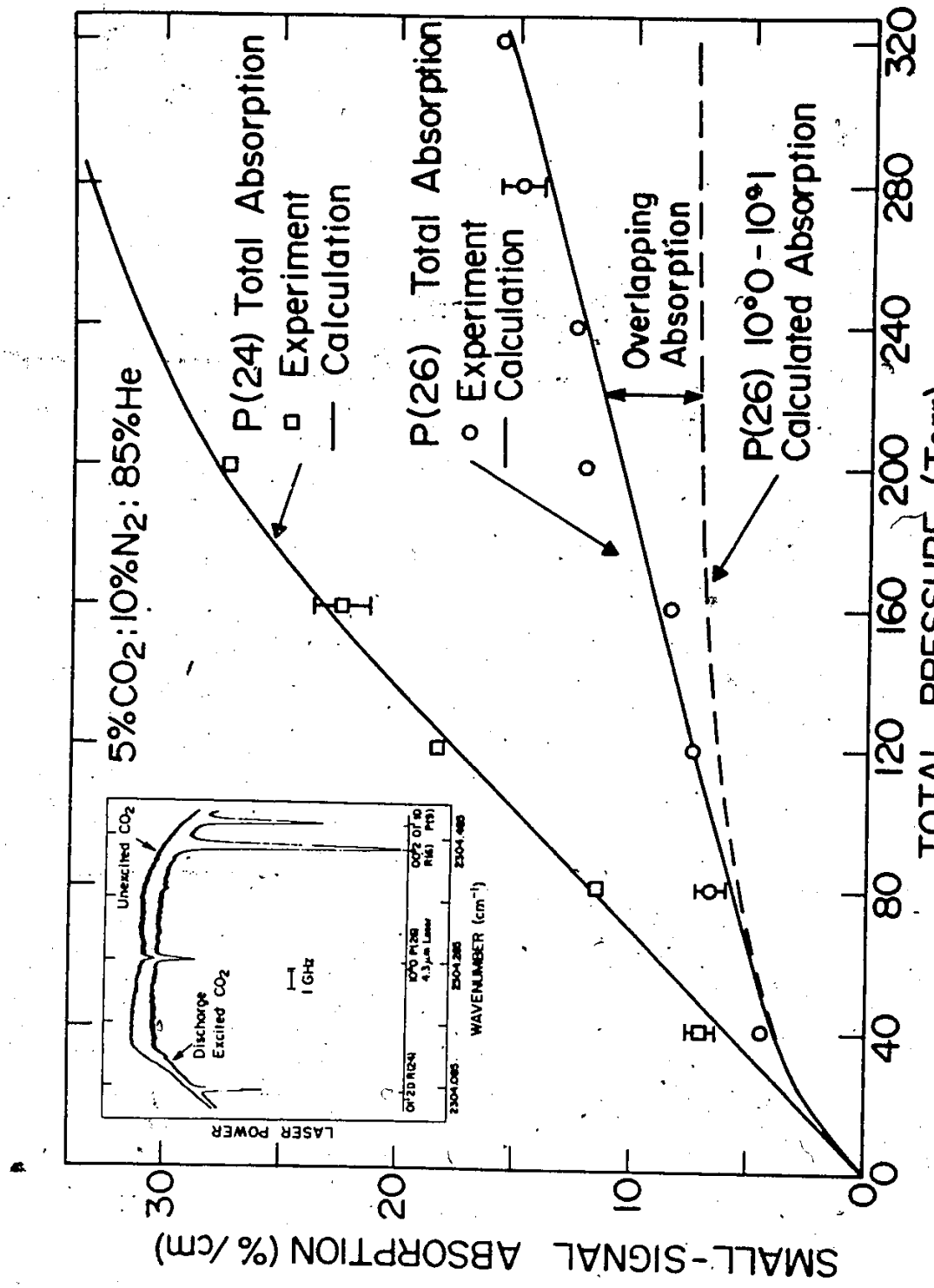
SMALL-SIGNAL ABSORPTION (% /cm)
TOTAL PRESSURE (Torr)
5%CO2:10%N2:85%He
P(24) Total Absorption
Experiment
Calculation
P(26) Total Absorption
Experiment
Calculation
Overlapping Absorption
P(26) 10°0-10°1 Calculated Absorption
Unexcited CO2
Discharge Excited CO2
1 GHz
LASER POWER
WAVENUMBER (cm-1)

diode laser scan taken near the P(26) 4.3-μm laser line in both an unexcited low pressure gas mixture and in the presence of a CW discharge. Note the three absorption lines which appear as a result of the discharge. The situation is similar in the pulsed 4.3-μm oscillator, but the gas is at much higher pressure. As a consequence, the absorption lines become pressure broadened and overlap nearby 4.3-μm laser lines. Small-signal absorption coefficients have been measured on several of the 4.3-μm laser lines.‡ Typical results are shown in Fig. 7-6. The magnitude of the overlapping absorption was calculated by considering 70 different bands in CO_2 in the 4.3-μm region and assuming the individual lines have a Voigt profile. The best available spectroscopic constants [78,143,162-164] and the theory of Sects. 2.5 and 2.6 were used in the calculation, together with the measured discharge temperatures (T, T_1, and T_3). Figure 7-6 shows a comparison of the measured and calculated absorption coefficients. There is good agreement over a wide range of pressure for both P(26) (affected little by overlapping absorption) and P(24) (significant overlapping absorption). Also shown in Fig. 7-6 is the absorption due to the P(26) laser transition alone. This absorption turns into gain in the presence of a sequence pump pulse; the additional absorption shown in Fig. 7-6 is due to overlap from nearby lines. Since it is generally the Lorentzian wings of these nearby lines which overlap the laser transitions, the absorption tends to be nonsaturable, and increases as the square of the

‡ The absorption coefficients at 4.3 μm were measured using the apparatus and procedure described in Chapt. 5 for small-signal gain measurements, except that the discharge-excited CO_2 gas mixture was not optically pumped by a sequence pulse.

discharge pressure. As a result, the output coupling for 4.3-μm lasers must be very large (~90 %) to minimize losses to this nonsaturable absorption, and the total discharge pressure cannot be increased much above 100 Torr without a significant loss of efficiency.

The reduction in 4.3-μm output energy with increased overlapping absorption was investigated experimentally. Output energy was measured on both the P(24) and P(26) 4.3-μm lines as a function of sequence pump energy at a discharge pressure of 80 Torr. Both lines were directly pumped, using the 10.4-μm P(23) and P(25) transitions, respectively. The results are plotted in Fig. 7-7. The P(24) pulse energies are significantly smaller than those measured for P(26) because P(24) suffers from a much larger overlapping absorption. Also shown in Fig. 7-7 is the pulse energy predicted by the model, including a calculation for P(26) where the overlapping absorption α has been set equal to zero. The difference between this calculation and that which uses the correct overlap indicates that ~20 % of the 4.3-μm photons are lost to the absorption, even though α is very small (0.18 %/cm) compared with the small-signal gain (~10 %/cm). This result is in agreement with calculations describing a similar situation in excimer lasers [165].

The method that has been used to calculate the loss of energy to the overlapping absorption is as follows. The rate-equation model is a point model, i.e., it assumes that the 4.3-μm intensity and gain saturation are uniform throughout the discharge. Hence, it has been assumed that the 4.3-μm photon creation per unit volume is uniform throughout the discharge. This uniform distribution of photons then exits at one end of the cavity in the presence of a nonsaturable

FIGURE 7-7

Measured and calculated 4.3-μm pulse energy on the P(24) and P(26) lines as a function of the sequence pump energy. The discharge temperatures are T=390 K, T_1=420 K, and T_3=2900 K. The large difference in output energy between P(24) and P(26) is due to the difference in overlapping absorption α.

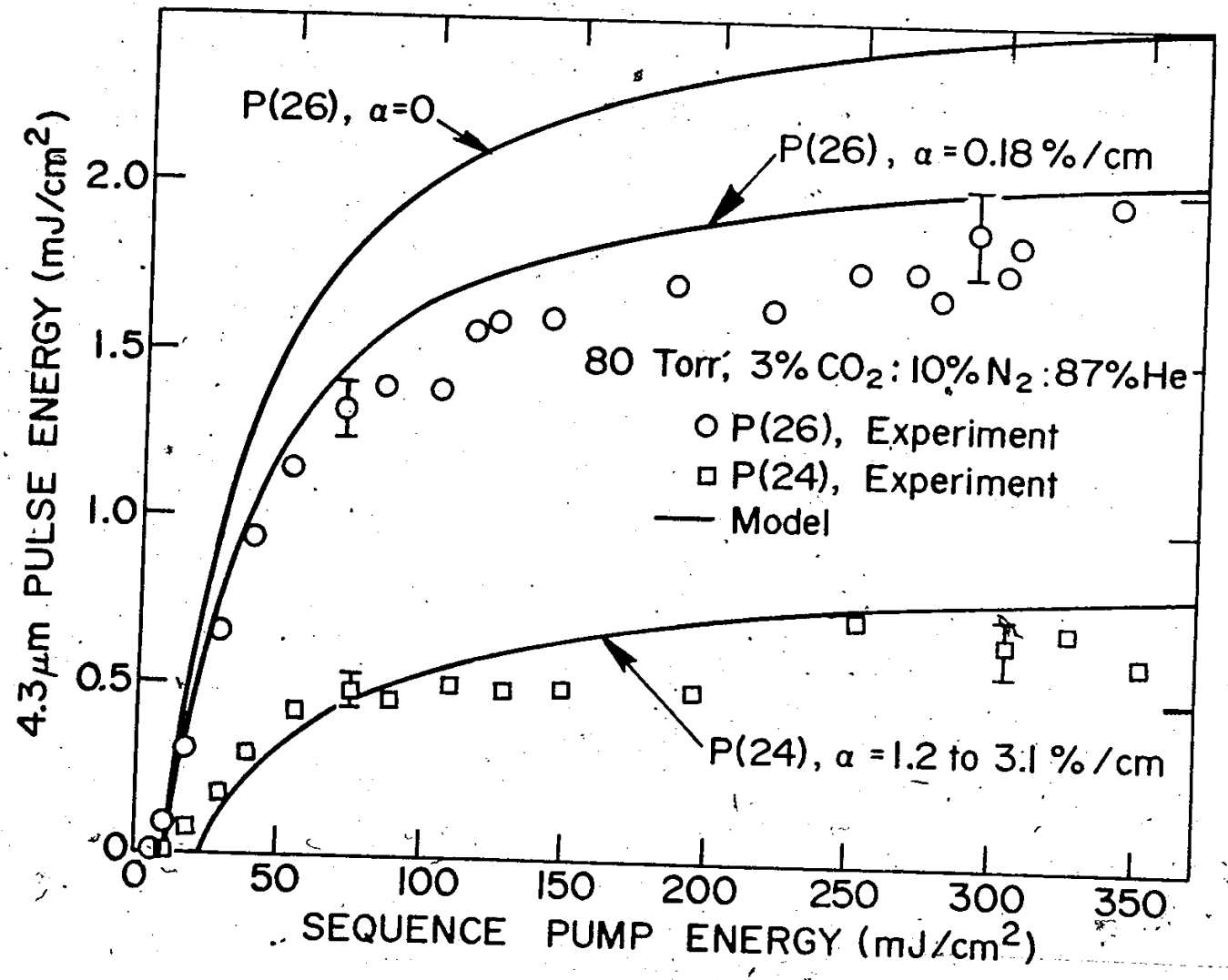
P(26), α=0
P(26), α = 0.18 %/cm
80 Torr, 3% CO2 : 10% N2 : 87% He
P(26), Experiment
P(24), Experiment
Model
P(24), α = 1.2 to 3.1 %/cm
4.3μm PULSE ENERGY (mJ/cm2)
SEQUENCE PUMP ENERGY (mJ/cm2)
0
0.5
1.0
1.5
2.0
50
100
150
200
250
300
350

absorption α in the discharge. The fraction of photons which are not absorbed, and thus give useful output, is given by:

$$\eta = \frac{(1-R)\,[1-\exp(-2\alpha\ell)]}{2\alpha\ell\,[1-R\,\exp(-2\alpha\ell)]}, \tag{7-9}$$

where ℓ is the discharge length. This equation is derived in Appendix C. The output pulse energy from the model is obtained by integrating the 4.3-μm stimulated emission term $\sigma_4\delta_4\rho_4 c$ of Eq. (7-8) over time, and multiplying by η and $h\nu_3$. This manner of calculating pulse energy gives good agreement with experiment, as shown in Fig. 7-7, for both P(26) and P(24).‡ (In Chapt. 4, a simpler method was used to account for hot cell losses in the sequence laser cavity (see Eq. (4-12)). In that case, the output coupling loss per pass was small and it could be treated as a uniformly distributed loss over the cavity length. In contrast, the output coupling is generally large in 4.3-μm lasers (~90 %). Thus, the output coupling loss cannot be considered as a uniformly distributed loss, and Eq. (7-9) must be used to calculate the energy extraction efficiency.)

To determine the optimum value of output coupling for the 4.3-μm laser, the variation in pulse energy with cavity reflectivity was measured. The results for the P(24) and P(26) lines (both directly pumped) are shown in Fig. 7-8. The discharge was operated with a

---

‡ The small-signal value of the overlapping absorption on P(24) cannot be considered nonsaturable because one of the overlapping lines has a very small frequency offset from P(24). Calculations indicate that the saturated value of the overlapping absorption ranges from a minimum of 1.2 %/cm to the unsaturated value of 3.1 %/cm, and the appropriate values have been used in the calculations of Fig. 7-7.

FIGURE 7-8

Measured and calculated 4.3-μm pulse energy as a function of cavity reflectivity. The calculated energies are scaled by 0.87 to agree with the measured P(26) energy at a reflectivity of R=0.07. The overlapping absorption values used in the calculation for P(24) and P(26) were 1.24 %/cm and 0.18 %/cm, respectively. The discharge temperatures are given in the caption to Fig. 7-7.

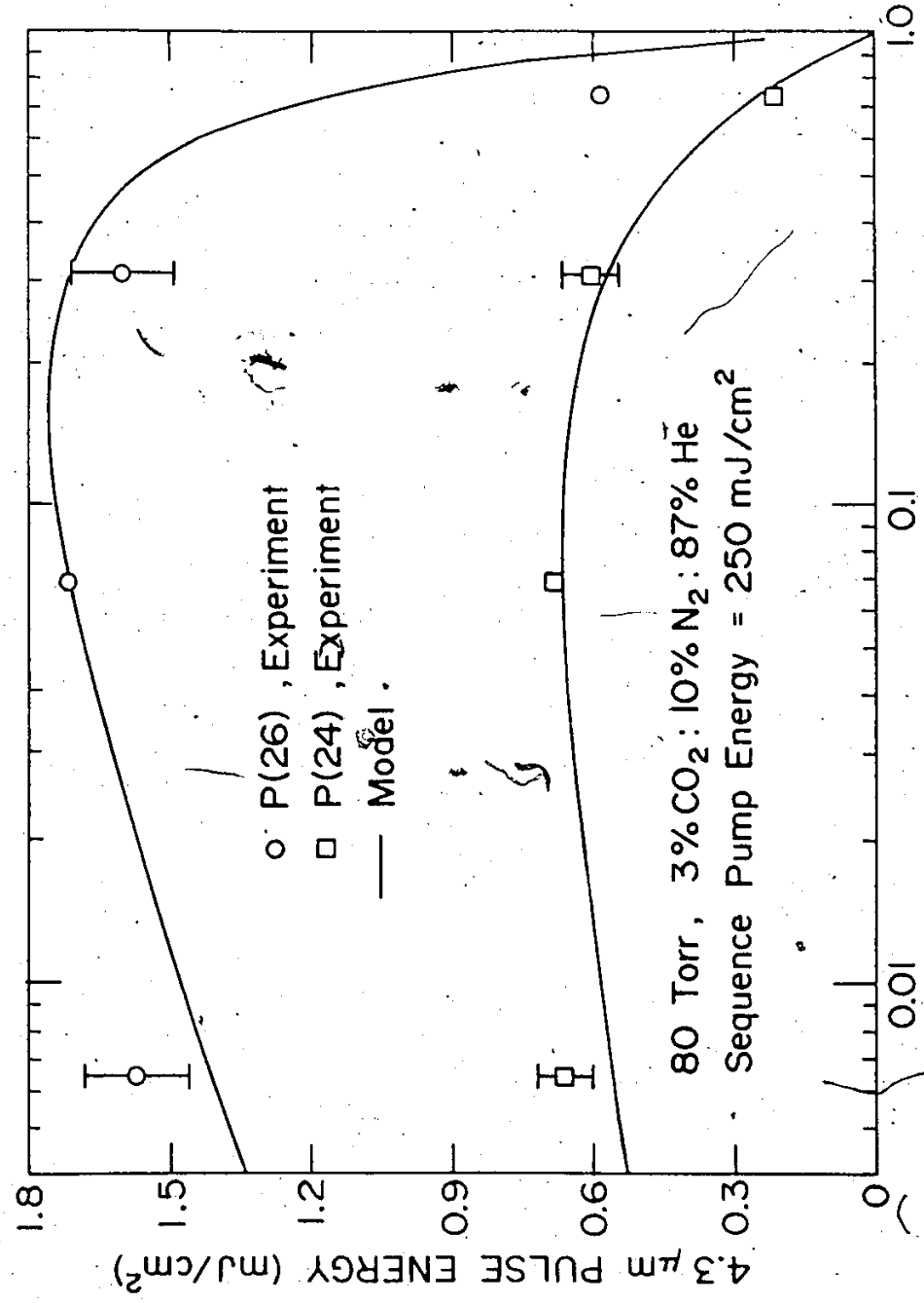
4.3 μm PULSE ENERGY (mJ/cm²)
1.8
1.5
1.2
0.9
0.6
0.3
0
0.01
0.1
1.0
CAVITY REFLECTIVITY
o P(26), Experiment
□ P(24), Experiment
— Model
80 Torr, 3% CO₂ : 10% N₂ : 87% He
Sequence Pump Energy = 250 mJ/cm²

3% CO_2: 10% N_2: 87% He gas mixture at 80 Torr, and a sequence pump energy of 250 mJ/cm^2 was used. The measured pulse energies represent the total output from both ends of the 4.3-μm oscillator.‡ Due to the high gain of the 4.3-μm system (see Chapt. 5), lasing was easily obtained with a very low-reflectivity cavity consisting of two uncoated NaCl flats. A slight increase in output energy was obtained by using the cavity configuration of Fig. 7-2, i.e., one dichroic mirror and one NaCl flat. Further increases in cavity reflectivity significantly reduced the pulse energy, as Fig. 7-8 shows. The sharp decrease in output energy with increased reflectivity is a consequence of the nonsaturable absorption in the discharge. As the reflectivity increases, the average time spent by a photon in the cavity increases and the probability of the photon being absorbed increases accordingly. The variation of output energy with cavity reflectivity is reasonably well predicted by the model for both P(24) and P(26), which have very different values of overlapping absorption. This agreement provides further validation of the energy extraction formula given by Eq. (7-9). The optimum output coupling is ~90 % in both cases (i.e., R=0.1). The experimental value of output coupling which is closest to optimum corresponds to the dichroic-mirror/NaCl-flat cavity. This cavity configuration was therefore used for all other measurements.

The performance of a line-tunable 4.3-μm laser is strongly affected by overlapping absorptions. However, the available pump energy

---

‡ All of the pulse energy measurements presented in this chapter represent the total output from both ends of the cavity. However, for the dichroic-mirror/NaCl-flat cavity of Fig. 7-2, 95 % of the output energy is transmitted by the NaCl flat.

and gain of the pump transition (relative to the peak of the rotational distribution) are also important. The highest 4.3-μm pulse energy has been obtained on the P(26) ($10^0$1-$10^0$0) line, both in this study and by others [6,7,11], primarily due to the small overlapping absorption on P(26). By expanding the sequence pump pulse to fill the aperture of the 4.3-μm oscillator, P(26) pulse energies of ~15 mJ were obtained with a 4% CO_2: 10% N_2: 86% He gas mixture at 60 Torr. Figure 7-9 shows the 4.3-μm pulse energy measured on P(26) as a function of sequence pump energy from both the full aperture and from only the central 6 cm^2. Model calculations are in good agreement with the pulse energies measured from the central 6 cm^2, where the discharge excitation, sequence intensity, and 4.3-μm intensity are reasonably uniform. The 4.3-μm pulse shape from the full aperture is shown in the inset oscilloscope photograph of Fig. 7-2.‡ To investigate line tunability, the 4.3-μm oscillator was tuned through several lines in both 4.3-μm bands (i.e., the ($10^0$1-$10^0$0) band and the ($02^0$1-$02^0$0) band) by grating tuning the pump laser.‡‡ Output energies were measured and the results are presented in Tables 7-1 and 7-2. Since the 4.3-μm oscillator was not grating tuned, laser action occurred on the directly-pumped line

---

‡ The 4.3-μm pulse of Fig. 7-2 is of longer duration than that shown in Fig. 7-3 because of nonuniformities in the excitation and optical pumping of the full discharge aperture. This in turn causes a variation in the timing of 4.3-μm emission over the area of the aperture, and hence an apparent lengthening of the pulse.

‡‡ The pump laser was tuned through only the P branches of the 9.4- and 10.4-μm sequence bands, because all P- and R-branch 4.3-μm lines can be directly pumped in this manner. In addition, the higher P-branch sequence gain (relative to the R branch) in both the pump laser discharge and the 4.3-μm discharge is beneficial to performance.

FIGURE 7-9

Measured pulse energy on the P(26) line from the full-aperture 4.3-μm oscillator as a function of sequence pump energy. The measured output from the central 6 cm^2 of the aperture is also shown, and is compared with the rate-equation model.

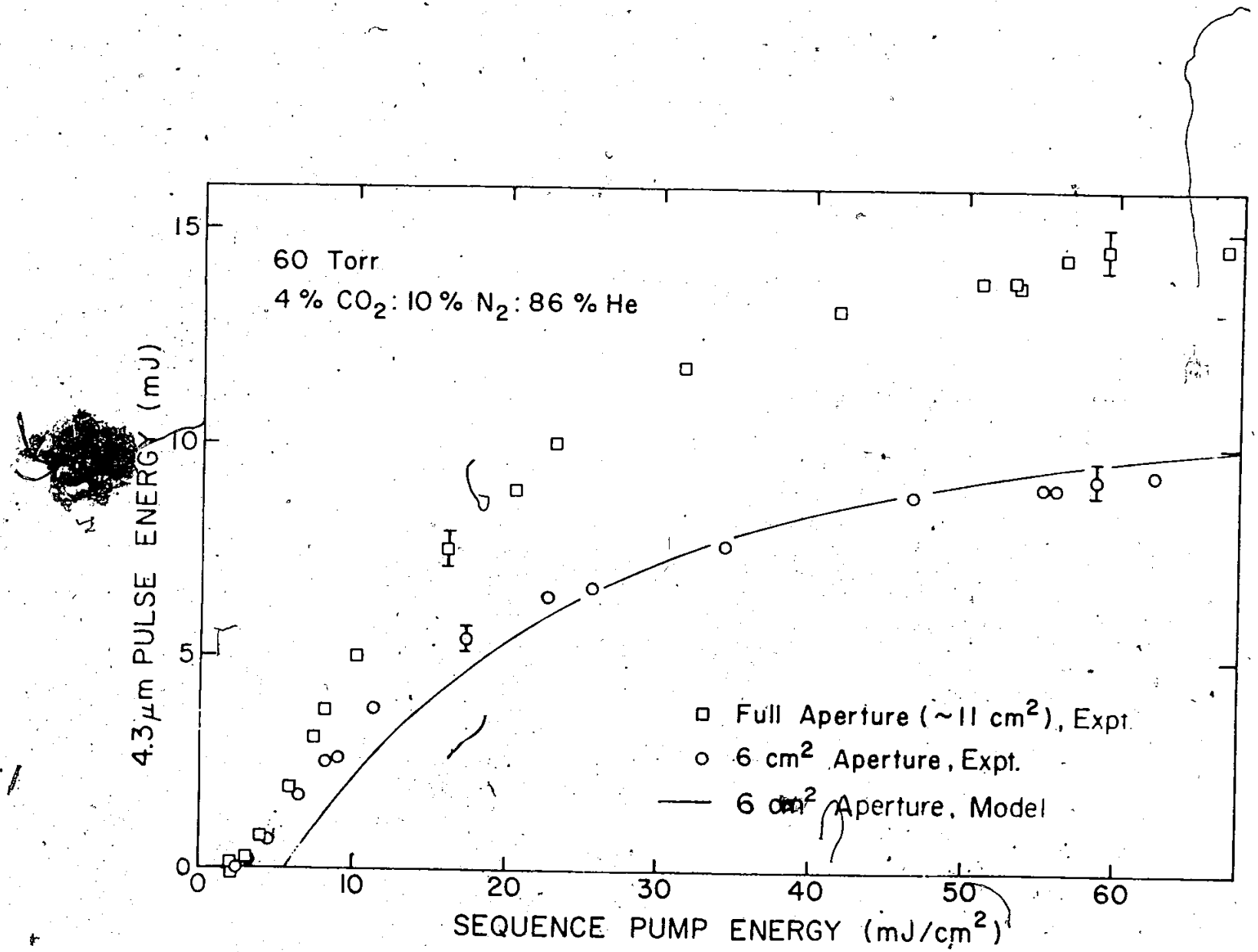
60 Torr
4 % CO_2 : 10 % N_2 : 86 % He
4.3μm PULSE ENERGY (mJ)
SEQUENCE PUMP ENERGY (mJ/cm²)
Full Aperture (~11 cm²), Expt.
6 cm² Aperture, Expt.
6 cm² Aperture, Model
0
5
10
15
0
10
20
30
40
50
60

TABLE 7-1

Measured pulse energy on 4.3-μm laser lines of the 10.4-μm pumped, ($10^0 1$-$10^0 0$) band. The 40 and 60 Torr gas mixtures contained 5 and 4 % CO_2 respectively, with 10 % N_2 and the balance He.

10.4-μm Pump		4.3-μm Output		Calculated Overlapping Absorption (%/cm)		Measured 4.3-μm Energy (mJ) [c]	
Line	Energy [a] (mJ/cm^2)	Line	Frequency [b] (cm^{-1})	40 Torr	60 Torr	40 Torr	60 Torr
P(13)	140	P(14)	2315.10525	0.65	1.10		0.1
		R(12)	2336.17322	0.28	0.44		0.3
P(15)	150	P(16)	2313.36384	0.36	0.59	2.7	2.4
P(17)	150	P(18)	2311.59761	1.42	1.66		2.3
		R(16)	2338.90594	0.30	0.44		1.5
P(19)	140	P(20)	2309.80658	0.44	0.70	9.0	8.3
P(21)	130	P(22)	2307.99077	0.46	0.54		7.8
		R(20)	2341.53792	0.08	0.14		2.0
P(23)	130	P(24)	2306.15022	1.56	2.55	5.7	4.8
P(25)	125	P(26)	2304.28494	0.07	0.13	12.0	15.0
P(27)	80	P(28)	2302.39497	0.05	0.09		7.6
		R(26)	2345.29668	0.13	0.25		1.5
P(29)	75	R(28)	2346.49907	0.07	0.12		2.8
P(31)	55	R(30)	2347.67616	0.57	0.89		0.1

a) Measured over the central 1 cm^2 of the input aperture to the 4.3-μm oscillator.

b) Ref. [143].

c) Uncertainty in the measurements is ± 10 %

TABLE 7-2

Measured pulse energy on 4.3-μm laser lines of the 9.4-μm pumped $(02^{0}1-02^{0}0)$ band. The gas mixture contained 5% CO_2: 10% N_2: 85% He.

9.4-μm Pump		4.3-μm Output		Calculated Overlapping Absorption (%/cm)	Measured 4.3-μm Energy (mJ) [c]
Line	Energy [a] (mJ/cm^2)	Line	Frequency [b] (cm^{-1})	40 Torr	40 Torr
P(15)	40	P(16)	2314.22514	0.16	1.0
P(17)	70	P(18)	2312.46766	0.29	2.0
P(19)	70	P(20)	2310.68662	0.12	3.4
P(21)	70	P(22)	2308.88203	0.32	1.8
		R(20)	2342.45100	0.27	0.2
P(23)	75	P(24)	2307.05393	1.32	1.0
P(25)	55	P(26)	2305.20235	0.20	3.0
P(27)	45	P(28)	2303.32730	0.44	1.5
P(29)	40	P(30)	2301.42883	0.24	2.2
P(31)	40	P(32)	2299.50696	0.12	2.5
P(33)	50	P(34)	2297.56171	0.58	0.5
		R(32)	2349.83920	0.18	0.1
P(35)	60	P(36)	2295.59311	0.23	1.5
P(37)	60	P(38)	2293.60119	0.48	0.7

a) Measured over the central 1 cm^2 of the input aperture to the 4.3-μm oscillator.

b) Ref. [143].

c) Uncertainty in the measurements is ± 10 %.

with the highest net gain. This was generally a P-branch line, although in some cases both a P-branch and an R-branch line, or only an R-branch line would lase. (Note that for every sequence pump line, there is a directly-pumped P-branch and R-branch 4.3-μm line.) The 4.3-μm lines were identified with a 0.5-m spectrometer, which was also used to determine the ratio of energy between two lines lasing simultaneously. For most lines, the optimum discharge pressure was 40 Torr with a 5% CO_2: 10% N_2: 85% He gas mixture. Laser action was observed on 28 4.3-μm lines in all. The pulse energies measured in the ($02^0 1$-$02^0 0$) 4.3-μm band were generally low because the 9.4-μm pump pulses had relatively slow risetimes and low energies, and the full aperture of the 4.3-μm oscillator could not be efficiently pumped. Improvements in these areas would lead to improved 4.3-μm pulse energies, and a grating-tuned 4.3-μm oscillator would result in lasing on many additional lines.

7.5 Scalability to Higher Pulse Energy

Increasing the pulse energy of the 4.3-μm CO_2 laser cannot be achieved by simply increasing the CO_2 content and the operating pressure of the discharge. The reasons for this have been discussed above, i.e., the $10^0 1$ lifetime is shortened, T_3 is reduced, and the overlapping absorptions increase. As a result, optimum performance is obtained with a gas mixture of 4% CO_2: 10% N_2: 86% He at 60 Torr. It has also been found that the 4.3-μm pulse energy cannot be increased significantly by increasing the optical pump energy. The output energy on P(26) was measured as a function of sequence pump energy for the optimum discharge

conditions. The pump beam was focussed to provide high pump energy densities and the 4.3-μm output from only the central 1 cm^2 was measured. The results are shown in Fig. 7-10. Also shown is the calculated output energy, which is in excellent agreement with experiment. Note that the output energy saturates with increasing pump energy. This result is common to all discharge operating conditions (see Figs. 7-7 and 7-9). Clearly, increased pulse energies can only be obtained by expanding the pump beam to fill a large discharge aperture. The results of Figs. 7-9 and 7-10 show that 4.3-μm pulse energies of ~1.2 mJ/cm^2 can be obtained from 30-mJ/cm^2 pump pulses, giving a conversion efficiency of 4 %. Measurements using the full aperture of the 4.3-μm oscillator indicate that the output energy scales approximately linearly with aperture size (see Fig. 7-9). By using 3-J pump pulses, which can readily be obtained on the P(25) sequence line (see Fig. 4-10), a 10 x 10 cm^2 discharge aperture could be pumped to obtain 4.3-μm pulse energies of ~100 mJ. The discharge length could be increased without using additional pump energy because the pump pulse is amplified in the discharge. However, the maximum discharge length is limited by the overlapping absorption to approximately one absorption length (i.e., $1/\alpha$) for efficient operation (see Eq. (7-9)).

In Fig. 7-11, an attempt has been made to summarize the performance characteristics of the 4.3-μm laser. Two representative discharge lengths (1 m and 3 m) are chosen, and the 4.3-μm pulse energy and pulse duration are plotted as a function of total discharge pressure. At each pressure, the gas mixture and cavity reflectivity are optimized (representative values are shown). The sequence pump pulse

FIGURE 7-10

Measured and calculated pulse energy on the P(26) 4.3-μm line as a function of the sequence pump energy. Output from the central 1 cm^2 of the aperture was measured. The discharge temperatures are given in the caption to Fig. 7-1.

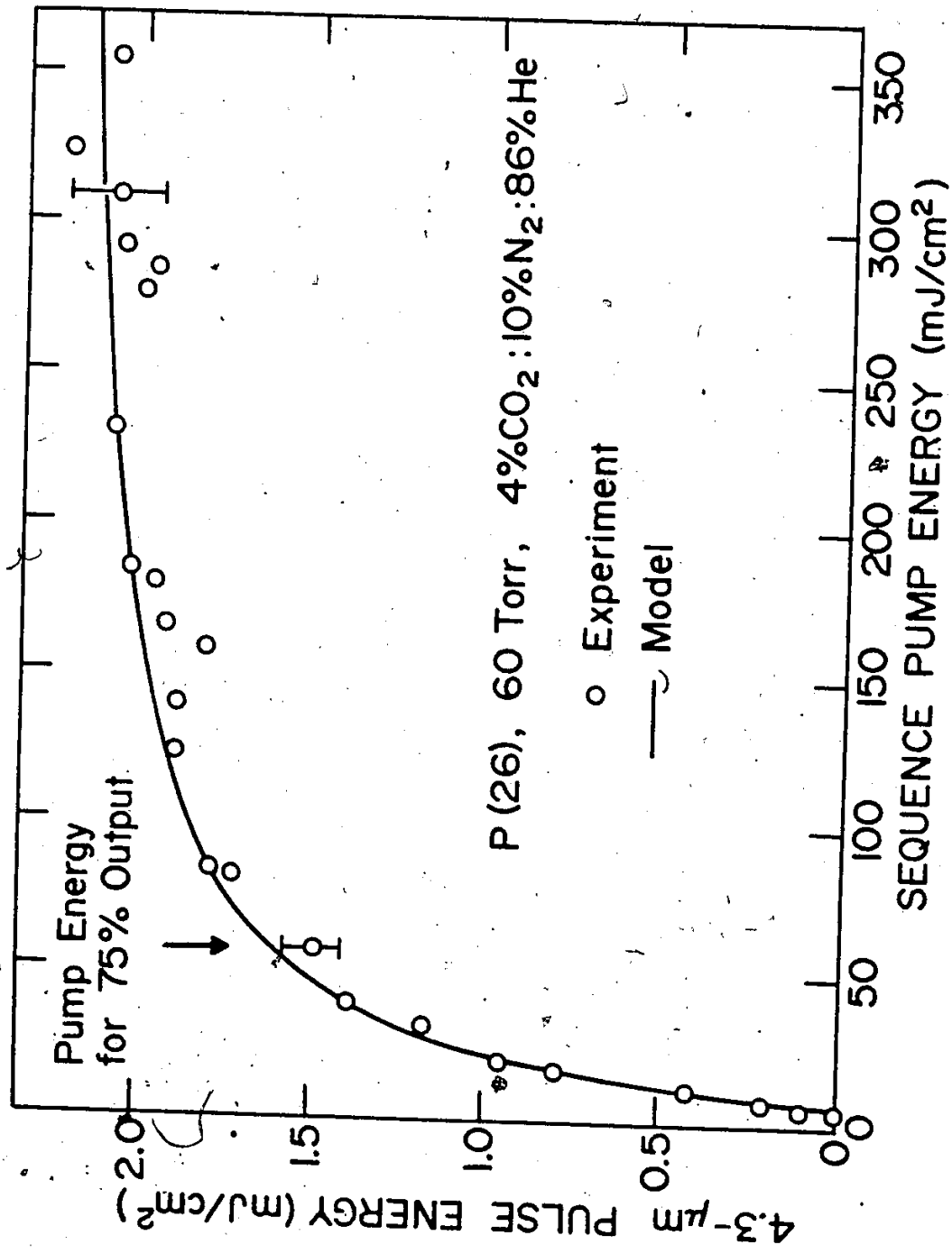
4.3-μm PULSE ENERGY (mJ/cm²)
SEQUENCE PUMP ENERGY (mJ/cm²)
0
0.5
1.0
1.5
2.0
50
100
150
200
250
300
350
Pump Energy
for 75% Output
P(26), 60 Torr, 4%CO2:10%N2:86%He
o Experiment
— Model

FIGURE 7-11

Calculated pulse energy on the P(26) 4.3-μm line as a function of discharge pressure for discharge lengths of 1 m and 3 m. At each pressure, the discharge conditions are optimized and the pump pulse duration (FWHM) is set equal to the $10^{o}1$ lifetime. See text for further details.

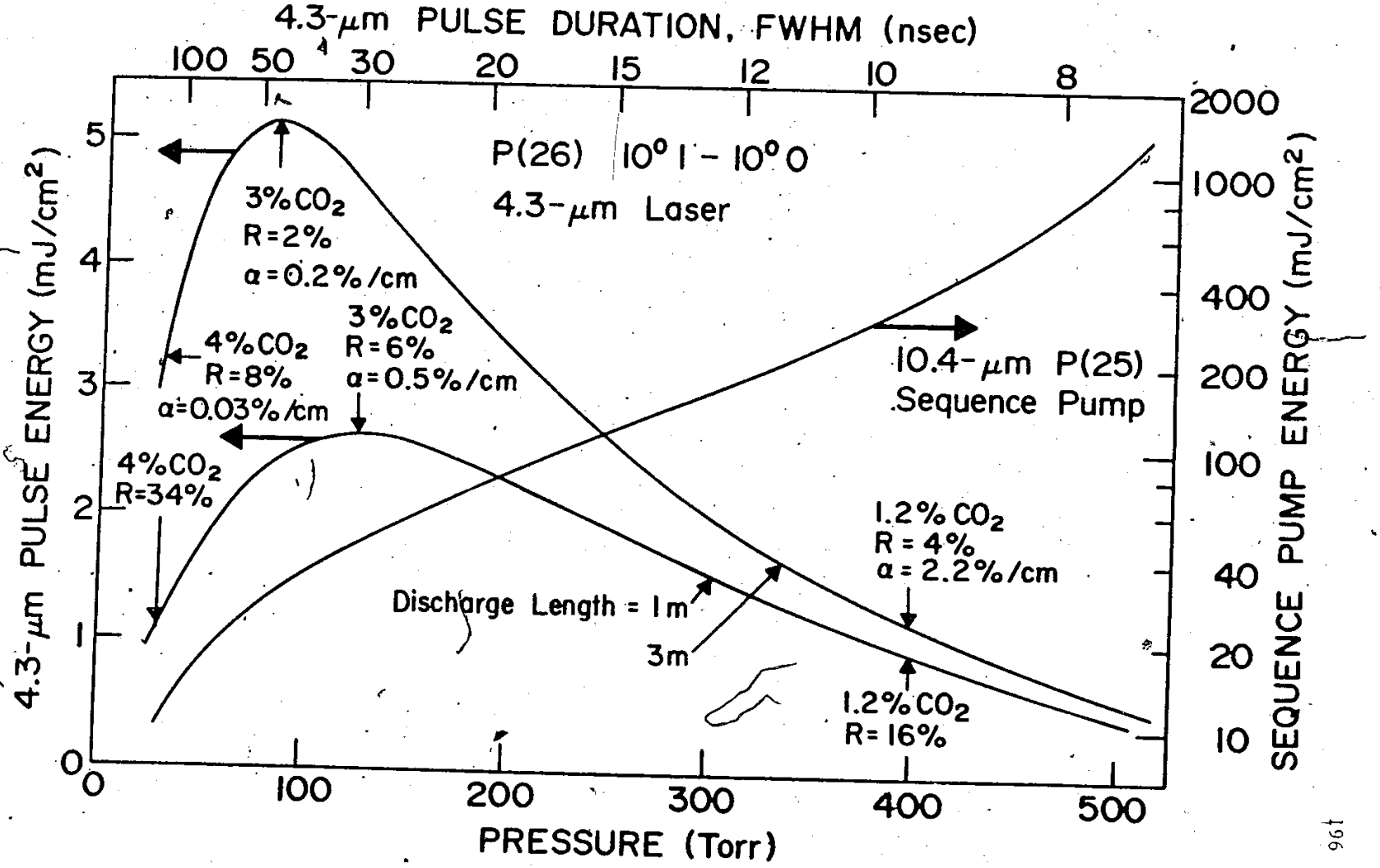
4.3-μm PULSE DURATION, FWHM (nsec)
100 50 30 20 15 12 10 8
P(26) 10°1 - 10°0
4.3-μm Laser
3%CO2
R=2%
α=0.2%/cm
3%CO2
R=6%
α=0.5%/cm
4%CO2
R=8%
α=0.03%/cm
4%CO2
R=34%
10.4-μm P(25)
Sequence Pump
1.2%CO2
R=4%
α=2.2%/cm
Discharge Length = 1m
3m
1.2%CO2
R=16%
4.3-μm PULSE ENERGY (mJ/cm2)
SEQUENCE PUMP ENERGY (mJ/cm2)
PRESSURE (Torr)
0 100 200 300 400 500
0 1 2 3 4 5
2000 1000 400 200 100 40 20 10

input to the calculation has a FWHM equal to the $10^{0}1$ lifetime, and sufficient energy to generate 75% of the saturated 4.3-μm output energy (see Fig. 7-10). Typical 4.3-μm pulses have a FWHM equal to one-half of the pump pulse FWHM.

Under the optimum conditions illustrated in Fig. 7-11, a 3-m discharge has a conversion efficiency of 35% at 30 Torr. This efficiency drops to 17% at 85 Torr, but a 4.3-μm pulse energy of 5 mJ/cm^2 is obtained for an input pulse energy of 30 mJ/cm^2. Thus a 10 cm x 10 cm aperture will give a 500-mJ output pulse from a 3-J input pulse. Further increases in discharge pressure result in reduced performance for all discharge lengths, and require very short and intense sequence pump pulses. This prediction is in agreement with the experimental observations of Bertel et al. [11] who found that 4.3-μm lasing ceased at discharge pressures greater than 400 Torr. However, in Ref. [11] the poor performance at high pressure was attributed only to the risetime of the sequence pump pulse being too slow for the high pressure conditions. In contrast, the present results show that overlapping absorptions are largely responsible for the reduced output energy and efficiency at high pressure. Thus, discharge operation at high pressure does not appear very promising even if very short and intense sequence pump pulses are utilized.

7.6 Simplified Cavity Design

The experimental arrangement for the 4.3-μm laser described in this chapter consists of a separate pump laser and 4.3-μm oscillator, as shown in Fig. 7-2. This is the most convenient setup for making

parametric studies of the 4.3-μm oscillator and for comparisions with calculations. However, more compact cavity configurations are possible in which the sequence and 4.3-μm cavities are combined [12,166]. A combined cavity suitable for pulsed discharge operation has been constructed [139] and is described in this section. The cavity operates with both the 44-cm TEA discharge and the 88-cm low-pressure TE discharge to produce 10-mJ 4.3-μm pulses, or with only the low pressure discharge to produce 1-mJ pulses in a cascade mode.

A cavity arrangement which combines the sequence and 4.3-μm oscillator in the same optical resonator is shown in Fig. 7-12. Gain at 4.3-μm is created in the 88-cm long low pressure discharge. This discharge is common to both the sequence and 4.3-μm cavities. The sequence cavity also contains the 44-cm long TEA discharge, and the 60-cm long hot CO_2 cell described in Sect. 5.3. The dichroic mirror is required to separate the 4.3-μm oscillator from the hot cell and TEA discharge (where large 4.3-μm absorptions are present). The low pressure TE discharge fires first, making the sequence laser a hybrid laser and thus ensuring a good linewidth match between the pump radiation and the low pressure discharge. The main sequence energy is provided by the TEA discharge, and the intracavity configuration results in very high sequence pumping intensities. It was necessary to insert either an SF_6 Q-switching cell or a rotating mirror Q-switch to hold off sequence oscillation until the atmospheric pressure discharge was fired, and to ensure a fast rising sequence pulse. Both the SF_6 cell and the rotating mirror restricted the aperture of the resonator to the central few cm^2.

FIGURE 7-12

Schematic diagram of a simplified cavity arrangement for the 4.3-μm CO_2 laser. Two alternative Q-switching techniques are indicated. The 12-cm long SF_6 cell contains ~1 Torr pure SF_6, while the rotating mirror spins at ~100 Hz.

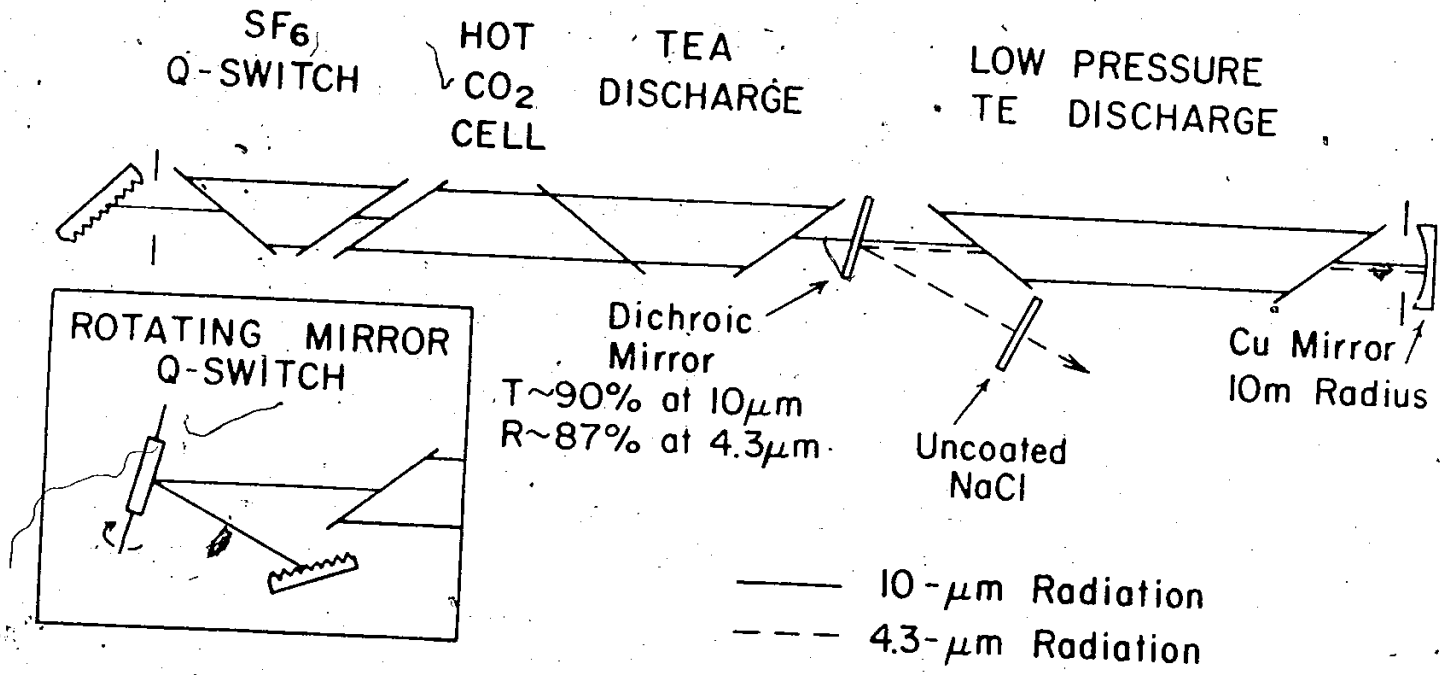
SF_6
Q-SWITCH
HOT
CO_2
CELL
TEA
DISCHARGE
LOW PRESSURE
TE DISCHARGE
ROTATING MIRROR
Q-SWITCH
Dichroic
Mirror
T~90% at 10μm
R~87% at 4.3μm
Uncoated
NaCl
Cu Mirror
10m Radius
10-μm Radiation
4.3-μm Radiation

The two Q-switching techniques gave very similar results in the combined cavity configuration. The sequence laser was tuned to the 10.4-μm P(25) line resulting in 4.3-μm operation on the P(26) line, and the optimum 4.3-μm gas mixture of 4% CO_2: 10% N_2: 86% He at 60 Torr was used. Both the SF_6 cell and the rotating mirror configuration produced 4.3-μm pulses of >2 mJ/cm^2 from the central few cm^2 of the discharge. Maximum pulse energy was ~10 mJ in each case, but would have undoubtedly increased to 15 - 20 mJ if the full discharge aperture was utilized. The SF_6 cell had the advantage of simplicity as electronic synchronization with the discharge was not required. However, the rotating mirror gave slightly better pulse-to-pulse stability. The energy extraction results for the combined cavity (>2 mJ/cm^2) are in agreement with the optimum 4.3-μm energies extracted from the separate cavity configuration (see Fig. 7-10). A further increase in energy extraction is anticipated with the use of a dichroic mirror having greater 10.4-μm transmission.‡

As a final step in simplifying the production of 4.3-μm photons, the TEA discharge was removed from the cavity shown in Fig. 7-12. In its simplest form the cavity now consists of a single low pressure TE discharge, a hot cell, and an SF_6 or rotating mirror Q-switch. The rotating mirror produced 4.3-μm energies of ~1 mJ/pulse, while operation with the SF_6 cell gave erratic output energies of ~0.3 mJ/pulse. The reduction of 4.3-μm energy occurs because the intracavity sequence intensity is now much lower, but this simple cascade laser system may

---

‡ Removal of the present dichroic mirror increases the intracavity sequence intensity by a factor of four.

find application where 4.3-μm pulses of only moderate energy are required.

7.7 Feasibility of 4.5-μm Lasing in N_2O

The pumping scheme described in this thesis for producing 4.3-μm lasing in CO_2 has been used with isotopic $^{13}CO_2$ to obtain 4.4-μm lasing [166,167]. The potential also exists for obtaining different wavelengths by using other molecules which have the appropriate energy level structure. As discussed in Chapt. 3, N_2O has energy levels and laser transitions similar to CO_2, including a regular (00^01-10^00) and sequence (00^02-10^01) laser band centered at 10.7-μm. The possibility exists for 4.5-μm lasing on the (10^01-10^00) band of N_2O by optically pumping discharge excited N_2O with a sequence pulse. An attempt to produce 4.5-μm lasing in N_2O is described in this section. The results of the experiment were negative, i.e., 4.5-μm output was not observed. It is shown that several characteristics of the N_2O system are responsible for the absence of 4.5-μm lasing.

The apparatus described in Sect. 7.3 was used for the 4.5-μm N_2O experiment. However, the pump laser was not operated on the sequence band of N_2O. Instead, it was operated on the 10.4-μm P(42) regular band transition of CO_2. P(42) is offset from the P(16) sequence transition of N_2O by only 40 MHz [92] and thus simulates an N_2O sequence pump line. This is a convenient coincidence, because the performance of sequence N_2O lasers is very poor, and the available output energies [97] are too low to be useful in the present experiment. Figure 7-13 is a simplified energy level diagram of N_2O showing the pump and 4.5-μm transitions.

FIGURE 7-13

Simplified energy level diagram of N_2O showing the transitions relevant to 4.5-μm lasing. The 10.4-μm P(42) regular CO_2 line is offset from the P(16) sequence N_2O line by only 40 MHz [92].

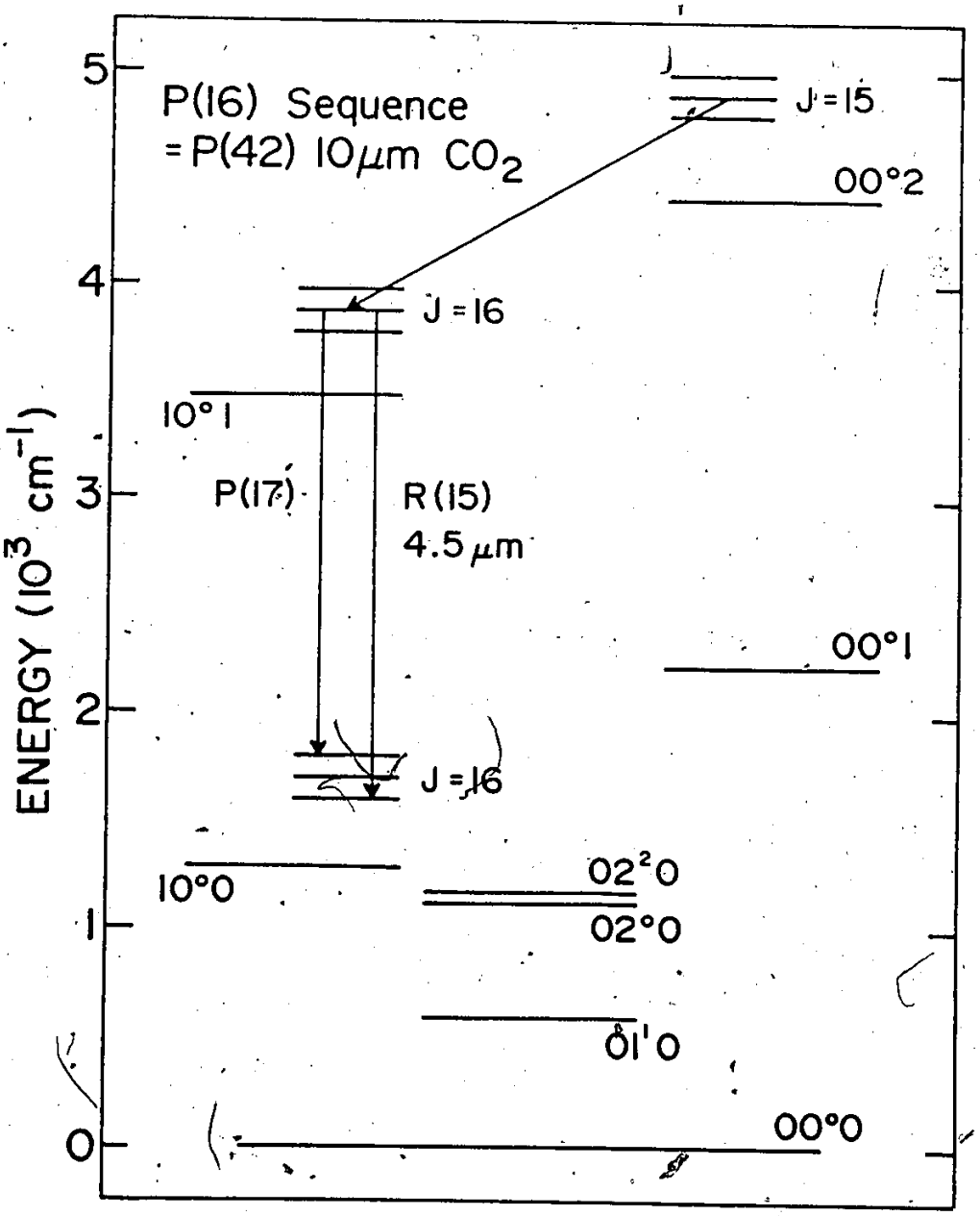
P(16) Sequence
= P(42) 10μm CO_2
J = 15
00°2
J = 16
10°1
P(17)
R(15)
4.5μm
00°1
J = 16
10°0
02²0
02°0
01¹0
00°0
ENERGY (10^3 cm^{-1})
5
4
3
2
1
0

The P(42) pump pulse, of ~2 J/cm^2 energy, directly pumps the P(17) and R(15) 4.5-μm N_2O lines. Calculations using the theory of Ref. [95] indicate that the overlapping absorption is minimal on both of these lines at pressures less than 100 Torr.

The 4.5-μm oscillator consisted of a totally reflecting Cu mirror with a .5-m radius of curvature, and a dichroic mirror. The dichroic mirror acted as an input coupler for the pump radiation, and a high-reflectivity output coupler for the 4.5-μm cavity. A dichroic beam splitter and a Ge:Au detector were used to monitor the output from the 4.5-μm cavity. The discharge in the 4.5-μm oscillator was operated over a range of pressures from 20 to 80 Torr, with various gas mixtures containing up to 3 % N_2O. The gas mixture also contained 15% N_2 and the balance He. In each case, the discharge excitation was optimized as described in Chapt. 3.

Laser oscillation at 4.5-μm could not be obtained under any circumstances. The reasons for this result are best illustrated by comparing the N_2O and CO_2 systems. Recall the comparison of T_3 values in N_2O and CO_2 which was made in Sect. 3.4. For a gas mixture containing 3 % N_2O the maximum attainable T_3 value is ~600 K, compared with 2900 K for CO_2. The influence of T_3 on gain and energy extraction in the 4.3-μm CO_2 laser is illustrated in Figs. 5-7 and 7-4 respectively. Both of these figures show that at the low values of T_3 typically found in discharge excited N_2O (1600 K to 2000 K), 4.3-μm gain and output energy are very low. The same low output could be expected from a 4.5-μm N_2O laser, if all other parameters were equal. However, the N_2O system has several additional disadvantages other than low T_3.

The 4.5-μm transition dipole moment is only 0.25 Debye in N_2O [95], compared to 0.32 Debye in CO_2 at 4.3-μm [78]. N_2O readily dissociates in an electrical discharge; for the gas mixtures used in the present study, it is estimated that 15 to 25 % of the N_2O dissociates [95]. The relaxation of the 10^01 level of N_2O by near-resonant collisions with N_2O molecules is slightly slower than the analogous process in CO_2 [9], and is thus favourable for 4.5-μm operation. However, $N_2O(10^01)$ is more rapidly de-excited by collisions with Ar than is $CO_2(10^01)$ [9], which suggests that N_2 and He are also more effective in de-exciting $N_2O(10^01)$. When all of these factors are considered, especially the low value of T_3, it is not surprising that 4.5-μm lasing was not obtained. Many of the factors described above are also responsible for the poor performance of sequence N_2O lasers. The energy extraction from sequence N_2O lasers is only 0.05 J/ℓ·atm [97], while 5.9 J/ℓ·atm can be obtained from CO_2 sequence lasers (see Chapt. 4). Since many of the same factors optimize sequence and 4.3/4.5-μm operation (especially high T_3), the comparison of sequence operation gives an indication of the comparitive performance to be expected of 4.3-μm CO_2 and 4.5-μm N_2O lasers.

The present experiment should not be interpreted as definitive proof that 4.5-μm lasing in N_2O is unattainable. However, it is clear that a 4.5-μm N_2O laser cannot be expected to perform as well as a 4.3-μm CO_2 laser. If 4.5-μm lasing were to be obtained in N_2O, the output energy and efficiency would be extremely low, chiefly because of the low value of T_3.

7.8 Summary

In this chapter, a detailed study of the energy output characteristics of the pulsed 4.3-μm CO_2 laser is described. A rate-equation model of the laser is presented and validated by comparison with experimental measurements over a wide range of conditions. The factors which dominate the operation of the laser are described. In particular, the short lifetime of the 4.3-μm upper laser level, the degree of discharge excitation, and the presence of interfering absorptions result in an optimum discharge gas mixture of 4% CO_2: 10% N_2: 86% He at 60 Torr in the 4.3-μm oscillator. The maximum measured 4.3-μm output energy is 15 mJ/pulse, and the experimental results show that scalability to several hundred mJ/pulse can be obtained by using a large-aperture discharge. With the present laser, tunability over 28 lines from 4.26 to 4.35 μm is demonstrated. This 4.3-μm CO_2 laser provides a powerful source of coherent radiation in a wavelength region of interest for laser photochemistry, optical pumping, and atmospheric monitoring.

In addition to the detailed 4.3-μm CO_2 laser study, the feasibility of making a 4.5-μm N_2O laser is briefly examined. Laser oscillation could not be obtained at 4.5 μm, and the N_2O system is not very promising in comparison with the 4.3-μm CO_2 laser.

CHAPTER 8

CONCLUSIONS

In this chapter, the important results and conclusions of this thesis are summarized. An overview of the study of 4.3-μm CO_2 laser dynamics is given, and the major results of each chapter and their overall significance are discussed. Finally, applications for 4.3-μm CO_2 lasers are described.

The aim of this work is to provide quantitative data regarding the operation of the 4.3-μm CO_2 laser, so that the pulse energy can be maximized and scalability to higher energy accurately predicted. This task is accomplished through an extensive experimental and theoretical study of 4.3-μm small-signal gain and energy extraction. The results of this study have led to a better understanding of the processes involved in 4.3-μm lasing and a significant improvement in the performance of the laser. In support of the detailed study of 4.3-μm laser dynamics, it was necessary to measure many characteristics of discharge excited CO_2, such as mode temperatures, degree of excitation, collision-broadened linewidths, and overlapping gain and absorption. These measurements provided accurate input data for use in computer modeling of the 4.3-μm dynamics. In addition, a high power sequence band CO_2 laser was designed and built to optically pump the 4.3-μm laser. The major results and conclusions of each chapter are discussed in greater detail below.

Chapter 3 describes in detail the characterization of discharge excited CO_2 in terms of the temperatures T, T_1, and T_3. To determine these temperatures accurately from small-signal gain measurements made in the 9.4- and 10.4-μm bands, a detailed knowledge of gain overlaps and collision-broadened linewidths is necessary. Therefore, gain measurements were made on over 150 lines and the results were used to verify calculated gain coefficients. It was found that the majority of the lines in high pressure CO_2 lasers possess significant additional gain due to overlaps, confirming previous calculations [110]. In addition to gain overlap, the J dependence of the collision-broadened linewidth was found to influence the determination of rotational temperature T. Since no reliable experimental data was available for CO_2 linewidths in He-dominated laser gas mixtures, measurements were made using a novel experimental technique. The technique utilized linecenter and offset probe lasers (CW CO_2 and N_2O lasers, respectively) to measure gain ratios; linewidth was accurately deduced by assuming a Lorentzian lineshape. In this manner, the linewidths of nine transitions from P(2) to P(46) in the 10.4-μm band were determined. These linewidth measurements are the first to be made in a TE CO_2 discharge, and represent the most accurate and extensive measurements available for He-broadened CO_2 linewidths as a function of temperature and rotational quantum number.

A high value of T_3 in a CO_2 laser discharge significantly improves the performance of the laser, particularly a sequence or 4.3-μm laser. In Chapt 3, it is shown that T_3 is maximized by minimizing E/N and maximizing input energy to the discharge. The variation of T_3 with

gas mixture is also investigated. Regardless of the type of discharge excitation (pulsed or CW) and independent of pressure, higher values of T_3 are always obtained with low CO_2 content gas mixtures. This important result has been observed previously [45,46], and is due to the effects of electron de-excitation [41,42]. The results of Chapt. 3 concerning discharge characterization and optimization are important to the study of 4.3-μm laser dynamics and also to many other areas of CO_2 laser research.

Chapter 4 concerns the development of a high power TEA sequence laser. The results show that the hot cell technique is an efficient means of producing TEA sequence lasing, contrary to the conclusions of Ref. [122]. However, proper cavity design is essential and the importance of factors such as hot cell loss and degree of discharge excitation are discussed. Sequence output energies as high as 6 J/pulse are observed from an 88-cm long by 11-cm^2 aperture discharge module, and emission from a grating-tuned cavity includes 54 sequence lines, of which 30 have energies > 2 J/pulse. This sequence laser not only provides a powerful pump source for 4.3-μm CO_2 lasers, but is also ideal for many other applications as discussed in Sect. 4.6.

In Chapt. 5, a detailed experimental and theoretical study of the gain dynamics of the 4.3-μm CO_2 laser is presented. The measured gain coefficients are typically of the order of 10 %/cm, but the gain is generally short lived (a few hundred ns). A single sequence line produces gain on many rotational-vibrational transitions of the ($10^0$1-$10^0$0) 4.3-μm band, enabling line-tunable operation. The rate-equation model which is described in Chapt. 5 uses no variable

parameters, and is validated by comparison with experimental results over a wide range of operating conditions. The parameters which most significantly influence the gain are identified. Discharge excitation is most important, with high values of T_3 being necessary to obtain the maximum gain. The requirement for high T_3 dictates the use of relatively low CO_2 content gas mixtures. In addition, the fast collisional de-excitation of $CO_2(10^0 1)$ and the presence of overlapping absorptions requires the use of low discharge pressures and low CO_2 contents. A maximum small-signal gain of 14 %/cm is obtained with discharge conditions of 40 Torr and 7.5 % CO_2, whereas the stored laser energy is maximized at 80 Torr and 5 % CO_2. The 4.3-μm gain does not increase significantly with pump power once the pump intensity reaches a certain saturation value (100 kW/cm^2 at 40 Torr), suggesting the use of an expanded pump beam and large-aperture 4.3-μm discharge for best efficiency.

The only significant discrepancy between the 4.3-μm small-signal gain model and experiment is the overestimation by the model of the peak gain on directly-pumped 4.3-μm lines. In Chapt. 6, it is shown that this discrepancy is a consequence of the dynamic Stark effect. The intense sequence pump radiation splits the 4.3-μm line and reduces the gain (or absorption) at the line center. Dynamic Stark splitting was observed, without the obscuring effects of population transfer by measuring 4.3-μm small-signal absorption in an unexcited CO_2 gas mixture as a function of sequence pump intensity. A reduction in linecenter absorption by a factor of five was observed. By comparison with theory, an empirical intensity scaling factor was obtained from the absorption

measurements. This factor was used in a modified version of the rate-equation model and better agreement between measured and calculated 4.3-μm gain coefficients was obtained. The results of Chapt. 6 demonstrate the importance of including coherent effects in considerations of directly-pumped transitions, and the same theoretical treatment can be applied to other optically-pumped pulsed laser systems.

A detailed study of energy extraction from a 4.3-μm oscillator is presented in Chapt. 7. The rate-equation model which was validated in Chapt. 5 by comparison with gain measurements is used in Chapt. 7 to calculate 4.3-μm pulse energies. Good agreement is obtained between the model and experiment, and the conditions for optimum performance are identified. In general, the conditions which optimize small-signal gain also optimize energy extraction (i.e., high T_3, low pressure, and low CO_2 content). However, the discharge pressure and CO_2 content which maximize energy extraction are lower than those which maximize stored laser energy. This is because losses to the overlapping absorptions severely limit the amount of stored energy which can be extracted as the discharge pressure and CO_2 content increase. A high value of output coupling (~90 %) is also necessary to minimize losses to the absorptions. Optimization of the operating conditions has resulted in single-line 4.3-μm energies of 15 mJ/pulse from an 88-cm long by 11-cm^2 aperture discharge. This represents a sequence to 4.3-μm energy conversion efficiency of 4 %. Tunability over 28 4.3-μm lines was obtained. Based on experimental results, scalability to 4.3-μm pulse energies of several hundred millijoules is shown to be feasible using a large-aperture discharge (10x10 cm^2) and currently available sequence

pump lasers (i.e., the sequence laser described in Chapt. 4). In an effort to simplify the 4.3-μm laser system, a compact cavity arrangement which combines the sequence and 4.3-μm lasers in the same optical resonator is investigated. Good performance is obtained. Also in Chapt. 7, an attempt to translate the 4.3-μm pumping scheme to the N_2O molecule and produce 4.5-μm lasing is described. However, 4.5-μm lasing was not observed due to the low value of T_3 in discharge excited N_2O.

The 15-mJ 4.3-μm pulses obtained in the present study are useful for many applications. Optical pumping experiments are presently underway in our laboratory using the 4.3-μm pulses to pump high pressure CO_2 (> 1 atm). At sufficiently high pressure (~20 atm), continuously-tunable operation from 9 to 11 μm should be possible. Of greater interest however, is the production of extremely high T_3 values (~5000 K), which may be attainable in the absence of electron de-excitation effects. These investigations will provide greater insight into the efficient excitation of CO_2 lasers.

New wavelengths are constantly in demand for laser isotope separation and laser photochemistry applications, particularly in the mid-infrared region where few lasers operate. Pulse energies as low as one millijoule are sufficient for many laboratory studies in these fields [154]. The 4.3-μm CO_2 laser described in this thesis, which provides pulse energies > 1 mJ on 21 lines, should prove useful in such applications. In addition, isotopic CO_2 could be used to increase the number of available wavelengths. Already, 4.4-μm operation on several lines has been demonstrated using isotopic $^{13}CO_2$ [166,167]. The 4.4-μm CO_2 laser is well suited to atmospheric monitoring applications, because

the output is shifted away from the strong absorption at 4.3-μm due to atmospheric CO_2, and there are few other atmospheric constituents which absorb in this wavelength region.

The results presented in this thesis enable one to maximize the pulse energy of a 4.3-μm CO_2 laser. The work is restricted to low repetition rate operation using TE discharges. However, the results apply equally to high repetition rate Q-switched operation using CW discharges [12], and operation using isotopic CO_2 [166,167]. The same factors are important in optimizing performance in all cases. Improved pulse energies in Q-switched operation, or the use of high repetition rate pulsed discharges should result in high average powers. Sealed off operation or the use of a closed gas-recirculation system would enable the use of isotopic CO_2. Furthermore, the 4.3-μm CO_2 laser is scalable to pulse energies of several hundred millijoules, providing a powerful source of coherent radiation in the mid-infrared region.

APPENDIX A

REGULAR BAND CO_2 LASER RATE-EQUATION MODEL

The model describing operation on the regular CO_2 laser bands is similar to the one described in Sect. 4.3 for sequence operation, except that the equations are modified to account for the different levels involved.

The seven differential equations governing regular operation of a TE CO_2 laser on the 10.4-μm (00^01-10^00) band are as follows:

$$\frac{dE_3}{dt} = N_e(t)N_{CO_2}h\nu_3\Sigma_3 + \frac{E_4 - E_4^e(T_3)}{\tau_{N_2}} - \frac{E_3}{\tau_3} - h\nu_3 G_{ov}\sigma_r\delta_r\rho_r c, \tag{A-1}$$

$$\frac{dE_{12}}{dt} = N_e(t)N_{CO_2}h\nu_{12}\Sigma_{12} + \frac{E_3}{\tau_3} - \frac{E_{12} - E^e_{12}(T)}{\tau_{VT}} + h\nu_1 G_{ov}\sigma_r\delta_r\rho_r c, \tag{A-2}$$

$$\frac{dE_4}{dt} = N_e(t)N_{N_2}h\nu_3\Sigma_4 - \frac{E_4 - E_4^e(T_3)}{\tau_{N_2}}, \tag{A-3}$$

$$\frac{dN_{001}}{dt} = - G_{ov}\sigma_r\delta_r\rho_r c - \frac{x_3[N_{001} - N^e_{001}(T_3)]}{\tau_{\nu_3}} - \frac{N_{001}}{\tau_3}, \tag{A-4}$$

$$\frac{dN_{100}}{dt} = G_{ov}\sigma_r\delta_r\rho_r c - \frac{N_{100} - N^e_{100}(T_1)}{\tau_{100}}, \tag{A-5}$$

$$\frac{d\delta_r}{dt} = - 2G_{ov}\sigma_r\delta_r\rho_r c - \frac{\delta_r - (K_{001}N_{001} - K_{100}N_{100}\, g_{001}/g_{100})}{\tau_R}, \tag{A-6}$$

$$\frac{d\rho_r}{dt} = FG_{ov}\sigma_r\delta_r\rho_r c - \frac{\rho_r}{\tau_c} + FG_{ov}\beta K_{001}N_{001} \quad \text{(A-7)}$$

The variables and constants are analogous to those described in Sect. 4.3 for the sequence model, except that the subscript r is used to denote regular (as opposed to sequence) operation, and the 00^02 and 10^01 vibrational levels have been replaced by the 00^01 and 10^00 levels, respectively. The difference in levels results in a different ν_3 intra-mode collisional coupling term, which is the second term on the right hand side of Eq. (A-4). The origin of this term is described in detail in Appendix B. The implementation of the regular model is the same as that described in Sect. 4.3 for the sequence model.

APPENDIX B

DERIVATION OF COLLISIONAL RELAXATION TERMS FOR RATE EQUATIONS

The rate-equation models presented in this thesis in Sects. 4.3, 5.2, 7.2, and in Appendix A possess terms which are derived from the collisional relaxation processes described in Sect. 2.4. The procedure followed in deriving these terms is outlined in this appendix.

A typical V-V collisional relaxation process involving population transfer between CO_2 levels that are close in energy is:

$$CO_2(10^0 1) + M \underset{k'_M}{\overset{k_M}{\rightleftharpoons}} CO_2(02^0 1) + M, \tag{B-1}$$

where M represents the collision partner and k_M and k'_M represent the forward (i.e., left to right) and reverse reactions, respectively. The relationship between k_M and k'_M is obtained by the principle of detailed balance. In equilibrium, $k_M N^e_{101} N_M$ is equal to $k'_M N^e_{021} N_M$, where N_i represents the number density in the state i, and the superscript e denotes equilibrium. Thus, k_M and k'_M are related by:

$$k_M = k'_M \frac{N^e_{021}}{N^e_{101}}. \tag{B-2}$$

If the $10^0 1$ level is perturbed from equilibrium and $N_{101} > N^e_{101}$, then the rate of loss from the $10^0 1$ level is $k_M N_{101} N_M$, and the rate into the $10^0 1$ level is $k'_M N^e_{021} N_M$. The difference between these terms is the rate of change of N_{101}, which is simplified by using Eq. (B-2) to give:

$$\left(\frac{dN_{101}}{dt}\right)_M = - k_M N_M (N_{101} - N^e_{101}). \qquad \text{(B-3)}$$

Equation (B-3) represents the relaxation of the $10^0 1$ level due to the process given in Eq. (B-1) and the collision partner M. The $10^0 1$ level is also de-excited by collisions with CO_2 molecules due to the near-resonant V-V process:

$$CO_2(10^0 1) + CO_2(00^0 0) \underset{k'}{\overset{k}{\rightleftharpoons}} CO_2(00^0 1) + CO_2(10^0 0). \qquad \text{(B-4)}$$

The relationship between k and k′ in this case is given by:

$$k = k' \frac{N^e_{001} N^e_{100}}{N^e_{101} N^e_{000}} \simeq k', \qquad \text{(B-5)}$$

where the populations N^e_i are defined by Eq. (2-15). If N_{101} is perturbed, the net rate of loss from the $10^0 1$ level due to the near-resonant process of Eq. (B-4) is $k(N_{101}N^e_{000} - N^e_{001}N^e_{100})$, which can be simplified to give $kN^e_{000}(N_{101} - N^e_{101})$. If all other near-resonant processes involving higher lying levels are included, then:

$$\left(\frac{dN_{101}}{dt}\right)_{\text{near-resonant}} = - kN_{CO_2} (N_{101} - N^e_{101}), \qquad \text{(B-6)}$$

where N_{CO_2} represents the total density of CO_2 molecules, and it is assumed that k is the same for the processes involving higher lying levels. If all collision partners and relaxation processes are included in a single relaxation time, defined by $1/\tau_{101} = kN_{CO_2} + k_M N_M + \cdots$, then the total rate of change of N_{101} is given by:

$$\frac{dN_{101}}{dt} = -\frac{N_{101} - N^e_{101}}{\tau_{101}} \qquad \text{(B-7)}$$

The format used in Eq. (B-7) is that which is used in the rate-equation models described in this thesis.

The sequence laser model of Chapt. 4 and the 4.3-μm laser models of Chapts. 5 and 7 all contain the relaxation term $(N_{002}-N^e_{002})/(2\tau_{\nu_3})$. The origin of the factor of 2 is as follows. Consider the ν_3 intra-mode relaxation process given by Eq. (2-13), i.e.:

$$CO_2(00^o1) + CO_2(00^o1) \underset{k'}{\overset{k}{\rightleftharpoons}} CO_2(00^o2) + CO_2(00^o0), \qquad \text{(B-8)}$$

where $k=k_{\nu_3}$, but the subscript is deleted for convenience. The forward and reverse rates are found to be approximately equal by the same analysis that led to Eq. (B-5). Suppose N_{002} is perturbed from equilibrium and $N_{002} < N^e_{002}$. Then the rate of production of N_{002} is $(1/2)k(N^e_{001})^2$ and the rate of loss of N_{002} is $(1/2)kN_{002}N^e_{000}$. The factor of 1/2 arises because the collision partners on the left hand side of Eq. (B-8) are indistinguishable [63]. Thus, the net rate into the 00^o2 level is $(1/2)k[(N^e_{001})^2-N_{002}N^e_{000}]$, which simplifies to give $(1/2)kN^e_{000}(N^e_{002}-N_{002})$. This is equivalent to the term used in the rate-equation models if N^e_{000} is replaced by N_{CO_2} and $1/\tau_{\nu_3}=kN_{CO_2}$.

The final relaxation term which will be considered is one that appears in the regular laser model of Appendix A, i.e., $x_3(N_{001}-N^e_{001})/\tau_{\nu_3}$, where x_3 is defined by Eq. (2-14). This term differs considerably from the one described in the preceding paragraph, even though both of the levels concerned belong to the ν_3 mode. When

considering the ν_3 intra-mode relaxation process given by Eq. (B-8), we are now concerned with the change in N_{001}, and the factor of 1/2 due to indistinguishability is not relevant [63]. If $N_{001} < N^e_{001}$, then the net rate into 00^01 is $k[N^e_{002}N^e_{000}-(N_{001})^2]$, which is equivalent to $k[(N^e_{001})^2-(N_{001})^2]$. This can be simplified to give $k(N^e_{001}+N_{001})(N^e_{001}-N_{001})$, which is approximately equal to $2kN^e_{001}(N^e_{001}-N_{001})$. The major difference between this result and the relaxation terms discussed previously is that k is now multiplied by N^e_{001} instead of N^e_{000}. Collisional coupling into 00^01 from many other levels is also significant. For example, consider the process given by Eq. (B-4). In this case, the net rate into 00^01 is $k_{101}(N^e_{101}N^e_{000}-N_{001}N^e_{100})$, which simplifies to $k_{101}N^e_{100}(N^e_{001}-N_{001})$. Similar terms are obtained due to coupling from the 01^11, 02^01, 02^21, and other levels, and thus the total rate into 00^01 is:

$$\frac{dN_{001}}{dt} = (2k_{\nu_3}N^e_{001} + k_{101}N^e_{100} + k_{011}N^e_{010} + \ldots)(N^e_{001}-N_{001}), \qquad \text{(B-9)}$$

where subscripts have been added to the k's to avoid confusion. The summation includes the populations of all levels except the ground state, and thus the total rate can be approximated by $k_{\nu_3}(N_{CO_2}-N^e_{000})(N^e_{001}-N_{001})$, where the weighted average of the rate constants is assumed to be k_{ν_3}. Further simplification results in the expression $k_{\nu_3}N_{CO_2}x_3(N^e_{001}-N_{001})$, and by letting $1/\tau_{\nu_3} = k_{\nu_3}N_{CO_2}$, the desired relaxation term is obtained.

APPENDIX C

OUTPUT COUPLING EFFICIENCY IN THE PRESENCE OF A LARGE NONSATURABLE ABSORPTION

Equation (7-9), which expresses the fraction of photons not lost to the overlapping absorption in a 4.3-μm CO_2 laser, is derived below.

Consider a laser cavity comprised of a total reflector and an output coupler of reflectivity R. The cavity contains a discharge of length ℓ, and in the discharge is a nonsaturable absorption with a coefficient α. It is assumed that the photon generation per unit length is uniformly distributed over the discharge, and is given by N_o/ℓ. If x is the position in the discharge (x=0 at the output coupler end of the discharge), then the number of photons generated over a length dx, which are then coupled out of the cavity is given by:

$$dN = \frac{N_o}{2\ell} [\{T\, e^{-\alpha x} + z\, T\, e^{-\alpha x} + z^2\, T\, e^{-\alpha x} + \ldots\}$$

$$+ \{T\, e^{-\alpha(2\ell-x)} + z\, T\, e^{-\alpha(2\ell-x)} + z^2\, T\, e^{-\alpha(2\ell-x)} + \ldots\}]\, dx, \quad \text{(C-1)}$$

where $T = 1-R$ and $z = R \exp(-2\alpha\ell)$. Two terms are present because there are two counter-propagating beams in the cavity causing stimulated emission of photons. Equation (C-1) can be simplified as follows:

$$dN = \frac{N_o}{2\ell} [\{T\, e^{-\alpha x} + T\, e^{-\alpha(2\ell-x)}\}\{1 + z + z^2 + \ldots\}]\, dx. \quad \text{(C-2)}$$

The infinite series can be expressed as $1/(1-z)$ since $z < 1$ for any case of interest, and Eq. (C-2) can be written:

$$dN = \frac{N_o\ (1-R)\ \{e^{-\alpha x} + e^{-\alpha(2\ell-x)}\}}{2\ell\ (1-z)}\ dx. \qquad (C-3)$$

The total number of photons coupled out of the cavity is obtained by integrating Eq. (C-3) over x, i.e.:

$$N = \frac{N_o\ (1-R)}{2\ell\ (1-z)}\ [\ \int_0^{\ell} e^{-\alpha x}\ dx + e^{-2\alpha\ell} \int_0^{\ell} e^{\alpha x}\ dx\ ]. \qquad (C-4)$$

The integrals in Eq. (C-4) are easily solved to give:

$$N = \frac{N_o\ (1-R)\ [1-\exp(-2\alpha\ell)]}{2\alpha\ell\ (1-z)}. \qquad (C-5)$$

The fraction of photons not lost to the absorption, η, is then given by N/N_o, which is the expression of Eq. (7-9).

REFERENCES

1. C.K.N. Patel, W.L. Faust, and R.A. McFarlane, "CW Laser Action on Rotational Transitions of the $\Sigma_u^+ - \Sigma_g^+$ Vibrational Band of CO_2," Bull. Am. Phys. Soc. 9, 500 (1964).

2. C.K.N. Patel, "Interpretation of CO_2 Optical Maser Experiments," Phys. Rev. Lett. 12, 588 (1964), and "Continuous-Wave Laser Action on Vibrational-Rotational Transitions of CO_2," Phys. Rev. 136, A1187 (1964).

3. C. Freed, "Status of CO_2 Isotope Lasers and Their Applications in Tunable Laser Spectroscopy," IEEE J. Quantum Electron. QE-18, 1220 (1982).

4. J. Reid and K. Siemsen, "New CO_2 Laser Bands in the 9-11-μm Wavelength Region," Appl. Phys. Lett. 29, 250 (1976).

5. J. Reid and K. Siemsen, "Laser Power and Gain Measurements on the Sequence Bands of CO_2," J. Appl. Phys. 48, 2712 (1977).

6. T.A. Znotins, J. Reid, B.K. Garside, and E.A. Ballik, "4.3-μm TE CO_2 Laser," Opt. Lett. 4, 253 (1979).

7. A.B. Petersen and C. Wittig, "Line-Tunable CO_2 Laser Operating in the Region 2280-2360 cm^{-1} Pumped by Energy Transfer from $Br(4^2P_{1/2})$," J. Appl. Phys. 48, 3665 (1977).

8. M.I. Buchwald, C.R. Jones, H.R. Fetterman, and H.R. Schlossberg, "Direct Optically Pumped Multiwavelength CO_2 Laser," Appl. Phys. Lett. 29, 300 (1976).

9. J. Finzi and C.B. Moore, "Relaxation of $CO_2(10^0 1)$, $CO_2(02^0 1)$, and $N_2O(10^0 1)$ Vibrational Levels by Near-Resonant V→V Energy Transfer," J. Chem. Phys. 63, 2285 (1975).

10. L.O. Hocker, M.A. Kovacs, C.K. Rhodes, G.W. Flynn, and A. Javan, "Vibrational Relaxation Measurements in CO_2 using an Induced-Fluorescence Technique," Phys. Rev. Lett. 17, 233 (1966).

11. I.M. Bertel, V.O. Petukhov, B.I. Stepanov, S.A. Trushin, and V.V. Churakov, "Laser Action at 4.3 μ in a TE CO_2 Laser," Sov. Phys. Dokl. 25, 1009 (1980).

12. T.A. Znotins, J. Reid, B.K. Garside and E.A. Ballik, "4.3-μm Cascade CO_2 Laser," Appl. Phys. Lett. 39, 199 (1981).

13. T.A. Znotins, "4.3-μm CO_2 Laser," Ph.D. Thesis, McMaster University (1981).

14. G. Herzberg, Molecular Spectra and Molecular Structure II. Infrared and Raman Spectra of Polyatomic Molecules (Van Nostrand, New York, 1945).

15. E. Fermi, "Uber den Ramaneffekt des Kohlendioxyds," Z. Phys. 71, 250 (1931).

16. G. Herzberg, Molecular Spectra and Molecular Structure I. Spectra of Diatomic Molecules (Van Nostrand, New York, 1950).

17. J.M. Brown, J.T. Hougen, K.-P. Huber, J.W.C. Johns, I. Kopp, H. Lefebvre-Brion, A.J. Merer, D.A. Ramsay, J.Rostas, and R.N. Zare, "The Labeling of Parity Doublet Levels in Linear Molecules," J. Mol. Spectrosc. 55, 500 (1975).

18. P.K. Cheo, "CO_2 Lasers" in Lasers, Vol 3, edited by A.K. Levine and A.J. DeMaria (Marcel Dekker, New York, 1971).

19. L.S. Rothman, and L.D.G. Young, "Infrared Energy Levels and Intensities of Carbon Dioxide - II," J. Quant. Spectrosc. Radiat. Transfer 25, 505 (1981).

20. C.K.N. Patel, "Selective Excitation Through Vibrational Energy Transfer and Optical Maser Action in N_2-CO_2," Phys. Rev. Lett. 13, 617 (1964).

21. W.L. Nighan and J.H. Bennett, "Electron Energy Distribution Functions and Vibrational Excitation Rates in CO_2 Laser Mixtures," Appl. Phys. Lett. 14, 240 (1969).

22. W.L. Nighan, "Electron Energy Distributions and Collision Rates in Electrically Excited N_2, CO, and CO_2," Phys. Rev. A2, 1989 (1970).

23. J.J. Lowke, A.V. Phelps, and B.W. Irwin, "Predicted Electron Transport Coefficients and Operating Characteristics of CO_2-N_2-He Laser Mixtures," J. Appl. Phys. 44, 4664 (1973).

24. O.P. Judd, "The Effect of Gas Mixture on the Electron Kinetics in the Electrical CO_2 Gas Laser," J. Appl. Phys. 45, 4572 (1974).

25. G.J. Schulz, "Vibrational Excitation of N_2, CO, and H_2 by Electron Impact," Phys. Rev. 135, A988 (1964).

26. L.J. Denes and J.J. Lowke, "V-I Characteristics of Pulsed CO_2 Laser Discharges," Appl. Phys. Lett. 23, 130 (1973).

27. J.P. Rink, "TEA Laser Power E/p for Atmospheric and Higher Pressures," J. Appl. Phys. 43, 2441 (1972).

28. C.B. Mills, "CO_2 Gas Laser Excitation and Gain," J. Appl. Phys. 45, 1336 (1974).

29. W.P. Allis and H.A. Haus, "Electron Distributions in Gas Lasers," J. Appl. Phys. 45, 781 (1974).

30. R.D. Hake,Jr. and A.V. Phelps, "Momentum-Transfer and Inelastic-Collision Cross Sections for Electrons in O_2, CO, and CO_2," Phys. Rev. 158, 70 (1967).

31. B.R. Bulos and A.V. Phelps, "Excitation of the 4.3-μm Bands of CO_2 by Low-Energy Electrons," Phys. Rev. A14, 615 (1976).

32. Y. Sakai, S. Kaneko, H. Tagashira, and S. Sakamoto, "A Boltzmann Equation Analysis of Electron Swarm Parameters in CO_2 Laser Mixtures," J. Phys. D 12, 23 (1979).

33. J. Lucas and H.T. Saelee, "A Comparison of a Monte Carlo Simulation and the Boltzmann Solution for Electron Swarm Motion in Gases," J. Phys. D 8, 640 (1975).

34. T. Taniguchi, H. Tagashira, and Y. Sakai, "Validity of a Boltzmann Equation Method for Predicting the Effect of Ionization and Attachment," J. Phys. D 10, 2301 (1977).

35. L.C. Pitchford, S.V. ONeil, and J.R. Rumble,Jr., "Extended Boltzmann Analysis of Electron Swarm Experiments," Phys. Rev. A23, 294 (1981).

36. C.S. Lakshminarasimha, J. Lucas, J.L. Moruzzi, and I.J. Spalding, "Electron Swarm Parameters in CO_2 Laser Gas Mixtures," J. Phys. D 9, 1727 (1976).

37. R.A. Sierra, H.L. Brooks, A.J. Sommerer, S.R. Foltyn, and K.J. Nygaard, "Effective Swarm Parameters and transport Coefficients in CO_2 Laser Mixtures," J. Phys. D 14, 1791 (1981).

38. R.A. Sierra, H.L. Brooks, and K.J. Nygaard, "Electron Drift Velocities in N_2, CO_2, and (N_2+CO_2) Laser Mixtures," Appl. Phys. Lett. 35, 764 (1979).

39. M.C. Cornell, I.M. Littlewood, H.L. Brooks and K.J. Nygaard, "Electron Drift Velocities in Gas Mixtures of He, N_2, and CO_2," J. Appl. Phys. 54, 1723 (1983).

40. W. Roznerski and K. Leja, "Electron Drift Velocity in Hydrogen, Nitrogen, Oxygen, Carbon Monoxide, Carbon Dioxide and Air at Moderate E/N," J. Phys. D 17, 279 (1984).

41. J. Mellis and A.L.S. Smith, "Gain Limitations in CO_2 Lasers," Opt. Commun. 41, 121 (1982).

42. C. Dang, J. Reid, and B.K. Garside, "Dynamics of the CO_2 Upper Laser Level as Measured with a Tunable Diode Laser," IEEE J.

Quantum Electron. QE-19, 755 (1983).

43. J. Reid, E.A. Ballik, and B.K. Garside, "Saturation of the Net Electron Excitation of the $CO_2(00^01)$ Laser Level as a Function of Discharge Input Energy," Opt. Commun. 12, 354 (1974).

44. E.A. Ballik, B.K. Garside, J. Reid, and T. Tricker, "Reduction of the Pumping Efficiency in CO_2 Lasers at High Discharge Energy," J. Appl. Phys. 46, 1322 (1975).

45. C. Dang, J. Reid, and B.K. Garside, "Gain Limitations in TE CO_2 Laser Amplifiers," IEEE J. Quantum Electron. QE-16, 1097 (1980).

46. K.J. Siemsen, J. Reid, and C. Dang, "New Techniques for Determining Vibrational Temperatures, Dissociation, and Gain Limitations in CW CO_2 Lasers," IEEE J. Quantum Electron. QE-16, 668 (1980).

47. M.J. Pechersky, "Shock Waves in Pulsed Gas Lasers," Laser Focus, 17 (12), 61 (1981).

48. R.R. Jacobs, K.J. Pettipiece, and S.J. Thomas, "Rotational Relaxation Rate Constants for CO_2," Appl. Phys. Lett. 24, 375 (1974).

49. R.L. Abrams and P.K. Cheo, "Collisional Relaxation of CO_2 Rotational Levels by N_2 and He," Appl. Phys. Lett. 15, 177 (1969).

50. M.D. Thomason, "Rapid Vibrational and Rotational Energy Transfer Rates in Heated Carbon Dioxide Collisions by Double Resonance Laser Spectroscopy," Ph.D. Thesis, University of Virginia, (Los Alamos National Laboratory: LA-9420-T, 1982).

51. C. Dang, J. Reid, and B.K. Garside, "Dynamics of the CO_2 Lower Laser Levels as Measured with a Tunable Diode Laser," Appl. Phys. B31, 163 (1983).

52. R.R. Jacobs, K.J. Pettipiece, and S.J. Thomas, "Rate Constants for the CO_2 $02^00 - 10^00$ Relaxation," Phys. Rev. A11, 54 (1975).

53. D.C. Clary and A.E. DePristo, "Application of Scaling Theory to Vibrational Relaxation in Linear Anharmonic Triatomic Molecules," J. Chem. Phys. 79, 2206 (1983).

54. E.E. Stark,Jr., "Measurement of the $10^00 - 02^00$ Relaxation Rate in CO_2," Appl. Phys. Lett. 23, 335 (1973).

55. R.N. Schwartz, Z.I. Slawsky, and K.F. Herzfeld, "Calculation of Vibrational Relaxation Times in Gases," J. Chem. Phys. 20, 1591 (1952).

56. F. Lepoutre, G. Louis, and H. Manceau, "Collisional Relaxation in CO_2 Between 180 K and 400 K Measured by the Spectrophone Method," Chem. Phys. Lett. 48, 509 (1977).

57. J. Taine and F. Lepoutre, "A Photoacoustic Study of the Collisional Deactivation of the First Vibrational Levels of CO_2 by N_2 and CO," Chem. Phys. Lett. 65, 554 (1979).

58. F. Lepoutre, G. Louis, and J. Taine, "A Photoacoustic Study of Intramolecular Energy Transfer in CO_2 Deactivated by Monatomic Gases Between 153 and 393 K," J. Chem. Phys. 70, 2225 (1979).

59. W.A. Rosser,Jr., A.D. Wood, and E.T. Gerry, "Deactivation of Vibrationally Excited Carbon Dioxide (ν_3) by Collisions with Carbon Dioxide or with Nitrogen," J. Chem. Phys. 50, 4996 (1969).

60. R.L. Taylor and S. Bitterman, "Survey of Vibrational Relaxation Data for Processes Important in the CO_2-N_2 Laser System," Rev. Mod. Phys. 41, 26 (1969).

61. L. Doyennette, M. Margottin-Maclou, A. Chakroun, H. Gueguen, and L. Henry, "Vibrational Energy Transfer from the (00^o1) Level of $^{14}N_2O$ and $^{12}CO_2$ to the $(m,n^1,1)$ Levels of these Molecules and their Isotopic Species," J. Chem. Phys. 62, 440 (1975).

62. I. Burak, Y. Noter, and A. Szoke, "Vibration-Vibration Energy Transfer in the ν_3 Mode of CO_2," IEEE J. Quantum Electron. QE-9, 541 (1973).

63. R.T. Pack, "Analytic Estimation of Almost Resonant Molecular Energy Transfer due to Multipolar Potentials. VV Processes Involving CO_2," J. Chem. Phys. 72, 6140 (1980).

64. R.J. Harrach, "Effect of Rotational and Intramode Vibrational Coupling on Short-Pulse Amplification in CO_2," IEEE J. Quantum Electron. QE-11, 349 (1975).

65. C. Dang, J. Reid, and B.K. Garside, "Detailed Vibrational Population Distributions in a CO_2 Laser Discharge as Measured with a Tunable Diode Laser," Appl. Phys. B27, 145 (1982).

66. C.B. Moore, R.E. Wood, B.-L. Hu, and J.T. Yardley, "Vibrational Energy Transfer in CO_2 Lasers," J. Chem. Phys. 46, 4222 (1967).

67. B.F. Gordietz, N.N. Sobolev, V.V. Sokovikov, and L.A. Shelepin, "Population Inversion of the Vibrational Levels in CO_2 Lasers," IEEE J. Quantum Electron. QE-4, 796 (1968).

68. A.M. Robinson, "Gain Distribution in a CO_2 TEA Laser," Can. J. Phys. 50, 2471 (1972).

69. S.R. Drayson, "Rapid Computation of the Voigt Profile," J. Quant. Spectrosc. Radiat. Transfer 16, 611 (1976).

70. C. Young and R.E. Chapman, "Line-Widths and Band Strengths for the

9.4- and 10.4-μm CO_2 Bands," J. Quant. Spectrosc. Radiat. Transfer 14, 679 (1974).

71. E. Arie, N. Lacome, et C. Rossetti, "Spectroscopie par Source Laser. I. Etude Experimentale des Intensites et Largeurs des Raies de la Transition $00^01-(10^00,02^00)_I$ de CO_2," Can. J. Phys. 50, 1800 (1972).

72. A.D. Devir and U.P. Oppenheim, "Line Width Determination in the 9.4-μ and 10.4-μ Bands of CO_2 Using a CO_2 Laser," Appl. Opt. 8, 2121 (1969).

73. C. Cousin, C. Rossetti, et C. Meyer, "Spectroscopie avec Source Laser. Etude des Transitions de Vibration-Rotation $\nu_3-\nu_1$, $\nu_3-2\nu_2$ et $(\nu_3+\nu_2)-(\nu_1+\nu_2)$ de l'Anhydride Carbonique," C.R. Acad. Sc. Paris 268B, 1640 (1969).

74. C. Boulet, E. Arie, J.P. Bouanich, et N. Lacome, "Spectroscopie par Source Laser. II. Etude Experimentale de l'Elargissement des Raies de la Transition $00^01-(10^00, 02^00)_I$ de CO_2 Perturbe par N_2. Application de la Theorie d'Anderson, Tsao et Curnutte au Calcul des Largeurs des Raies de CO_2 Pur, et Perturbe par N_2," Can. J. Phys. 50, 2178 (1972).

75. R.L. Abrams, "Broadening Coefficients for the P(20) CO_2 Laser Transition," Appl. Phys. Lett. 25, 609 (1974).

76. R.T. Pack, "Pressure Broadening of the Dipole and Raman Lines of CO_2 by He and Ar. Temperature Dependence," J. Chem. Phys. 70, 3424 (1979).

77. G. Yamamoto, M. Tanaka, and T. Aoki, "Estimation of Rotational Line Widths of Carbon Dioxide Bands," J. Quant. Spectrosc. Radiat. Transfer 9, 371 (1969).

78. V. Malathy Devi, B. Fridovich, G.D. Jones, and D.G.S. Snyder, "Diode Laser Measurements of Strengths, Half-Widths, and Temperature Dependence of Half-Widths for CO_2 Spectral Lines near 4.2 μm," J. Mol. Spectrosc. 105, 61 (1984).

79. G.L. Tettemer and W.G. Planet, "Intensities and Pressure-Broadened Widths of CO_2 R-Branch Lines at 15 μm from Tunable Laser Measurements," J. Quant. Spectrosc. Radiat. Transfer 24, 343 (1980).

80. S.S. Penner, Quantitative Molecular Spectroscopy and Gas Emissivities (Addison Wesley, 1959) pp. 151-153.

81. S.R. Drayson and C. Young, "Band Strength and Line Half-Width of the 10.4 μ CO_2 Band," J. Quant. Spectrosc. Radiat. Transfer 7, 993 (1967).

82. J. Reid, J. Shewchun, and B.K. Garside, "Measurement of the

Transition Strength of the $00^{o}2$ 9.4 μm Sequence Band in CO_2 Using a Tunable Diode Laser," Appl. Phys. 17, 349 (1978).

83. B. Fridovich, W.C. Braun, G.R. Smith, and E.E. Champion, "Strengths of Single Lines in the $^{12}C^{16}O_2$ ν_3 Band at 4.3 μm," J. Mol. Spectrosc. 81, 248 (1980).

84. J. Reid, "TE CO_2 Laser Dynamics," Ph.D. Thesis, McMaster University, 1974.

85. T.Y. Chang and O.R. Wood, "Optically Pumped 33-atm CO_2 Laser," Appl. Phys. Lett. 23, 370 (1973).

86. B.K. Garside, J. Reid, and E.A. Ballik, "Studies of the Inversion and Lower Level Relaxation in Pulsed TE CO_2 Discharges," IEEE J. Quantum Electron. QE-11, 264 (1975).

87. N. Djeu, T. Kan, and G.J. Wolga, "Gain Distribution, Population Densities, and Rotational Temperature for the $(00^{o}1)$-$(10^{o}0)$ Rotation-Vibration Transitions in a Flowing CO_2-N_2-He Laser," IEEE J. Quantum Electron. QE-4, 256 (1968).

88. L.A. Weaver, L.H. Taylor, and L.J. Denes, "Rotational Temperature Determinations in Molecular Gas Lasers," J. Appl. Phys. 46, 3951 (1975).

89. W.T. Leland, M.J. Kircher, M.J. Nutter, and G.T. Schappert, "Rotational Temperature in a High-Pressure Pulsed CO_2 Laser," J. Appl. Phys. 46, 2174 (1975).

90. C.K.N. Patel, "CW Laser Action in N_2O (N_2-N_2O System)," Appl. Phys. Lett. 6, 12 (1965).

91. G. Moeller and J.D. Rigden, "Observation of Laser Action in the R-Branch of CO_2 and N_2O Vibrational Spectra," Appl. Phys. Lett. 8, 69 (1966).

92. K. Siemsen and J. Reid, "New N_2O Laser Band in the 10 μm Wavelength Region," Opt. Commun. 20, 284 (1977).

93. K.O. Tan, Lumonics Inc., private communication.

94. W. Berger, K. Siemsen, and J. Reid, "In-Cavity Hot Cell for use with Sequence CO_2 Lasers," Rev. Sci. Instrum. 48, 1031 (1977).

95. K.E. Fox and J. Reid, "Dynamics of the N_2O Laser as Measured with a Tunable Diode Laser," J. Opt. Soc. Am. B, June (1985).

96. N. Djeu, T. Kan, and G. Wolga, "Laser Parameters for the 10.8-μ N_2O Molecular Laser," IEEE J. Quantum Electron. QE-4, 783 (1968).

97. H. Hara and W.T. Whitney, "Transversely Excited N_2O Sequence Band

Laser," Appl. Phys. Lett. 44, 155 (1984).

98. H. Oodate and T. Fujioka, "Measurements of 4.2 μm CO_2 Pressure Broadening by using an HBr Chemical Laser," J. Chem. Phys. 68, 5494 (1978).

99. R.S. Taylor, A.J. Alcock, W.J. Sarjeant, and K.E. Leopold, "Electrical and Gain Characteristics of a Multiatmosphere UV-Preionized CO_2 Laser," IEEE J. Quantum Electron. QE-15, 1131 (1979).

100. A.H.M. Olbertz and W.J. Witteman, "Mode-Locked Pulses in Multi-Atmosphere CO_2 Lasers," Opt. Commun. 30, 447 (1979).

101. W.J. Witteman and A.H.M. Olbertz, "Pulse-Forming and Line-Broadening in AM Mode Locking of the TEA-CO_2 Laser," IEEE J. Quantum Electron. QE-13, 381 (1977).

102. R.K. Brimacombe and J. Reid, "Accurate Measurements of Pressure-Broadened Linewidths in a Transversely Excited CO_2 Discharge," IEEE J. Quantum Electron. QE-19, 1668 (1983).

103. B.G. Whitford, K.J. Siemsen, H.D. Riccius, and G.R. Hanes, "Absolute Frequency Measurements of N_2O Laser Transitions," Opt. Commun. 14, 70 (1975).

104. T.W. Meyer, C.K. Rhodes, and H.A. Haus, "High-Resolution Line Broadening and Collisional Studies in CO_2 using Nonlinear Spectroscopic Techniques," Phys. Rev., A12, 1993 (1975).

105. A.M. Robinson and J.S. Weiss, "Temperature Dependence of the Linewidth of the CO_2 Laser Transitions," Can. J. Phys. 58, 512 (1980).

106. R. Ely and T.K. McCubbin,Jr., "The Temperature Dependence of the Self-Broadened Half-Width of the P-20 Line in the 001-100 Band of CO_2," Appl. Opt. 9, 1230 (1970).

107. R.S. Eng and A.W. Mantz, "Tunable Diode Laser Spectroscopy of CO_2 in the 10- to 15-μm Spectral Region - Lineshape and Q-Branch Head Absorption Profile," J. Mol. Spectrosc. 74, 331 (1979).

108. S. Singer, "Observations of Anomalous Gain Coefficients in TEA Double-Discharge CO_2 Lasers," IEEE J. Quantum Electron. QE-10, 829 (1974).

109. H. Brinkschulte and R. Lang, "Gain Measurements in a TEA CO_2 Laser," Phys. Lett. 47A, 455 (1974).

110. J. Reid and K.J. Siemsen, "Gain of High-Pressure CO_2 Lasers," IEEE J. Quantum Electron. QE-14, 217 (1978).

111. R.K. Brimacombe and J. Reid, "Measurements of Anomalous Gain

Coefficients in Transversely Excited CO_2 Lasers,"IEEE J. Quantum Electron. QE-19, 1674 (1983).

112. J.C. Goldstein, R.F. Haglund,Jr., and J.C. Comly,Jr., "Small Signal Gain Spectrum of an 1800 Torr CO_2 Amplifier," SPIE Los Alamos Conference on Optics 288, 164 (1981).

113. D. Bailly and C. Rossetti, "$^{12}C^{16}O_2$-Spectroscopic Constants of the Fermi Dyad $[10^0\nu_3, 02^0\nu_3]$ and Wavenumbers of Laser Sequence Band Transitions," Opt. Commun. 42, 323 (1982).

114. B.G. Whitford, K.J. Siemsen, and J. Reid, "Heterodyne Frequency Measurements of CO_2 Laser Hot-Band Transitions," Opt. Commun. 22, 261 (1977).

115. J. Dupré-Maquaire and P. Pinson, "Emission Spectrum of CO_2 in the 9.6 μm Region," J. Mol. Spectrosc. 62, 181 (1976).

116. P. Lavigne, J.-L. Lachambre, and G. Otis, "Gain Measurements on the Sequence Bands in a TEA-CO_2 Amplifier," J. Appl. Phys. 49, 3714 (1978).

117. R. Giles and A.A. Offenberger, "Multiline Injection Mode Locking of a Transversely Excited Atmosphere CO_2 Laser," Appl. Phys. Lett. 40, 944 (1982).

118. R.K. Brimacombe, J. Reid, and T.A. Znotins, "Multi-Joule Pulses from a Sequence Band Transversely Excited Atmospheric CO_2 Laser," Appl. Phys. Lett. 39, 302 (1981).

119. T.A. Znotins, J. Reid, and R.K. Brimacombe, "Design of Efficient Transversely Excited Sequence CO_2 Lasers," J. Appl. Phys. 53, 2843 (1982).

120. C.O. Weiss, M. Grinda, and K. Siemsen, "FIR Laser Lines of CH_3OH Pumped by CO_2 Laser Sequence Lines," IEEE J. Quantum Electron. QE-13, 892 (1977).

121. B.J. Feldman, R.A. Fisher, C.R. Pollock, S.W. Simons, and R.G. Tercovich, "Intense High-Pressure Sequence-Band CO_2 Laser," Opt. Lett. 2, 16 (1978).

122. P. Lavigne, J.-L. Lachambre, and G. Otis, "TEA-Laser Emission on the Sequence Bands of CO_2," Opt. Lett. 2, 127 (1978).

123. I.M. Bertel, B.F. Kuntsevich, V.O. Petukhov, B.I. Stepanov, S.A. Trushin, and V.V. Churakov, "Intense Pulsed Lasing at Lines of the P and R Branches of the $00^02-[10^01,02^01]_{I,II}$ in a CO_2 TEA Laser," Sov. Tech. Phys. Lett. 4, 532 (1978).

124. I.M. Bertel, V.O. Petukhov, S.A. Trushin, and V.V. Churakov, "Investigation of the Output Parameters of a TEA CO_2 Laser Emitting

Lines in the $00^0 2-[10^0 1, 02^0 1]_{I,II}$ Bands," Sov. J. Quantum Electron. 11, 213 (1981).

125. K.R. Manes and H.J. Seguin, "Analysis of the CO_2 TEA Laser," J. Appl. Phys. 43, 5073 (1972).

126. K. Smith and R.M. Thomson, Computer Modeling of Gas Lasers (Plenum, New York, 1978).

127. B.K. Garside, J. Reid, and E.A. Ballik, "TE CO_2 Laser Pulse Decay and Molecular Relaxation Rates," IEEE J. Quantum Electron. QE-11, 583 (1975).

128. D. Marcuse, "Classical Derivation of the Laser Rate Equation," IEEE J. Quantum Electron. QE-19, 1228 (1983).

129. R.W. Hamming, Numerical Methods for Scientists and Engineers, 2nd Ed. (McGraw-Hill, New York, 1973) p. 407.

130. T. Stamatakis and J.M. Green, "Fine Frequency Tuning of a High Power CO_2 Laser and its Application to Optically-Pumped Molecular Lasers," Opt. Commun. 30, 413 (1979).

131. I.M. Bertel, V.O. Petukhov, S.A. Trushin, and V.V. Churakov, "Influence of the Active Medium Composition on the Gain in the $00^0 2-[10^0 1, 02^0 1]_I$ Band for a TEA CO_2 Laser with Ultraviolet Preionization," Sov. J. Quantum Electron. 12, 894 (1982).

132. T.A. Znotins, J. Reid, B.K. Garside, and E.A. Ballik, "12-μm NH_3 Laser Pumped by a Sequence CO_2 Laser," Opt. Lett. 5, 528, (1980).

133. P.L. Kelley, R.A. McClatchey, R.K. Long, and A. Snelson, "Molecular Absorption of Infrared Laser Radiation in the Natural Atmosphere," Opt. and Quantum Electron. 8, 117 (1976).

134. T.R. Lawrence, M.J. Post, R.M. Hardesty, R.J. Keeler, R.A. Richter, R.M. Huffaker and F.F. Hall,Jr., "Long-Range Wind Sensing Using a Pulsed Doppler CO_2 Lidar," Conference on Lasers and Electro-Optics, Washington, D.C., June 1981, paper WD3.

135. R.K. Brimacombe, J. Reid, and T.A. Znotins, "High-Power Pulses from a 4.3-μm CO_2 Laser," Conference on Lasers and Electro-Optics, Baltimore, MD, May 1983, paper WT1.

136. R.K. Brimacombe and J. Reid, "15-mJ Pulses from a 4.3-μm CO_2 Laser," Appl. Phys. Lett. 45, 813 (1984).

137. R.K. Brimacombe and J. Reid, "Gain Dynamics of the 4.3-μm CO_2 Laser," Opt. Lett. 9, 205 (1984).

138. R.K. Brimacombe and J. Reid, "Design of Efficient 4.3-μm CO_2 Lasers," Conference on Lasers and Electro-Optics, Anaheim, CA, June

1984, paper TuB5.

139. R.K. Brimacombe and J. Reid, "Simplified Cavity Design for a 4.3-μm Transversely Excited CO_2 Laser," Appl. Opt. 23, 4464 (1984).

140. R.K. Brimacombe, J. Reid, and T.A. Znotins, "Gain Dynamics of the 4.3-μm CO_2 Laser," Appl. Phys. B, in press,(1985).

141. R.K. Brimacombe and J. Reid, "Influence of the Dynamic Stark Effect on the Small-Signal Gain of Optically-Pumped 4.3-μm CO_2 Lasers," submitted to J. Appl. Phys.

142. R.K. Brimacombe and J. Reid, "Optimization of Pulse Energy from 4.3-μm CO_2 Lasers," J. Appl. Phys., in press,(1985).

143. D. Bailly and C. Rossetti, "$^{12}C^{16}O_2$: Σ and Π Fermi Dyads in the 4.5-μm Region: Wavenumbers and Spectroscopic Constants," J. Mol. Spectrosc. 102, 392 (1983).

144. P.V. Gatenby, K.C. Hawkins, and H.N. Rutt, "Line Narrowed TEA CO_2 Laser for Optical Pumping of Molecular Gas Lasers," J. Phys. E 14, 56 (1981).

145. R.L. Panock and R.J. Temkin, "Interaction of Two Laser Fields with a Three-Level Molecular System," IEEE J. Quantum Electron. QE-13, 425 (1977).

146. S.H. Autler and C.H. Townes, "Stark Effect in Rapidly Varying Fields," Phys. Rev. 100, 703 (1955).

147. H.R. Gray and C.R. Stroud,Jr., "Autler-Townes Effect in Double Optical Resonance," Opt. Commun. 25, 359 (1978).

148. R.E. Grove, F.Y. Wu, and S. Ezekiel, "Measurement of the Spectrum of Resonance Fluorescence from a Two-Level Atom in an Intense Monochromatic Field," Phys. Rev. A15, 227 (1977).

149. Z. Drozdowicz, R.J. Temkin, and B. Lax, "Laser-Pumped Molecular Lasers - Part II: Submillimeter Laser Experiments," IEEE J. Quantum Electron. QE-15, 865 (1979).

150. J. Heppner, C.O. Weiss, U. Hubner, and G. Schinn, "Gain in CW Laser Pumped FIR Laser Gases," IEEE J. Quantum Electron. QE-16, 392 (1980).

151. Z. Drozdowicz, R.J. Temkin, and B. Lax, "Laser Pumped Molecular Lasers - Part I: Theory," IEEE J. Quantum Electron. QE-15, 170 (1979).

152. C.H. Townes and A.L. Schawlow, Microwave Spectroscopy (Dover, New York, 1975) p. 23.

153. Z. Drozdowicz, R.I. Rudko, S.J. Linhares, and B. Lax, "High Gain 4.3-4.5 μm Optically Pumped CO_2 Laser," IEEE J. Quantum Electon.. QE-17, 1574 (1981).

154. M.-K. Au, P.A. Hackett, M. Humphries, and P. John, "Infrared Multiphoton Dissociation of Unsubstituted Metal Carbonyls at 5 μm," Appl. Phys. B33, 43 (1984).

155. N. Menyuk and P.F. Moulton, "Development of a High-Repetition-Rate Mini-TEA CO_2 Laser," Rev. Sci. Instrum. 51, 216 (1980).

156. N. Menyuk, G.W. Iseler, and A. Mooradian, "High-Efficiency High-Average-Power Second-Harmonic Generation with $CdGeAs_2$," Appl. Phys. Lett. 29, 422 (1976).

157. O.R. Wood and T.Y. Chang, "Transverse-Discharge Hydrogen Halide Lasers," Appl. Phys. Lett. 20, 77 (1972).

158. P. Arrowsmith, J.C. Polanyi, H.H. Telle, and B. Yang, "Short-Cavity Hydrogen-Halide Laser," Appl. Opt. 22, 2716 (1983).

159. T.Y. Chang and O.R. Wood, II, "Optically Pumped Continuously Tunable High-Pressure Molecular Lasers," IEEE J. Quantum Electron. QE-13, 907 (1977).

160. H.N. Rutt, "A High-Energy Hydrogen Bromide Laser," J. Phys. D 12, 345 (1979).

161. L. Mannik and S.K. Brown, "Tunable Infrared Difference-Frequency Generation in Lithium Iodate," Opt. Commun. 47, 62 (1983).

162. D. Bailly, R. Farrenq, G. Guelachvili, and C. Rossetti, "$^{12}C^{16}O_2$ Analysis of Emission Fourier Spectra in the 4.5-μm Region: Rovibrational Transitions $^0v_2{}^{\ell}v_3-^0v_2{}^{\ell}(v_3-1)$, $v_2=1$," J. Mol. Spectrosc. 90, 74 (1981).

163. G. Guelachvili, "High-Resolution Fourier Spectra of Carbon Dioxide and Three of Its Isotopic Species near 4.3 μm," J. Mol. Spectrosc. 79, 72 (1980).

164. D. Bailly, R. Farrenq, and C. Rossetti, "Vibrational Luminescence of CO_2 Excited by DC Discharge," J. Mol. Spectrosc. 70, 124 (1978).

165. G.M. Schindler, "Optimum Output Efficiency of Homogeneously Broadened Lasers with Constant Loss," IEEE J. Quantum Electron. QE-16, 546 (1980).

166. R.P. Johnson, "Further Characterization of the 4.4-μm $^{13}C^{16}O_2$ Cacade Laser," Appl. Phys. Lett. 44, 1119 (1984).

167. R.P. Johnson, D. Cornelison, and C.J. Buzcek, "4.4-μm Cascade $^{13}C^{16}O_2$ Laser," Appl. Phys. Lett. 44. 162 (1984).